

NIAC Phase II Orbiting Rainbows: Future Space Imaging with Granular Systems¹

February 2017

Phase II Final Report

by Dr. Marco B. Quadrelli
Jet Propulsion Laboratory
California Institute of Technology

Final Report
Early Stage Innovation
NASA Innovative Advanced Concepts (NIAC)
NNH14ZOA001N

NIAC Phase II Orbiting Rainbows: Future Space Imaging with Granular Systems²

Team:

Dr. Marco B. Quadrelli (P.I., JPL)

JPL Co-Investigators: Dr. Scott Basinger,

Dr. Darmindra Arumugam

R.I.T external collaborator³: Prof. Grover Swartzlander

February 2017

² © 2017 California Institute of Technology. Government sponsorship acknowledged. This research was carried out at the Jet Propulsion Laboratory, California Institute of Technology, under a contract with the National Aeronautics and Space Administration. The cost information contained in this document is of a budgetary and planning nature and is intended for informational purposes only. It does not constitute a commitment on the part of JPL and/or Caltech.

³ The contribution from Rochester Institute of Technology is made under subcontract No.1515295 with Jet Propulsion Laboratory.

Acknowledgements

© 2017 California Institute of Technology. Government sponsorship acknowledged.

This research was carried out at the Jet Propulsion Laboratory, California Institute of Technology, under a contract with the National Aeronautics and Space Administration.

Team Acknowledgments:

Dr. Scott Basinger, JPL Adaptive Optics Section, Co-Investigator
Dr. Erkin Sidick, JPL Adaptive Optics Section
Dr. David Palacios, JPL Adaptive Optics Section
Dr. Michael Rud, JPL Adaptive Optics Section
Dr. Harold Yorke, JPL Science Division
Dr. Henry Garrett, JPL Mission Assurance
Dr. Darmindra Arumugam, JPL Radar Section, Co-Investigator
Dr. Simone Tanelli, JPL Radar Section
Dr. Mike DiNicola, Dr. Hamid Habib-Agahi, JPL Mission Costing
Dr. Andrew Shapiro-Scharlotta, JPL NIAC Program Office
Dr. Adrian Stoica, JPL Robotics Section
Dr. Jonathan Cameron, JPL Robotics Section
Mr. Steven Myint, JPL Robotics Section
Dr. Saptarshi Bandyopadhyay, JPL Robotic Section
Mr. Edward Cabrera, Mr. Randy Odle, JPL Program Office
Prof. Grover Swartzander, Rochester Institute of Technology, Co-Investigator
Prof. Mario Gomes, Rochester Institute of Technology Mechanical Engineering Dept.
Prof. Alan Raisanengy, Rochester Institute of Technology College of Applied Science and Technology
Prof. Linda Barton, Rochester Institute of Technology School of Physics and Astronomy
Prof. Chris Dainty, University College, London, UK
Prof. James Fienup, University Rochester, Rochester, NY
Prof. Francesco Braghin, Politecnico di Milano, Italy
Prof. Alessandro Tasora, University of Parma, Italy

Student contributions:

Priya Kikani (M.I.T.)
Luca Lanzoni (Politecnico di Milano, Italy)
Paolo Ius, Ausra Voveryte (Politecnico di Torino, Italy)
Xiaopeng Peng, Garreth Ruane, Ying-Ju Lucy Chu, Alexandra Artusio-Glimplse, Daniel Schuster, (Rochester Institute of Technology)

Executive Summary

Inspired by the light scattering and focusing properties of distributed optical assemblies in Nature, such as rainbows and aerosols, and by recent laboratory successes in optical trapping and manipulation, we propose a unique combination of space optics and autonomous robotic system technology, to enable a new vision of space system architecture with applications to ultra-lightweight space optics and, ultimately, in-situ space system fabrication.

Typically, the cost of an optical system is driven by the size and mass of the primary aperture. The ideal system is a cloud of spatially disordered dust-like objects that can be optically manipulated: it is highly reconfigurable, fault-tolerant, and allows very large aperture sizes at low cost. This new concept is based on recent understandings in the physics of optical manipulation of small particles in the laboratory and the engineering of distributed ensembles of spacecraft swarms to shape an orbiting cloud of micron-sized objects. In the same way that optical tweezers have revolutionized micro- and nano-manipulation of objects, our breakthrough concept will enable new large scale NASA mission applications and develop new technology in the areas of Astrophysical Imaging Systems and Remote Sensing because the cloud can operate as an adaptive optical imaging sensor. While achieving the feasibility of constructing one single aperture out of the cloud is the main topic of this work, it is clear that multiple orbiting aerosol lenses could also combine their power to synthesize a much larger aperture in space to enable challenging goals such as exo-planet detection. Furthermore, this effort could establish feasibility of key issues related to material properties, remote manipulation, and autonomy characteristics of cloud in orbit. There are several types of endeavors (science missions) that could be enabled by this type of approach, i.e. it can enable new astrophysical imaging systems, exo-planet search, large apertures allow for unprecedented high resolution to discern continents and important features of other planets, hyperspectral imaging, adaptive systems, spectroscopy imaging through limb, and stable optical systems from Lagrange-points. Furthermore, future micro-miniaturization might hold promise of a further extension of our dust aperture concept to other more exciting smart dust concepts with other associated capabilities.

Our objective in Phase II was to experimentally and numerically investigate how to optically manipulate and maintain the shape of an orbiting cloud of dust-like matter so that it can function as an adaptable ultra-lightweight surface. Our solution is based on the aperture being an engineered granular medium, instead of a conventional monolithic aperture. This allows building of apertures at a reduced cost, enables extremely fault-tolerant apertures that cannot otherwise be made, and directly enables classes of missions for exoplanet detection based on Fourier spectroscopy with tight angular resolution and innovative radar systems for remote sensing. In this task, we have examined the advanced feasibility of a crosscutting concept that contributes new technological approaches for space imaging systems, autonomous systems, and space applications of optical manipulation. The proposed investigation has matured the concept that we started in Phase I to TRL 3, identifying technology gaps and candidate system architectures for the space-borne cloud as an aperture. Summarizing the findings, we found that the technology enabling the

Granular Imager is feasible, but is also complex and requires advancements in different areas. During Phase II, technology readiness levels for the various component technologies were determined, as well as mass, power, and cost for a representative system configuration. The wavefront control process follows the following steps of a multistage control architecture: Granular Cloud Shaping, Sub Aperture Coarse Alignment, Figure Control, and Computational Imaging. The main application considered was a reflective imaging system for astrophysics, but many unexplored applications of granular spacecraft are yet to be discovered, including refractive and diffractive systems. Granular media in space can also be used in the radar and microwave bands to enable imaging of previously inaccessible regions of targets with high geophysical variations with time, such as comets. We conducted experiments and simulation of the optical response of a granular lens and, in all cases, the optical response was closely comparable to that of the spherical mirror, we found a marked sensitivity to fill factor and no sensitivity to grain shape. However, we found that at fill factors as low as 30%, the reflection from a granular lens is still excellent. We applied multi-frame blind deconvolution techniques to experimental and numerical data and found the expected image of a reference binary light source. We developed techniques for the modeling and simulation of trapped granular media, and the results of the numerical tests indicate that it is possible, with structural arrangements of rings and plates at different levels of electrostatic potential, to stably confine one or more charged particles, when driven by voltages that can be modulated in time and space. On the experimental side, we have successfully stably levitated single particles and aggregates of multiple particles inside an ion trap.

Our vision is to enable the large-scale electromagnetic utilization of an active cloud of incoherent matter. Near-term proof-of-concept space demonstrations might be possible within a decade, but laboratory-scale tests on Earth are possible much sooner. This concept is technically feasible given that it is drawn from real-world examples of dust/droplet systems like rainbows. Our solution would completely rewrite our approach to ultra-large space-based telescopes for potential NASA applications. All the foundations of the concept are solidly based on established physical laws. The challenge is extending what has been proven in small lenses in an Earth environment to a space environment under various forces and the means to predict and control those forces for a long time to get the full benefit of the concept. There is no guarantee that this breakthrough innovative system will meet the configuration or design of a large aperture system at various parts of the electromagnetic spectrum, but even if a few of those areas are or can be identified, the benefit to NASA will be immense.

Table of Contents

Executive Summary 4

1. The proposed Granular Imager 17

 1.1 Background 20

 1.2 Limitations of Related Current Approaches 24

 1.3 Benefits of the Study 25

 1.4 Contributions to space technologies..... 26

 1.5 Potential Impact..... 26

 1.6 Technical and Programmatic Risks and Mitigation Plan 26

 1.7 Technology Challenges 27

2. Summary of Work Done in Phase II 29

3. Granular Imager Architecture 33

 3.1 JPL Team-A Study 33

 3.2 Imaging Architectures for Astrophysics and Remote Sensing..... 35

 3.3 Applicability of Granular Imager to Astrophysics..... 37

 3.3.1 Exo-Planet Measurement Requirements..... 37

 3.3.2 SNR and Exposure Time Computation 38

 3.4 Applicability of Granular Imager to Earth Science 43

4. Granular Imager Systems Engineering..... 48

 4.1 Interaction of cloud with space environment..... 52

 4.2 System Configurations 53

 4.3 List of Key Enabling Technologies 58

5. Radar Modeling and Experiments 61

 5.1 Radar System Architectures 62

 5.2 Methods to simulate full-wave scattering of arbitrary clouds..... 64

 5.2.1 The finite-difference time-domain modeling and back-projection
 technique 65

 5.2.2 Analytical solutions to scattering using the T-matrix boundary value
 method..... 74

 5.3 Simulations and Experiments using Granular Media 77

 5.4 Radar Experiments 88

 5.5 Effect of cloud geometry and spatial randomness on system performance.... 90

 5.6 Radar imaging of granular media for feedback control..... 91

6. Interaction of Granular Medium with Incident Wavefront 93

 6.1 Sensitivity Studies 93

 6.2 Imaging Properties of Granular Imager: Preliminary Experiment with
 Hexagonal Reflectors..... 106

 6.3 T-matrix modeling approach..... 110

 6.4 Laser confinement subsystem 114

 6.6 Experimental tests of Radiation Pressure 116

7. Granular Imager Optical System Design 120

 7.1 Reflective Optical Designs 120

 7.2 Refractive Optical Designs..... 122

 7.3 Bruggeman Effective Medium..... 122

 7.4 Diffractive Optical Design 124

8. Granular Imager Multi-stage Sensing and Control.....	126
8.1 Wavefront Sensing.....	129
8.2 Multiframe Blind Deconvolution	130
8.3 Sequential Control Steps	130
8.4 Wavefront Sensing and Control System Performance	134
8.5 Contrast Analysis.....	136
9. Granular Imager Integrated Modeling.....	139
9.1 Granular Imager Dynamics and Control.....	141
9.1.1 Reference Frames	142
9.1.2 Kinematics and Kinetics of System in Orbit.....	142
9.2 Confined Aperture Pointing Control	146
9.3 Formation Control, Sensing, and Estimation.....	148
9.4 Granular Media/Molecular Dynamics Simulation Effort	151
9.5 Stochastic Guidance of Granular Medium using Optimal Transport	152
10. Granular Medium Trapping and Confinement	154
10.1 Trapping and Confinement Techniques	154
10.1.1 Paul Trap.....	158
10.1.2 Penning Trap.....	162
10.1.3 Trapping simulations with rings and plates.....	164
10.2 Inverse determination of electric and magnetic fields for confinement	174
10.3 Ion trap Levitation Experiments.....	179
10.4 Other Levitation Techniques	187
10.4.1 Magnetic Levitation for Radiation Pressure Experiments	187
10.4.2 Acoustic Levitation for Radiation Pressure Experiment.....	191
10.5 Alignment Control of Grain under Uniform Illumination.....	195
11. Image reconstruction simulation and experiments	225
11.1 Experimental and Numerical Model in the Far-Field.....	226
11.2 Experimental and Numerical Model in the Near-Field.....	234
1.2 Pathway for Development of a Technology Roadmap	239
12.1 Expected Technology Developments	240
12.2 Proposed roadmap.....	241
13. Papers and reports written as a result of Phase II.....	242
14. Findings and Recommendations	243
14.1 Findings	244
14.2 Recommendations.....	247
15. Bibliography	248

List of Figures

Figure 1. Scenarios of application: astrophysics and planetary remote sensing 17

Figure 2. The Granular Imager: going from a monolithic aperture, to a cloud of dust.
 18

Figure 3. The Granular Imager: a cloud trapped that operates as an active
 electromagnetic device..... 19

Figure 4. Granular Imager in operation. 20

Figure 5. Multiphysics aspects of Granular Imager. 21

Figure 6. Granular Imager technology space..... 22

Figure 7. Evolution of large space telescopes..... 25

Figure 8. Effective imaging system mass and cost vs. effective diameter, for
 monolithic and cloud aperture. Cost-benefit analysis is essential to make the
 cloud aperture more promising compared to the monolithic aperture. 29

Figure 9. Phase II Task Flow. 31

Figure 10. Concept #1: Tomography of small bodies. 34

Figure 11. Concept #2: Habitable Worlds..... 34

Figure 12. Concept #3: Imaging of KBO's..... 35

Figure 13. Concept #4: Advanced Solar Concentrator. 35

Figure 14. SNR vs. apparent magnitude for 10% fill factor..... 40

Figure 15. SNR vs. apparent magnitude for 50% fill factor..... 40

Figure 16. SNR vs. apparent magnitude for 70% fill factor..... 41

Figure 17. SNR vs. apparent magnitude for 100% fill factor..... 41

Figure 18. Exposure time vs. apparent magnitude for 10% fill factor. 42

Figure 19. Exposure time vs. apparent magnitude for 50% fill factor. 42

Figure 20. Exposure time vs. apparent magnitude for 70% fill factor. 43

Figure 21. Exposure time vs. apparent magnitude for 100% fill factor..... 43

Figure 22. Ground resolution vs. fill factor of GI passive radiometer at GEO..... 47

Figure 23. Detector area of passive radiometer at GEO at 1.4 GHz vs. ground
 resolution. 47

Figure 24. Number of grains vs. ground resolution for different grain sizes for
 passive radiometer at GEO at 1.4 GHz. 48

Figure 25. Number of grains vs. ground resolution for different grain sizes for active
 100kW radiometer at GEO at 1.4 GHz..... 48

Figure 26. Granular Imager configuration..... 49

Figure 27. Elements of system in formation. 50

Figure 28. Configuration with multiple apertures. 50

Figure 29. Space and time scales involved in Granular Imager technology..... 51

Figure 30. 0.3 mm hemispherical grain. 51

Figure 31. Sun-Earth L2 orbit and relation to magnetopause..... 53

Figure 32. Prototype configuration for 10 meter Granular Imager with
 Electromagnetic confinement rings..... 54

Figure 33. Configuration inside inflatable canopy. 55

Figure 34. Scalable architecture with multiple inflatable apertures..... 55

Figure 35. Prototype configuration for 10 meter Granular Imager inside inflatable envelope..... 56

Figure 36. System configuration for granular imager inside inflatable envelope..... 57

Figure 37. Inflatable canopy..... 57

Figure 38. Retargeting of granular cloud inside inflatable canopy..... 58

Figure 39. Tomographic and Topographic Imaging using granular media..... 63

Figure 40. Elements of radar system architectures..... 63

Figure 41. The Yee grid in 3D FDTD and the limiting cases for 2D TE and TM simulations in FDTD 65

Figure 42. Forward model for 3D FDTD to include the analytical field propagator (AFP) and the perfectly matched layers (PML) 67

Figure 43. The near-field to far field transform. 69

Figure 44. Three time steps of the point target scattering in 3D. The electric fields on the NFFT plane is a shown for T3 70

Figure 45. The spherically injected pulse used in the simulations. 71

Figure 46. 2D FDTD forward modeling of the comet and time –domain back-projection to obtained inverted dielectric maps..... 72

Figure 47. Time-domain back-projected result of the image for a small inclusion comet model using FDTD. 73

Figure 48. Description of the multiple particle scattering (adapted from [Lee1990, Schafer2008]) 75

Figure 49. Multiple scattering model applied to a few particles..... 79

Figure 50. Analytical computation of scattered field. 80

Figure 51. Results of tomography analysis for ice and water particles..... 81

Figure 52. Sensitivity results for simultaneous cross-track imaging..... 81

Figure 53. Scattering result for finite planar cloud mirror..... 82

Figure 54. Results for bi-static measurement. 84

Figure 55. The point-target simulation for quick-analysis of scattering..... 84

Figure 56. The FDTD technique for full-wave simulation of scattering..... 85

Figure 57. The time-domain back-projection algorithm. 85

Figure 58. Results from experiments using a VNA and horn antenna over a wide microwave band, and using time-domain back-projection for the inversions.. 86

Figure 59. Exact solutions for the radiative transfer from granular media 87

Figure 60. Exact solutions for the radiative transfer from two types of granular media 87

Figure 61. Analysis of re-directed signaling using granular media 88

Figure 62. Experiments to verify imaging through a planar reflector as an idealized granular media cloud. 89

Figure 63. Results of experiment using a planar reflector as a granular media..... 89

Figure 64. Inverted results showing target imaging. 90

Figure 65. Effect of randomness on system performance as simulated using the analytical field solutions described in the previous sections. 91

Figure 66. Granular cloud geometry and forward model assumptions..... 92

Figure 67. One frame of a video for the imaging of a shrinking cloud..... 92

Figure 68. One frame of a video for the imaging of a rotating cloud..... 93

Figure 69. Plots on the random mask without the exclusion process compared to the filled aperture..... 94

Figure 70. Plots on the random mask calculations with disks with Poisson exclusion process (non-overlapping grains), fill factor = 5%. 94

Figure 71. Plots on the random mask calculations with random needles with Poisson exclusion process (non-overlapping grains), fill factor = 5%, using a lognormal grain distribution (shown at right)..... 95

Figure 72. Plots on the random mask calculations with aligned needles with Poisson exclusion process (non-overlapping grains), fill factor = 5%..... 95

Figure 73. Pupil amplitude for 20% fill factor. 96

Figure 74. Point spread function for 20% fill factor..... 96

Figure 75. Contrast metric for 20% fill factor..... 97

Figure 76. Sensitivity of Modulation (MTF) to fill factor..... 97

Figure 77. Generation of elliptical random mask. 98

Figure 78. Generation of elliptical random masks with random orientations..... 98

Figure 79. Pupil partially filled with random masks..... 99

Figure 80. Generation of six different random masks at different fill factor levels.. 99

Figure 81. MTF of six sets of random masks compared to ideal monolithic aperture. 100

Figure 82. Strehl ratio vs. fill factor. 100

Figure 83. Single pixel random mask..... 101

Figure 84. 2x2 pixel random mask..... 101

Figure 85. 3x3 pixel random mask..... 102

Figure 86. 4x4 pixel random mask..... 102

Figure 87. 5x5 pixel random mask..... 103

Figure 88. Rounding edges in single grain..... 103

Figure 89. 5x5 pixel random mask with rounded edges. 104

Figure 90. Rounded edges with more pixels..... 104

Figure 91. 7x7 pixel random mask with rounded edges. 105

Figure 92. Effect of grain shape and pixel size on system MTF..... 105

Figure 93. Different granular lenses used in the experiments..... 106

Figure 94. Schematic diagram of experimental setup to measure the Modulation Transfer Function of the Granular Imager..... 107

Figure 95. two sets of images generated with the hexagonal reflectors and captured at different reflectors-camera distances..... 107

Figure 96. PSF and MTF of ideal lens. 108

Figure 97. Comparison of MTF of ideal lens, spherical mirror, and granular hexagonal mirror. 109

Figure 98. Comparison of experimental modulation transfer function (MTF) of continuous mirror with granular mirror with hexagonal elements..... 110

Figure 99. The cube has faces of $2\lambda/n_{medium}$ across, refractive index $n = 1.59$, and is trapped in water. Force and torque depend on orientation and position, to find equilibrium – we “release” the cube and calculate the change in position and orientation for appropriate time steps 113

Figure 100. The ellipsoid, with refractive index $n = 1.59$, trapped in water 114

Figure 101. Laser confinement subsystem drivers..... 115

Figure 102. Calculation of laser spot size and distance from cloud..... 116

Figure 103. Glass hemisphere in sodium polytungstate solution to achieve near-neutral buoyancy. Frames separated by 4 second intervals, advancing left to right starting from the top: $t = 0, 4, 8, \dots$ [sec]. Laser is turned on at 4sec, off at 12sec, on again at 20 sec. Hemisphere moves toward beam center and flips from bottom side down, to bottom side at $\sim 60^\circ$ 117

Figure 104. Measured transmission spectrum of near-saturated aqueous solution of sodium polytungstate. 118

Figure 105. Refractive index of sodium polytungstate as a function of density at 20°C . Source: Dr. Rainer Kamps, TC-Tungsten-Compounds, Germany. Red dashed lines have been added to indicate the refractive index and density of BK7 glass..... 118

Figure 106. Density (left) and viscosity (right) of sodium polytungstate. Source: GEoliquids Inc. 119

Figure 107. Raytracing model of the predicted forces (x is along the beam and y is transverse) and torque on a hemisphere having a relative refractive index of 1.1. The inset hemispheres show the orientation of the hemisphere that corresponds to the values along the abscissa. Light is assumed to strike those hemispheres from a source on the left hand side of the figure (light travels from left to right)..... 119

Figure 108. A two-dimensional slice of a multi-patch reflective system, with optical rays shown in red, is displayed on the right. An expanded view of the Optical “Bench” is displayed on the left..... 120

Figure 109. An expanded view of the corrector part of the optical “bench” that explicitly show the Shack- Hartmann wavefront sensor in blue. The SH sensor will be below the main optical path to avoid vignetting..... 121

Figure 110. 3D solid optics view of the reflective imaging system concept design with 8 cloud patches forming the aperture. 121

Figure 111. Refractive optical system design, both 2-D and solid optics views..... 123

Figure 112. Diffractive Optical system chromatic corrector. 125

Figure 113. Wavefront Control Architecture..... 126

Figure 114. Electric Field Conjugation Correction..... 127

Figure 115. EFC probing. 128

Figure 116. EFC probe pattern..... 128

Figure 117. EFC probe responses..... 128

Figure 118. Comparison of the actual and estimated pupil fields. 129

Figure 119. Cloud inside capture volume. 131

Figure 120. Modal shapes of hexagonal segment. 133

Figure 121. Influence functions for hexagonal segment (left), and Zernike polynomials used to describe wavefront aberrations (right). 134

Figure 122. High-resolution imager with WFS&C 135

Figure 123. Granular Imager MTF vs. fill factor. 136

Figure 124. Granular Imager MTF vs. wavefront error..... 137

Figure 125. HLC Control system..... 137

Figure 126. Granular Imager HLC Contrast vs Fill Factor..... 138

Figure 127. Granular Imager contrast vs. phase errors..... 139

Figure 128. Granular Telescope Integrated Modeling Diagram..... 139

Figure 129. JPL’s super-precision formation flying telescope [from Mettler2005].141

Figure 130. Geometrical description of orbiting cloud in orbit..... 143

Figure 131. Proposed Formation Command & Control Functional Diagram. 149

Figure 132. Proposed architecture for Formation Laser and RF Metrology Systems.
..... 150

Figure 133. Proposed Formation Estimator 151

Figure 134. Snapshots of molecular dynamics simulation with N=1000..... 152

Figure 135. The inputs to the optimal transport optimization problem..... 153

Figure 136. Evolution of the granular medium distribution under the optimal
transport guidance policy. 153

Figure 137. Various types of electrodynamic traps (from [Davis2012]) 155

Figure 138. Electrode structure of a 3D quadrupole field. 160

Figure 139. Stability diagram for Mathieu equation. 162

Figure 140. Typical trajectories in Paul trap (from [Gosh1995])..... 162

Figure 141. Typical trajectories in Penning trap (from [Gosh1995])..... 164

Figure 142. Two dimensional electrode geometry. 166

Figure 143. 3D geometry, case 1..... 166

Figure 144. 3D geometry, case 2..... 167

Figure 145. 3D geometry, case 3..... 167

Figure 146. Electrostatic potential along x-axis. The two rings are at $x=-1$ m and $x=+1$
m..... 168

Figure 147. Two ring configuration, and components of particle position vs time. 168

Figure 148. Trapped particle trajectories in two-ring configuration, and phase plane.
..... 170

Figure 149. Paul trap configuration, and trajectory vs. time..... 171

Figure 150. Close-up of confined particle trajectories, and phase plane. 171

Figure 151. (left) Trapping system. (right) L2-norm of particles position 173

Figure 152. (left) y-position Vs y-velocity in the case of 100 spheres. (right) Time Vs
current $I(t)$ in the case of 100 spheres 174

Figure 153. N=1000 grains aligned to wavefront..... 175

Figure 154. Re-shaping of a) amorphous cloud to b) disk and c) paraboloid..... 177

Figure 155. Components of Electric field, as a function of Julian date, involved in the
trapping mechanism required to rigidly retarget the parabolic shaped cloud of
60 degrees about the x-axis (in cloud body frame)..... 178

Figure 156. Components of Magnetic field, as a function of Julian date, involved in
the trapping mechanism required to rigidly retarget the parabolic shaped cloud
of 60 degrees about the x-axis (in cloud body frame). 178

Figure 157. Installed ion trap set-up..... 180

Figure 158. Elements of ion trap used in tests (from Newtonian Labs)..... 180

Figure 159. Schematics of ring trap (top), linear trap (middle) and single particle
trap (bottom). From Newtonian Labs..... 181

Figure 160. Top view of ion trap chassis, showing camera with zooming lens,
illuminated laser, and trap..... 182

Figure 161. Photo of levitated cloud of silver coated hollow glass microspheres (100
micron diameter)..... 182

Figure 162. Photo of levitated cloud of silver coated hollow glass microspheres (100 micron diameter)..... 183

Figure 163. Photo of levitated cloud of silver coated hollow glass microspheres (100 micron diameter)..... 183

Figure 164. Photo of levitated cloud of silver coated hollow glass microspheres (100 micron diameter)..... 184

Figure 165. Photo of levitated cloud of silver coated hollow glass microspheres (100 micron diameter)..... 184

Figure 166. Photo of levitated cloud of silver coated hollow glass microspheres (100 micron diameter)..... 185

Figure 167. Photo of levitated grain of silver coated hollow glass microsphere (100 micron diameter)..... 185

Figure 168. Photo of levitated grain of silver coated hollow glass microsphere (100 micron diameter)..... 186

Figure 169. Photo of levitated hexagonal grain (100 micron diameter)..... 186

Figure 170. Photo of levitated grains of silver coated hollow glass microspheres (100 micron diameter)..... 187

Figure 171. Helmholtz coils of unitless radius $r=350$. Left: Magnetic field strength (log grayscale) and field direction (red vectors). Center: Lines of force for a massless particle. Right: Lines of force for a massive particle..... 189

Figure 172. Two coils of radius $r=550$ in a quad trap configuration. Left: Magnetic field strength (log grayscale) and field direction (red vectors). Center: Lines of force for a massless particle. Right: Lines of force for a massive particle..... 190

Figure 173. Calculated value of B_z (dBz/dz) required to levitate (against gravity) a glass hemisphere of radius R atop a diamagnetic film of thickness d for silver, bismuth, and pyrolytic graphite. 191

Figure 174. Stable magnetic levitation of glass hemisphere atop a sheet of pyrolytic graphite with (right) and without (left) exposure to red laser light. 191

Figure 175. Wavelength vs. frequency of sound for acoustic levitation experiment. 192

Figure 176. Acoustic levitation apparatus for measuring laser-induced radiation pressure. 194

Figure 177. Demonstration of acoustic levitation of round glass disks. The front surface reflects light from a light emitting diode array..... 195

Figure 178. Radiation pressure force and torque efficiency plots for a refractive hemisphere of refractive index 1.6 in vacuum. Generated with a modified POV-Ray ray-tracing program. 196

Figure 179. Radiation pressure torque efficiency plots for a refractive hemisphere of refractive index 1.6 in vacuum. Generated with a modified POV-Ray ray-tracing program..... 196

Figure 180. Trajectory of a micron-scale hemisphere at three initial angles of attack (relative to the light source) showing two cycles pure precessional motion (2.8[s]) when illuminated with $\Gamma = 10[\mu\text{W}/\mu\text{m}^2]$ irradiance. Generated using Matlab's ode45 differential equation solver. 196

Figure 181. Results of simulated 3D attitude control of grain guided from +30 degrees to -30 degrees in pitch by one uniform collimated beam (frv= angles,

therr=angular error, werr=angular rate error, aoa=angle of attack, aoad=rate of angle of attack, f=control force, tau = control torque, bottom right plot is irradiance).197

Figure 182. Results of simulated 3D attitude control of grain guided from +10 degrees to -30 degrees in pitch by one uniform collimated beam (theta, phi, psi=Euler angles, therr=angular error, werr=angular rate error, aoa=angle of attack, aoad=rate of angle of attack, f=control force, tau = control torque, bottom right plot is laser intensity)..... 197

Figure 183. *Angles with $\Theta_0 = 10\text{deg}$* 204

Figure 184. *Displacements in scattering and lift directions with $\Theta_0 = 10\text{deg}$* 205

Figure 185. *Fast Fourier Transfer Function of oscillation of the displacement in lift direction with $\Theta_0 = 10\text{deg}$* 205

Figure 186. *Displacement in scattering Vs lift directions with $\Theta_0 = 10\text{deg}$* 206

Figure 187. *Phase diagram of displacement in lift direction with $\Theta_0 = 10\text{deg}$* 206

Figure 188. *Phase diagram of angle of attack with $\Theta_0 = 10\text{deg}$* 206

Figure 189. *Angle of attack with $\Theta_0 = 10\text{deg}$ and $I = 10^6 \frac{W}{m^2}$* 207

Figure 190. *Angle of attack with $\Theta_0 = 10\text{deg}$ and $I = 10^8 \frac{W}{m^2}$* 207

Figure 191. *Fast Fourier Transfer Function of oscillation of the angle of attack with $\Theta_0 = 10\text{deg}$ and $I = 10^6 \frac{W}{m^2}$* 208

Figure 192. *Fast Fourier Transfer Function of oscillation of the angle of attack with $\Theta_0 = 10\text{deg}$ and $I = 10^8 \frac{W}{m^2}$* 208

Figure 193. *Angles with $\Theta_0 = 110\text{deg}$* 209

Figure 194. *Displacements in scattering and lift directions with $\Theta_0 = 110\text{deg}$* 209

Figure 195. *Displacement in scattering Vs lift directions with $\Theta_0 = 110\text{deg}$* 210

Figure 196. *Velocity in lift direction with $\Theta_0 = 110\text{deg}$* 210

Figure 197. *Phase diagram of angle of attack with $\Theta_0 = 110\text{deg}$* 211

Figure 198. *Angle of attack of the hemisphere with the introduction of control with $P_q = 10$, $P_w = 4$ and $\Theta_0 = 10\text{deg}$* 213

Figure 199. *Detailed view of the angle of attack of the hemisphere with the introduction of control with $P_q = 10$, $P_w = 4$ and $\Theta_0 = 10\text{deg}$* 213

Figure 200. *Angle of attack of the hemisphere with the introduction of control with $P_q = 20$, $P_w = 4$ and $\Theta_0 = 10\text{deg}$* 214

Figure 201. *Angle of attack of the hemisphere with the introduction of control with $P_q = 100$, $P_w = 4$ and $\Theta_0 = 10\text{deg}$* 214

Figure 202. *Euler angles with initial conditions equal to $\alpha_0 = 10\text{deg}$ and $\beta_0 = 2.25\text{deg}$. The system is stable*219

Figure 203. Euler angles with initial conditions equal to $\alpha_0 = 10\text{deg}$ and $\beta_0 = 21.5\text{deg}$.
The system is still stable 220

Figure 204. Euler angles with initial conditions equal to $\alpha_0 = 10\text{deg}$ and $\beta_0 = 44.5\text{deg}$. The
system becomes unstable 220

Figure 205. Angle of attack α with initial angular velocity equal to $0 \frac{\text{rad}}{\text{sec}}$ 221

Figure 206. Phase diagram showing periodic motion for a hemisphere at varying of
initial angle of attack α with initial angular velocity equal to $0 \frac{\text{rad}}{\text{sec}}$ 221

Figure 207. Phase diagram showing periodic motion for a hemisphere at varying of
initial angle of attack α with initial angular velocity equal to $1000 \frac{\text{rad}}{\text{sec}}$ 222

Figure 208. Phase diagram showing periodic rocking motion for a semicircular wing
by Swartzlander. 222

Figure 209. Multi-body system (100 hemispheres) controlled using the average
orientation..... 224

Figure 210. Detailed view of the convergence in the multi-body system (100
hemispheres) controlled using the average orientation..... 225

Figure 211. Sketch of granular imager. 227

Figure 212. Schematic of randomized aperture imaging system. 228

Figure 213. Illustration of numerical model of randomized aperture imaging system
in far field scheme..... 230

Figure 214. Sensitivity of MTF to (a) tip-tilt error, (b) piston error, (c) fill-factor (FF)
without phase error, and (d) fill factor, with phase error (tip-tilt $5\lambda/D$, piston 1
wave)..... 231

Figure 215. Image reconstruction result from experimental images of a broadband
(400-730 nm) binary source..... 233

Figure 216. Image reconstruction result from numerical images of a broadband
(400-730 nm) binary source in presence of phase aberration and noise..... 234

Figure 217. A geometric representation of the near field numerical model of a
granular imager. 235

Figure 218. Comparison of image reconstruction results of multiframe blind
deconvolution applied to a numerically simulated far field sequence and a near
field sequence for monochromatic illumination. 237

Figure 219. Schematic of randomized aperture imaging system for a near field
experiment..... 238

Figure 220. Typical near field image from glittered surface using quasi-
monochromatic red light. 238

Figure 221. Comparison of ground truth and near field results. 239

Figure 222. Proposed Roadmap 241

List of Tables

Table 1. State of the art of current telescope technology..... 25

Table 2. Observation dependent parameters, based on Hubble detector model
[taken from Schroeder2000]. 39

Table 3. System Configuration and perceived TRL 59

Table 4. Preliminary system mass..... 59

Table 5. Preliminary system cost. Assumes: 8 granular patches; D=1 m/patch; 0.001
kg/m² areal density; 6 lasers for confinement; 100 W power levels for WFSC;
100 K temperature during operation; Laser system not included..... 60

Table 6. Proposed Design Reference Missions for Granular Imager..... 60

Table 7. Comparison of three optical systems125

Table 8. Comparison to state of the art.125

Table 9, Different behaviors of component plasma depending on the coupling value.
..... 157

Table 10. Values of the distance within the ions in order to obtain a given structural
behavior.157

Table 11. Simulation parameters for case with two rings, and case with one ring and
two plates.170

Table 12. Common data for the simulations of the 3D hemisphere203

1. The proposed Granular Imager

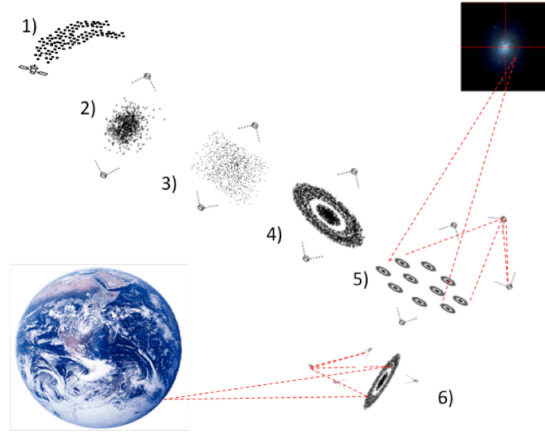


Figure 1. Scenarios of application: astrophysics and planetary remote sensing.

Inspired by the light scattering and focusing properties of distributed optical assemblies in Nature, such as rainbows and aerosols, and by recent laboratory successes in optical trapping and manipulation, we propose a unique combination of space optics and autonomous robotic system technology, to enable a new vision of space system architecture with applications to ultra-lightweight space optics and, ultimately, in-situ space system fabrication. We call this system the Granular Imager (GI).

The Orbiting Rainbows paradigm: The paradigm that makes this granular imager possible is based on: a) avoiding any physical structure and sensing/actuation hardware on the primary aperture, thus lowering the system cost (driven by the mass and complexity of the primary); b) using at-a-distance trapping and manipulation to confine and shape the cloud acting as primary aperture; and c) relaxing the optical figure control requirements by doing the best possible job in software with state-of-the-art computational imaging algorithms.

Typically, the cost of a space-borne imaging system is driven by the size and mass of the primary aperture. The solution that we propose uses a method to construct an imaging system in orbit in which the nonlinear optical properties of a cloud of reflective particles, shaped into a stable surface by electromagnetic means, allow one to form a lightweight aperture of an imaging system, hence reducing overall mass and cost. This new concept is based on recent understandings in the physics of optical manipulation of small particles in the laboratory and the engineering of distributed ensembles of spacecraft swarms to shape an orbiting cloud of micron-sized objects. In the same way that optical tweezers have revolutionized micro- and nano-manipulation of objects, our breakthrough concept will enable new large scale NASA mission applications and develop new technology in the areas of Astrophysical Imaging Systems and Remote Sensing because the cloud can operate as an adaptive optical imaging sensor. While achieving the feasibility of constructing one single aperture out of the cloud is the main topic of this work, it is clear that multiple orbiting aerosol lenses could also combine their power to synthesize a much larger aperture

in space to enable challenging goals such as exo-planet detection. Furthermore, this effort could establish feasibility of key issues related to material properties, remote manipulation, and autonomy characteristics of cloud in orbit. There are several types of endeavors (science missions) that could be enabled by this type of approach, i.e. it can enable new astrophysical imaging systems, exo-planet search, large apertures allow for unprecedented high resolution to discern continents and important features of other planets, hyperspectral imaging, adaptive systems, spectroscopy imaging through limb, and stable optical systems from Lagrange-points. Furthermore, future micro-miniaturization might hold promise of a further extension of our dust aperture concept to other more exciting smart dust concepts with other associated capabilities.

Our objective is to experimentally and numerically investigate how to optically manipulate and maintain the shape of an orbiting cloud of dust-like matter so that it can function as an adaptable ultra-lightweight surface ($<1\text{g}/\text{m}^2$) with electromagnetic properties useful to NASA science missions. Our solution is based on the aperture being an engineered granular medium, instead of a conventional monolithic aperture. This allows building of scalable apertures at a reduced cost, enables extremely fault-tolerant apertures that cannot otherwise be made, and directly enables classes of missions for exoplanet detection based on Fourier spectroscopy with tight angular resolution (~ 100 milliarcsec) and novel radar systems for remote sensing (See Figure 1). These goals are important due to the current need for low-cost implementations of spaceborne imaging system architectures that can enable new science missions.



Figure 2. The Granular Imager: going from a monolithic aperture, to a cloud of dust.

The most innovative aspect of our concept uses light to shape granular media in space. As shown in Figure 2, we want to revolutionize the way telescopes (or antennas) are built by replacing the heavy and complex monolithic aperture in a telescope by a cloud of reflective dust. Inspired by rainbows and scattering from atmospheric aerosols we asked, “Can light radiation pressure techniques create an artificial rainbow or aerosol with specific electromagnetic properties?” *The goal of this research is to identify ways to optically manipulate and maintain the shape of an orbiting cloud of dust-like matter so that it can function as an adaptive surface for imaging objects in the electromagnetic spectrum.* See Figure 3. For example, a coherent

cloud of reflective or refractive micrometer-sized particles could be made to concentrate light in a focal region across a limited frequency band. In this proposal, we equivalently use the term “aerosol” or “swarm” for the cloud of dusty material that we want to manipulate, and we use the term “grain” or “element” to refer to the single elements of the cloud.

This new concept for imaging system architectures relies on an advanced method to build apertures, which results in many benefits, including reduced cost, enabling of apertures that cannot otherwise be made. The advantage of a laser-trapped space system is the potential to enable autonomous reflective, refractive, and diffractive imaging architectures. These systems are ultra-lightweight, and made of very simple, low-cost units. The cloud aperture can distribute itself to large scales (from meters to tenths of meters, using sparse aperture technology), without the need to fill the aperture. It is easy to package, transport, and deploy; is reconfigurable; and can be retargeted and repointed with non-mechanical means. It is a highly self-healing and fault-tolerant system with very low vulnerability to impacts. It can achieve combinations of properties (combined transmit/receive), variable focal length, combined refractive and reflective lens designs, and hyper-spectral imaging. This effort will provide a solution to key issues related to materials, optical manipulation, and autonomy characteristics of clouds in orbit. This would enable new technology in the areas of Astrophysical Imaging Systems and Remote Sensing. Furthermore, it will lay the foundation for large-scale autonomous optical manipulation of micron-sized material in space, thereby truly opening the door to revolutionary applications of in-situ space manufacturing.

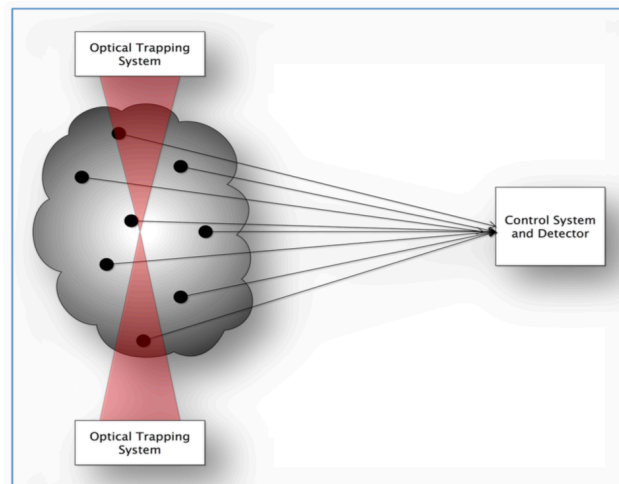


Figure 3. The Granular Imager: a cloud trapped that operates as an active electromagnetic device.

This concept has the potential to completely revolutionize the technology of ultra-large aperture optical elements (e.g., >1,000-km class telescope mirrors, lenses). If successful, this would represent a fundamental breakthrough in our ability to detect extra-solar planets, image surface features, and spectroscopically search for molecular signs of life. A conventional approach to form large scale in-space gossamer

structures is to assemble physical solid surfaces; however, these are fundamentally limited in their maximum size, cost, and ability to be efficiently launched. The proposed method is to use laser-assisted radiation pressure to shape the dust cloud and control the alignment of the elements. Radiation pressure forces and torques applied to various materials types, shapes, and sizes, forming a distributed granular medium provides the opportunity for space system architectures that are suitable for ultra-lightweight space optics, and ultimately, for in-situ space systems fabrications. The proposed investigation matured the concept that we started in Phase I, raising the TRL from 2 to 3 by identifying technology gaps and candidate system architectures for the spaceborne cloud as an aperture. We have examined the advanced feasibility of a crosscutting concept that contributes new technological approaches for space imaging systems, autonomous systems, and space applications of optical manipulation.

A scenario is depicted in Figure 1: (1) the cloud is first released; 2) it is contained by laser pressure to avoid dissipation and disruption by gravitational tidal forces; 3) it is shaped by optical manipulation into a two-dimensional object (coarse control); and 4) ultimately into a surface with imaging characteristics (fine control). The cloud shape has to be maintained against orbital disturbances by periodic figure control, which is also achieved optically. Applying differential light pressure retargets the entire cloud, so that a change of the optical axis can be induced. Selected parts of the cloud are reshaped when required for wavefront control, thus enabling higher quality optics. The entire imaging system is now in full operation, as 5) a multilens system searching for exoplanets, or 6) as a radio antenna engaged in remote sensing investigations. Figure 4 shows a snapshot of the simulation of the Granular Imager in GEO.

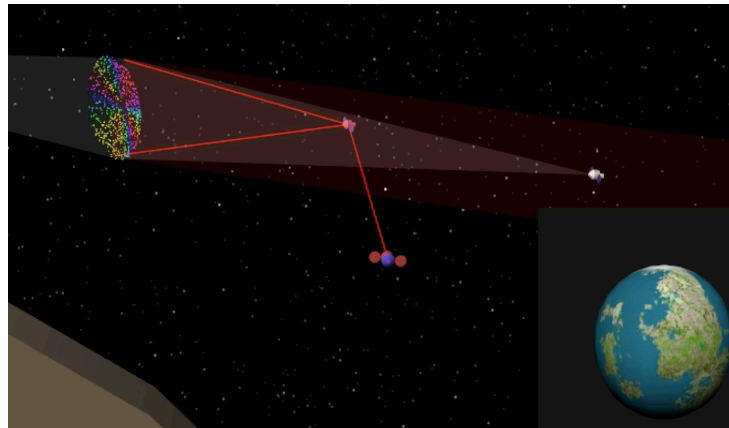


Figure 4. Granular Imager in operation.

1.1 Background

Granular matter is considered to be the 5th state of matter (after solid, liquid, gaseous, and plasma) by virtue of its peculiar response characteristics (cohesiveness, fluid behavior, compactification, phase transformation capability, and other

properties [Friedlander1977, Fuchs1989]). However, the dynamics, controllable properties, and consequent benefits of engineering and manipulating granular matter, such as dust grains, powders, and aerosols, is poorly known to the space exploration community. Inspired by the light scattering and focusing properties of distributed optical assemblies in nature, such as rainbows and aerosols [Kpkhanovsky2006], and by recent laboratory successes in optical trapping and manipulation [Ashkin1970, Ashkin1978, Ashkin1986, Ashkin1997, Bekey1999, BornWolf1964, Dienerowitz2010, Grzegorzcyk2006a, Grzegorzcyk2006b, Grzegorzcyk2014, McCormack2006, Summers2009, Swartzlander2011], we propose a unique combination of space optics and autonomous robotic system technology, to enable a new vision of space system architecture with applications to ultra-lightweight space optics and, ultimately, in-situ space system fabrication. This research will leverage the expertise developed in autonomous space systems technology at NASA/JPL (specifically, formation flying for astrophysical imaging [Mettler2005]); adaptive optics of astrophysical spaceborne observatories, such as the Spitzer Space Telescope, SIM Planetquest, Terrestrial Planetfinder, and the James Webb Space Telescope [Andersen2011, Zhao2005, Mosier1998, Mosier2000]; and recent achievements in optical manipulation at Rochester Institute of Technology on radiation pressure force and torque [Swartzlander2011], to investigate the possibility of deploying, focusing, retargeting the cloud in space, and adding autonomy to the cloud of particles in order to produce an adaptive optics light collector. Typically, the cost of an optical system is driven by the size and mass of the primary aperture. The solution that we propose is to construct an optical system in space in which the nonlinear optical properties of a cloud of micron-sized particles are shaped into a specific surface by light pressure, allowing it to form a very large and lightweight aperture of an optical system, hence reducing overall mass and cost.

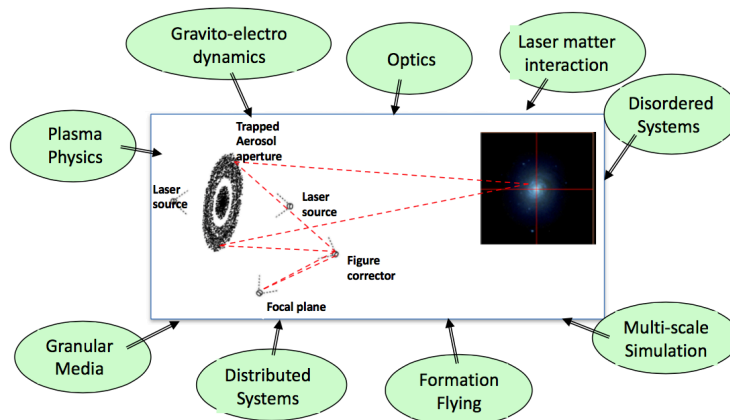


Figure 5. Multiphysics aspects of Granular Imager.

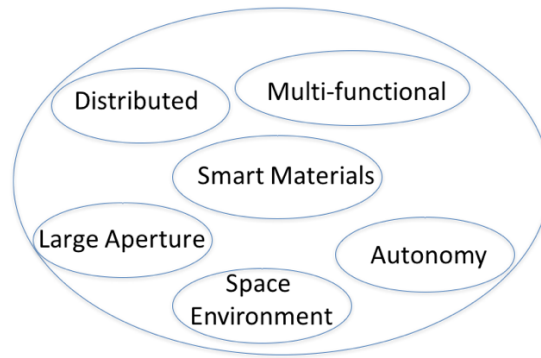


Figure 6. Granular Imager technology space.

This new concept is based on recent understandings in the physics of optical manipulation of small particles in the laboratory and the engineering of distributed ensembles of spacecraft swarms to shape an orbiting cloud of micron-sized objects. Figure 5 shows the multi-physical elements involved in the technology development of the Granular Imager. Figure 6 shows the parameter space of the Granular Imager, which includes distributed spacecraft, multi-functional materials, large apertures smart materials, system autonomy, and interaction with the space environment. The objectives of Phase II were: a) to mature the feasibility of large-scale optical manipulation of granular media to enable optical and radar imaging architectures; b) to identify optimal methodologies to deploy and maintain an active cloud in space; c) to experimentally characterize the optical cooling for motion control and speckle imaging for optical sensing; and d) to provide a system-level assessment through multiscale simulation.

As background, A.J. Palmer [Palmer1980, Palmer1983, Palmer1991], proposed to use an aerosol of dielectric particles as a holographic lens. Labeyrie's pellicle telescope [Labeyrie1970, Labeyrie2005] was the inspiration for a prior NIAC study [McCormack2006]. More recently, the optical trapping of aerosols at the micro-scale has been demonstrated in the laboratory [Dienerowitz2010, Summers2009]. In May 1963, the US Air Force launched 480 million tiny copper needles to create an artificial ionosphere (Project West Ford [Shapiro1964]) to enable across-the-globe communication. The West Ford copper needles were each 1.8 cm long and 0.0018 cm in diameter and weighed only 40 micrograms. They were designed to be exactly half of the wavelength of 8000 MHz microwaves. This length created strong reflections when the microwaves struck the copper needles, in effect making them tiny dipole antennae each repeating in all directions the exact same signal they received. While it was a passive reflector, this experiment demonstrated the large-scale electromagnetic utilization of a passive cloud of incoherent matter. *Our concept is to enable the large-scale electromagnetic utilization of an active cloud of incoherent matter.*

Recent and rapid advances in the optical manipulation area have the potential to revolutionize micro- and nano-manipulation of objects in much the same way that the discovery of optical tweezers, now routinely used for DNA manipulation, did 40 years ago. Although the radiation pressure force on a macroscopic body is weak, a

few milliwatts of laser power are sufficient to achieve a force in the pico-newton range. There is also another major advantage. For some NASA applications, the synthesis of large apertures made of large numbers of emitters/receivers placed with structural disorder is desirable. For a disordered cloud, focusing of light from an object is achieved by modulating the phase of the distributed radiators so as to obtain a conic phase surface; it was observed that by randomizing the emitter positions, the beam achieves better quality [Bekey1999, BornWolf1964, Yavuz1964]. *The ideal system is a cloud of spatially disordered dust-like objects that can be optically manipulated: it is highly reconfigurable, fault-tolerant, self-healing, and scalable to very large aperture sizes at low cost.*

The solution that we propose is to construct a distributed imaging system in space in which the primary element is a cloud of micron-sized engineered particles, shaped along a specific surface by light pressure, allowing it to form a very large and lightweight aperture of an imaging system, hence reducing overall mass and cost. A cloud of spatially disordered dust-like objects can be optically manipulated to be highly reconfigurable, self-healing, and fault-tolerant to allow very large aperture sizes at low cost. The optical system can have a variable focal length, combined reflective and refractive lens designs, and hyperspectral imaging capabilities. Near-term proof-of-concept space demonstrations might be possible in a decade, but laboratory-scale tests on Earth are possible much sooner. This concept is technically feasible given that it is drawn from real-world examples of dust/droplet systems like rainbows. Our solution would completely rewrite our approach to ultra-large space-based telescopes for potential NASA origins, Earth sensing, and potentially also for military applications. All the foundations of the concept are solidly based on established physical laws. The challenge is extending what has been proven in small lenses in an Earth environment to a space environment under various forces and the means to predict and control those forces for a long time to get the full benefit of the concept. There is no guarantee that this breakthrough innovative system will meet the configuration or design of a large aperture system at various parts of the electromagnetic spectrum, but even if a few of those areas are or can be identified, the benefit to NASA and national security will be immense. The adaptive properties of the cloud emerge by virtue of the local anisotropy that can be induced by light, electric, magnetic, and gravitational fields, and/or a combination of them. A modulation of the scattering field of the grains would enable varying optical properties of the entire system. In Phase I, we have identified various options for cloud control and adaptability under various degrees of freedom and actuation mechanisms. With properly chosen materials of the grain, grain size, distribution, density, and orientation, the cloud may indeed behave as a reflective or refractive lens, a set of fringes, or even a hologram.

The focusing of electromagnetic radiation from randomly distributed orbiting arrays has never been investigated. The imaging through retargeting and realization of boresight and wavefront control of an orbiting cloud represent a rich area of investigation, independently of the applications because of the multiple spatial and temporal scales involved to enable an integrated mission design in astrophysical imaging, exoplanet search, large aperture that allows unprecedented high resolution,

and hyperspectral imaging, and spectroscopy, as well as novel radar imaging concepts.

1.2 Limitations of Related Current Approaches

In this section, we identify the limitations of past work, and how we addressed those issues in our study. In the past NIAC study on the laser-trapped mirror [McCormack2006], a main challenge identified by the investigators was related to cloud overheating from a focused beam. Since most of the optical manipulation experiments are done on Earth in water or air, there is natural heat dissipation into a conductive medium. In space, there is no intervening medium (except for the tenuous space plasma, which provides less heat dissipation than air or water), hence cooling in optical binding experiments, such as those carried out in the past NIAC study, cannot be achieved. Although those earlier experiments achieved small-scale coherent structures in a constrained two-dimensional aqueous chamber using spherical particles, large-scale three-dimensional structures composed of optically functional particles in a space environment presented untested challenges. In our study, we avoid tightly focused beams, opting instead to gently nudge the particles using combinations of radiation pressure and electromagnetic torque induced by polarizing the beam with relatively low irradiance, thereby minimizing the source of heat. Furthermore, we engineer the particles to radiate heat and optimize their response to the applied fields. For example, each grain has a tail that may be aligned to the polarization direction of a laser beam, thereby achieving a coherent alignment of all the exposed particles. In the earlier NIAC study, optical binding required weakly interacting spherical particles over a short range. In contrast, our approach assumes non-interacting, arbitrarily shaped particles that may be widely spaced.

Figure 7 depicts the evolution of large space observatories, indicating that solutions with very low area to mass ration are highly desirable. The uniqueness and innovation of our concept lies in that: a) it would be a very lightweight, self-healing system, leading to areal densities of 1 g/m^2 or less, compared to 10 kg/m^2 of an inflatable antenna; b) one cloud could combine with other clouds to form much larger apertures than the 6.5-meter size of the James Webb Telescope; c) it would be easy to transport and deploy, not requiring structural elements; and d) line-of-sight (LOS) retargeting and figure control would be realized optically. These properties enable new mission architectures, and are in contrast to current state-of-the-art systems, which are limited to much smaller sizes and are quite massive. Table 1 compares the Granular Imager to existing telescope technologies.

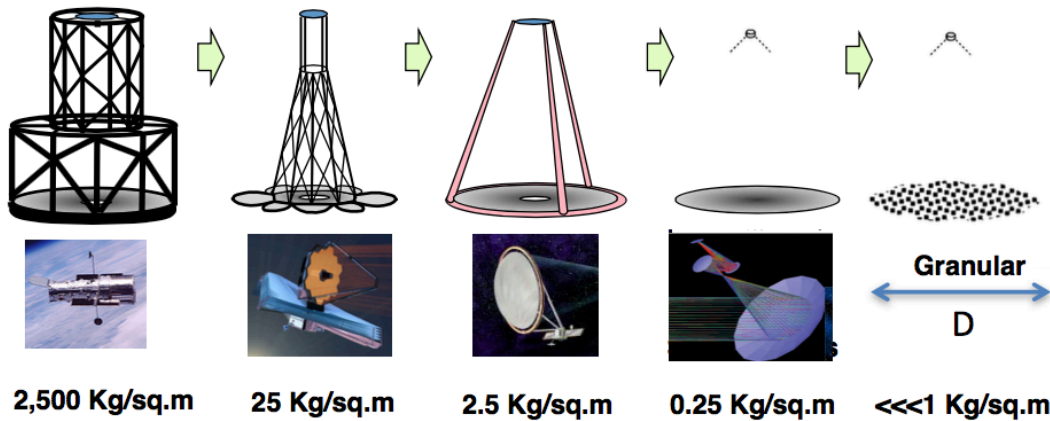


Figure 7. Evolution of large space telescopes.

Table 1. State of the art of current telescope technology.

Metric	Conventional Mirror SoA	Light-Weight Mirror SoA	Inflatable	Liquid mirror	Granular Imager
Mass Areal Density	40-100 kg/m ²	10-20 kg/m ²	<5 kg/m ²	100-200 kg/m ²	<<0.1 kg/m ²
Surface Figure Error	10 nm RMS	14 nm RMS	<5 micro-m RMS	<5 micro-m RMS	<100 nm RMS
Surface microroughness	<5Å	<10Å	500 nm	20 nm	< 100Å
First free-free mode	>100Hz	>100Hz	>1 Hz	>10 Hz	< 1 mHz
Size	0.1 to 2.4m and larger	0.3 to 1.35m and larger	1 to 10 m	1 to 10 m	> 10 m
Deployable	No	No	Yes	No	Yes
Thermal stability	Low CTE	Thermally controlled	Thermally Controlled	Thermally Controlled	Thermally Controlled
Formation Flying	No	No	No	No	Yes
Wavelength	Visible	Visible	Visible/Radar	Visible	Visible/Radar
Orbit	L2	L2	LEO	Ground	GEO/L2
Backing Structure	Yes	Yes	Yes	Yes	No
Packaging	Complex	Complex	Medium	N/A	Simple
Retargeting	RCS	RCS	RCS	No	Optical/EM
Fault-tolerance	Low	Low	Low	Low	High

1.3 Benefits of the Study

The novel concept hereby proposed addresses challenges for development of: a) new autonomous systems, as it may open the door to innovative applications of formation flying and autonomy technology in space; b) novel approaches to large

precision imaging systems; and c) innovative applications of granular media as multi-scale, multi-physics, multi-functional systems. In Phase II we have assessed the basic elements of granular imaging systems in the context of two relevant mission scenarios: an astrophysical imager and a radar mapper. From a science perspective, the granular imager concept will open new frontiers of exploration and scientific discovery in space science. From a robotic system perspective, we have studied autonomy solutions and multiscale behavior of complex aerospace systems. From the materials perspective, we have explored a novel use of granular media in space. From a systems perspective, we have matured the Phase I concept to TRL 3.

1.4 Contributions to space technologies

Granular imaging systems address the following NASA's Space Technology Grand Challenges: a) TA04, Robotics and Autonomous Systems, as we may open the door to innovative applications of formation flying and autonomy technology for large optical systems in space; b) TA08, Science Instruments, Observatories, and Sensor Systems, as we develop a system that may provide advancements in high contrast imaging, optical systems, and detector and focal planes; c) TA12, Materials, Structures, Mechanical Systems and Manufacturing, as we address innovative types of lightweight and multifunctional structures.

1.5 Potential Impact

Similar to the way optical tweezers revolutionized micro- and nano-manipulation of objects, our breakthrough concept will enable new large-scale NASA mission applications and develop new technology in the areas of Astrophysical Imaging Systems and Remote Sensing because the cloud-based system can operate as an adaptive optical/microwave imaging sensor. While achieving the feasibility of constructing one single aperture out of the cloud is the main topic of this work, it is clear that multiple orbiting aerosol lenses could also combine their power to synthesize an array of much larger aperture in space to enable challenging goals such as exoplanet detection. Furthermore, this effort will establish feasibility of key issues related to material properties, remote manipulation, and autonomy characteristics of clouds in orbit. There are several types of endeavors (science missions) that could be enabled by this type of approach, including: new astrophysical imaging systems, exoplanet search, large apertures to allow for unprecedented high resolution for discerning continents and important features of other planets, hyperspectral imaging, adaptive systems, spectroscopy imaging through limb, and stable optical systems from Lagrange points. Furthermore, future micro-miniaturization might hold promise of a further extension of our dust aperture concept to other more exciting smart dust concepts with other associated capabilities.

1.6 Technical and Programmatic Risks and Mitigation Plan

A key programmatic risk was that the scope of NIAC Phase II was not deemed sufficient for conclusive optical cooling demos at large scales and for system-level tests. These might need to be addressed in follow-on activity. Nevertheless, sufficient

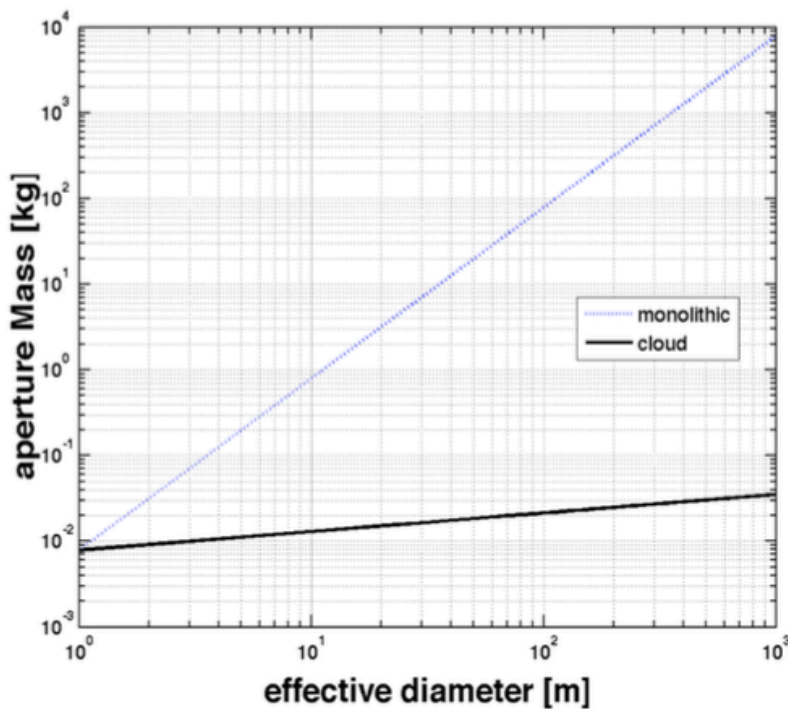
progress was made to mature the concept to TRL 3. From an operational perspective, the key concept maturation risks related to infrastructure cost are excessive infrastructure (spacecraft in formation, multiple lasers), and insufficient system testing and system integration. Mitigation plan: Explore alternative solutions for optical trapping, which include one laser system and electrostatic/magnetic containment fields, and propose a follow-on path with extensive ground testing program at component level and a sequence of in-orbit demos (from small-scale demos in KC-135 and ISS, to suborbital demos) to progressively demonstrate system integration. The key concept maturation risks related to obtaining the required system performance are related to insufficient system verification and validation. Mitigation plan: Complete extensive error budgeting at imager scale, cloud scale, and granular medium scale, which uses system simulation to predict performance at system level, while the complexities of the physics are provided experimentally. The key concept maturation risks related to system development time are insufficient maturity of the cooling and speckle imaging experiments, and the technological complexity of these potential risks. First, high levels of light scattering may be deleterious for image formation. This is a serious problem for reflective imagers. Mitigation plan: Consider refractive and diffractive options. Second, it is challenging to provide the needed phase coherence between elements of the cloud to be able to be of any use in visible band. Mitigation plan: Address problem in the radar band. Third, optical manipulation at large scales may require very large laser power, or too many lasers, hence excessive cost to implement. Mitigation plan: Currently, the Air Force uses 1-MW lasers for missile defense, so in 20–30 years, larger laser power (possibly relying on space-based solar power) will likely be available. Fourth, any dust clouds might create unwanted orbital debris due to leakage. However, this issue can be dismissed by the fact that at altitudes >1,000 km, orbital debris smaller than 10 cm is not easily tracked, and the collisional cross-section of debris in the micron size is negligible compared to larger debris. Mitigation plan: Turn off one bank of the counter-propagating containment lasers to apply preferential pressure to cloud, which will be accelerated away into space. Fifth, electrostatic charging might cause undesired aggregation and clustering that might affect the surface accuracy of the aperture. Mitigation plan: Explore appropriate material for grains and electrostatic behavior. Lastly, the previous NIAC study on the Laser-trapped Mirror [Grzegorzcyk2014] identified a difficulty with the lack of natural optical cooling of the grains in space. Mitigation plan: Our work in Phase I [Quadrelli2012] has led to the discovery that we can induce optical cooling *actively* via modulation of the light polarization, thus reducing the cooling problem to an active control problem.

1.7 Technology Challenges

Key technologies that were relevant to mature the concept in Phase II are discussed next. Granular imaging systems will require complex multistage control methodologies and diffractive optics techniques. To achieve this goal, the Phase II multiscale system simulation of the science campaign was essential to assess system-level performance for representative scenarios. Also, system-level integrated modeling and simulation of reflective, refractive, and diffractive configurations in different frequency bands is essential to flow down requirements. Speckle imaging experiments are essential to demonstrate that optical imaging based on spatial disorder is practical, and we have begun experimenting with computational optics

techniques (IBD) to retrieve the image in the presence of noise. Optical cooling experiments are essential to demonstrate the multiple levels of precision in trapping and containment of the granular aperture, and were done in Phase II. Recent work based on the optical vortex [Valdlen2010] expands optical manipulation of particles into a gas media and provides full control over trapped particles, including the optical transport and pinpoint positioning of 100 micron objects over a meter-scale distance with 10 micron accuracy. Finally, a cost-benefit analysis is essential to make the cloud aperture more promising compared to a monolithic aperture. Preliminary evaluations of total system cost done in Phase I, based on existing cost models available in literature [Stahl2010], demonstrate the enormous cost reduction for the orbiting cloud, compared to a monolithic system (Figure 8). In our view, the cost savings alone was sufficient reason to mature the concept in Phase II.

The key feasibility issues related to cost are system testing and system integration. In this regard, the in-depth study of reflective, refractive, and diffractive systems will provide a unique approach to flow down imaging requirements down to the cloud level. The key feasibility issues related to system performance are analyzing whether there is sufficient sensing and control authority to ensure a stable wavefront through the granular medium. In this regard, we will also explore imaging architectures in a less demanding frequency band (i.e., radar), thus accelerating the maturation at the system level. The key feasibility issues related to risk are providing sufficient system verification and validation, and the development of a multiscale system simulation will make requirement verification possible. The key feasibility issues related to system development time are sufficient maturity of the cooling and speckle imaging experiments. Successful cooling experiments (critical technology) will enable the demonstration of the concept feasibility in a ground laboratory, and successfully accomplishing these experiments will contribute to raising the system TRL.



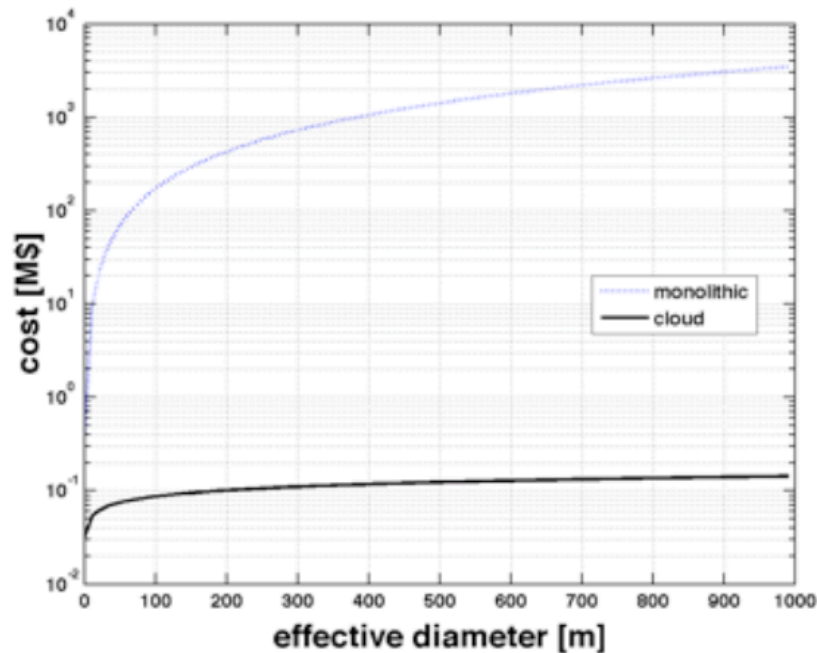


Figure 8. Effective imaging system mass and cost vs. effective diameter, for monolithic and cloud aperture. Cost-benefit analysis is essential to make the cloud aperture more promising compared to the monolithic aperture.

2. Summary of Work Done in Phase II

The approach for Phase II combined both experiments and simulations to mature the concept to TRL 3. Our specific near-term objective was to conduct small-scale experiments to demonstrate optical manipulation of tenuous granular media in water, complemented by a parallel analysis effort to model and simulate the behavior of the granular medium as an element of an imaging system in orbit being controlled by light.

The design concept in Phase II followed a top-down approach. At the large-scale, the imaging system is held in shape by means of formation flying technology. Macroscopically, the aerosol cloud forming the primary aperture can then be thought of behaving as an equivalent rigid object. Established wave front sensing and control techniques of adaptive optics are then used to stabilize the image assuming the granular aperture behaves as an equivalent monolithic aperture. We then invoke methods of sparse aperture technology, such as Golay arrays [Brady2009], to precisely formation-fly many clouds, which, at the microscale, are spatially random, but at the macroscale form a regular array. Through optical manipulation technology, we sense and control the average alignment of the grains within each cloud to provide a cloud figure shape that is adequate for our goals. Therefore, the top-down formation flying and adaptive optics approach merges with the bottom-up optical manipulation approach to achieve our goal. The elements of this approach are discussed next.

In Phase II, the following steps were completed to mature the concept: a) an enhanced focus on reflective, refractive, and diffractive optical systems; b) exploration of radar imaging architectures and identification of the most promising applications; c) experimentation and simulation to prove the active cooling approach based on optical feedback mechanisms; and d) use of integrated modeling and simulation to determine adaptive optics needs required by aperture to function as an imaging system. Experiment design, as well as preliminary experimental work conducted in Phase II, were based on demonstrating the grain cooling and alignment approach on an optical bench.

In flow diagram form, Figure 9 describes the overall Phase II task flow. It starts in the upper left corner with the particle simulation engine, which was developed in Phase I. This engine computes the motions of the particles that make up the primary optic at the granular level. The orange rectangles represent the microscale control system of the particles. Its purpose is to “corral” the particles, keep them functioning as a unit, and ensure the optical properties of the conglomerate meet the requirements for the next stages of control. From the position and orientation of the particles, a complex electromagnetic pupil function is computed, from which the optical figure and pupil can be determined (green box). The red boxes represent the next stage of control, which is the relative position and orientation of the separate spacecraft imaging system. The spacecraft has its own thrusters and reaction wheels to maintain precision optical alignment using a laser metrology truss developed at JPL as a precision sensor. The light blue boxes represent the mid-level control systems. A STOP integrated model was created for a single patch/cloud and its corresponding correction/collections system. Drivers to the STOP model include thermal variations (purple circle) based on the trajectory of the system relative to the Sun and other thermal sources. The STOP model has two main control systems, one for LOS correction and an adaptive optics control system that uses a Shack-Hartmann sensor to control a deformable mirror. Combining information from multiple STOP models (one for each patch), a time-varying PSF is computed (green box). The relative positions of each cloud may vary with respect to each other; therefore, an outer control system for maintaining precision phasing between the patches is necessary (shown in yellow). An IPO (In-focus PSF Optimizer) is another WFS&C algorithm developed at JPL for segmented optical systems. This algorithm will drive the optical delay lines to maintain the relative phase of each patch and will also provide feedback information to the LOS control to maintain pointing. Finally, the time-varying PSF is convolved with an image (or “scene”). Speckle imaging and multiframe blind deconvolution algorithms was investigated to “clean up” the imagery to get an accurate estimate of the original scene.

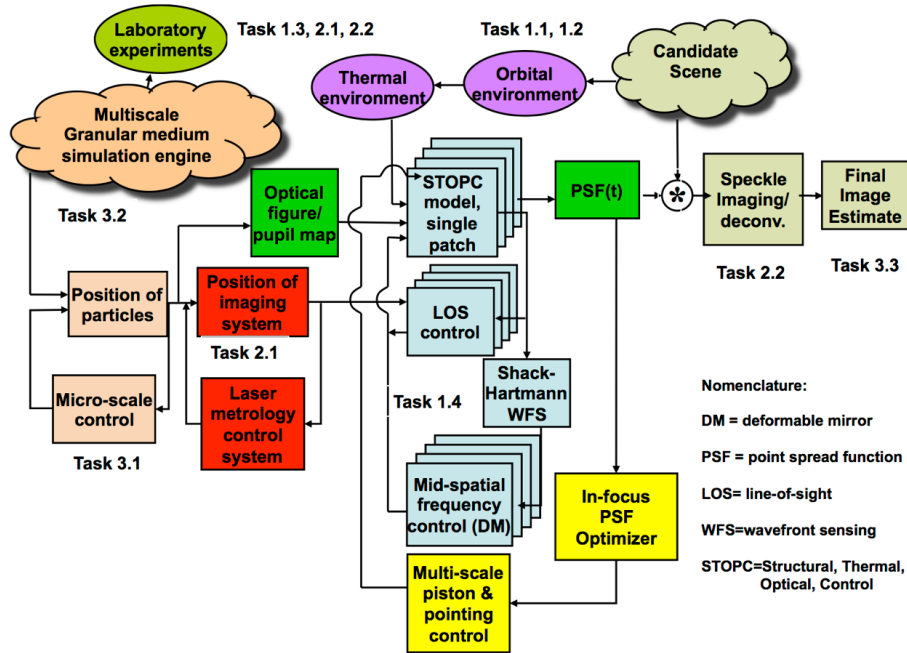


Figure 9. Phase II Task Flow.

Accordingly, the Phase II work was distributed in the following tasks/subtasks:

2.1 Tasks Related to Systems Engineering

Task 1.1: Imaging systems requirements: Imaging requirements for exoplanet imaging and spectroscopy was researched and flowed into our optical system design. JPL has a strong history of exoplanet technology development coupled with real experience via the Caltech astronomy department. In addition, JPL designed the coronagraphic masks for the James Webb Space Telescope. We leveraged this experience to put together an imaging error budget via existing software models. In Phase I, we developed Code V optical system designs for three different applications of the aerosol optic since we didn't limit ourselves to just one concept for the "cloud". In Phase II, we converted these optical designs to a JPL-based optical analysis package called "MACOS", which allowed us to compute optical sensitivities of the system and thereby create a covariance-based error budget for the individual optical elements. The STOP model that provides a time-domain simulation of the entire system also uses the optical sensitivities.

Task 1.2: Conceptual radar system study: In this task, we explored the physics of clouds applied to radar remote sensing instruments. Specifically, we will developed a vector radiative transfer method for use with short wavelength radar instruments, and a Rayleigh or small particle approximation method for use with long wavelength radar instruments. We validated the models using a full-wave electromagnetic solver for a specific set of fixed configuration and property of the cloud. Next, we developed a few radar instrument architectures that utilize the models developed to obtain higher-resolution remote sensing. Specifically, we developed a radar imaging architecture for topographic mapping where the cloud physics modeled using the radiative transfer theory is shown to provide higher resolution. Similarly, to study the operation on the other end of the spectrum, we developed a radar sounding architecture for subsurface or ionospheric sounding,

where the cloud physics modeled using the Rayleigh phase or the small particle approximation method is shown to provide higher resolution.

- Task 1.3: Theoretical analyses at grain scale: A theoretical description of the forces and torques on a small umbrella-shaped optical element was developed. The model includes radiation pressure and polarization effects. The model was used to develop a means to achieve a fixed attitude and position of a perturbed umbrella-shaped granular element in space. The control process was used to minimize the rotational and kinetic energy of each element, thereby cooling the motion of the granular medium.*
- Task 1.4: Adaptive optics approaches: Controllable spatial frequency and dynamic range requirements for our system were determined based on the expected residuals of the microscale control (e.g., laser containment, optical lift, corraling, etc.) of the aerosol cloud. The secondary WFS&C system, which uses a Shack-Hartman sensor and a deformable mirror for correction, was designed to meet these requirements. A model of the WFS&C system was constructed, leveraging previous work from other programs. This model was part of a time-domain simulation that, ultimately, will use the particle motion model as a driver and will assess the overall performance by applying corrections on the deformable mirror and evaluating the resulting wavefront.*
- Task 1.5: Cost-benefit analysis and roadmap development: Cost-benefit analysis is essential to make the cloud aperture more promising compared to the monolithic aperture. In Phase I, we started an effort on the preliminary evaluation of total system cost, based on existing cost models available in literature. The preliminary results of these computations, i.e., the effective aperture mass and imaging system cost vs. effective diameter, for monolithic and cloud apertures, have already demonstrated the enormous cost reduction for the orbiting cloud, compared to a monolithic system. This preliminary effort constitutes the basis of a more detailed cost-benefit analysis that was conducted in Phase II, which culminated in a detailed assessment of cost and identification of key technology gaps for the selected system architectures. The roadmap for technology maturation was also developed in this task.*

2.2 Tasks Related to Experiments

- Task 2.1: Optical manipulation experiments: Micro-structures composed of space-qualified CP1 polyimide were micro-fabricated at the R.I.T. Semiconductor and Microsystems Fabrication Laboratory. Radiation pressure and torque experiments were conducted on single spinning structures under free-fall or in a neutrally buoyant liquid to investigate and demonstrate stable control of the position and attitude of the element.*
- Task 2.2: Optical imaging experiments: For the scope of this Phase II task, experiments were done in water, since they were achievable in the timeframe of the task. In water, we showed that hemispherical bodies aligned with the control laser direction. A laboratory model of a thin swarm of reflectors was built by randomly adhering small mirrors across the concave surface of a blackened parabolic reflector. The piston and pitch of the elements were randomized, but stationary. A collimated laser beam, collinear with the axis of the parabolic reflector was used to determine the point-spread function speckle pattern. The laser was then removed to allow the parabola to collect light from a scene of distant paraxial point sources.*

The measured speckles, combined with the PSF, were used to reconstruct an image of the paraxial scene.

Tasks Related to Numerical Studies

Task 3.1: Optical manipulation simulation studies: Previously developed ray-tracing software at RIT was used to compute the forces and torques on the individual grain. The analysis was used to refine the design of the grains and to motivate measurements in our laboratory experiments.

Task 3.2: Physics-based system simulations: These simulations have the ultimate goal to verify and validate system requirements, and were further developed to form a multiscale, physics-based simulation engine with which to test operational architectures of the imaging system in different frequency bands.

Task 3.3: Imaging simulations: Since our optical system will be continuously in motion, we expect that it will require extensive image processing utilizing multiple fast-frame images to estimate a single resolved scene. In Phase I, we did a comprehensive literature search of various phase retrieval and phase diversity approaches that could be used for this system. In Phase II, we created an image-processing plan, develop simulations of the techniques we plan to use, and evaluated their effectiveness for imaging scenarios in the visible and microwave bands.

3. Granular Imager Architecture

3.1 JPL Team-A Study

The Team-A study goals were to identify the most promising science mission for a granular imager. The study objectives were to complete the parameter space for a granular imager, identify the strongest science mission for this technology, generate one or more mission architectures for the strongest science mission, and identify driving mission requirements. The key results were that the team identified opportunities and challenges for a range of wavelengths, then brainstormed promising future mission concepts that would take advantage of granular imager technology. The four most promising of these were explored in more detail. Finally, the team outlined a technology development roadmap to take the concept from its current state to flight. The Granular Imager configuration considered in this Study included the following assumptions:

- The Granular imager (GI) will be in geosynchronous Earth orbit (GEO)
- Focal length about 100 km
- Particles could stay in orbit for a long time
- GI is reconfigurable and can be "self-healing"
- GI is susceptible to solar wind, coronal mass ejections are really bad
- Need 6 trapping-system S/C per GI (per cloud)
- GI fill factor is ~30%

Finally, the Study resulted in the definition of several mission concepts for the Granular Imager, as depicted in Figures 10 through 13.

Tomography of Small Bodies	
<p><u>Concept</u></p> <ul style="list-style-type: none"> • Orbit comet/asteroid • 80 to 200 MHz (radar) • 3- to 10-m dia cloud • Metallic or metamaterial cloud • High fill factor (~50%) • ConOps: <ol style="list-style-type: none"> a. Redirected imaging b. High-resolution imaging 	<p><u>Driving Requirements</u></p> <ul style="list-style-type: none"> • High fill factor (~50%) • Control of cloud while in orbit (position) & alignment • GI w/o balloon • Low mass & power of shaping lasers
<p><u>Needed Technologies</u></p> <ul style="list-style-type: none"> • Cloud control • (See driving reqts) • Metallic and metamaterial cloud properties • Formation-flying & control <ul style="list-style-type: none"> • Need orbital demonstration 	<p><u>Going-Forward Plan/Potential Sponsors</u></p> <ul style="list-style-type: none"> • 4X • DoD • Planetary defense • Near-Earth Objects Office

Figure 10. Concept #1: Tomography of small bodies.

Habitable Worlds	
<p><u>Concept</u></p> <ul style="list-style-type: none"> • At L2 • Near-IR to Vis, 0.5 to 2.0 μm • 15- to 20-m-diameter primary • Order-of-magnitude light-gathering [improvement] over JWST • GI particles in a balloon • Low fill factor • Sun-shade for thermal loads • Starshade for light-suppression 	<p><u>Driving Requirements</u></p> <ul style="list-style-type: none"> • Balloon material for Prime Mission • Pointing stability (m to μm stability) • Vibration isolation
<p><u>Needed Technologies</u></p> <ul style="list-style-type: none"> • Light-gather vs. fill factor • Star-shade/occultation mask coronagraphy • Straylight mitigation <ul style="list-style-type: none"> • Need experiments • Formation-flying and control <ul style="list-style-type: none"> • Need orbital demonstration • More advanced computational imaging 	<p><u>Going-Forward Plan/Potential Sponsors</u></p> <ul style="list-style-type: none"> • Getting to orbital demo w/ component maturity • 7X • 8X

Figure 11. Concept #2: Habitable Worlds.

Imaging of KBOs	
<p><u>Concept</u></p> <ul style="list-style-type: none"> • At L2 • 25 to 50 μm (emissions) (temperature) • 0.3 to 0.9 μm (optical) (composition) • 15- to 20-m-diameter primary • GI particles in a balloon • Obtain spectra • Sun-shade 	<p><u>Driving Requirements</u></p> <ul style="list-style-type: none"> • KBO tracking • Pointing and stability • Passive cooling of telescope structure
<p><u>Needed Technologies</u></p> <ul style="list-style-type: none"> • Straylight mitigation <ul style="list-style-type: none"> • Need experiments • Formation-flying & control <ul style="list-style-type: none"> • Need orbital demonstration • Inverse advanced computational imaging 	<p><u>Going-Forward Plan/Potential Sponsors</u></p> <ul style="list-style-type: none"> • 4X • Near-Earth Object Office

Figure 12. Concept #3: Imaging of KBO's.

Solar Concentrator	
<p><u>Concept</u></p> <ul style="list-style-type: none"> • LEO (Sun-synchronous), secondary @ GEO • Reflector • Send light to a secondary S/C • Convert thermal to microwave @ 85% efficiency • Transmit microwave power to whoever needs it 	<p><u>Driving Requirements</u></p> <ul style="list-style-type: none"> • Track the Sun • Align GI primary to secondary
<p><u>Needed Technologies</u></p> <ul style="list-style-type: none"> • Align GI particles such that reflected light is sent to a focus by the secondary S/C • Thermal control • Solar pressure active control • How to get microwaves from GEO 	<p><u>Going-Forward Plan/Potential Sponsors</u></p> <ul style="list-style-type: none"> • DoD • DOE • Aerospace Corporation

Figure 13. Concept #4: Advanced Solar Concentrator.

3.2 Imaging Architectures for Astrophysics and Remote Sensing

The three optical system designs from Phase I were evolved to become a part of a larger simulation, as described in the Work Plan. The first optical design assumed the

cloud would contain reflective particles and be controlled in a manner to produce a semi-coherent reflective phase sheet. Although not continuous, the surface would need to have variations less than $\lambda^2/24\lambda$, where λ is the bandwidth of light, to achieve meaningful imagery (in any frequency band)). A second design treats the cloud as a refractive element, e.g., a lens. Using effective medium theory, we derived a theoretical focal length of a system based on particles having an index of refraction close to glass and having a fairly dense (1 part in 1000) fill factor. Finally, we developed a third optical system design for a diffractive, or “holographic”, lens such as Palmer [Palmer1980, Palmer1983, Palmer1991] had outlined. Compared to refractive systems in the visible band or radar imagers in the microwave band, which do not require grain level control, reflective and diffractive imaging systems would require fine control down to the grain level.

The control system architecture for each of these designs was developed and simulated as well in Phase II. The highest bandwidth control system is the line-of-sight (LOS) control system, which uses a fast steering mirror to maintain the pointing of each of the individual cloud optics. The next fastest control system is the mid-spatial frequency wavefront sensing and control (WFS&C) system, which uses a Shack-Hartmann (SH) wavefront sensor to control a deformable mirror to correct for surface figure changes of the primary optic up to several waves. We plan to use a combination of fast steering mirror and deformable mirror, which is currently under development by Northrop Grumman Xinetics. Requirements for the temporal bandwidth of the LOS control system will need to be evaluated as well as the necessary pitch, stroke, and speed required of the deformable mirror wavefront sensing and control system. Finally, the optical delay lines of each individual optical system will also need to be evaluated to keep each of the “patches” of the multiscale design in phase with each other. Since we expect the drivers of the overall patch movement to be thermal effects, the bandwidth of this control system is expected to be much lower than the previous two systems. The Structural Thermal Optical (STOP) simulation model will allow us to explore the requirements for this integrated control system. The diffractive optical system design created in Phase I was a strictly monochromatic design, however, it was mentioned in the final report that JPL has experience in designing a diffractive optical correction system with a 10% bandwidth.

To combine the light from the separate clouds to create an effectively larger aperture, we proposed to use a technique developed at JPL called In-focus Point Spread Function Optimizer (IPO) to optically maintain the relative positions of all the clouds. This technique captures non-optimal images from a point source on the science camera and matches the images to a physical model of the system. The simulation will allow for each individual cloud to move with respect to the other clouds and IPO will determine each cloud’s position and orientation with respect to the collector spacecraft. Once IPO determines these values, it can compensate using the optical delay line for phase differences between the patches and the fast steering mirror for LOS differences. IPO is a proven, robust technique. Prof. Fienup and his research group at the University of Rochester [Fienup2010] have had tremendous success using nonlinear optimization techniques with numerous kinds of diversity to solve for phase errors and estimate the object. They solve for the full complex pupil function using phase-diverse data. In addition, they have invented a new kind of diversity, called transverse translation diversity, which uses a shifting pupil mask to provide image diversity. Our design includes a microshutter array in the pupil plane for a similar result. Thurman and Fienup [Fienup2010] described an algorithm that

can handle random misregistrations of the point-spread functions (PSFs) collected for a single image data set, a situation that our ever-shifting aerosol optic may find itself needing to exploit. To combine data from several apertures, a piston diversity technique was also developed. In addition to obtaining satisfactory images from a single cloud, we are also planning on combining data from multiple clouds to increase or effective aperture.

In Phase II, we explored phase diversity to estimate the object under investigation. Phase diversity is a technique to jointly estimate an object, i.e., extended scene, and phase errors in an optical system. The phase errors are used to deconvolve a better estimate of the measured object. This technique requires a set of diverse images to be taken nearly simultaneously. The most common form of diversity is “phase diversity”, and the phase is most commonly a focus term. In other words, a set of imagery, each with different focus terms, can be used to create a better overall estimate of the scene under interrogation. Multiple techniques exist to solve for phase errors, including iterative and using global optimization. If the diversity between images is not known or not known well, then other techniques are used such as “blind deconvolution.” Multiframe blind deconvolution was developed for speckle imaging, where a precise measurement of a stellar object from the ground is not possible due to the changing index of refraction caused by the Earth’s atmosphere.

3.3 Applicability of Granular Imager to Astrophysics

3.3.1 Exo-Planet Measurement Requirements

This section makes extensive use of the Exo-C STDT Final Report (2014). The work accomplished by the Exo-C mission concept study is leveraged to quickly derive system requirements to achieve a similar mission. The direct detection of exo-planets requires an imaging system to be able to detect the faint reflected light from the exo-planet while not being blinded by the glare of the parent star the planet orbits. This places stringent requirements on the system to be able to suppress the light from the parent star while leaving the light from the exo-planet intact. For example, as seen from outside our solar system, the brightness of Jupiter at quadrature is given by, $B=1/4$ (albedo)· $(R_J/5.2 \text{ AU})^2 \cong 10^{-9}$ and detection of an Earth like planet would require starlight suppression on the order of 10^{-10} . Of course it is not enough to just suppress the starlight, you must also maintain starlight suppression stability over the time of a measurement. Otherwise, your signal will be contaminated with stellar light and your contrast will degrade. Exo-planets with stellar contrasts of 10^{-9} will have brightness in the range of $V=23-29$, with a median of $V=27$. Therefore depending on the collection area of the imaging system, the integration time may be on the order of multiple days. As a point of reference, the recent Exo-C mission study report quoted integration times of 10 days to spectrally characterize a planet for that system’s 3m^2 collecting area.

The spatial field of view (FOV) is the area around a star where planets may be visible to our imaging system. The spatial FOV is defined by two angular measurements: the inner and outer working angles. The inner working angle (IWA) defines how close to a parent star you can see the planet at the required contrasts stated above. The IWA is

limited by the imaging system's resolving power and the control bandwidth of an imaging systems starlight suppression system. The outer working angle (OWA) defines how far away from a parent star you can see a planet at or above the required contrast. The OWA is typically limited by the control bandwidth of an imaging system's starlight suppression system. For an ideal perfect imaging system the OWA is limited by the detector's FOV. The EXO-C mission study report quoted a desired IWA of 0.26" at 900nm (0.16" at 550 nm) and a desired OWA of 1.4" at 900nm.

After detecting an exo-planet, it will be highly desirable to characterize the spectral features of the exo-planet's signal. Detailed spectral analysis of an exo-planet can be used to determine if a planet has an atmosphere or not. If the exo-planet does have an atmosphere, spectral analysis may enable us to determine the composition of the atmosphere as well. In the previously mentioned Exo-C mission study report, it was determined that to achieve exo-planet characterization a wavelength range of 0.45-1.0µm was desired. This range encompasses several absorption features that are characteristic to molecules needed to support life. They also determined that Exo-planet characterization requires fine spectral sampling to discern features in the spectra. a spectral resolving power of, $R \sim 70$ was required to achieve exo-planet characterization. Achieving a spectral resolving power of $R \sim 70$ requires the system to maintain a decent signal to noise (SNR) over spectral elements on the order of $SNR \sim 10$.

3.3.2 SNR and Exposure Time Computation

One of the outcomes of the A-Team study was the need to look into how many photons would be collected by the granular aperture, and how that photon count would be useful for astronomy. We took the performance parameters of the Hubble detector (see Table 2), and derived an expression for the SNR (signal to noise ratio) and for the exposure time. Some of the parameters used in the equations below are shows in Table 2. For the star Vega, which is magnitude zero and of spectral type A0, $N_0 = 10^8$ photons/(sec-m²-nm) centered at a wavelength of 550 nanometers in the visible. The photon flux hitting the detector is [Schoreder2000]:

$$S = (N_0 10^{-0.4m})(\pi D^2/4)(1 - \varepsilon^2)(\tau)(\Delta\lambda)$$

The background sky-photon flux hitting the detector is [Schoreder2000]:

$$B = (N_0 10^{-0.4m'})(\phi\phi')(\pi D^2/4)(1 - \varepsilon^2)(\tau)(\Delta\lambda)$$

(1)

The signal-to-noise ratio can be written as [Schoreder2000]:

$$\text{SNR} = \frac{\kappa SQ t}{\sqrt{(\kappa S + B)Q t + (C_{\text{dark}} t + R^2) \cdot n_{\text{pixel}}}}$$

(2)

The exposure time can be written as [Schroeder2000]:

$$t = \frac{1}{2} \left(\frac{(\text{SNR})^2}{\kappa SQ} \right) \left\{ \left(1 + \frac{(BQ + C_{\text{dark}})n_{\text{pixel}}}{\kappa SQ} \right) + \sqrt{\left(1 + \frac{(BQ + C_{\text{dark}})n_{\text{pixel}}}{\kappa SQ} \right)^2 + \left(\frac{2R}{\text{SNR}} \right)^2 n_{\text{pixel}}} \right\}$$

(3)

Table 2. Observation dependent parameters, based on Hubble detector model [taken from Schroeder2000].

Grain diameter	100 microns
Cloud encircled diameter, D*fillFactor	1 m
Star magnitude, m	m
Detector area projected onto sky	0.1 x 0.1 micron ²
Instrument filter bandpass, Δλ	100 nm
Secondary mirror optical blockage, ε	0.33
System transmittance, τ	0.324
fraction of 550nm transmitted light to detector, κ	0.8
quantum efficiency within filter BW, Q	0.8
Dark noise, C _{dark}	0.003 electrons/s/pixel
Readout noise	5 electrons-rms/pixel

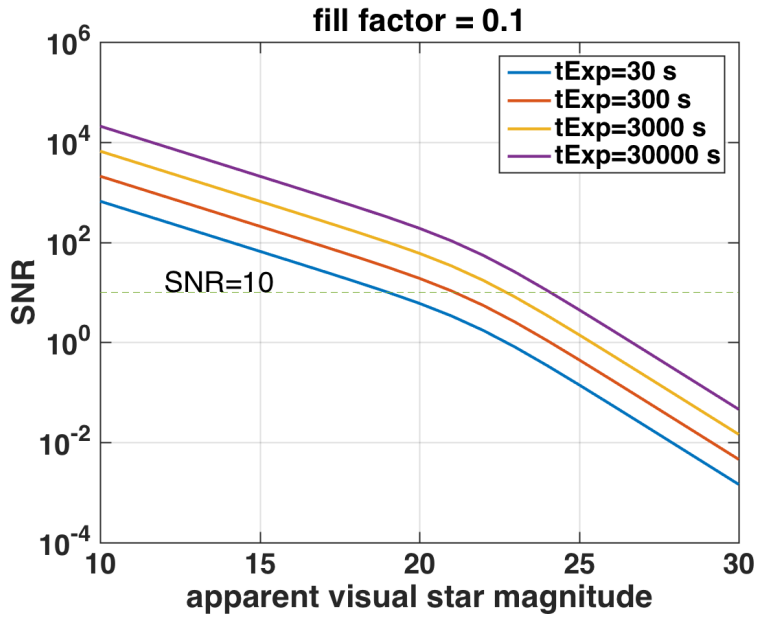


Figure 14. SNR vs. apparent magnitude for 10% fill factor.

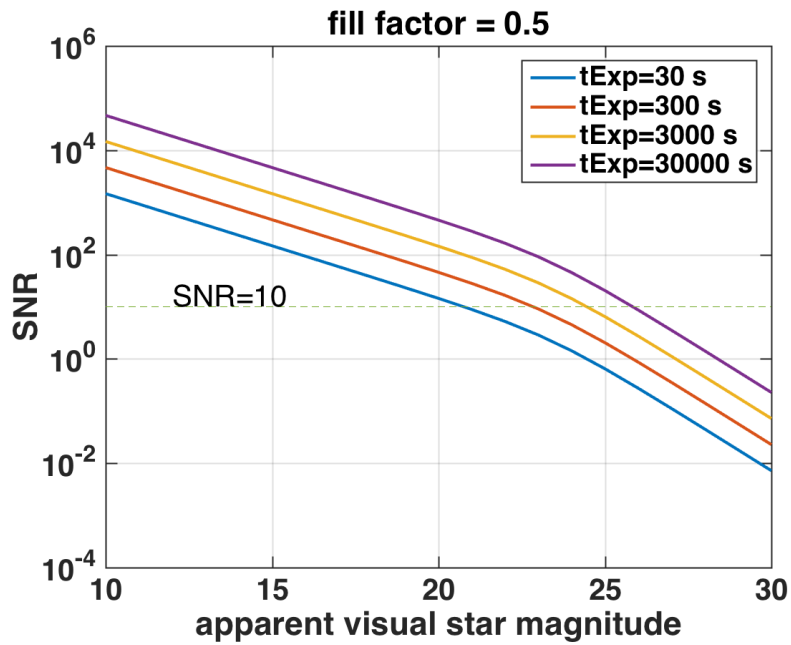


Figure 15. SNR vs. apparent magnitude for 50% fill factor.

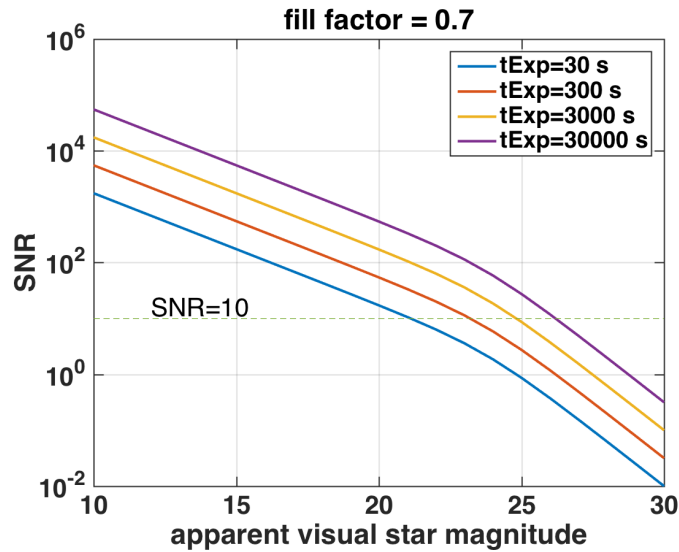


Figure 16. SNR vs. apparent magnitude for 70% fill factor.

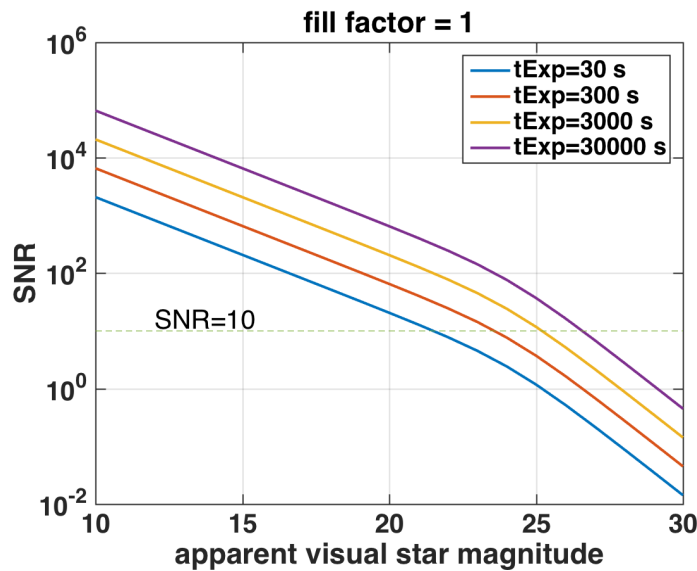


Figure 17. SNR vs. apparent magnitude for 100% fill factor.

Figure 14 shows the SNR vs. apparent magnitude for 10% fill factor. Figure 15 shows the SNR vs. apparent magnitude for 50% fill factor. Figure 16 shows the SNR vs. apparent magnitude for 70% fill factor. Figure 17 shows the SNR vs. apparent magnitude for 100% fill factor. Figure 18 shows the exposure time vs. apparent magnitude for 10% fill factor. Figure 19 shows the exposure time vs. apparent magnitude for 50% fill factor. Figure 20 shows the exposure time vs. apparent magnitude for 70% fill factor. Figure 21 shows the exposure time vs. apparent magnitude for 100% fill factor. These plots indicate that, even for low fill factor, the performance of the granular cloud as a photon bucket is still satisfactory, and can be used as a science instrument of performance comparable to HST (assuming all other detector parameters remain the same).

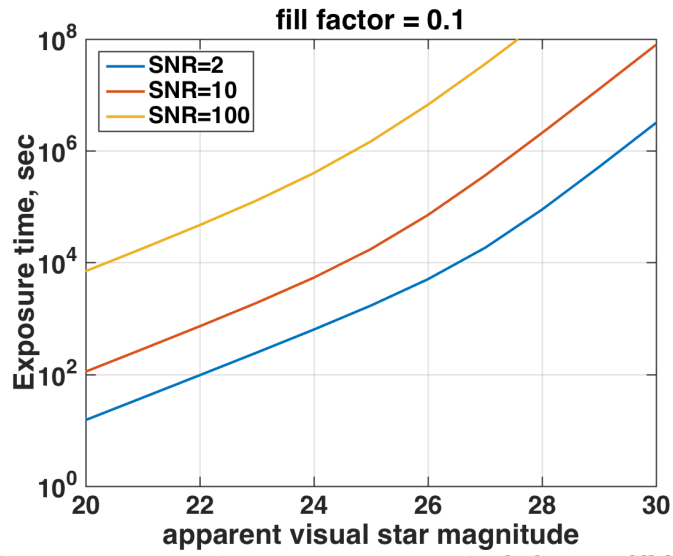


Figure 18. Exposure time vs. apparent magnitude for 10% fill factor.

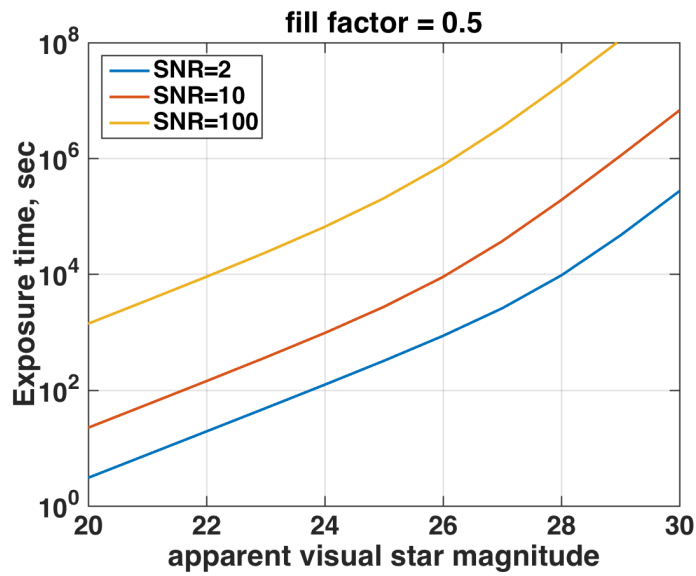


Figure 19. Exposure time vs. apparent magnitude for 50% fill factor.

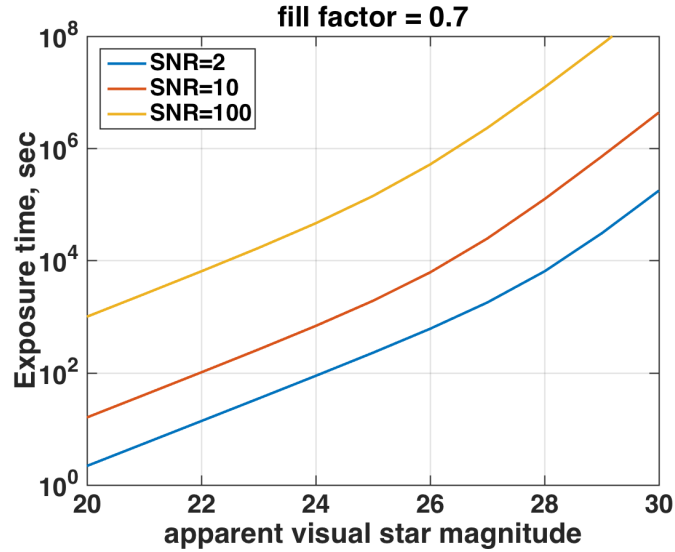


Figure 20. Exposure time vs. apparent magnitude for 70% fill factor.

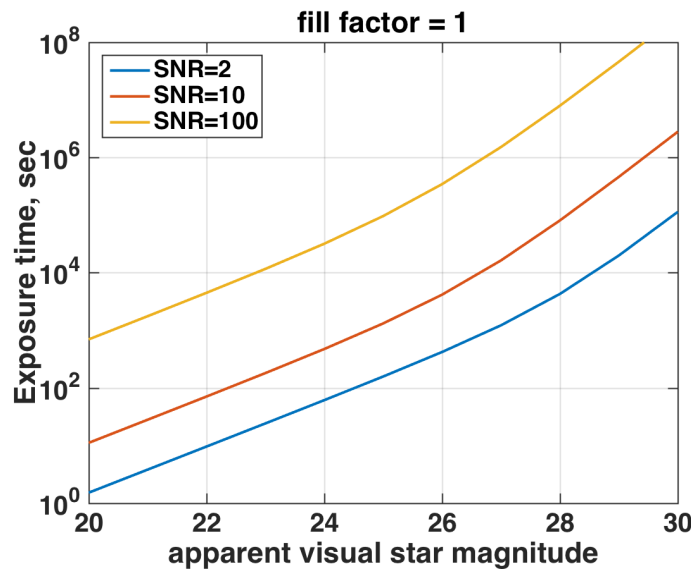


Figure 21. Exposure time vs. apparent magnitude for 100% fill factor.

3.4 Applicability of Granular Imager to Earth Science

Large light-weight aperture collectors and high-efficiency detectors are identified as a critical technology both in microwave and optical technology applications within and without NASA [NASA2004, NASAESTO2016a, NASAESTO2016b]. In general, deployable large apertures can relax requirements on transmitter technologies (because of the higher gain provided), enable measurement scenarios from small satellite platforms, and enable observations with sufficient resolution from specific vantage points such as Sun-Earth Lagrangian Points (L1, L2)

or Geostationary orbit. In [Michel2012], the possibility of imaging the propagation of seismic waves from a very large space-based optical telescope is discussed. Images of seismic waves propagating at the Earth's surface would be an invaluable source of information for investigating earthquake physics and the effect of the subsurface on earthquake ground motions. This application would require ground displacement measurements at about every 100 m, with cm accuracy, and temporal sampling on the order of 1 Hz. A geostationary optical telescope with a large aperture appears to be the most promising system, and [Michel2012] considers a telescope with an angular field of view of 0.8° and with an aperture greater than 4 m, and show that key details of the seismic wave field, hardly detectable using ground-based instruments, would indeed be imaged by such a system. Another application is in the area of atmospheric spectroscopy from L2, as discussed in [Mettler2004]. There are strong scientific motivations for placing an Earth observatory at L2. The occultation due to the orbital geometry at L2 is best suited for long-term climate change studies. We can obtain high vertical and spatial resolution maps of many chemical species twice per day for the use in near-real time predictive assimilation models. A similar capability would require a constellation of multiple spacecraft in low Earth orbit. Near real-time production of the final products for time-critical consumption (forecast models) would be feasible. The co-alignment of the spectrographic instruments and the synchronization of the operations of a large aperture system in formation with a detector spacecraft would provide a sampling of the same air mass over a wide band of wavelengths (0.25 to 10.5 microns). Atmospheric monitoring would involve obtaining global maps of the vertical distribution of O₃, CO₂, CH₄, H₂O, N₂O, key members of the NO_x and Cl_x, and the upper tropospheric and stratospheric clouds, sulfate aerosol mass, temperature, and pressure with sampling near the stratopause, twice per day. Long-lived chemical species would be used to monitor the global circulation (mean meridional and planetary wave dynamics) at a lower vertical resolution, and the changes would be observed in the tropopause region, and the stratospheric-tropospheric exchange processes. These capabilities will enable such a system to determine the changes in the forcing and the responses of the Earth's atmosphere, where forcing is due to natural and artificial factors that influences the atmosphere; to understand and quantify the mechanisms of these changes, be it of chemical or dynamical origin; to improve the short and long term predictive capability of the climatic changes through the use of near real time measurements and an improved understanding of the dynamical, chemical, and radiative processes in the atmosphere. The required resolution for the observations of the atmosphere at the distance of L2 dictates that the telescope would need a primary mirror with an unprecedented diameter of many 10's of meters. A traditional mirror of that size, or a multi-mirror array, would have an impractical mass, and would be extremely difficult to build, and maintain with the necessary optical precision. This is where the Granular Imager becomes competitive.

For lidar, deployable apertures larger than 2 m would enable reduced laser power or improve system performance, and could enable some missions from smallsats [Cubesat2016]. Athermal large aperture field-widened interferometers are needed for wind and aerosols. An emerging technology is miniaturization: the burgeoning additive manufacturing field offers potential solutions for previously

impossible enabling constructs (e.g., large-area mirrors that are light-weighted in ways that cannot be accomplished through other means). An emerging ancillary receiver technology is large effective area, lightweight telescopes, with areal density $< 25 \text{ kg/m}^2$, and $>3 \text{ m}$ aperture diameter.

For microwave applications apertures of several tens of m would enable observations of earth from Geostationary Orbit at spatial and temporal resolution sufficient to resolve the evolution of several processes related to weather and the water cycle [NRC2007]. Among the several microwave applications requiring GEO deployment of large apertures summarized in [NRC2007] we note: water vapor, hurricanes, biomass, winds. In general, the great advantage of GEO or Lagrangian Point observations (that is, providing a time-continuous record capable to resolve various processes as they evolve) is countered by the significant investments necessary to develop very large instruments necessary to achieve sufficient horizontal resolution. LEO solutions are often simply the workable compromise where affordability becomes the fundamental limiting factor. For active systems (i.e., radars) the problem of GEO and Lagrangian Point is further exacerbated by the transmit power needed to obtain detectable returns. Once again, the use of very large apertures is, in principle, capable of mitigating this aspect because of the higher gain provided by the aperture.

Rather than attempting to enumerate in how many scenarios an extremely large and tenuous aperture could enable Earth Science measurements that cannot otherwise be achieved, we will provide here a few representative examples. A 35 GHz radar, with a 35 m primary reflector, was identified more than a decade ago as a viable solution to place a Hurricane monitoring radar in GEO [Smith2007, Lewis2011]. Several key technologies were developed and demonstrated, and the final hurdle was confined to the actual engineering and financial challenges associated with the implementation of a full scale instrument to be deployed. The measurement concept remains desired by the scientific and operational hurricane communities and yet despite the specific encouragement in [NRC2007], little progress has been made in the last decade to make this instrument any more affordable. Furthermore, its size was already a compromise, since, ideally, an aperture of a 200 m would have been truly the definitive answer (to provide an horizontal resolution of 2 instead of 12 km). That concept relied on a spherical reflector geometry, with a feed array designed with fixed configuration to pre-compensate for the resulting constant aberration and moving mechanically to achieve angular scan and the desired coverage of the central Atlantic, low sidelobe pulse compression and a 150W solid state power amplifier completed the configuration to achieve the desired detection of light precipitation (i.e., 10 dBZ). Fast forward to present time. Digital and electronic scanning active phased array technologies have advanced as expected demonstrating that the feasibility and affordability of the feed.

If GI technology were to mature in the next few years, and a 200 m hemispherical shell were to become feasible, it would suffice to radiate a few tens of Watts (similar to for example the RainCube from a 6U cubesat [Peral2015]) to achieve continuous monitoring of hurricanes at a 2 km horizontal resolution. Going to longer wavelengths, an aperture of this class could enable for example biomass and soil moisture monitoring across the diurnal cycle at horizontal resolutions of 10-30 km.

Going to shorter wavelengths one could envision instruments in the IR deployed at Sun-Earth L1 to provide time continuous radiation budget measurements that account in real time for the incoming solar radiation. The principle of GI could also potentially augment closer-to-Earth systems in LEO by enabling larger apertures because of higher deployed-to-packed size ratios.

To accomplish the goals for Earth science, spatial coherence at low frequency, or the aperture rigidity in orbit, must be achieved, by relative grain control. The system libration dynamics in orbit must be stable, i.e. the attitude dynamics of the aperture must be stable with respect to the local orbiting frame. This can be achieved by a favorable orbital distribution of the grains. [Bekey1999, Bekey2005] consider large swarm arrays of picosats for Astrophysics and Earth science. In addition, large swaths of the Earth could be continuously monitored with an extremely fault-tolerant system. Also, spatial coherence at high frequency must be achieved, and could be obtained by containing the cloud dispersion electromagnetically. Finally, the signal transmitted or received by the aperture must exhibit spatio-temporal phase coherence so that intensity at the maximum peak lobe of the array pattern is maintained. This could be achieved by limiting the differential effects of orbital perturbations. The incoming signal must be also in phase to within the diffraction limit to add coherently (this amounts to approx. 1 cm of relative grain motion within the cloud at 1.4 GHz). The motion of elements near the symmetry axis will cause defocus, and higher order aberrations (coma, astigmatism) result from motion of the off-axis elements from the figure plane. Consequently some form of figure control (i.e. wavefront control) is necessary. Also, to accommodate multiple look angles (i.e., boresight control), the plane of the aperture must be able to tip/tilt as an equivalent rigid aperture. The determination of the effective aperture size and cloud density to fill the aperture, will depend strongly on the chosen wavelength, the noise-equivalent temperature at the detector, and also on the diffraction limited ground resolution, surface reflectivity, dwell time, ground spot diameter, and source temperature.

In this regard, Figure 22 shows the ground resolution vs. fill factor of GI passive radiometer at GEO at several wavelengths, showing that the resolution would increase, as expected, with GI fill-factor (nominally, we used 10,000 grains in the calculation). Preliminary trends of the GI performance as a passive or active radiometer from GEO looking at a spot on the ground at 1.4 GHz, for three different grain sizes, are shown in Figures 23, 24, and 25, indicating that adequate performance, quantified as detector area and achievable ground resolution, can be achieved with a much lower mass GI, and that the total number of grains would much smaller in the case of an active system.

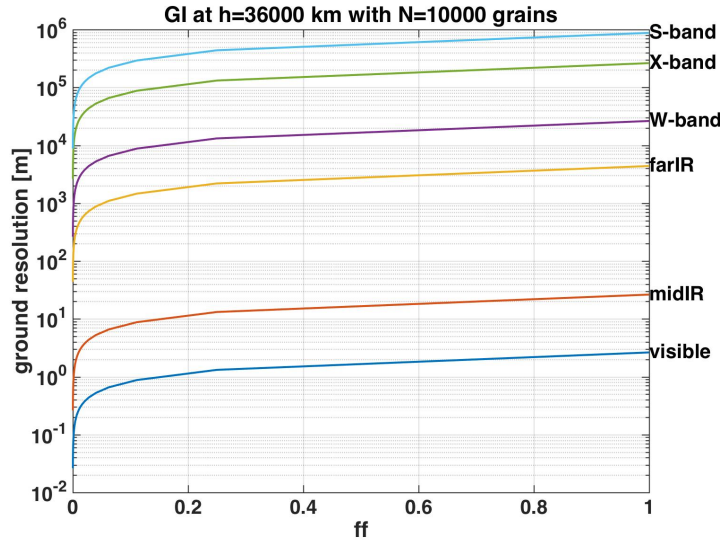


Figure 22. Ground resolution vs. fill factor of GI passive radiometer at GEO.

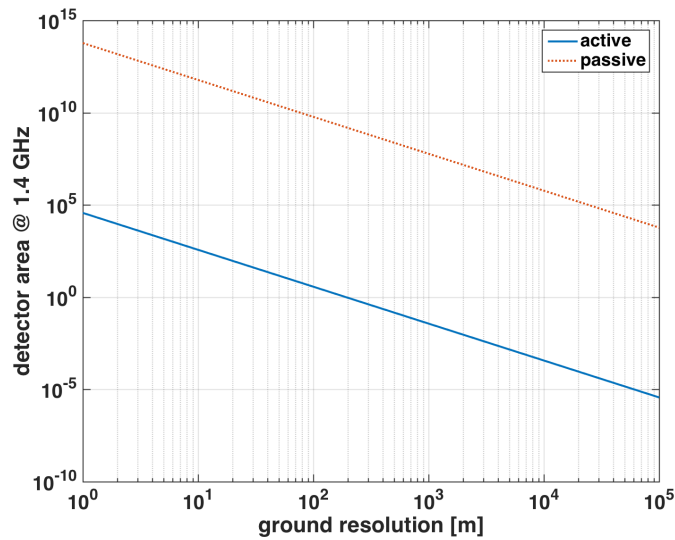


Figure 23. Detector area of passive radiometer at GEO at 1.4 GHz vs. ground resolution.

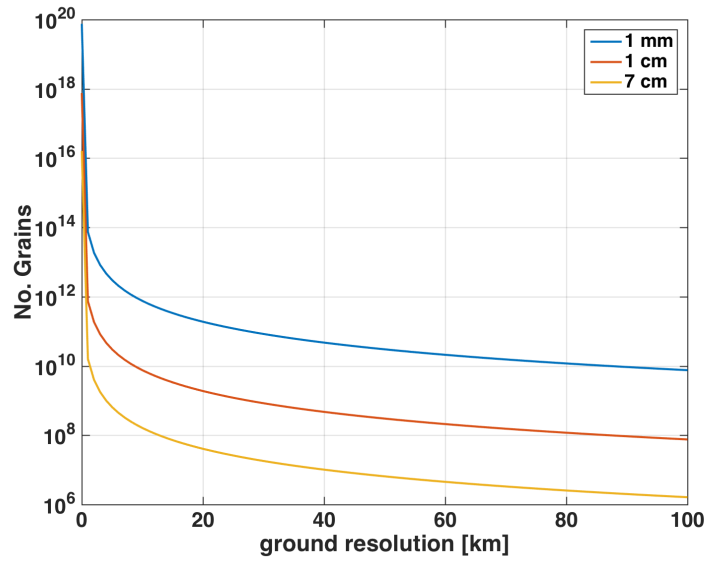


Figure 24. Number of grains vs. ground resolution for different grain sizes for passive radiometer at GEO at 1.4 GHz.

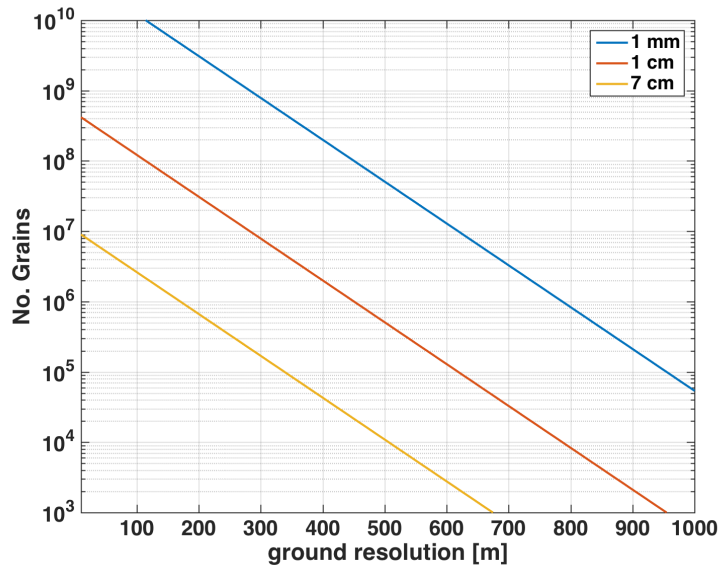


Figure 25. Number of grains vs. ground resolution for different grain sizes for active 100kW radiometer at GEO at 1.4 GHz.

4. Granular Imager Systems Engineering

A notional system architecture of the Granular Imager in operation is shown in Figure 26. Figure 27 shows a snapshot of the simulation of the system, which includes a sun-shade, a figure corrector spacecraft, a science detector spacecraft, and a minimum of two laser sources to align the grains and shape the cloud as a conic surface. Figure 28 shows the elements of the imaging system, including multiple granular apertures to synthesize an equivalent large aperture for astrophysics or remote sensing. More details are discussed in the section on the system optic designs and on wavefront sensing and control.

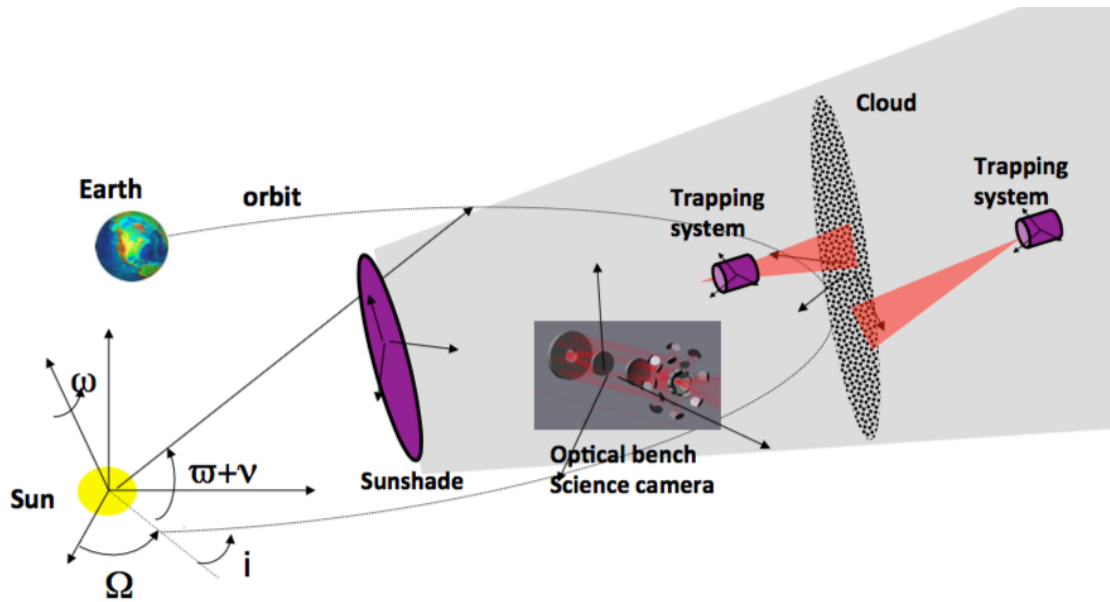


Figure 26. Granular Imager configuration.

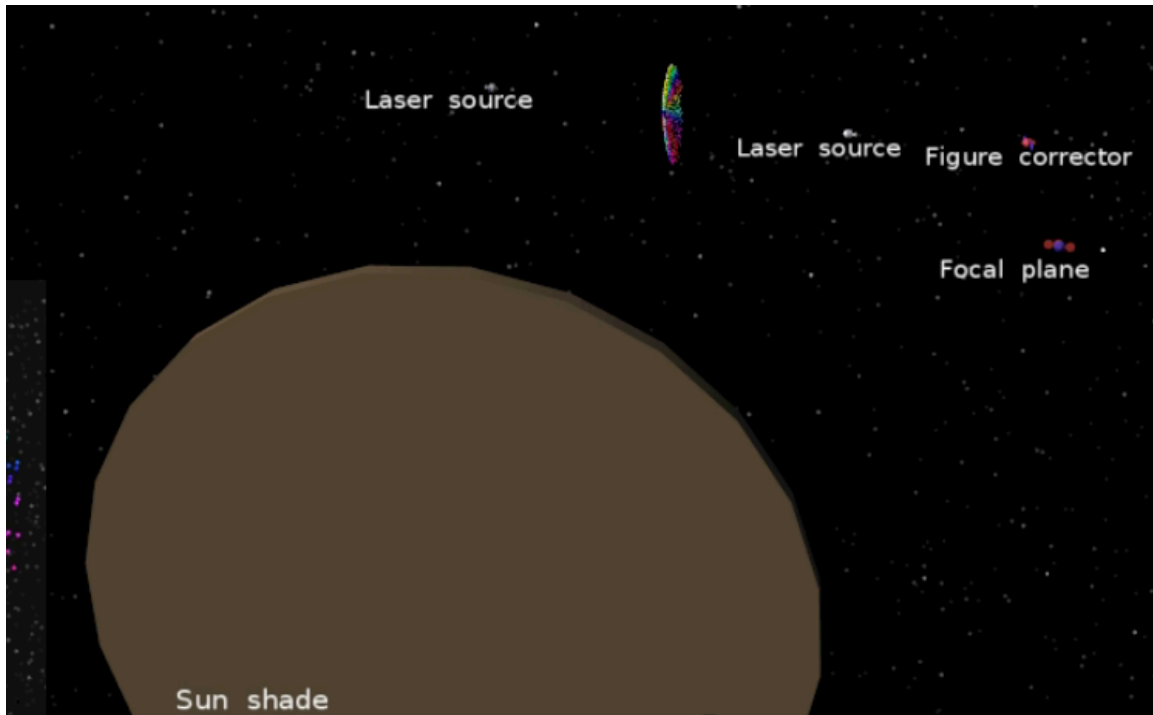


Figure 27. Elements of system in formation.

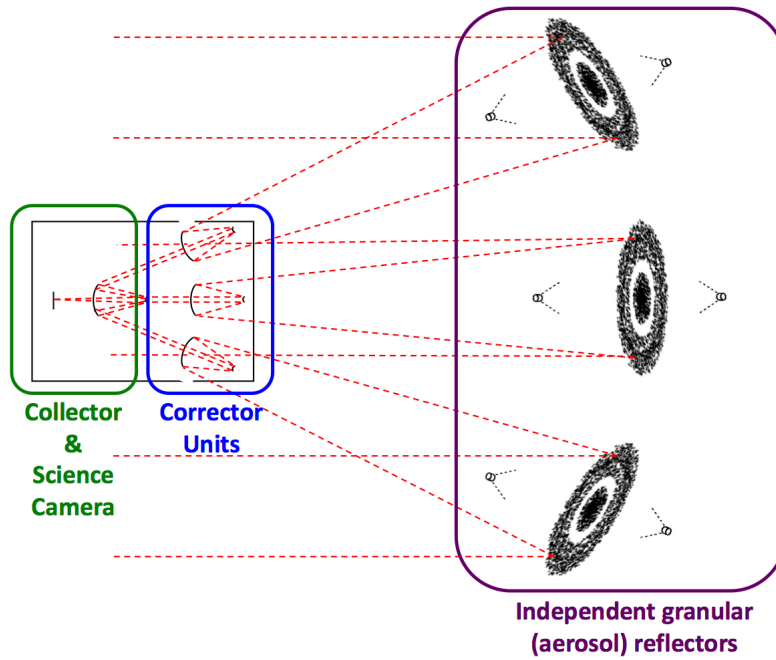


Figure 28. Configuration with multiple apertures.

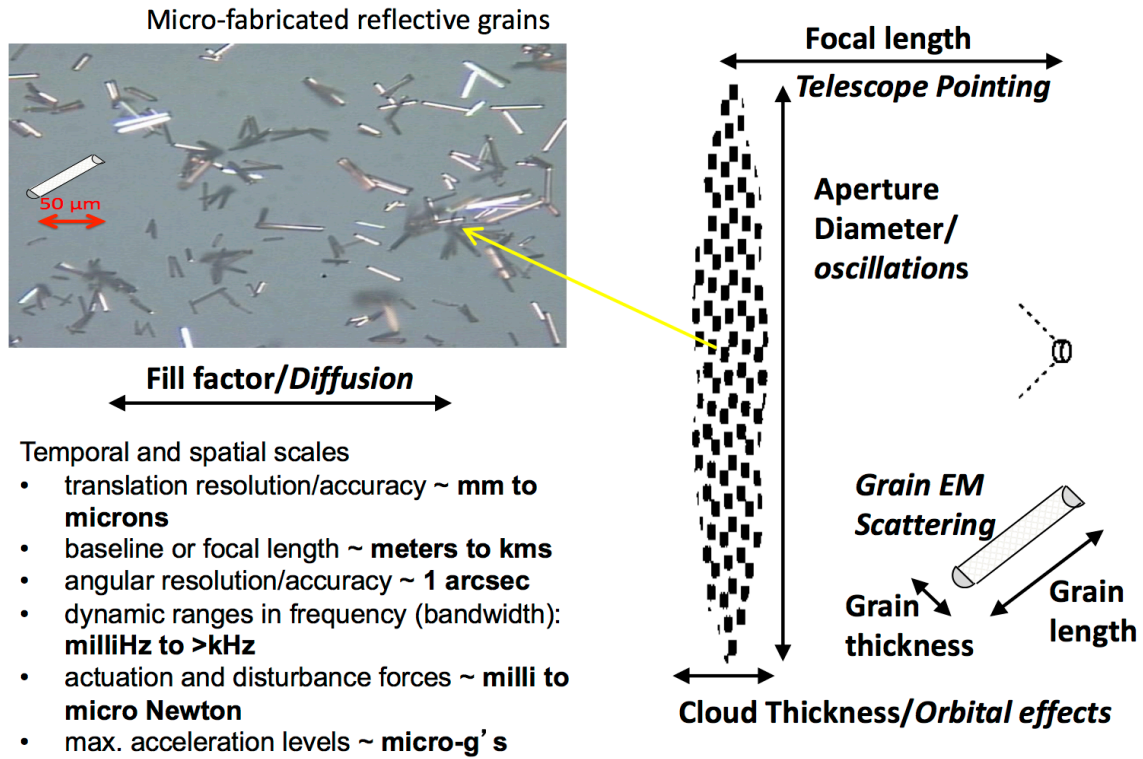


Figure 29. Space and time scales involved in Granular Imager technology.



Figure 30. 0.3 mm hemispherical grain.

Figure 29 depicts the various spatial and temporal scales involved in the Granular Imager operation. Finally, Figure 30 shows a photograph of one micro-fabricated 0.3 mm diameter grain that was tested in the buoyant liquid experiments, discussed later in this report.

4.1 Interaction of cloud with space environment

We had several discussions with Dr. Henry Garrett from JPL, space environment expert, on the interaction of the cloud with the space environment, and we learned the following. Small grains can be dielectric, or not conducting, but they will charge negative when in equilibrium with local plasma (and shadowed), due to continuous bombardment from electrons—the ambient electron current typically exceeds the proton current as the electrons, for roughly the same thermal energy, have significantly higher velocities. Once illuminated by Sun, UV radiation will cause photoemission, equilibrium potential will be offset, and grains will become positively charged, hence disrupting equilibrium. Continuous electromagnetic trapping becomes necessary in the solar wind as the solar plasma will entrain the charged dust (e.g., a comet's plasma tail)—a sun-shade might alleviate the problem or enveloping the cloud inside a balloon (inflatable). Continuous solar wind and radiation pressure exposure in L2 could complicate particle containment. Therefore:

- 1) Within the Earth's magnetosphere at GEO, we need to expect additional political problems associated with possible space debris generation and associated impact on expensive assets. Also, the Debye length is large, grains can interact with each other, which will not preclude clustering of grains, like West Ford needles.
- 2) Outside of magnetosphere (Figure 31), in Sun-Earth L2, the Debye length is moderate, grains will still interact with each other. The dynamics will be dominated by solar wind, from 400 km/s when Sun quiescent and up to 3000 km/s during CME. Hence grains might be entrapped easily by the solar wind. In this regime, it will need continuous confinement mechanism, or balloon containment. In any case, experiments in vacuum will become necessary for next Phase of work after NIAC. Also plasma PIC (particle-in-cell) simulations are needed to show cloud stability in space environment, under different space environment and trapping mechanisms.

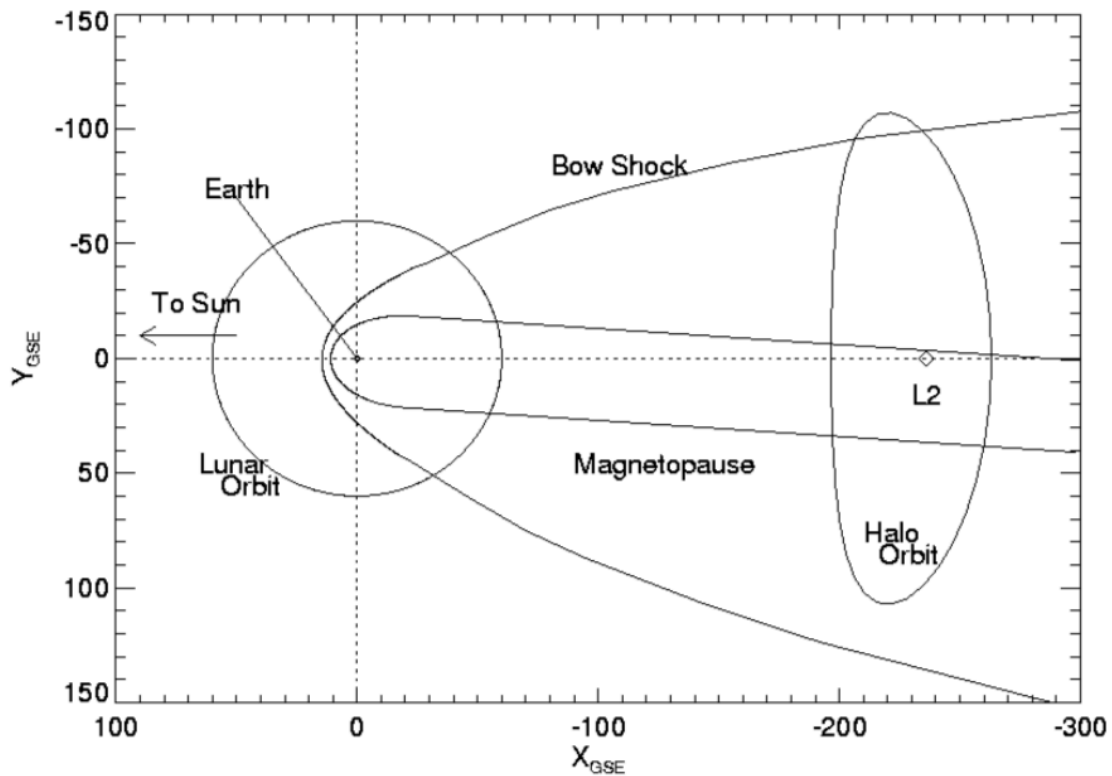


Figure 31. Sun-Earth L2 orbit and relation to magnetopause.

4.2 System Configurations

Figure 32 shows a prototype configuration for 10 meter Granular Imager with electromagnetic confinement rings. This configuration is examined in more detail in the section on the modeling and simulation of various levitation mechanisms. In Figure 32, the set of two rings in the lower part of the figure represents a double-ring electromagnetic confinement system, and the cylinder above represents the adaptive optics stage, with science camera. The top inflatable ring is empty inside, while the bottom inflatable ring is a torus which keeps the membrane with the electrode patches taut. The granular aperture is trapped in the space between the two electrode systems. The model in Figure 32 is obtained via finite elements, in which 168 triangle elements and 121 nodes form the membrane, 72 nodes in the bottom ring, 63 elements and nodes in the top ring. Figures 33 to 38 shows the configuration of the Granular Imager where the granular medium is kept floated inside an inflatable envelope, filled with a buffer gas such as Argon. The need for this confinement inside an inflatable envelope originates in the need to mitigate the orbital debris generation problem. Figure 33 shows the configuration inside inflatable canopy. Figure 34 shows a scalable architecture with multiple inflatable apertures. Figure 35 shows a prototype configuration for 10 meter Granular Imager inside inflatable envelope. Figure 36 shows a system configuration for granular imager inside inflatable

envelope. Figure 37 shows details of the inflatable canopy. Figure 38 depicts the mechanism of retargeting of the granular cloud inside inflatable canopy.

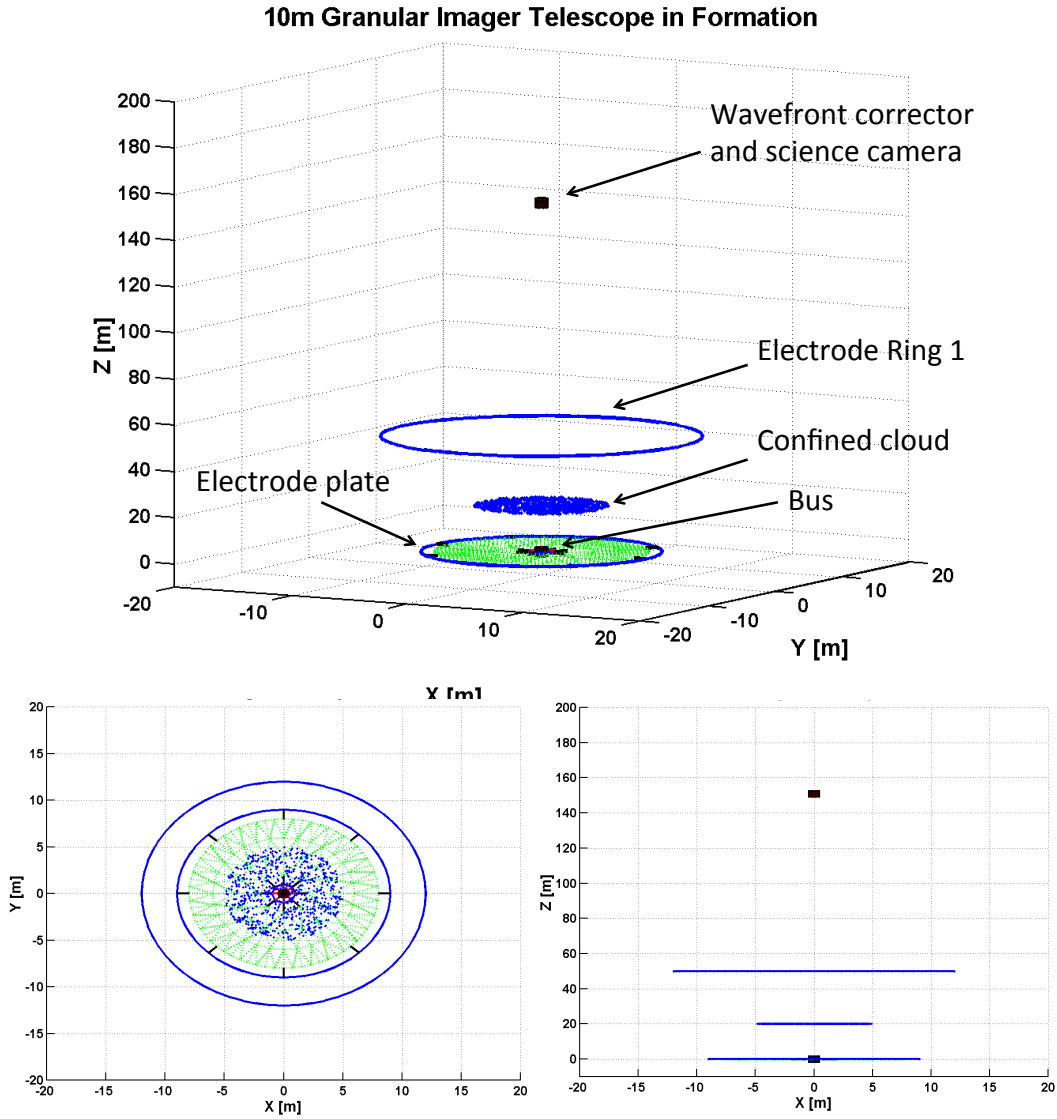


Figure 32. Prototype configuration for 10 meter Granular Imager with Electromagnetic confinement rings.

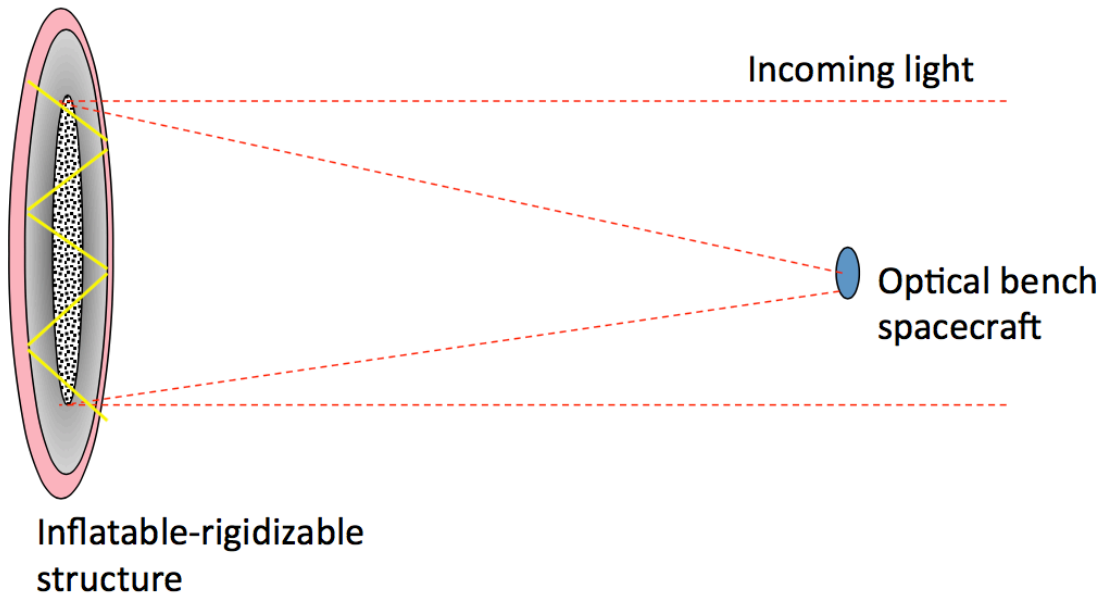


Figure 33. Configuration inside inflatable canopy.

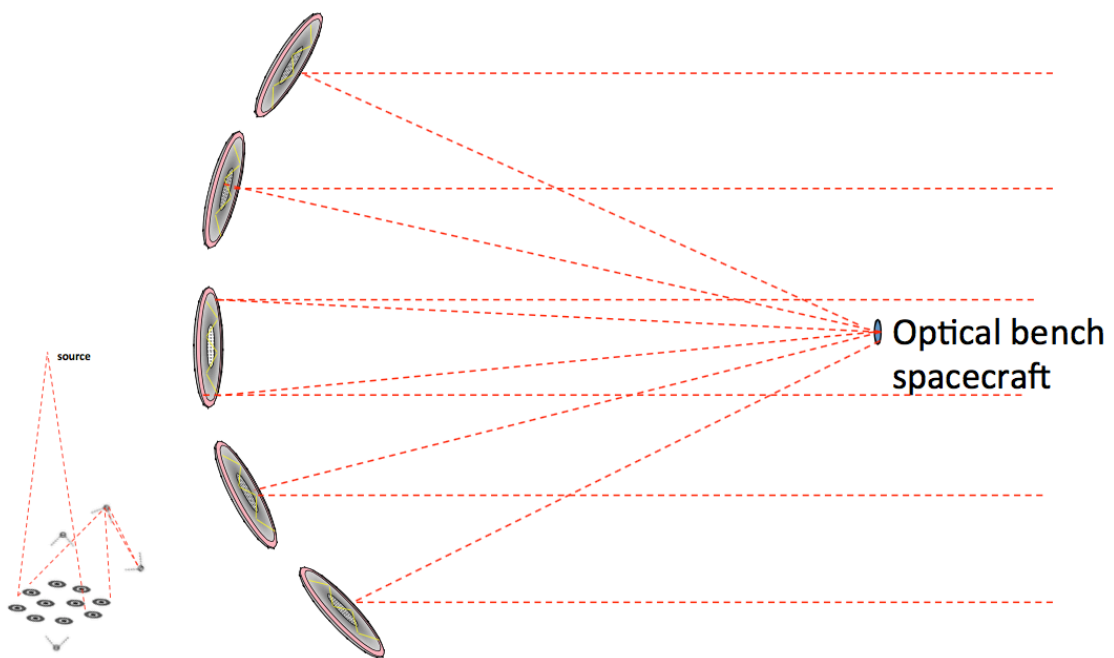


Figure 34. Scalable architecture with multiple inflatable apertures.

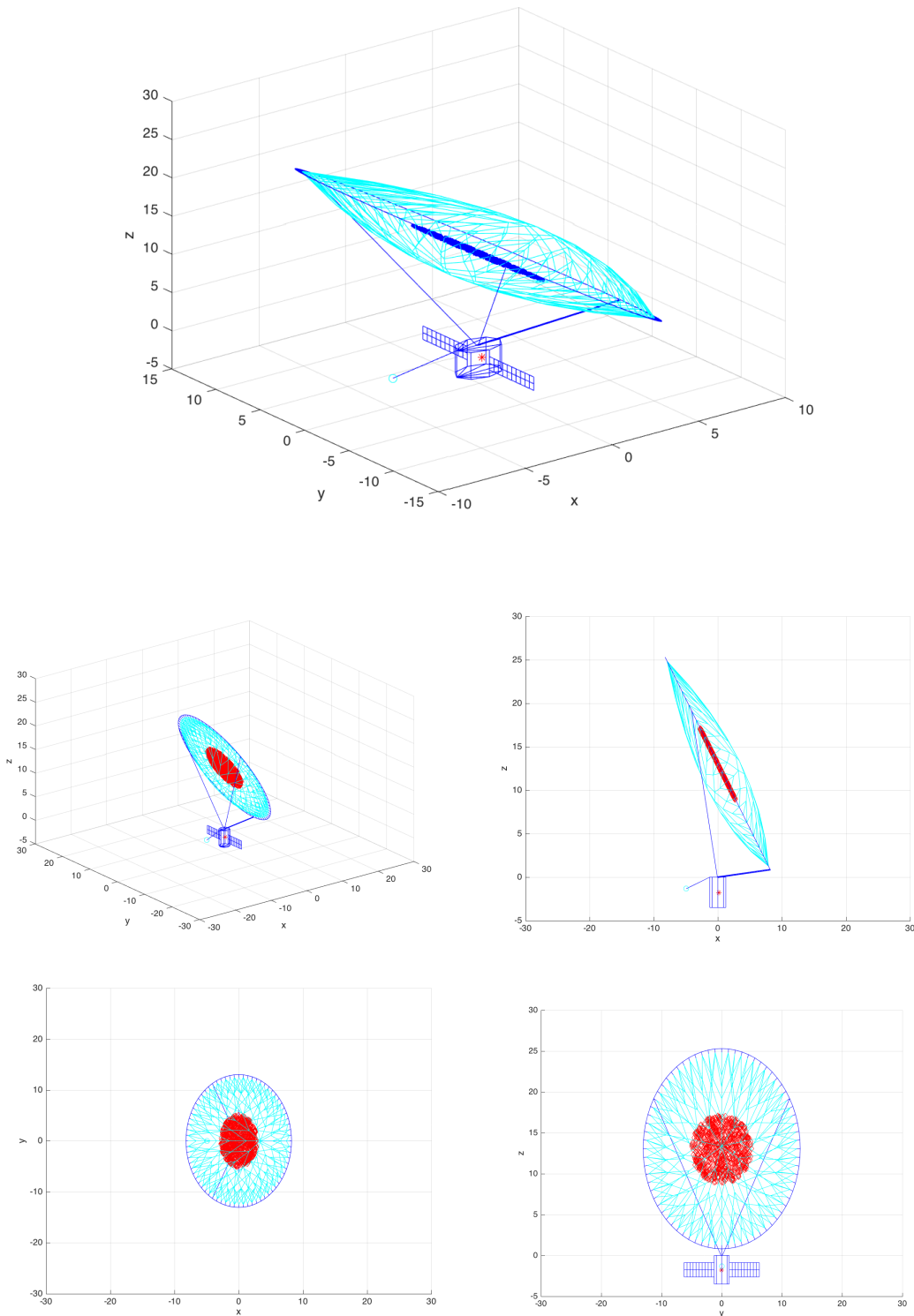


Figure 35. Prototype configuration for 10 meter Granular Imager inside inflatable envelope.

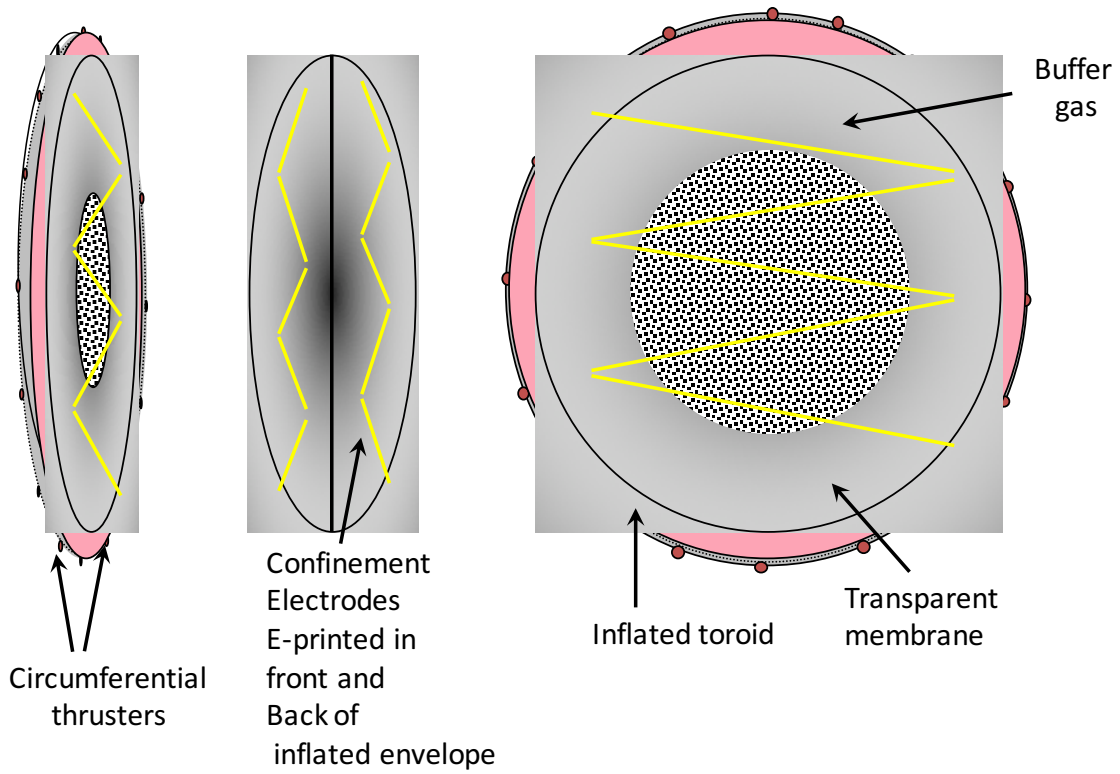


Figure 36. System configuration for granular imager inside inflatable envelope.

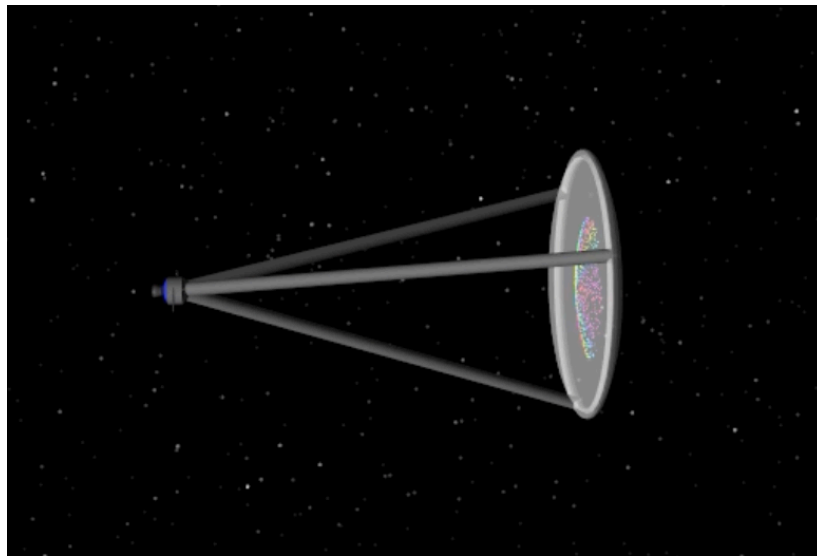


Figure 37. Inflatable canopy.

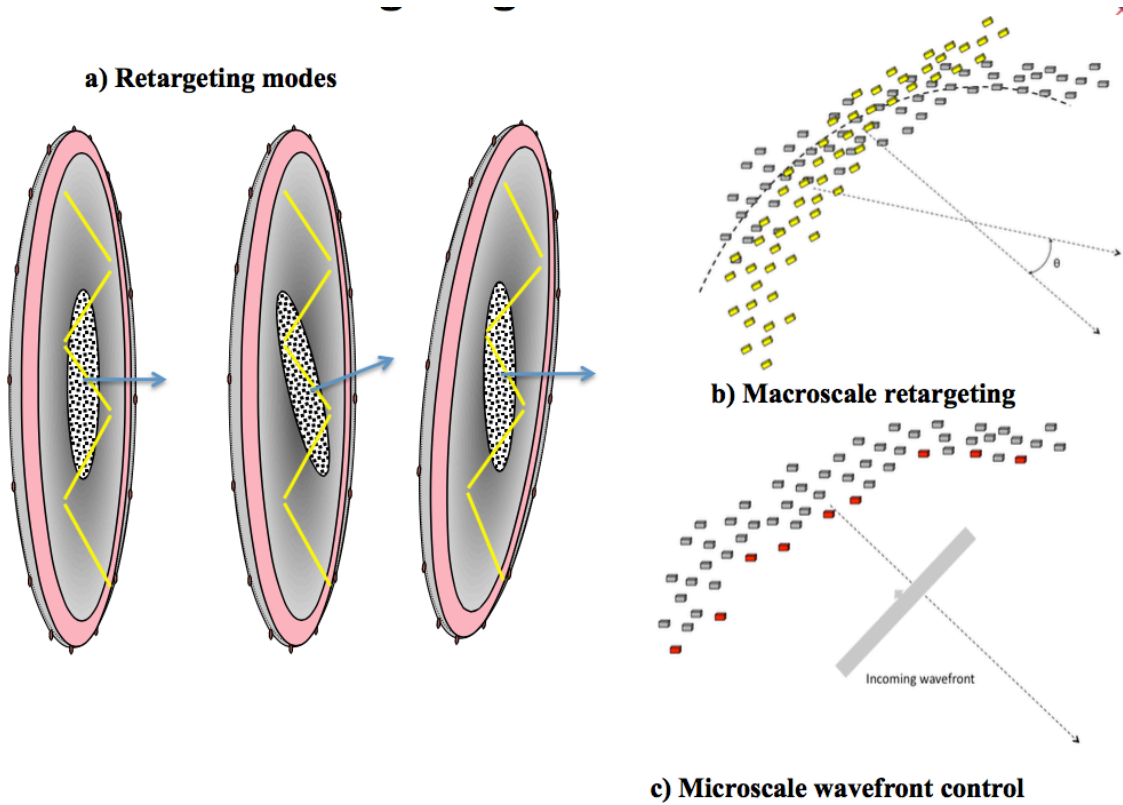


Figure 38. Retargeting of granular cloud inside inflatable canopy.

4.3 List of Key Enabling Technologies

We engaged JPL Costing Group (Hamid Habib-Agahi and Michael Dinicola), who provided some initial support material based on the preliminary discussions we had (basis of cost analyses and proposed costing approach). One of their recommendations was to put together an itemized list of elements of the system configuration, with perceived TRL levels. Now we have a preliminary TRL, mass, and cost assessment for the existing configuration of the Granular Imager. Some of this material was presented at the Symposium in Seattle. See Tables 3, 4, and 5. Table 6 summarizes the details of three proposed Design Reference Missions, that were also examined in detail during the Team-A Study.

Table 3. System Configuration and perceived TRL.

Element	Comments	Perceived TRL
Imager configuration	Formation flying telescope, from NASA TA	2-3
Science	Exoplanet detection, coronagraphy, synthetic aperture radar imager, tested on ground	8
Adaptive optics	Multistage WFSC, tested on Keck telescope	6
Imaging technology	Computational imaging	3-4
Radar imaging technology	Radar ultra-wideband imaging. Many systems flown. Reflector technology at low TRL.	3-4 (reflector) 9 (system)
Primary (Cloud) deployment and maintenance	Electrodynamic confinement, laser trapping developed at component level. Cloud containment and maintenance maneuvers would be done periodically once the system has been deployed.	6-7 (component) 2 (system)
Grains	Microfabricated, deployed from sublimating drum	5-6
Orbit	GEO (many telecomm satellites) or Sun-Earth L2 (Herschel, Planck)	9
Payload size	1m patch, scalable	2
Conops	In all phases the cloud is stabilized. All sensors/actuators, control loops, comm., have been checked-out prior to science operations. Both Integration and Testing, and Systems Engineering require development.	2 (IT) 2 (SE)

Table 4. Preliminary system mass.

Key Subsystem involved in Granular Imager	Mass [Kg]
8 sub-apertures (each D=1 m, and 0.001 Kg/m ²)	0.01
Laser containment system	100x6
Optical bench	110
Power Electronics	20
Thermal	20
Structure	50
Communication	20
GN&C	20
C&DH	20
Power Storage	30
Propulsion	30
Total	940

Table 5. Preliminary system cost. Assumes: 8 granular patches; D=1 m/patch; 0.001 kg/m² areal density; 6 lasers for confinement; 100 W power levels for WFSC; 100 K temperature during operation; Laser system not included.

Key Subsystem	Cost \$M
Aperture	0.1
Optics/metrology	20
Electronics	15
Optical/EM confinement	140
Structure/Thermal	50
Instrument/Detector	20
SW	80
Management	20
Systems Engineering	15
Product Assurance	15
Integration and test	25
Total	400

Table 6. Proposed Design Reference Missions for Granular Imager.

	DRM-1	DRM-2	DRM-3
Principal mission	Small Body Remote sensing	Astrophysics	Astrophysics
Secondary mission	Tomographic/topographic radar	Exoplanet detector, coronagraphy	Exoplanet imager, coronagraphy
Orbit	Low-altitude mapping	Sun/Earth-moon L2	Sun/Earth-moon L2
Cloud diameter	10	1-10	1-10
Number of clouds	2 side looking	6-9	>9
Primary diameter, m	N/A	20-100	100-1000
Fill factor	TBD%	< 50 %	< 50%
Wavelength	Microwave (X-W band)	Visible/IR	Visible/IR
Spectral width	Hyperspectral	Broadband	Broadband
Sunlight exposure	No need for shielding	Sun-shade	Sun-shade
FOV	5 deg	1 millirad	<1 millirad
Resolution	1-10 m	<1 milliarcsec	<1 micro arcsec
Average retargeting, deg	No need	10	10
Retargeting time, min	No need	60	60
Targets imaged in 5 yr.	Surface or interior	1e3-1e4	1e3-1e4

10

5. Radar Modeling and Experiments

The objective of the radar modeling and simulations work was to investigate the conditions to manipulate and maintain the shape of an orbiting cloud of dust-like matter so that it can function as an ultra-lightweight surface with useful and adaptable electromagnetic characteristics in the RF, or microwave bands.

The proposed cloud architecture is to construct an optical system in space in which the nonlinear optical properties of a cloud of micron-sized particles are shaped into a specific surface by light pressure, allowing it to form a very large and lightweight aperture of an optical system, hence reducing overall mass and cost. Other potential advantages offered by the cloud properties as optical system involve possible combination of properties (combined transmit/receive), variable focal length, combined refractive and reflective lens designs, and hyper-spectral imaging.

A cloud of highly reflective particles of micron size acting coherently in a specific electromagnetic band, just like an aerosol in suspension in the atmosphere, would reflect the Sun's light much like a rainbow. The only difference with an atmospheric or industrial aerosol is the absence of the supporting fluid medium. This new concept is based on recent understanding of the physics of optical manipulation of small particles in the laboratory, and the engineering of distributed ensembles of spacecraft swarms to shape an orbiting cloud of micron-sized objects.

While achieving the feasibility of constructing one single aperture out of the cloud is the main topic of this work, it is clear that multiple orbiting aerosol lenses could also combine their power to synthesize a much larger aperture in space to enable challenging goals such as exoplanet detection.

The concept and potential of these granular media extends into the microwave bands, where active imaging can be performed in the radar bands through either refocusing or redirecting energy scattered from targets and mediums. Conceptually, the goal within the radar bands, which include RF, or microwave, is to develop active radar techniques that use cloud physics and scattering through granular media in space to enable:

1. Tomographic imaging: Imaging in previously inaccessible areas of bodies (comets, asteroids, etc.) and
2. Topographic imaging: Higher-resolution imaging through focusing (ground mapping, etc.).

The purpose of this innovation is simple: when a satellite sensor mission is employing synthetic aperture imaging (SAR) imaging, the imaging resolution is high in the azimuth direction (direction of sensor motion), but low in the cross-track direction (direction perpendicular to the sensors motion). For target bodies with little geophysical activity, this is not problematic since the satellite will eventually sense the entire object and be able to integrate all the data to obtain imaging of the interior. However, for target bodies with high activity, simultaneous high-resolution cross-track imaging is extremely desirable. These include targets such as comets, which are of current interest to the science and geophysics community. While this can be

achieved through use of multiple or many satellite radar sensors, there is usually a prohibitive cost associated with additional satellites or sensors.

To summarize, the granular medium can be used to image previously inaccessible regions of these target bodies, or perform higher resolution imaging, by redirecting or focusing energy scattered by these bodies in such a way that permits very large aperture SAR imaging through a very limited aperture. A direct application of this is the simultaneous high-resolution cross-track SAR imaging that can be accomplished using scattering through granular media in space.

5.1 Radar System Architectures

Radar remote sensing instruments that use radar imaging and sounding enable the exploration of planets, comets, asteroids, their atmospheres and interiors at higher resolutions than possible with other non-penetrating instrumentation. Due to continued success in scientific exploration of these subjects, the next generation of remote sensing architectures will demand even higher resolutions to enable more detailed probing and experimentation. Generally speaking, radar resolution has two components: the “range” resolution and the “azimuth” resolution. These are determined by many factors, including the wavelength of the electromagnetic excitation and the intervening medium within which the electromagnetic wave propagates. Traditionally, radar instrument resolutions have frequently been limited by the characteristic of the medium due to propagation losses, dispersion, and coherence property of the medium. For example, low-frequency sounding radars such as the Mars Advanced Radar for Subsurface and Ionosphere Sounding (MARSIS) is able to detect what lies beneath the surface of Mars (up to about 3 km), but at a low azimuth resolution due to ionospheric scattering and dispersion. MARSIS operates with a very high fractional bandwidth: 1 MHz bandwidth allows a vertical resolution of 150 m in vacuum, which corresponds to 50–100 m in the subsurface. MARSIS is an unfocused synthetic aperture radar with best-case along-track resolution of 2 km. Another example in sounding radars is the Mars Shallow Subsurface Radar (SHARAD) on board the NASA Mars Reconnaissance Orbiter spacecraft. SHARAD operates with a center frequency of 20 MHz and 10 MHz bandwidth. These parameters allow vertical resolution on the order of 10–20 m. Data coming from SHARAD can be processed with focusing algorithm (chirp scaling algorithm), giving a best horizontal resolution of 300 m. Another class of examples are high-frequency altimetry mapping radars such as the Poseidon 3 altimeter radar onboard the Jason 2 satellite provides high-resolution range measurements but poor along-track resolution due to practical but large antenna beam-widths.

Our approach is to increasing the resolution of a typical radar remote sensor was to create a medium, denoted by a cloud of objects (reflectors, etc.), within which the physics of scattering or radiative transfer provides a favorable or focused result (Figure 39).

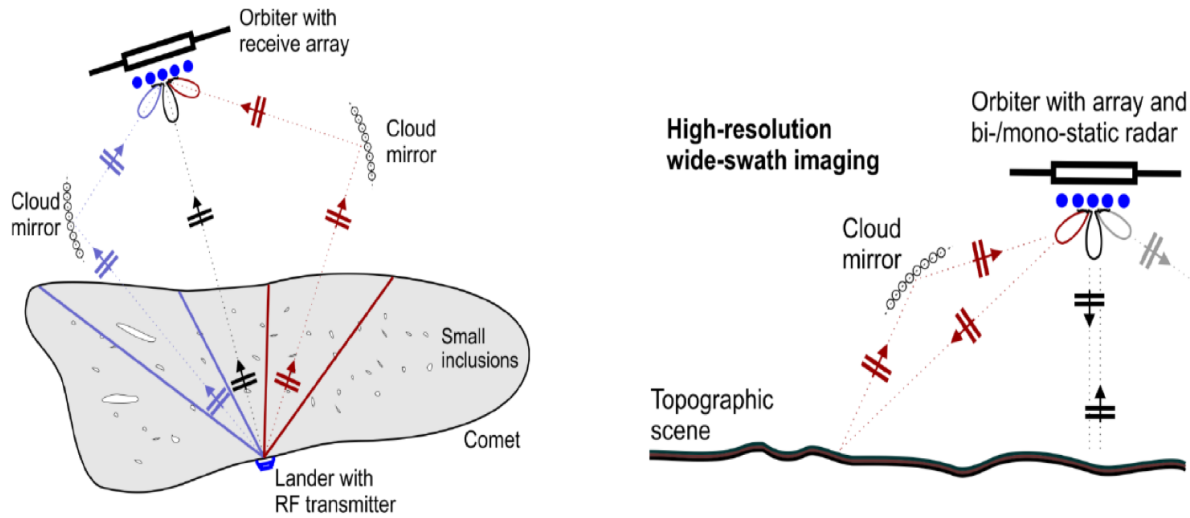


Figure 39. Tomographic and Topographic Imaging using granular media.

This includes focusing through generation of a large aperture or through the manipulation of the array factor of the cloud reflector objects. The ability to control the resolution of such a technique would be limited to the wavelength of the excitation and properties of the cloud, such as configuration, material properties, shape, etc., as well as the instrument design and configuration. The least understood of these topics being the cloud material properties, shape of objects within the cloud, and cloud configuration. For example, radar ionospheric, atmospheric, and subsurface sounding often use long wavelengths, which allow use of the Rayleigh phase function or the small particle approximation for calculating the effect of cloud properties and configuration on the bulk electromagnetic response. On the other hand, high-resolution radar imaging, for example, interferometric topography mapping, typically using very short wavelengths preclude use of the Rayleigh phase method or small particle approximations, and must instead be developed using Mie scattering for spherical objects, or vector radiative transfer theory, as noted in Figure 40. Use of vector radiative transfer theory will enable the analysis of the cloud in the microwave band.

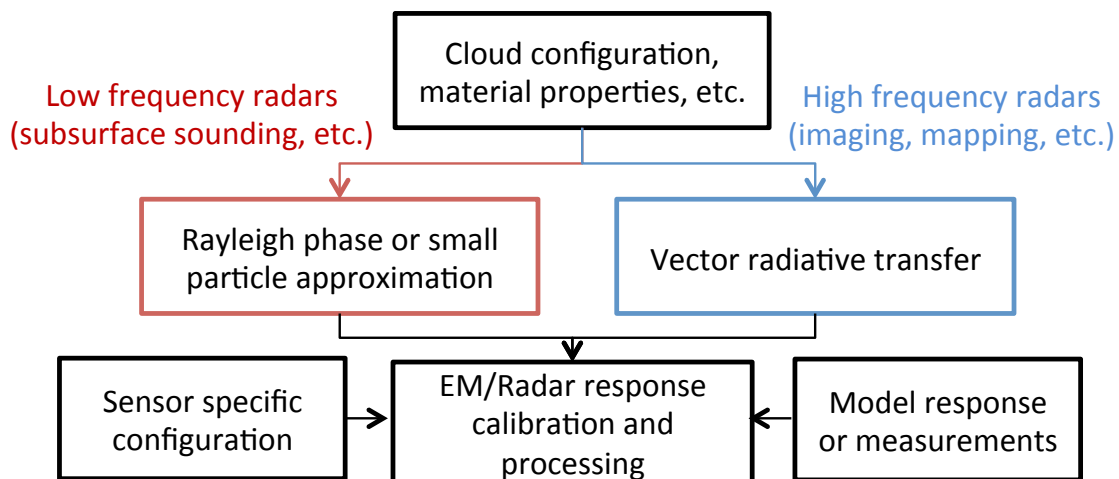


Figure 40. Elements of radar system architectures.

The team has made substantial progress in demonstrating experimental capabilities for controlling granular medium in space. Theoretical electromagnetic scattering work has demonstrated potential for lasers to be used in the control of the particles in space. Recent levitation experiments conducted by the team has verified some of these theoretical works in a laboratory, where heavy liquid was used to suspend glass hemispheres and irradiated with 980nm lasers. These works have resulted in a number of new technology reports: NTR's 30708, 48950, 49187.

Conceptually, we are trying to develop radar instrument architectures that use cloud physics and scattering to enable (Figures 39 and 40):

- A. Tomographic imaging: Imaging in previously inaccessible areas of bodies (comets, asteroids) - Rayleigh or small particle approximations to model cloud physics
- B. Topographic imaging: Higher resolution imaging through focusing (ground mapping) - Radiative transfer theory to model cloud physics

5.2 Methods to simulate full-wave scattering of arbitrary clouds

The key methods to model full-wave scattering of arbitrary clouds and their effectiveness as a granular medium to image in the radar bands are developed using numerical finite differences and using an analytical exact solution based on series expansions of harmonic solutions. The numerical finite difference technique is very useful in the time-domain, and can be used to simulate relatively complex heterogeneous clouds with large relative bandwidths, however is limited by very limited ability to study the effect of variation in cloud geometry. This limitation is primarily due to the large computation and memory resources required, as well as computation time needed to conduct a numerical simulation using finite-differences. To permit numerical simulation of large spectral bandwidths via a single simulation, the finite-difference time-domain simulations are used.

When the effect of cloud geometry, particle size, spatial distribution, et cetera is required to be studied, then an analytical method is better suited as it is computationally efficient and would require substantially lower computational resources, time, and memory. The analytical technique will however have to consider multiple scattering, though it can be practically truncated via a finite series expansion of some sort. The analytical technique is typically better suited and can be convergent if constructed in the frequency domain, as opposed to the finite-difference which is the time domain. The technique developed in this work to simulate the full-wave scattering uses a boundary value method and a T-matrix solution to simulate transverse electric or transverse magnetic scattering of plane-waves via an arbitrary distribution of particles in space. To simplify the technique and convergence, the technique is developed in two-dimensions.

5.2.1 The finite-difference time-domain modeling and back-projection technique

The finite-difference time-domain (FDTD) technique permits simulations of the full electromagnetic interaction and propagation in space and time. FDTD utilizes uniquely defined spatial cell structures to discretize the fields in the spatial domain. The purpose of the spatial discretization is to enable numerical calculation of the electric and magnetic field in space. A common method to discretize the cells is to use the Yee-cell model as shown in Figure 41. In the three-dimensional (3D) case, the Yee grid cell is configured in such a way that the electric (E field) field grid centroid is spaced a half spatial step from the magnetic (H field) field grid centroid. In FDTD, the electric field grids throughout the entire simulation space are updated numerically before the magnetic field grids. Through this time stepping between the electric and magnetic field, and due to the offsets in the Yee-cell model, the electromagnetic wave can be modeled for propagation and scattering behavior until all transient phenomena or steady state processes are complete. This is done by simply by calculating the electric field and magnetic field in subsequent manner under the Yee-grid configuration. FDTD allows accurate transient and steady state simulations for scattering and propagation, which makes it ideal to study scattering from complicated bodies such as a comet – both for transient analysis, and for scattering sensing or imaging purposes.

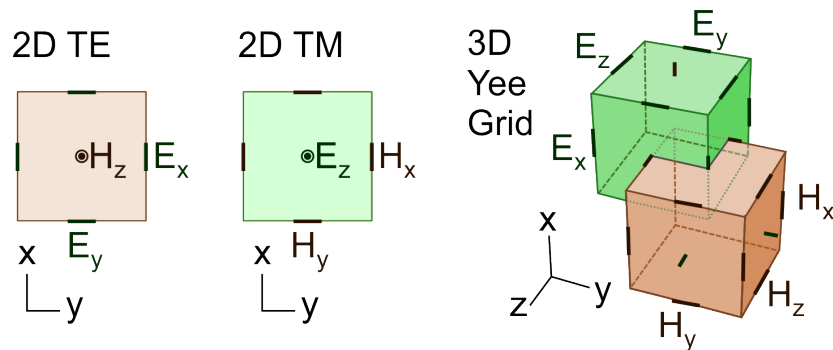


Figure 41. The Yee grid in 3D FDTD and the limiting cases for 2D TE and TM simulations in FDTD

FDTD can be developed for 2D or 3D. We developed FDTD for both the 2D and 3D problem.

In 2D, the simulations can take the form of the 2D transverse electric (TE) and transverse magnetic (TM) domains. In comet applications, the most common scattering stems from the transverse magnetic domain. The FDTD model used here is a 2D transverse-magnetic simulation (TM-z) [Taflove2000, Scheider2010], where simulation is performed on the x-y plane cutting through the comet model. For the 2D simulations, the comet has a scale of about 4-5km on each side. The FDTD simulations were developed for an arbitrary wavelength or excitation frequency, though the simulations conducted so far focused on the 1MHz center frequency, for which the

FDTD comet model can be considered electrically large. We satisfy the FDTD stability criterion using a rectangular spatial Yee-cell mesh of $1/30$ of the wavelength for very good amplitude and phase stability [Taflove2000]. Due to use of TM-z in the 2D simulations, the magnetic fields are parallel to the x-y plane, whereas the electric fields are perpendicular to the plane. Specifically, we use H_x to model the magnetic field along the x-direction, H_y along the y-direction, and E_z along the z-direction. The 3D FDTD simulations consider the full electromagnetic coupling (not limited to TE or TM slice), and is developed using the framework defined in Figure 41. The fields generated for the 3D FDTD is defined as an exact dipole field (by deriving the time-domain transient electric and magnetic field of a dipole in 3D space). The dipole is located at a user-defined location on the 3D space, though typically far away from actual simulations space. For comet simulations, the source dipole is typically located at 20-100km in distances from the simulation domain. The field of the dipole is complete in the sense that it accounts for the near and far fields of the comet (quasistatic, intermediate, and radiation regions). The analytical field of the dipole in 3D space is used to calculate the electric and magnetic fields on the simulation domain. Specifically, the fields can either be injected into the simulation space at the top surface region or it can be used to calculate the fields in all regions of the 3D spatial domain. The analytical fields are calculated once before the E-H time-stepping, and the FDTD time-stepping subsequently propagates the field and waves into the simulation space transiently and until steady-state is achieved and the time-stepping is stopped.

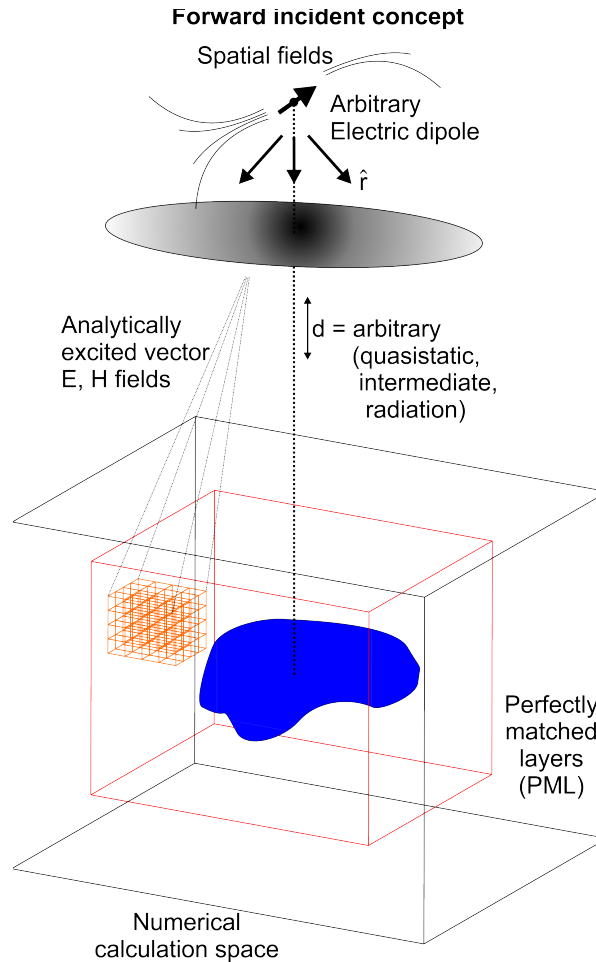


Figure 42. Forward model for 3D FDTD to include the analytical field propagator (AFP) and the perfectly matched layers (PML)

The comet body or the target to be simulated is located inside the simulation zone. The body needs to be discretized to the FDTD cell discretization size, and the 3D dielectric and conductivity maps for the discretized model needs to be geometrically interpolated or averaged at the sub-cell level to enable correct location and value definition of the electric material (permittivity and conductivity) and magnetic material (magnetic permeability and magnetic conductivity) properties. The electric materials must be defined on the electric Yee-grid, whereas the magnetic materials must be defined on the magnetic Yee-grid. This step is critical to ensure that the intended isotropy of the medium is preserved.

Once the FDTD time-stepping is started, the fields and waves will propagate into the simulation domain. They will then reflect off the hard outer boundary of the simulation zone, causing substantial perturbation of the sensed field (fields and waves scattered back into the simulation domain instead of propagating outward). This is due to the impedance boundary at the simulation edge, and is a major problem in full-wave numerical simulations. To solve this problem, a perfectly-matched layer

(PML) is specially designed to absorb the fields, with an effective isolation measured to about 100dB [Scheider2010]. The PML (Figure 42) ensures that scattering in the computational domain is not generated when the waves hit the edge of the computational domain. One obvious value of the FDTD software developed at JPL is that it permits an arbitrary PML definition, which allows a systems engineer to control the effectiveness of the PML absorption vs. size of the FDTD domain or computing time. This is a critical feature that is not found in commercial tools and that is valuable in space research and systems engineering applications.

Once the fields and waves scatter from the target, the resultant waves will propagate outward in all directions. There will be no reflections from the edge of the simulation boundary, but the waves will not travel to the sensor either. To collect the energy of the fields and waves at the sensor, we need to calculate the scattered fields and waves at a chosen location of the sensor. We assume a mono-static sensor, for simplicity, and use the source dipole as the collector or receiver as well. We use a near-field to far-field (NFFT) transform as shown in Figure 43 to transform the field seen at the boundary of the PML to the far fields seen at the receiver dipole.

The NFFT transform uses the formalism of the surface equivalence principle. The surface equivalence principles requires calculation of the electric and magnetic vector current densities on a surface enclosing the body in order to enable calculation of the far fields. In the setup shown in Figure 43, this relates to the 8 planar surfaces at the boundary of the PML and simulation space, and on each side of the FDTD region. However, since we are interested in the mono-static scattering and since the sensor is located in the +z direction and aligned to the centroid of the top FDTD plane, it becomes only necessary to use the top plane to calculate the NFFT transform. This is indicated in Figure 43 as the colored field region. The NFFT collects these fields and converts it to the far field. This can be done in the frequency domain or in the time domain. We choose to apply the transform in the time-domain, as it permitted a manipulation that enables calculation of the far-field solution in real-time (on-the-fly).

To study the 3D FDTD simulations, we developed an integrated simulation module that permitted the complete simulations described in the previous section. The simulation domain was kept small (about 8x8x8 wavelengths or 2.4x2.4x2.4 km) to permit rapid simulations. Figure 4 describes the simulation results as a snapshot in time.

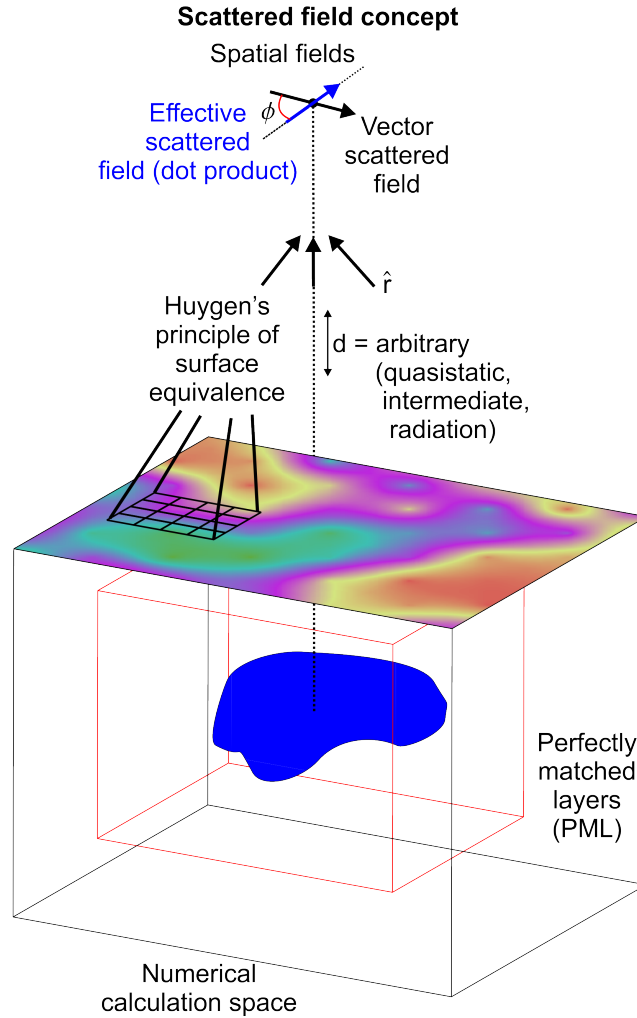


Figure 43. The near-field to far field transform.

TN denotes the simulations at step an arbitrarily chosen step N. Figure 44 shows T1 to T3, where the time snapshots 1-3 occurs in increasing time. At T1 we see the wave being injected into the simulation domain. A backward propagating field is seen propagating into the PML. The PML absorbs the backward propagating wave so that it does not scatter into the active simulation domain. For T1, the left plot shows the result in the xz cut-plane, whereas the right plot shows results in the yz cut-plane. The target is located in the center of the simulation space as indicated in the figure. The point target is not an ideal point target, but rather defined as a good conductor occupying an FDTD material cell. The field propagating into the simulation is spherical in nature, but from a source far away (100km), so that it does not look spherical. Figure 44 shows a view of the injected field, showing its spherical nature.

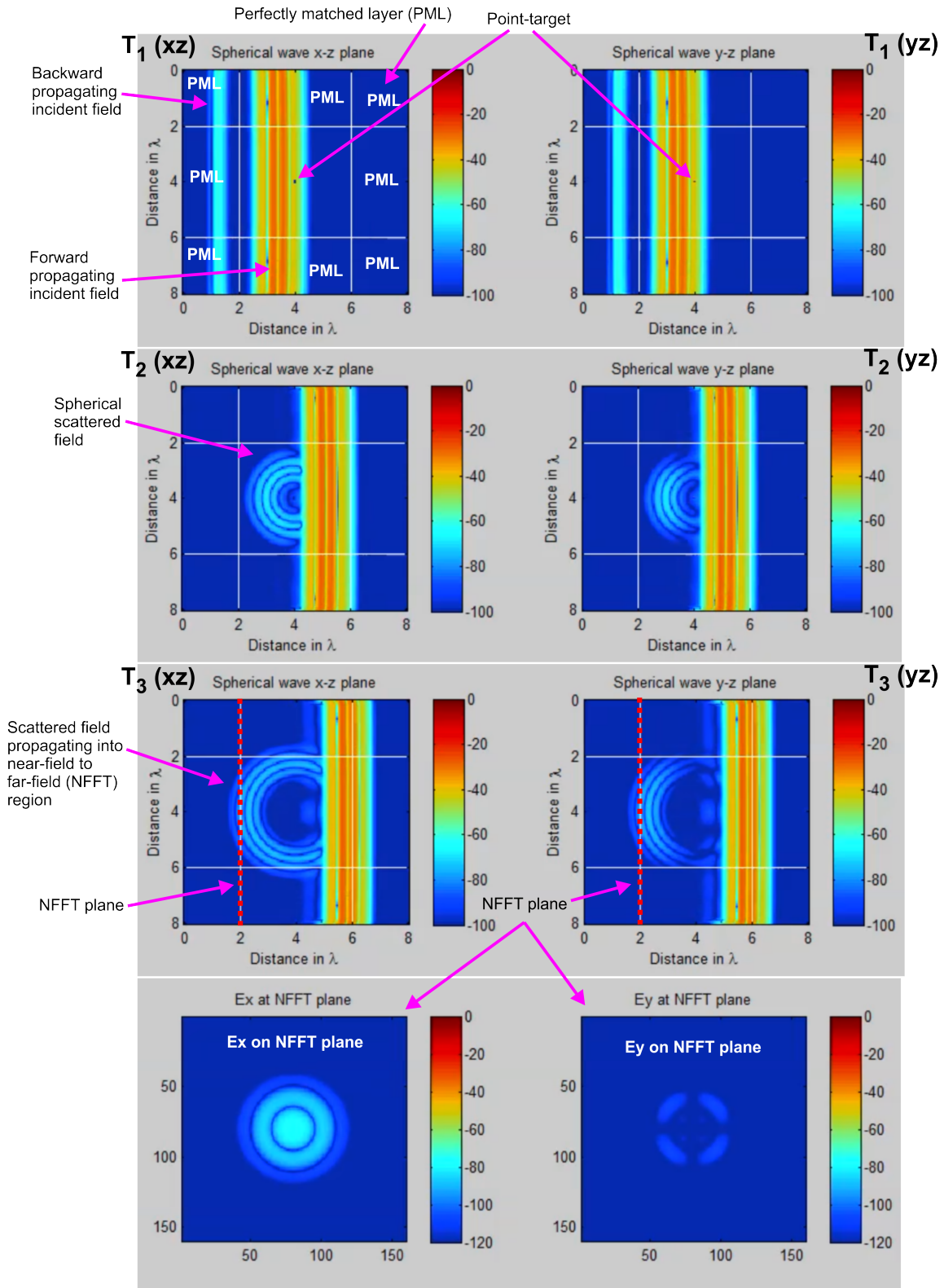


Figure 44. Three time steps of the point target scattering in 3D. The electric fields on the NFFT plane is shown for T_3

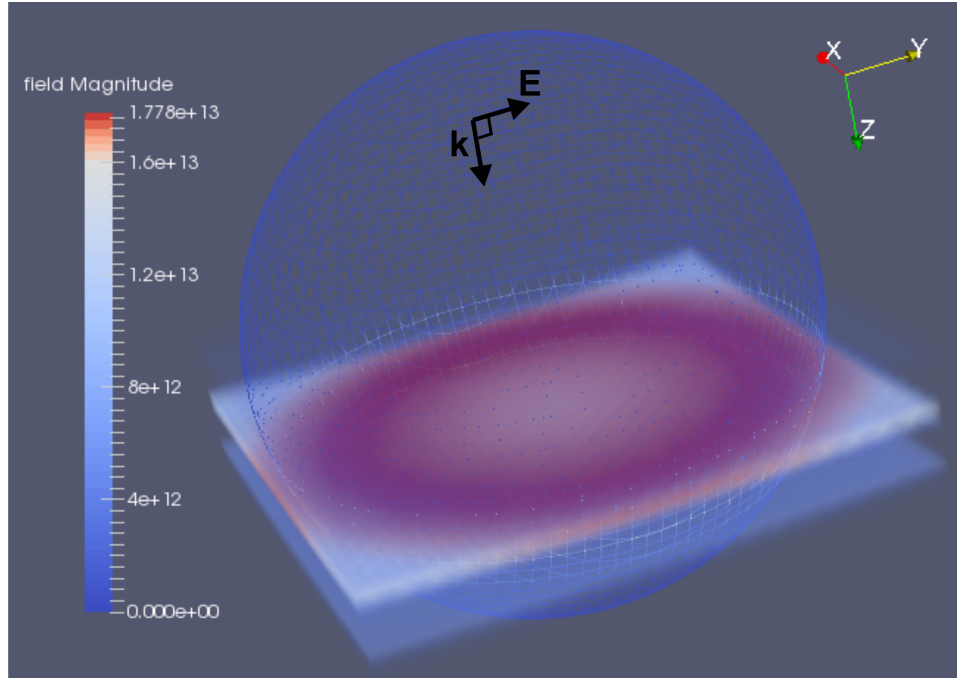


Figure 45. The spherically injected pulse used in the simulations.

When the injected field passes the point-target, energy is scattered toward in the backward direction, causing a strong spherical wave to propagate backwards in T2. In T3, this wave passes through the NFFT boundary and into the PML. The PML absorbs the wave so that it is not reflected back into the active simulations space. The bottom plots in Figure 44 show the electric field components tangential to the NFFT boundary at T3. These results are used by the NFFT transform to calculate the far fields seen at the sensor.

For the 2D comet simulations, the sensor is located at 20km range from the center of the comet. The space between the sensors location and the edge of computational domain is not simulated in order to reduce computational space, as described before. Instead, an analytical-field-propagator (AFP) is used to mathematically inject the fields of the sensor into the top vertical edge of the computation domain [Tan2010]. Due to use of TM-z, we use a z-directed dipole at the sensor location and model the exact fields of the dipole at the top interface of the FDTD computational domain. The calculated fields are determined in the frequency domain using the Hankel function in the frequency domain [Scheider2010], and then converted into the time-domain prior to injection. The E and H fields are injected in a leap-frog manner corresponding to the FDTD method of time-stepping [Tan2010]. After this, the simulations are time-stepped until all scattered waves are undetectable. Based on the stability criterion and frequency, this typically corresponds to 3-8k time-steps with a simulation time of about 30-50 minutes on a quad-core Intel 2.8Ghz computer. The RAM memory usage was typically less than

about 1 GB. Finally, the scattered fields detected at the top vertical edge were integrated using the modified near-field to far-field transformation (NFFT) to determine numerically the fields sensed at the sensor dipole [Li2005]. The setup is shown in Fig. 46.

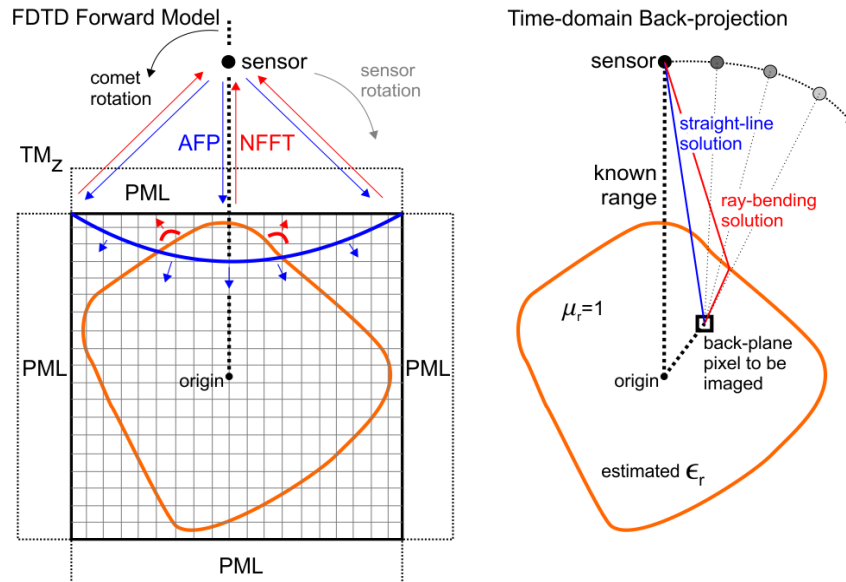


Figure 46. 2D FDTD forward modeling of the comet and time-domain back-projection to obtain inverted dielectric maps

To simulate the circular orbit movement of the sensor, we instead rotated the comet in a counter-direction to that of the intended sensor circular orbit. This is simpler in the sense that only the comet can easily be rotated and re-meshed. For the simulation setup and frequency used here, we used rotation angle step of about 0.3 deg., resulting in about 120 simulations for 0-360 deg. simulations of the comet. This was achieved through parallelization of 6-8 simulations simultaneously within each batch on a multi-core Intel platform. The total duration 0-360 deg. simulations were approximately 2 days. These produced complete radar-grams for the comet imaging radar, which are used with time-domain back-projection to obtain inverted maps of the comet. The radar-grams obtained from the 0-360 simulations contain scattered field solutions from the outer and interior of the comets in time-domain. Often the solutions also include multi-path and multiple reflections and can be ambiguous.

To obtain a spatial dielectric map of the comet, the time-domain back-projection algorithm is used [Li2005]. First, the radar-grams are interpolated using a sinc interpolator and converted into complex values by taking matched filter or convolution with the transmitted analytical signal used in the AFP. The purpose of the complex valued radargram is to obtain a coherent radar signal with accurate phase information of the scattered field. Once the complex valued radargram is obtained, the time-domain back-projection can be initiated. The method used here is known as the pixel-driven methodology, where each pixel in the image back-plane is solved in a sequential manner. A two-dimensional loop is used to sequentially step through all

x-y pixels, where pixel size is chosen to be about 10m, which corresponded to the FDTD simulation space Yee-cell discretization as well. For each pixel, the distance from the pixel to each sensor locations (0-360, or about 1200 sensor locations) is calculated. Once the distance to each sensor is known, the interpolated complex field values corresponding to each pixel are found through a search using the nearest neighbor on the range domain. Using this approach the complex value at the pixel is found for all 1200 sensor locations. The pixel target function is calculated as the sum of all complex values at the pixel. This is repeated for every pixel on the image back-plane to obtain an image target function. Finally, the image target function is normalized to obtain a measure of the relative pixel-target signal strength. This image product can be related to the dielectric map when the conductive losses are low, i.e., for low-loss dielectrics such as in most comets. As an additional higher-order correction, we also implemented a ray-bending solution as shown in Figure 46.

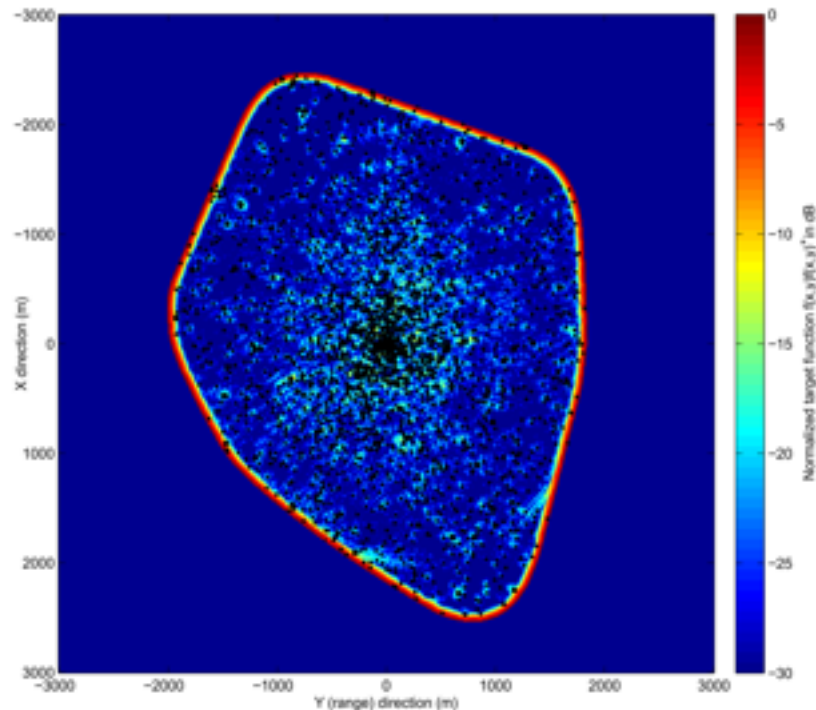


Figure 47. Time-domain back-projected result of the image for a small inclusion comet model using FDTD.

Here the propagation is assumed to penetrate the comet at an angle that statistically corresponds to the shortest propagation path between the sensor and the pixel. By assuming knowledge the comet mean background dielectric, we calculate this shortest path numerically for known comet exterior boundary. This new shortest path is used instead of the direct pixel to sensor range.

Figure 47 shows the solution for a model of the comet with 10m resolution and sensor angular step of 0.2 deg. in the circular orbit. The mean relative dielectric permittivity used in about 3.86, which is found from the comet model, and is used in the ray-bending calculations. This model is known as a small-inclusion comet model,

where the interior has slowly varying spatial dielectric profile with embedded point-like targets. The point-like targets exhibit some realistic dielectric contrast that can be seen on the back-projected image at values of about -12dB to -20dB. The black dots in the image are the actual targets embedded within the comet. The imaged result shows that the complete AFP-NFFT-FDTD with time-domain back-projection works well to form an accurate image in 2D.

5.2.2 Analytical solutions to scattering using the T-matrix boundary value method

The analytical approaches are developed using series expansions in either the transverse electric and transverse magnetic planes. To simplify the solutions, the theoretical formulations are considered for the two-dimensional case only. With this assumption, the cylinders can be considered semi-infinite along the axis of the cylinder. The cylinders are then used to represent spherical particles in the three-dimensional problem, and thus the solutions are analogous to the extent that the polarization response and the spreading loss differences can be neglected, and particles can be assumed to be located in a 2D space only. The technique can be extended to 3D, however the insight gained from a fully parametrized 3D problem over that of a 2D problem may be inconsequential.

The boundary value method uses the solutions of the Hertz potential near the boundary of a collection of semi-infinite cylinders. The cylinders represent particles, and can have an arbitrary size, and dielectric and loss property. A representation of the two-particle system, for simplicity, is shown in Figure 10. The cylinders are non-overlapping, and are located at arbitrary locations in space. The cylinders are located at P_i and the observation is at location P . The far-field solution due to plane-wave scattering of a mono-chromatic incoming wave has been given in [Gu2006], and the near field solutions of the same problem has been given in [Lee1990].

The medium surrounding the particles can be assumed to be homogenous given by a refracting index n , and the solutions for electric and magnetic fields can be found by solving the two Hertz potentials [Schafer2008]:

$$(\Delta + (nk_0)^2) \cdot \begin{bmatrix} u \\ v \end{bmatrix} = 0. \tag{4}$$

Once the solutions to the potentials are known, the fields are given by [Schafer2008]:

$$nk_0 \nabla \times \nabla \times \vec{u} + \nabla \times \vec{v},$$

$$\vec{H} = -n \nabla \times \vec{u} + \frac{i}{k_0} \nabla \times \nabla \times \vec{v},$$

$$\vec{u} = (0, 0, u)^T,$$

$$\vec{v} = (0, 0, v)^T.$$

(5)

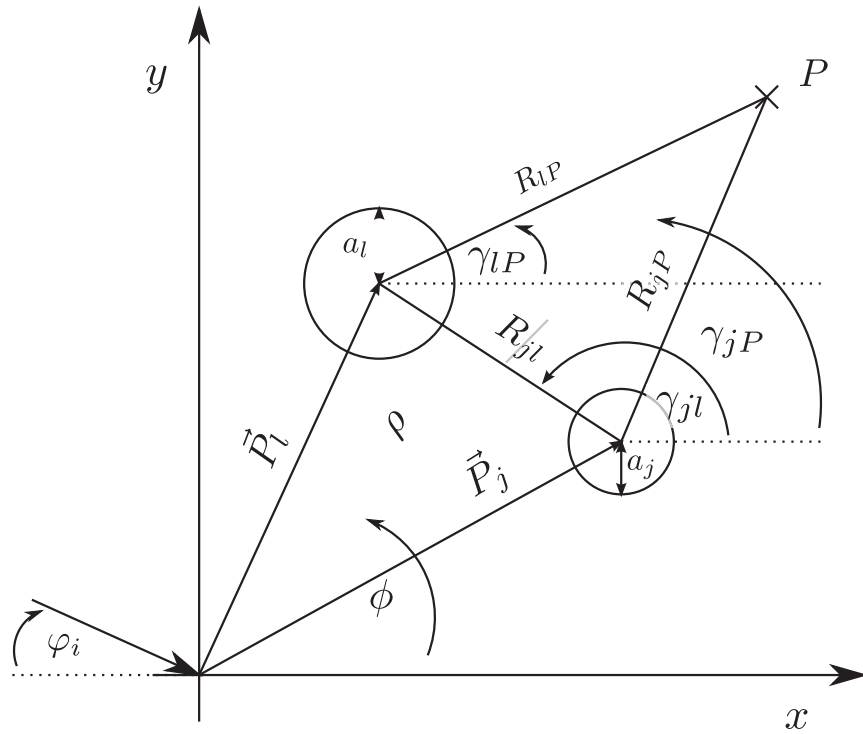


Figure 48. Description of the multiple particle scattering (adapted from [Lee1990, Schafer2008])

It is convenient to formulate the problem in the Cylindrical coordinate frame and basis due to the use of semi-infinite cylindrical as 2D representation of particles. In the coordinate frame, as described by Figure 48, the symmetry is chosen along the z-axis, and the z-derivates are therefore non-existent and can be removed from the derivations. Therefore, the solutions to the field equations can be given by:

$$\begin{aligned} & \frac{1}{\rho} \frac{\partial v}{\partial \phi}, \\ H_\rho &= -\frac{n}{\rho} \frac{\partial u}{\partial \phi}, \\ E_\phi &= -\frac{\partial v}{\partial \rho}, \\ H_\phi &= n \frac{\partial u}{\partial \rho}, \\ E_z &= -\frac{i}{nk_0} \left[\frac{1}{\rho} \frac{\partial}{\partial \rho} \rho \frac{\partial}{\partial \rho} + \frac{1}{\rho^2} \left(\frac{\partial}{\partial \phi} \right)^2 \right] u, \\ H_z &= -\frac{i}{k_0} \left[\frac{1}{\rho} \frac{\partial}{\partial \rho} \rho \frac{\partial}{\partial \rho} + \frac{1}{\rho^2} \left(\frac{\partial}{\partial \phi} \right)^2 \right] v. \end{aligned}$$

(6)

The total potential outside the cylinders can be written as a combination of the incident potentials and due to the scattered potentials [Bohren1998]:

$$\begin{bmatrix} u^t(P) \\ v^t(P) \end{bmatrix} = \begin{bmatrix} u^0(P) \\ v^0(P) \end{bmatrix} + \begin{bmatrix} u^s(P) \\ v^s(P) \end{bmatrix},$$

(7)

where the superscript 0 denote the incident potentials and the superscript S denote the scattered potentials, whereas the total potentials are given by the superscript t. The incident field potentials are given as [Bohren1998]:

$$\begin{bmatrix} u^0(P) \\ v^0(P) \end{bmatrix} = \begin{bmatrix} \delta_{TM} \\ 1 - \delta_{TM} \end{bmatrix} \sum_{n=-\infty}^{\infty} (-i)^n e^{in\phi} e^{in\phi_i} J_n(k_m \rho),$$

(8)

where the J_n is a Bessel function of the first kind, and the delta function is used to describe a transverse magnetic or transverse electric solution. The scattered field potentials are given by [Bohren1998]:

$$\begin{bmatrix} u^s(P) \\ v^s(P) \end{bmatrix} = - \sum_{j=1}^N \sum_{n=-\infty}^{\infty} (-i)^n e^{in\gamma_{jp}} H_n(k_m R_{jp}) \begin{bmatrix} b_{jn} \\ a_{jn} \end{bmatrix}, \quad (9)$$

where the H_n is a Hankel function of the second kind, and a and b are the expansion constants that can be found by solving a system of equations [Schafer2008, Bohren1998]. For simplicity, we present the co-oriented solutions of the fields, though all components can be found in [Schafer2008, Bohren1998]. For the transverse magnetic solutions, the electric field equation is given by [Bohren1998]:

$$E_z^s = -ik_m \sum_{j=1}^N \sum_{n=-\infty}^{\infty} (-i)^n e^{in\gamma_{jp}} H_n(k_m R_{jp}) b_{jn}. \quad (10)$$

For the transverse electric solutions, the magnetic field equation is given by [Bohren1998]:

$$H_z^s = -ik_m n_m \sum_{j=1}^N \sum_{n=-\infty}^{\infty} (-i)^n e^{in\gamma_{jp}} H_n(k_m R_{jp}) a_{jn}. \quad (11)$$

The reader is referred to [Schafer2008, Bohren1998] for the detail derivations and solutions, and for truncation techniques for the summations or series solutions.

5.3 Simulations and Experiments using Granular Media

The problem of using granular media to aid in microwave imaging requires the study of two general bodies of problems. The first general problem involves the

vector radiative transfer theory to describe the exact phase sensitive scattering of incident waves by the granular medium, which may be complex in nature with various particle sizes, distributions, and dielectric and conductive properties. The second general problem involves the exact image inversion theory based on phase sensitive scattering of a general distributed scene to be imaged – which may also contain various inclusion/target sizes, distributions, and dielectric and conductive properties. These two problems can be somewhat decoupled to permit development of each independent of the other. To avoid undue and unnecessary complications, the approach has been to limit the problem to two-dimensions and to use cylindrical media for both the granular medium constituents and the targets in the imaging scene. To permit coherent imaging of the target with aid from the granular media in directing energy, both problems must permit multiple scattering and complex dielectric properties to allow volume currents inside the media, as opposed to just surface scattering found from perfect conducting mediums.

The first problem has been recently addressed using a boundary value method to account for multiple scattering from particles using various sizes, distributions, and complex permittivity values. This approach decomposed the problem into transverse electric (TE) and transverse magnetic (TM) wave components, and solves the boundary conditions for each cylindrical particle using the usual boundary conditions. Presented in a T-matrix solution, the technique permits efficient calculations of the exact plane-wave scattering of TE and TM waves by the arbitrary granular media. See Figure 49.

Summary of multiple scattering model applied to a few particles

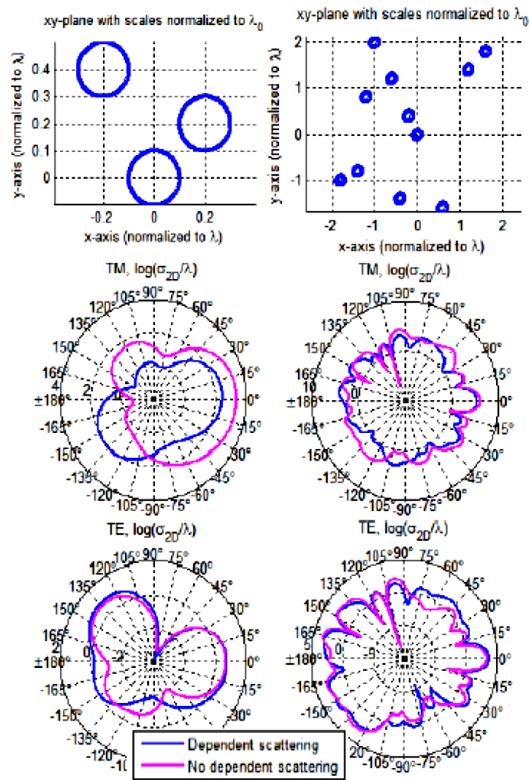
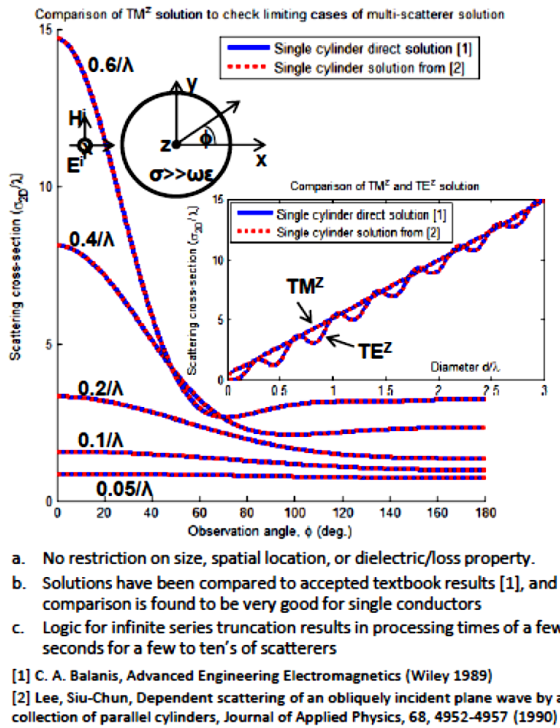


Figure 49. Multiple scattering model applied to a few particles.

The second problem is addressed using a similar technique. The scattered field is computed in a similar manner, but instead of calculating the scattering of the granular media, we calculate the scattering of the target scene. This scattered wave solution is then used to form an image using the time-domain back-projection technique, which projects scattered fields in time into specific pixels within the imaging plane in a coherent manner (Figure 50). To simplify the current development, we use back-scatter from the target scene – therefore describing a mono-static microwave radar problem. The exact scattering permits use of various properties and configurations of the scene to be imaged. We first study the point-target response, where we simulate scattering and then image a collection of small targets, where the targets diameter is significantly smaller than a skin-depth (skin-depth of EM penetration in the target).

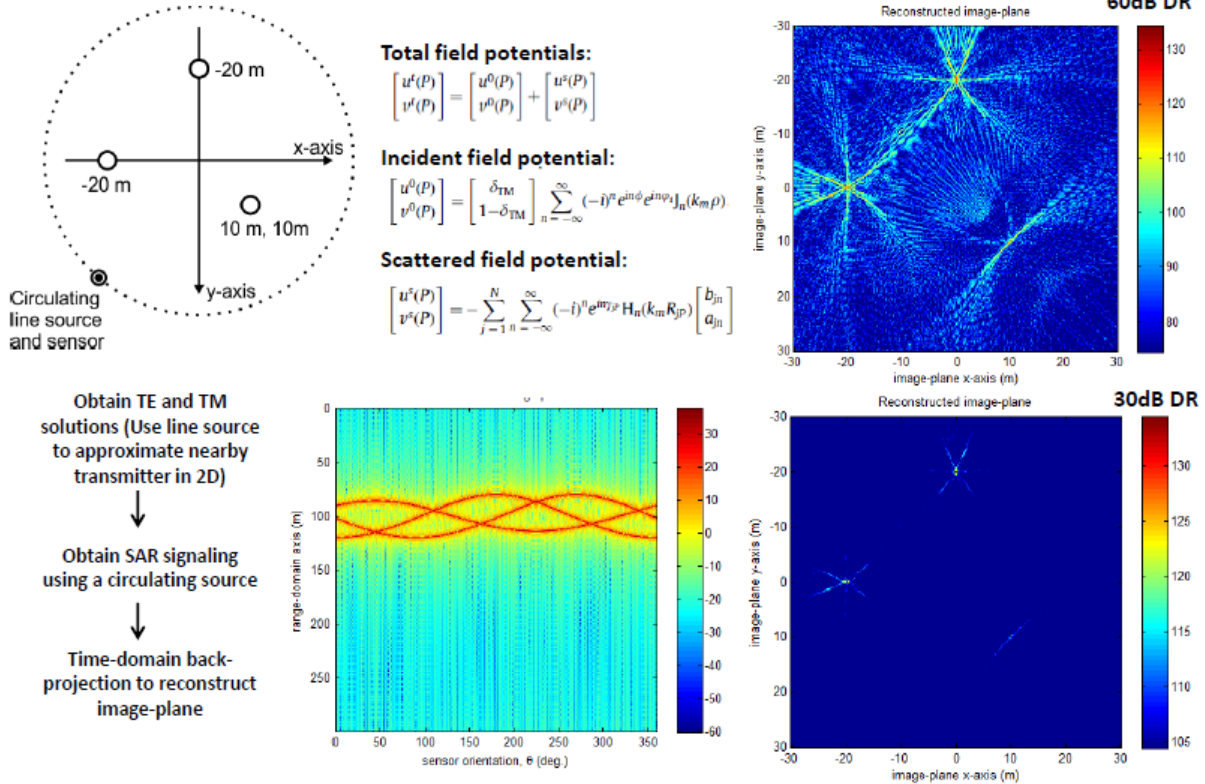


Figure 50. Analytical computation of scattered field.

With the verification of the scattering and imaging complete on point-targets, we next study semi-realistic targets. As an example, the image below shows a small collection of four targets being imaged using coherent and incoherent versions of the time-domain back-projection inversion. The particles are of different sizes and the image-plane is shown for particles that have properties of ice, pure water, salt water, and the ideal target case of perfect conductors (Figure 51). Even in this simple example, we see the artifacts of scattering in the image due to low-loss dielectrics. Coherent imaging is shown to reduce these artifacts considerably when compared to incoherent imaging.

The goal is then to complete the theory and development to study multiple scattering in the imaging plan, and to integrate both granular scattering and imaging problems. The combined analysis will permit a sensitivity analysis of the exact imaging problem in the context of an arbitrary granular medium. The purpose is simple, when a satellite mission is conducting SAR imaging, the imaging resolution is high in the azimuth direction, but low in the cross-track direction. For target bodies with little geophysical activity, this is not problematic since the satellite will eventually sense the whole object and be able to integrate all the data to obtain imaging of the interior. However, for target bodies with high activity, simultaneous cross-track imaging is extremely desirable. While this can be achieved through a second or

multiple sensors, there is usually a prohibitive cost associated with additional satellites or sensors.

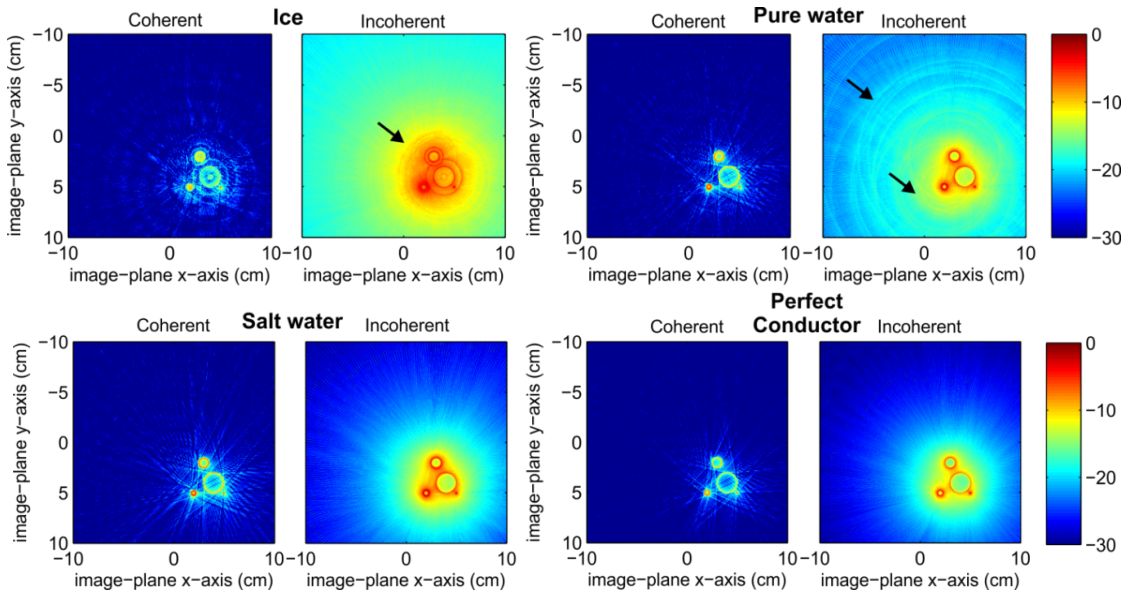
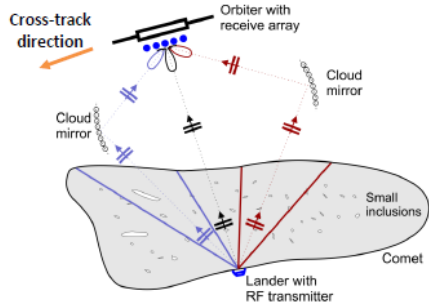


Figure 51. Results of tomography analysis for ice and water particles.



During an azimuth SAR orbit, the cross-track resolution suffers in objects with dynamic geophysical activity.

1. Dynamic cross-track aperture approaches 0°
2. Ambiguity in coherent reconstructed image-plane is pronounced

An ideal representation of a cross-track solution can be formed by enabling a large aperture in the cross-track direction

1. Sensor is not sampling sufficiently in this direction, but the cloud medium can be used to focus

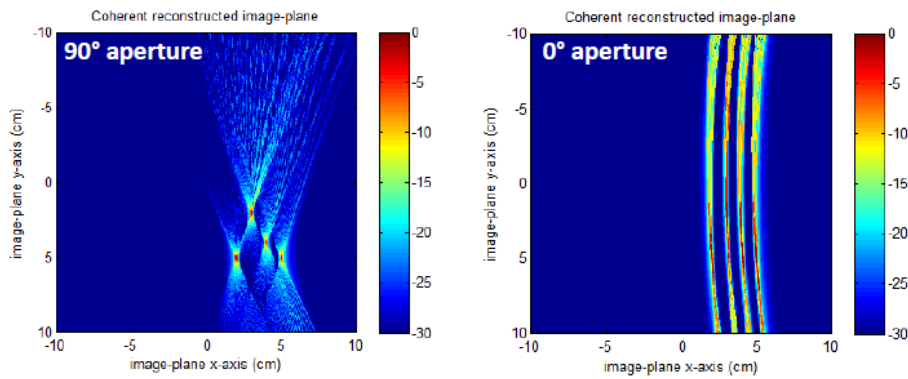


Figure 52. Sensitivity results for simultaneous cross-track imaging.

The artifacts due to cross-track imaging is further illustrated using a limited aperture problem and results are shown in Figure 52 to show the benefit of simultaneous cross-track imaging. The images are simulated and back-projected SAR images using an observed aperture in the cross-track. Note that the 90 deg. aperture in cross-track permits a good reconstruction of the 4 targets, whereas with a 0 deg. aperture, extremely poor resolution is obtained (note, the satellite is on the x-axis at $y = 0$, thus the arc of solutions for the 0 deg. aperture case).

The above considerations permit us to state that for targets with high geophysical variability in cross-track or inaccessible regions, it is useful to use scattering via some re-directed means to image the body. This mechanism of re-direction can be achieved via preferential scattering of waves through a granular-based medium. In addition, since higher resolution can be obtained by measuring a wider aperture through use of scattering via a granular media, it is obvious, though observed through Figure 52 as well, that higher resolution can be achieved.

To simulate the effect of the medium, we first obtain a model for the scattering the target body, then redirect scattering through the granular medium. This redirected scattering is essentially a second scattering problem, where the waves scattered from the target body is scattered again by the granular medium. The redirected waves are then focused to the sensor, which collects the energy and focuses the target image in the cross-track. The top left figure below (Figure 53) shows a setup for the simple case of a finite planar cloud mirror. Here the mirror is constructed of a number of closely spaces granular media to form a planar surface that is about 18λ wide.

Example: A simple finite planar cloud mirror

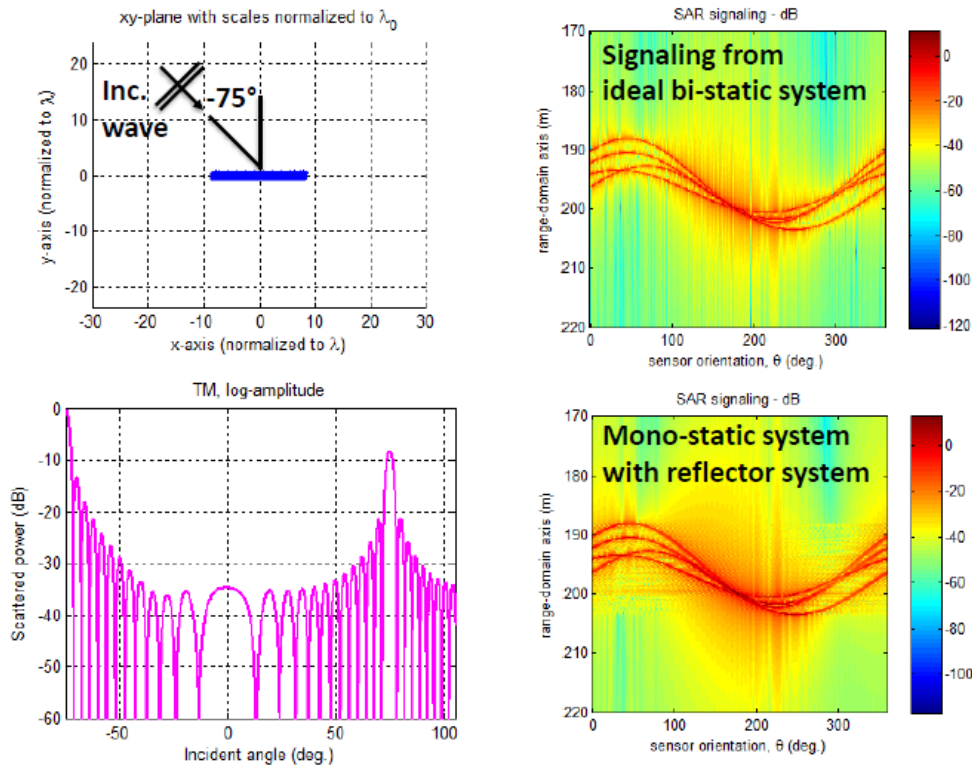


Figure 53. Scattering result for finite planar cloud mirror.

Through measurement of the bi-static transverse magnetic TM scattering, we obtain the angular dependence of the scattered amplitude and phase over the frequencies required for the radar operation. The TM scattering as a function of scattered angles is obtained for each frequency bin needed for radar imaging. Next, the planar mirror is placed at a desirable location in the problem space such that its reflectance properties become useful to redirect the energy. For example, from the bottom left of Figure 53, it's clear that a substantial reflection cross-section occurs at about -75 deg., so we place this mirror at a location based on that angle. This optimization step is to be discussed in detail in the future.

Once the location is selected, the scattered waves from the target is calculated using the usual scattering theory, and then the scattering function of the granular medium derived previously is used to obtain the scattered field at the sensor. A synthetic aperture in the cross-track is obtained by rotating the medium to image different perspectives of the target body. With the assumption of known scattering function of the granular medium, we can remove the phase perturbation from the granular medium, and are left with the correct amplitude and phase of the redirected signal after removing phase artifacts of the granular medium. This result is shown in the bottom right figure of the same figure. To compare to an ideal representation without the granular medium, we show in Figure 54 the same result using a bi-static measurement on the top right of the same figure. Note that similarities in the result. Note also that the bi-static approach would require a second satellite sensor, whereas the mono-static approach with granular medium only required a single satellite sensor. The result of this, after processing for imaging through SAR approaches is shown below. The figure on the top right is from using a mono-static sensor and granular medium for cross-track SAR imaging.

We studied two critical topics and completed some initial studies on both topics. The first addressed the microwave based imaging or radar imaging of a target, by scattering energy through a granular media. The purpose is to enable imaging of targets that are either occluded, or to image previously inaccessible parts of the target. This is achieved by re-directing energy through reflection from the granular media. The second topic addresses microwave imaging of the granular media itself, for the purpose of enabling feedback control.

For the first topic, we developed two types of forward simulation methods, one using analytical series expansion of the scattered field – for a quick simulation of scattering from finite spheres (Figure 55), and the second using finite-difference time-domain (FDTD) to simulate full-wave scattering of arbitrarily shaped objects (Figure 56).

Cross-track– Finite planar mirror

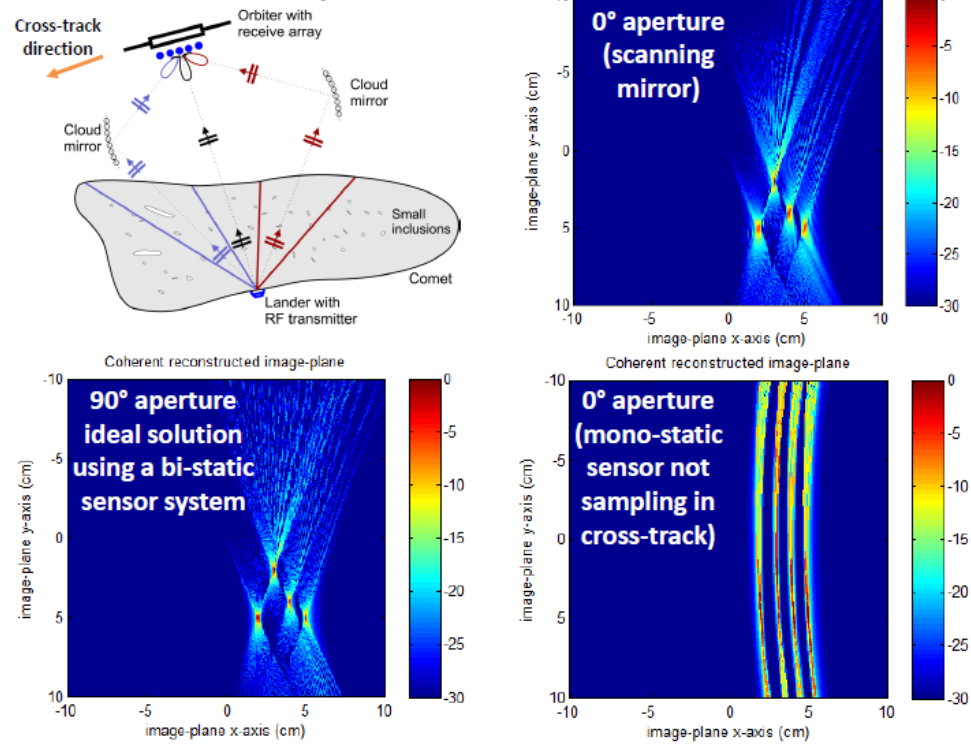


Figure 54. Results for bi-static measurement.

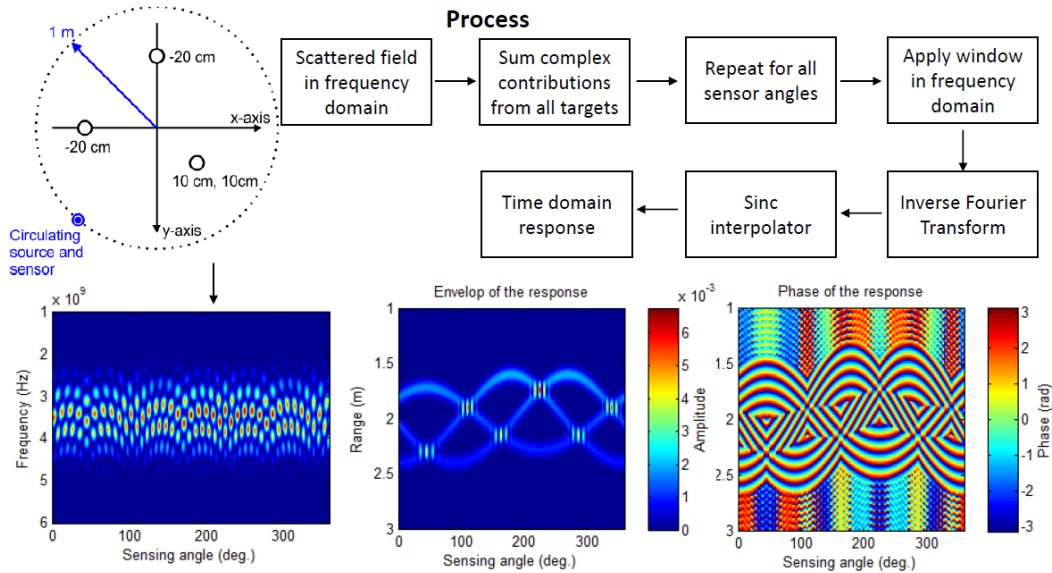


Figure 55. The point-target simulation for quick-analysis of scattering

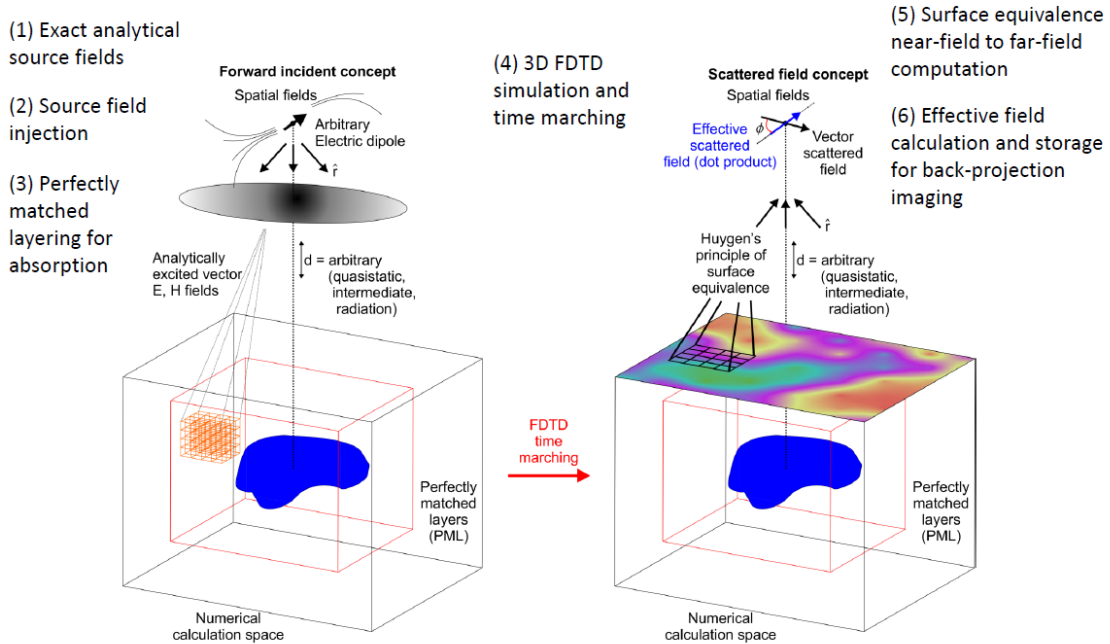


Figure 56. The FDTD technique for full-wave simulation of scattering

We used the simulations to develop a reconstruction algorithm using time-domain back-projection as described in a previous section (Figure 57), and verified that it worked correctly using the simulated results from simple scatterers (Figure 57).

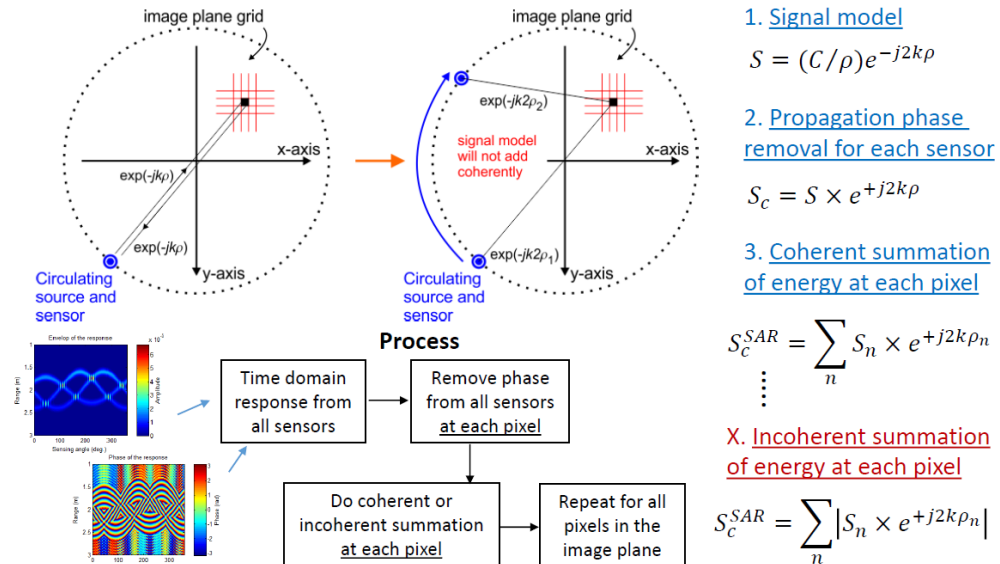


Figure 57. The time-domain back-projection algorithm.

In addition, we conducted some simple experiments to first verify the time-domain back-projection algorithm using data collected from a point-target scattering experiment of a small metallic ball collected using a vector network analyzer (VNA) in free-space and located in an outdoor environment. The ball was held in space and interrogated using a VNA for a wide spectrum of frequencies using a simple wideband horn antenna (see Figure 58).

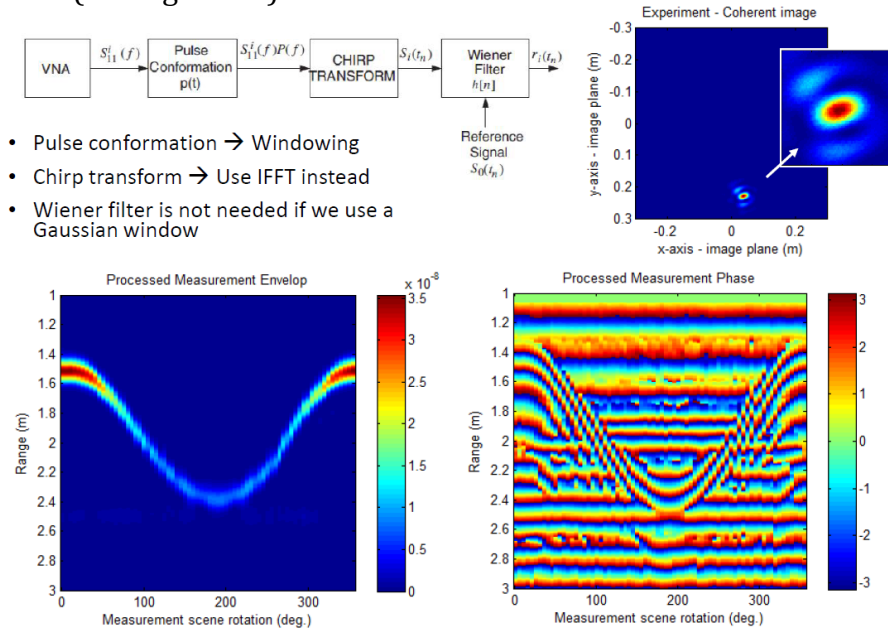


Figure 58. Results from experiments using a VNA and horn antenna over a wide microwave band, and using time-domain back-projection for the inversions.

The next step, was to develop a radiative transfer model that permits multiple scattering from the granular media, in order to re-direct the energy from/to the target. We developed this using exact transverse electric (TE) and transverse magnetic TM derivation using electromagnetic potentials and boundary conditions on particles. We used the derivations and approach described in the previous sections to describe the scattering by multiple cylinders using the analytical scattered fields which includes multiple scattering (Figures 59 and 60).

Total potentials outside the cylinders:

$$\begin{bmatrix} u^t(P) \\ v^t(P) \end{bmatrix} = \begin{bmatrix} u^0(P) \\ v^0(P) \end{bmatrix} + \begin{bmatrix} u^s(P) \\ v^s(P) \end{bmatrix}$$

Potentials due to incident fields Potentials due to scattered fields

Incident potentials:

$$\begin{bmatrix} u^0(P) \\ v^0(P) \end{bmatrix} = \begin{bmatrix} \delta_{TM} \\ 1 - \delta_{TM} \end{bmatrix} \sum_{n=-\infty}^{\infty} (-i)^n e^{in\phi} e^{in\phi_i} J_n(k_m \rho)$$

Scattered potentials:

$$\begin{bmatrix} u^s(P) \\ v^s(P) \end{bmatrix} = - \sum_{j=1}^N \sum_{n=-\infty}^{\infty} (-i)^n e^{in\gamma_j \rho} H_n(k_m R_{j\rho}) \begin{bmatrix} b_{jn} \\ a_{jn} \end{bmatrix}$$

Example – Scattered E_z field for TM mode:

$$E_z^s = -ik_m \sum_{j=1}^N \sum_{n=-\infty}^{\infty} (-i)^n e^{in\gamma_j \rho} H_n(k_m R_{j\rho}) b_{jn}$$

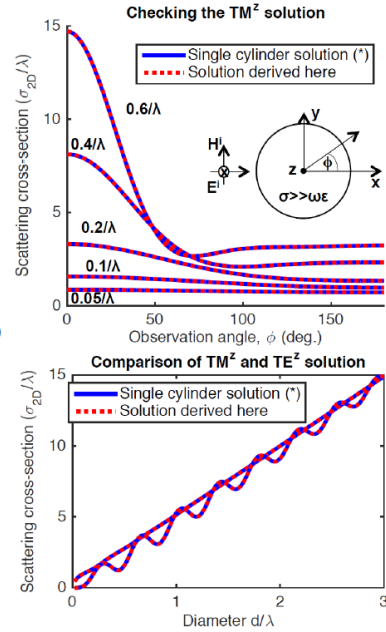


Figure 59. Exact solutions for the radiative transfer from granular media

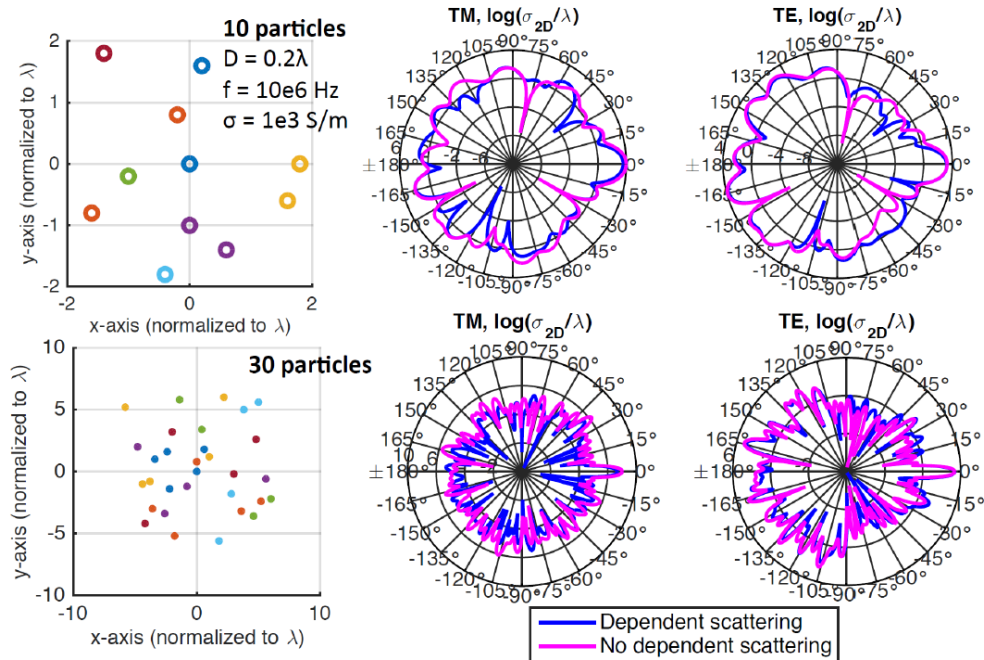


Figure 60. Exact solutions for the radiative transfer from two types of granular media

Once the transfer model was complete, we studied the re-directing of signaling using some simplified structures for granular media. Specifically, we studied the planar mirror as introduced in Figure 54, with a scheme developed to permit imaging using SAR techniques (Figure 61).

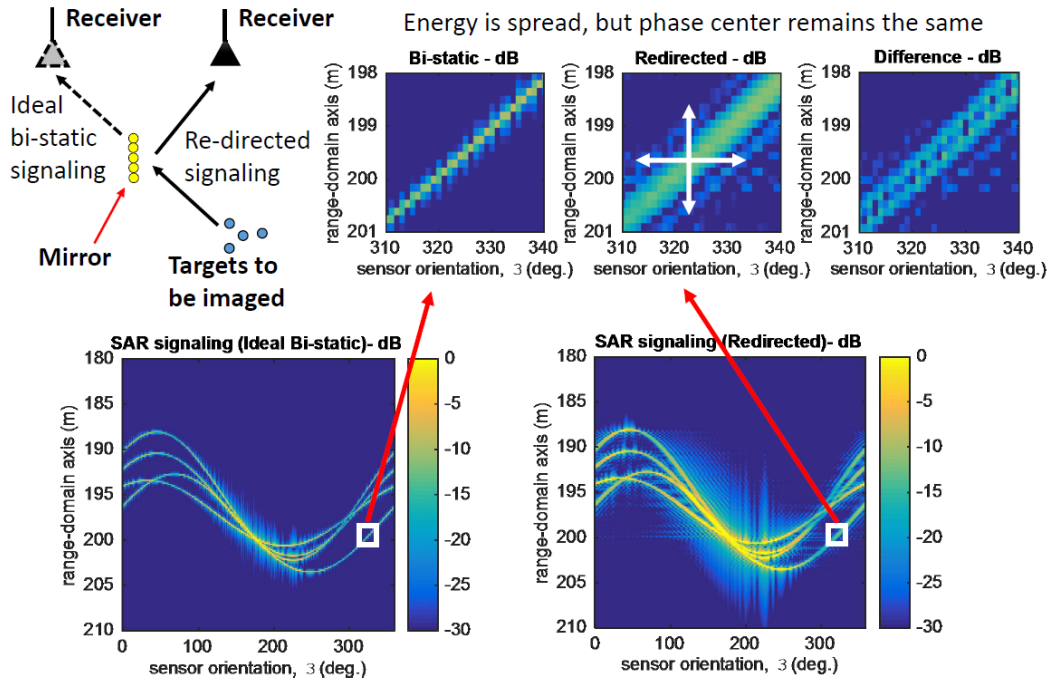
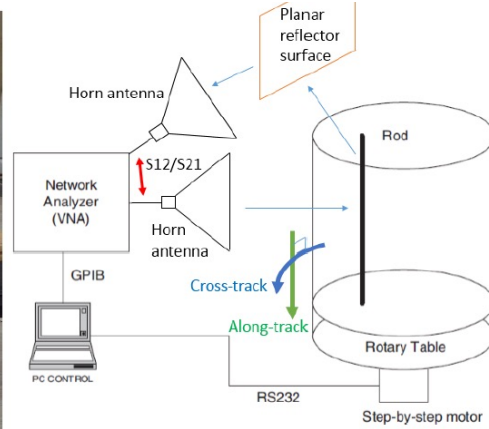
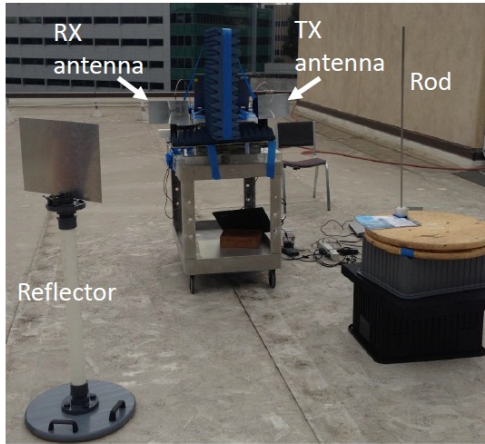


Figure 61. Analysis of re-directed signaling using granular media

5.4 Radar Experiments

To complete this work, we conducted some experiments to verify the validity of the models and algorithms. In these experiments, we used a planar reflector to re-direct the energy and image a target through the re-directed energy, scattered through the planar reflector.

Figure 62 depicts the nature of the experiments conducted. A vector network analyzer is used to measure the scattered electromagnetic fields in the far field of the object to be imaged. For simplicity, the object to be imaged is a simple particle. To further simplify the experiment, we restrict the study to two dimensions, which permit the use of a cylinder to model the particle. We use a rod to model the cylinder or particle in two-dimensions, and use two wide-band horn antennas to generate and sense the fields. A planar finite reflector is used as a simple reflector system to re-direct the energy and fields. A frequency of 1-6 GHz is used.



- Rod-Reflector-Antenna separation distances of about 1-2 m
- Rod is rotated at steps of 5deg. between 0-360deg.
- Network analyzer programmatically captures wideband frequency response
- Frequency of 1-6 GHz is used

Figure 62. Experiments to verify imaging through a planar reflector as an idealized granular media cloud.

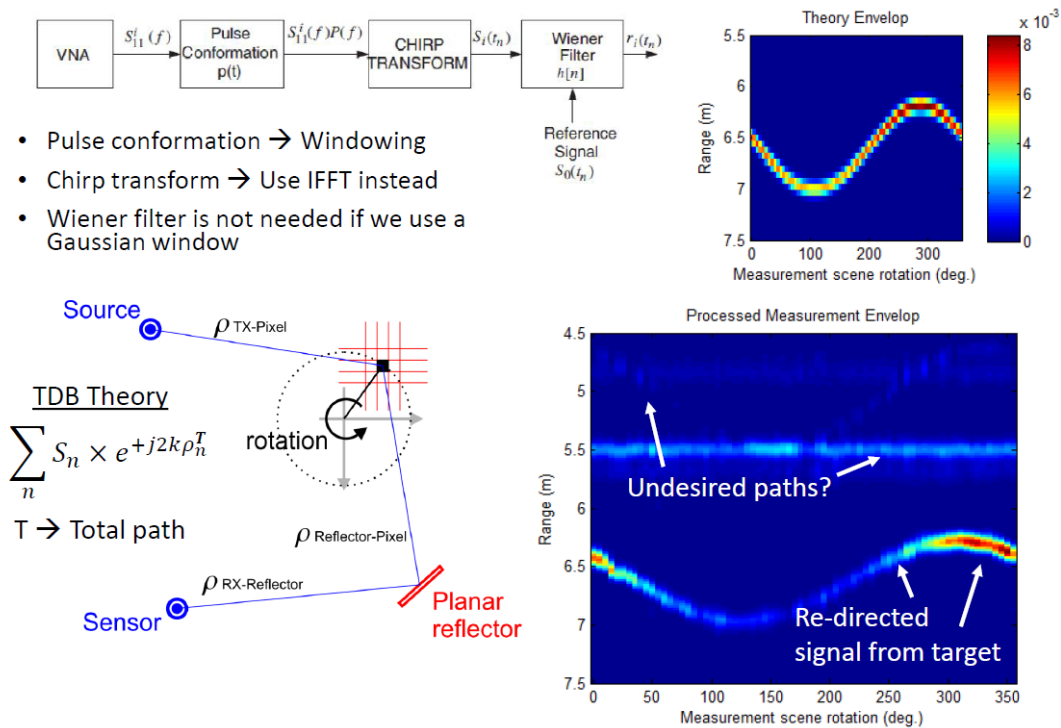


Figure 63. Results of experiment using a planar reflector as a granular media.

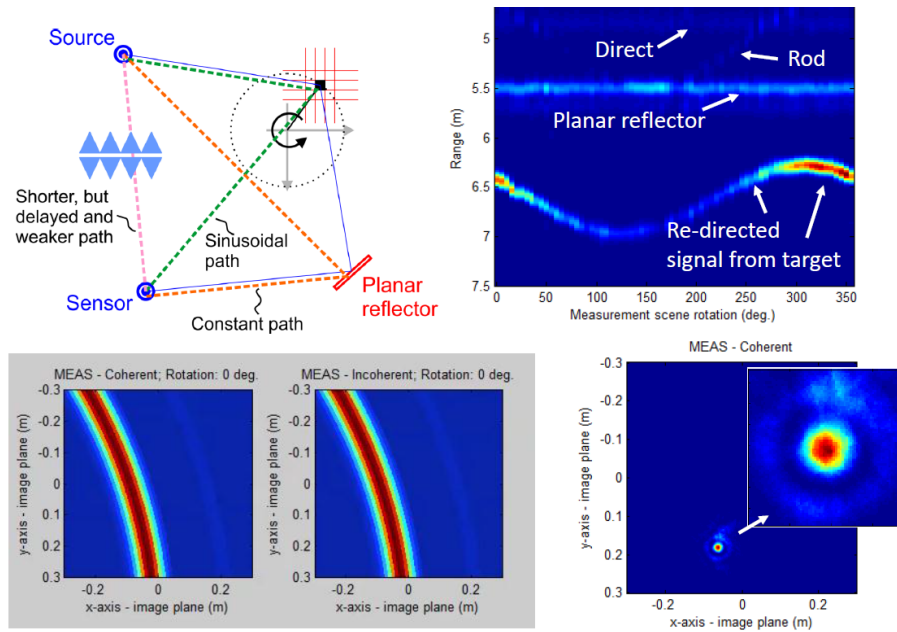


Figure 64. Inverted results showing target imaging.

Figures 63 show the results of the experiments and signal processing, along with pulse conformation, chirp transforms, and filtering as well as range gating to remove artifacts of the experiments. The results of the inversions are shown in Figure 64, where the time domain back-projection technique described in a previous section is used. The results confirm the ability to image via a re-directed means using scattered fields through a granular media in space.

5.5 Effect of cloud geometry and spatial randomness on system performance

The effect of the cloud geometry plays a significant role in the scattering process. In addition, the spatial randomness effects the beam collimation (see Figure 65) and can have an effect on the imaging qualities as it effects effective aperture, coverage, and resolution of the radar techniques. These must be studied to inform about the control of the granular media clouds in space for future re-directed imaging applications.

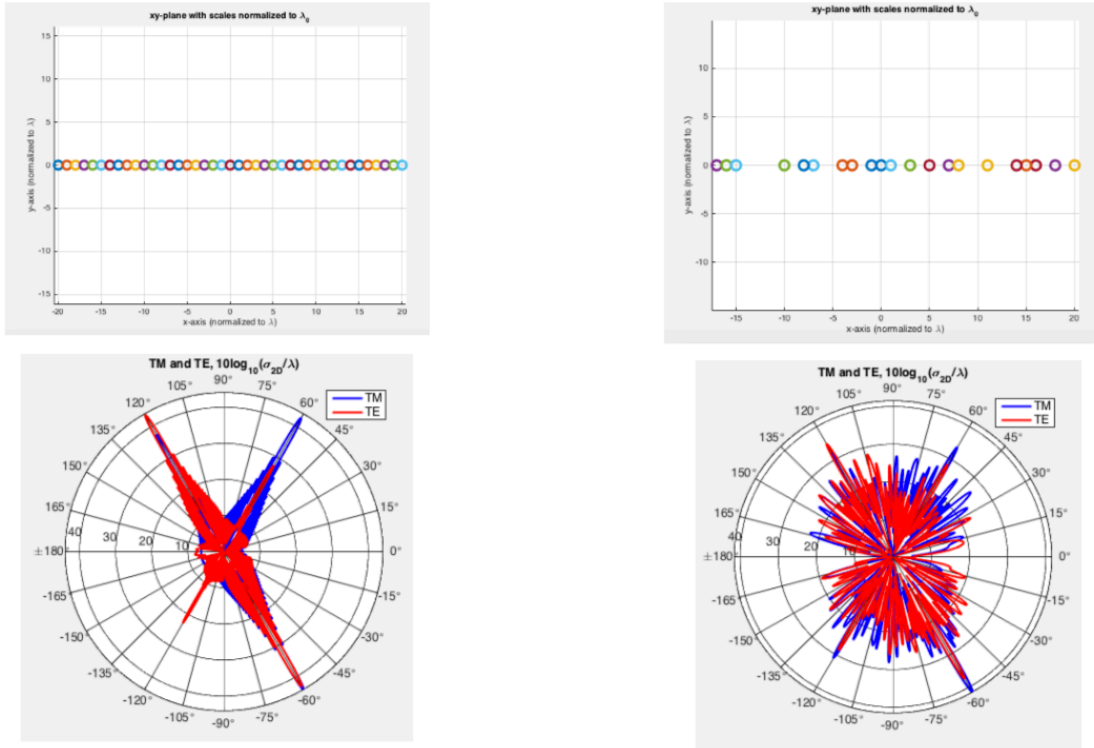


Figure 65. Effect of randomness on system performance as simulated using the analytical field solutions described in the previous sections.

5.6 Radar imaging of granular media for feedback control

In addition to the above discussions, we also developed imaging techniques to enable imaging of the granular media for feedback control. We used the cloud physics simulator described in the previous sections, that use point-target scattering functions in cylindrical coordinates, to derive scattered fields from a cloud undergoing variation in time that includes shrinking and rotating cloud configurations. The cloud geometry is described as point-like targets for simplicity, so that the scattered fields are dominated by Rayleigh scattering mechanisms. The exact solutions developed by analytical means are used in two-dimensions to simplify the problem, as implemented in previous sections. The imaging is achieved in transverse magnetic (TM) basis, again for simplicity, and in addition, the particles are assumed to be good conductors.

Figure 66 shows an example of shrinking and rotating cloud configuration chosen to be imaged. The figures show snapshots in time. Figures 67 and 68 shows results for the forward model (exact analytical solutions in TM basis) and inverse solutions using time domain back-projection techniques as described in previous sections. The results show that the general nature and geometry of the cloud can

indeed be easily imaged. Higher resolution is expected in the imaging plane by considering wider bandwidths and coherent back-projection algorithms.

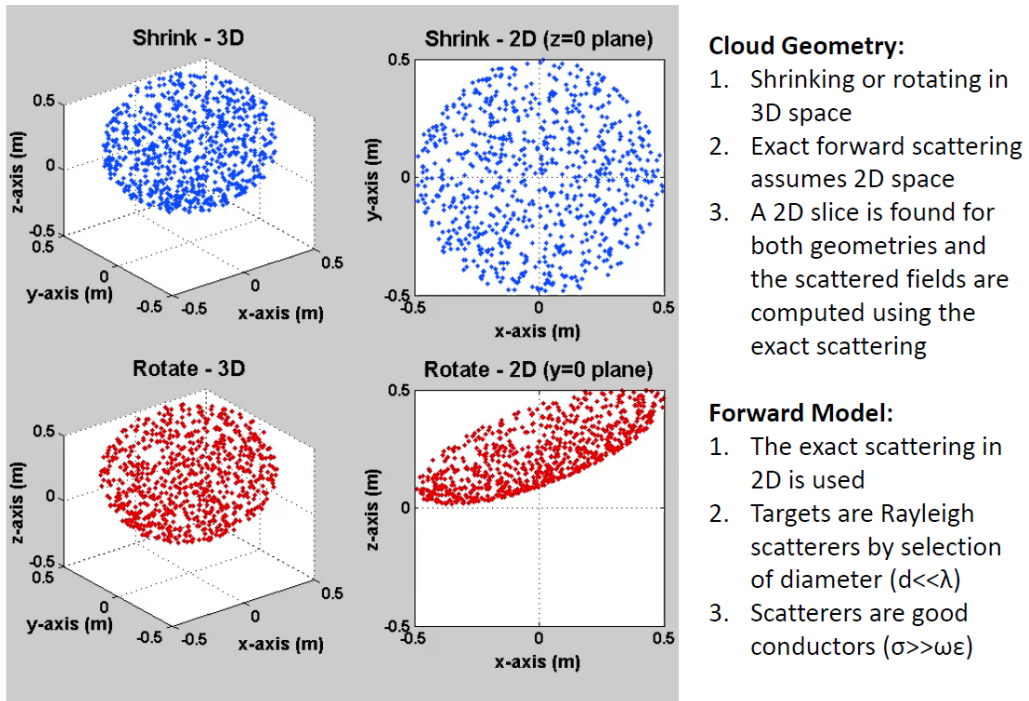


Figure 66. Granular cloud geometry and forward model assumptions.

Shrinking Cloud – Forward Model and TDB

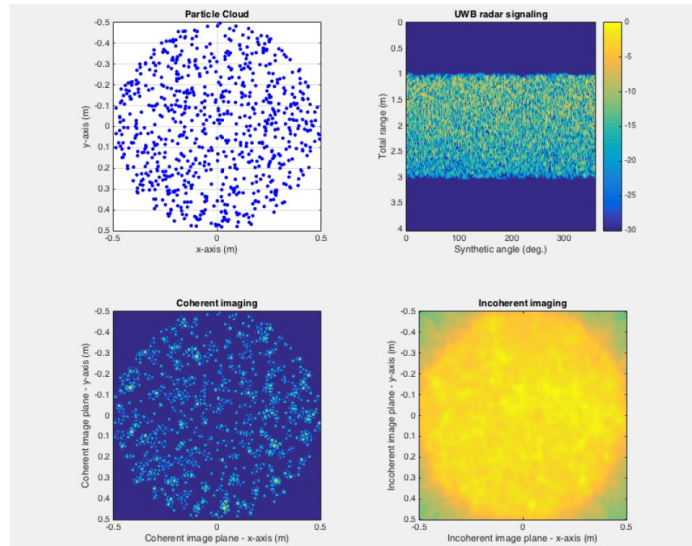


Figure 67. One frame of a video for the imaging of a shrinking cloud.

Rotating Cloud – Forward Model and TDB

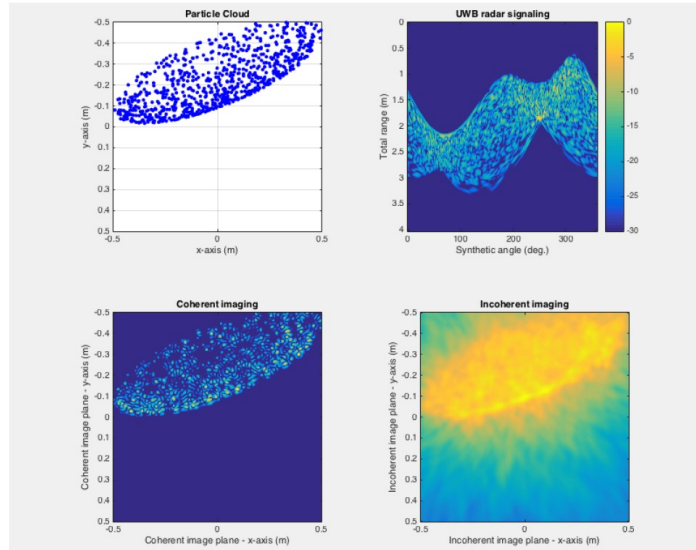


Figure 68. One frame of a video for the imaging of a rotating cloud.

6. Interaction of Granular Medium with Incident Wavefront

We conducted experiments and simulation of the optical response of a granular lens. In all cases, the optical response, measured by the Modulation Transfer Function (MTF), of the hexagonal reflectors was closely comparable to that of the spherical mirror. We conducted the analyses further by evaluating the sensitivity to fill factor and grain shape, and we found a marked sensitivity to fill factor and no sensitivity to grain shape. However, we found that at fill factors as low as 30%, the reflection from a granular lens is still excellent. In fact, we replaced the monolithic primary of an existing integrated model of an optical system (W-First Coronagraph) with a granular lens, and we found that excellent contrast levels are provided by the granular lens that can be useful for exoplanet detection.

6.1 Sensitivity Studies

Analyses have been carried out at JPL to compute the optical modulation transfer function (MTF) of the entire aperture as a function of spatial randomness, wavelength, fill factor, and other errors such as random tip and tilt of the grains, on the wavefront. These analyses, which began in the last period, provide insight on the sensitivity of the optics to spatial randomness, fill factor levels, and positioning and stabilization requirements that need to be placed on the aperture. Some preliminary results are shown in Figures 69 through Figure 72. Figure 69 shows plots of the random mask, generated without the exclusion process (so some overlap between grains can take place), compared to the filled aperture. Figures 70 to 72 show results

of the random mask calculations with disks, ellipsoids, and aligned ellipsoids, generated with a Poisson exclusion process (non-overlapping grains), and fill factor = 5%, at a fixed wavelength. As expected, the shape of the grains is not very important, but the distribution, or fill factor, is.

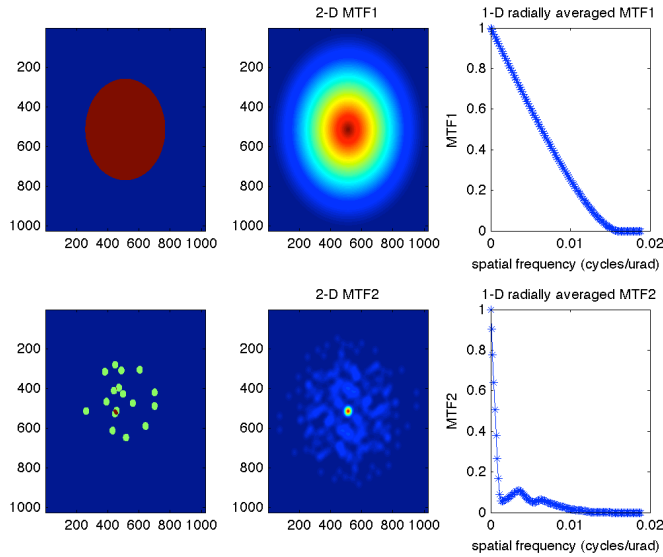


Figure 69. Plots on the random mask without the exclusion process compared to the filled aperture.

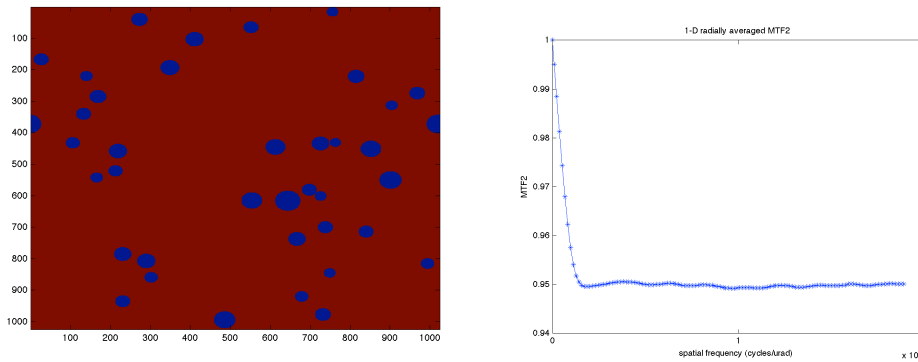


Figure 70. Plots on the random mask calculations with disks with Poisson exclusion process (non-overlapping grains), fill factor = 5%.

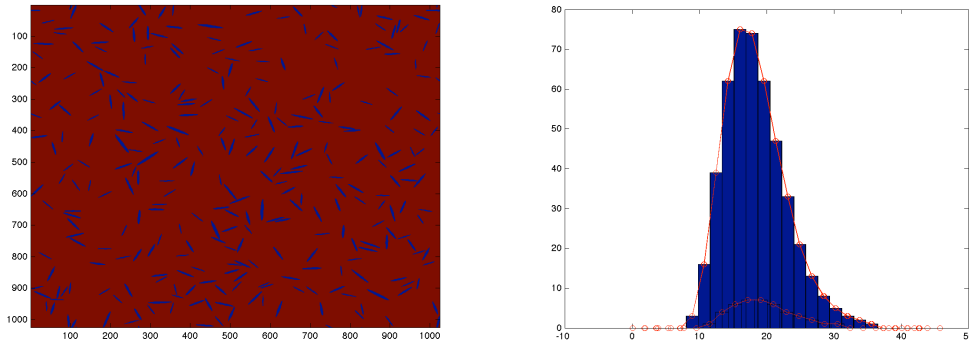


Figure 71. Plots on the random mask calculations with random needles with Poisson exclusion process (non-overlapping grains), fill factor = 5%, using a lognormal grain distribution (shown at right).

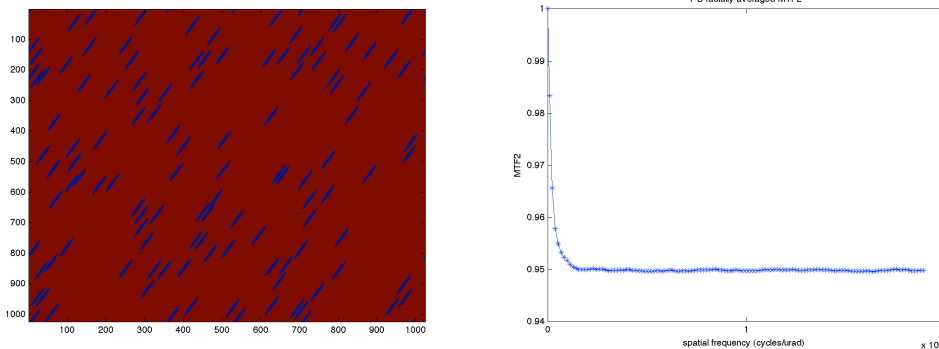


Figure 72. Plots on the random mask calculations with aligned needles with Poisson exclusion process (non-overlapping grains), fill factor = 5%.

By varying 11 error parameters of the MCB/HLC optical system (AFTA), we wanted to verify that we could get a good agreement between the measured and the simulated closed-loop mean contrast, and determine the degree of accuracy of the 11 error parameters chosen by comparing the measured and the simulated open-loop contrast curves, changing the value of one error term at a time. This exercise validated the results obtained last year just before the midterm review, and give us confidence of the advantages of the random spatial disorder and low fill factor to synthesize an image with sufficient photon count. Figure 73 shows the pupil amplitude, Figure 74 the point spread function, Figure 75 the contrast metric for 2 mm particles with 20% fill factor, Figure 76 shows the sensitivity of the Modulation (MTF) to fill factor, and Figure 77 shows the details of the generation of an elliptical random mask. Figure 78 shows the results of the generation of elliptical random masks with random orientations. Figure 79 shows the details of a pupil with partially filled with random masks. Figure 80 shows the generation of six different random masks at different fill factor levels. Figure 81 shows the result of the MTF of six sets of random masks compared to ideal monolithic aperture. Finally, Figure 82 shows the Strehl ratio vs. fill factor. In the next period, we will continue the sensitivity analyses on the imaging

performance of the system as a function of fill factor, wavelength, and various spatial and temporal scales of interest, which will lead to the determination of requirements for the telescope.

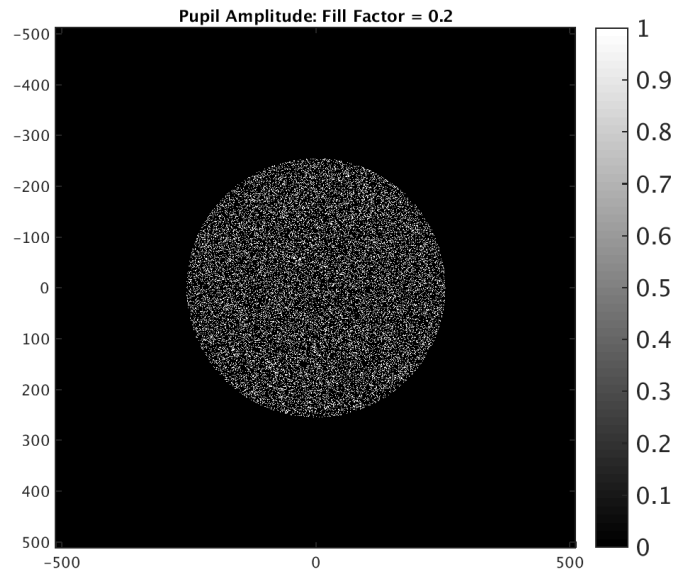


Figure 73. Pupil amplitude for 20% fill factor.

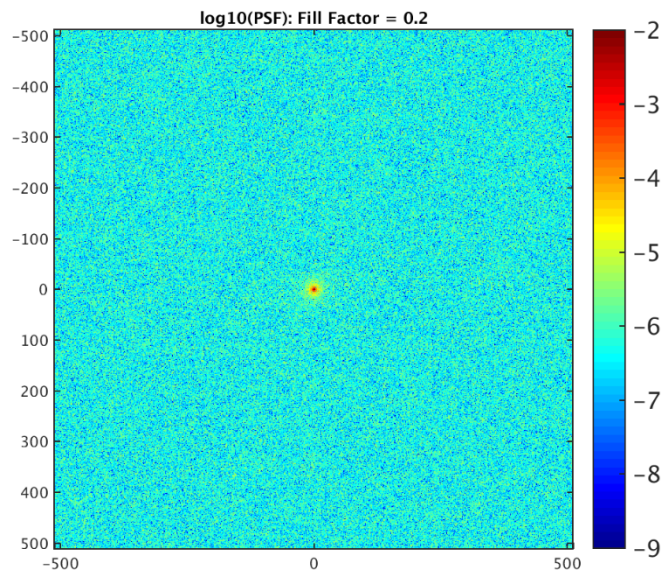


Figure 74. Point spread function for 20% fill factor.

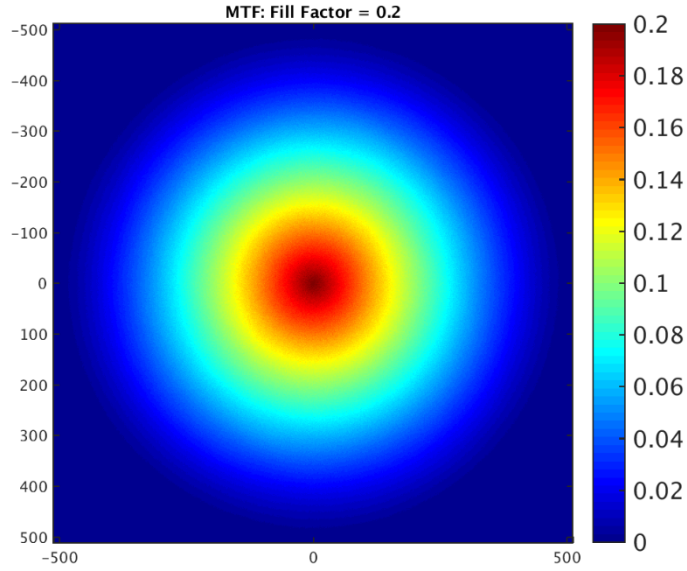


Figure 75. Contrast metric for 20% fill factor.

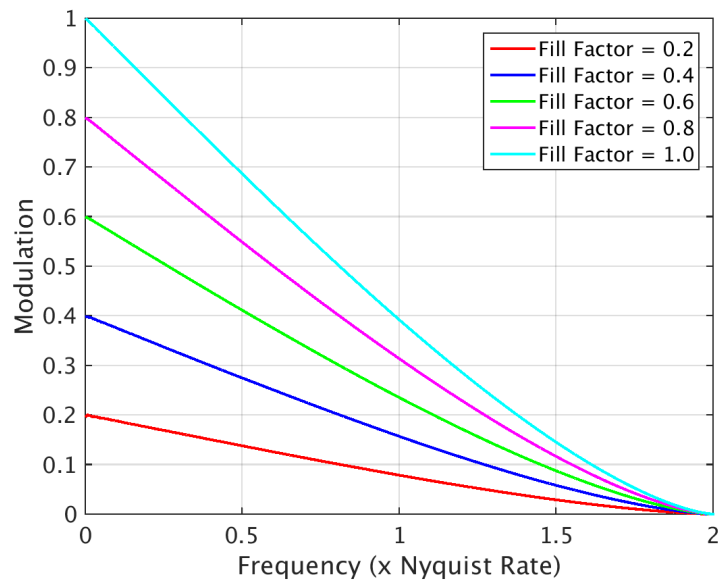


Figure 76. Sensitivity of Modulation (MTF) to fill factor.

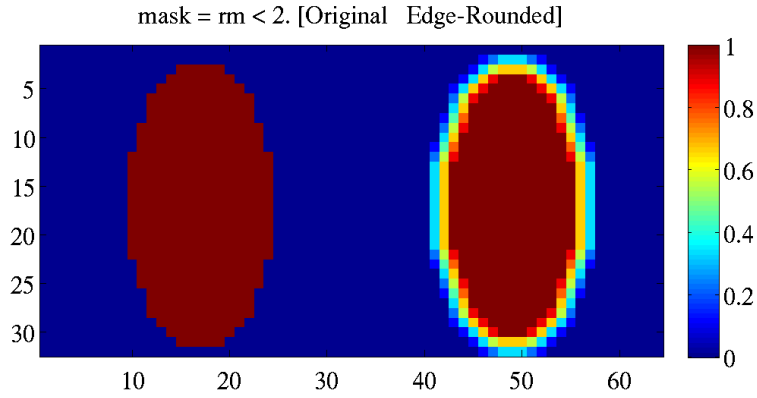


Figure 77. Generation of elliptical random mask.

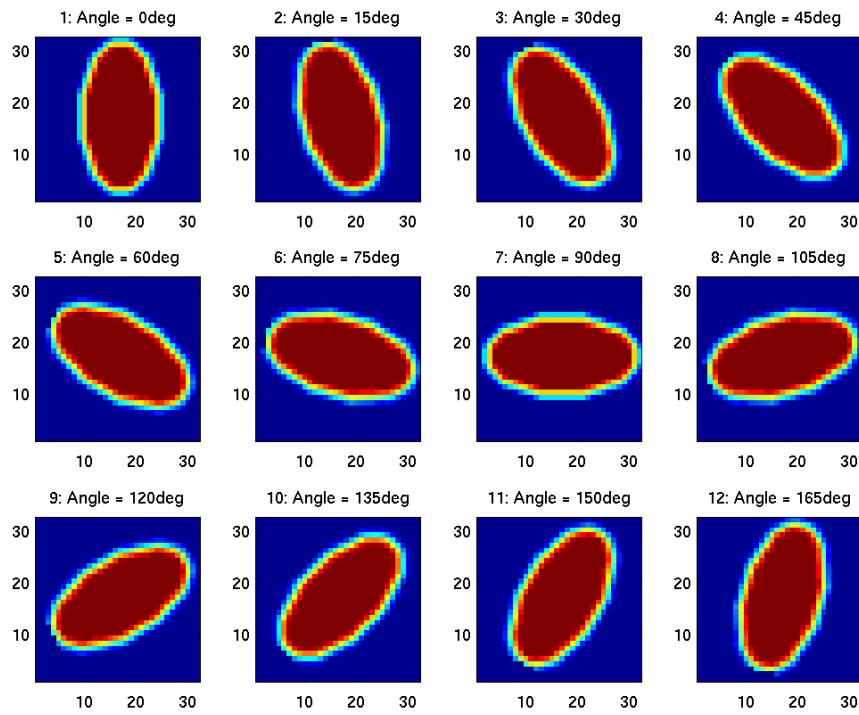


Figure 78. Generation of elliptical random masks with random orientations.

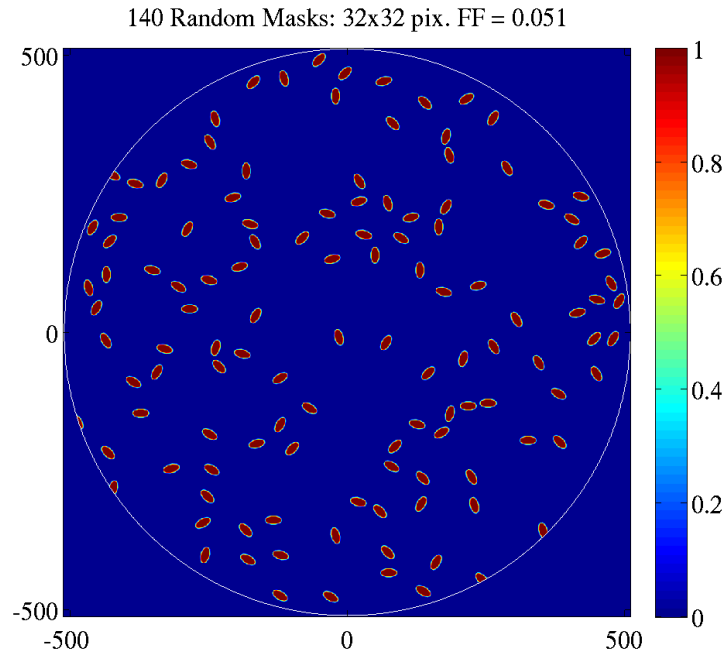


Figure 79. Pupil partially filled with random masks.

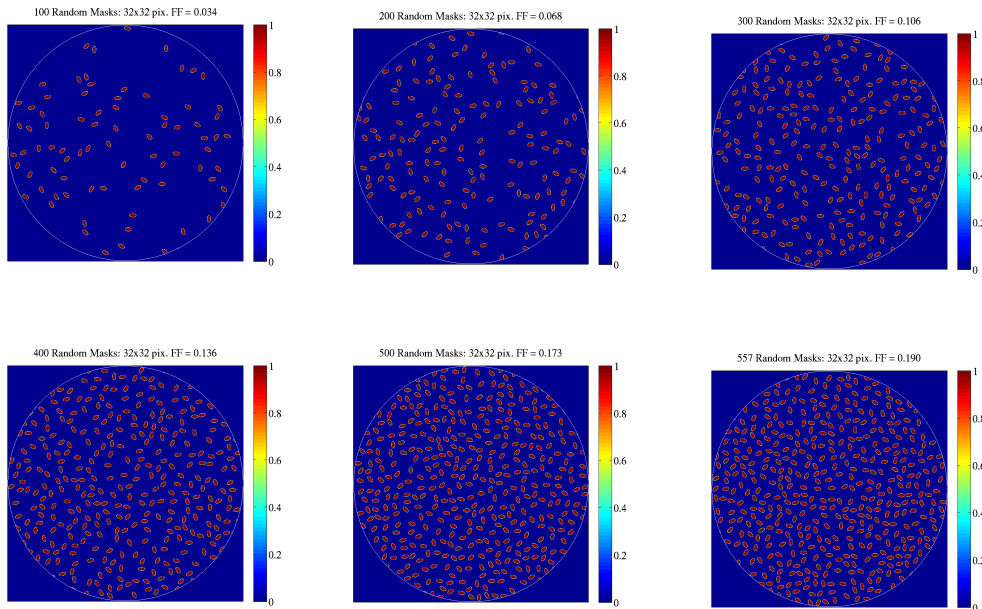


Figure 80. Generation of six different random masks at different fill factor levels.

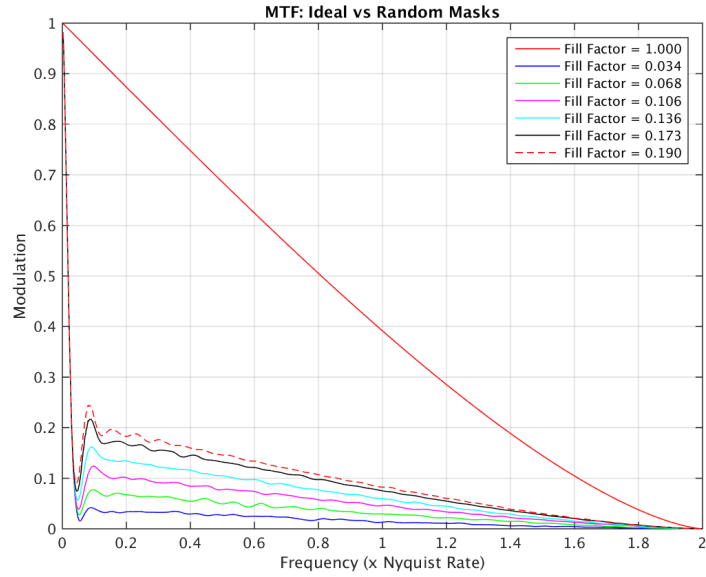


Figure 81. MTF of six sets of random masks compared to ideal monolithic aperture.

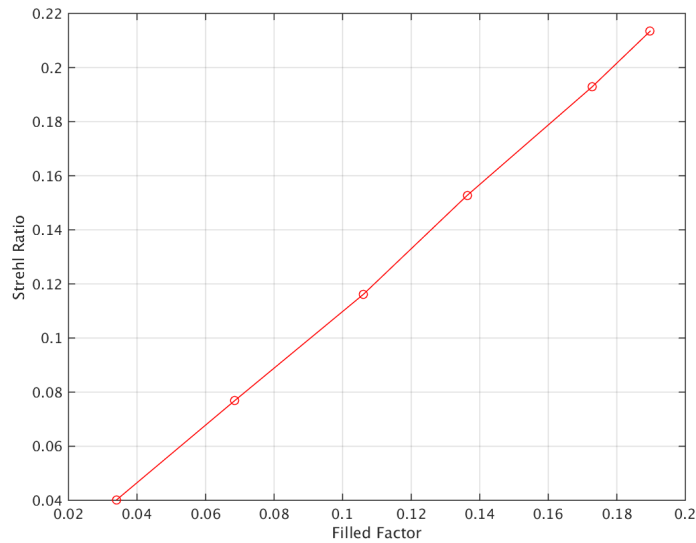


Figure 82. Strehl ratio vs. fill factor.

The Modulation Transfer Functions (MTF) of various random masks were evaluated numerically, including the effect of the grain shape. Figure 83 shows a single pixel random mask. Figure 84 shows a 2x2 pixel random mask. Figure 85 shows a 3x3 pixel random mask. Figure 86 shows a 4x4 pixel random mask. Figure 87 shows a 5x5 pixel random mask. Figure 88 shows the effect of rounding edges in single grain. Figure 89 shows a 5x5 pixel random mask with rounded edges. Figure 90 shows grains with rounded edges with more pixels. Figure 91 shows a 7x7 pixel random mask with rounded edges. Figure 92 shows the effect of grain shape and pixel size on

system MTF for a 40% fill factor, indicating that the shape of the grains does not have a pronounced effect on the optical response.

Single-Pixel Random Masks

AGranular / pr0_masksize.m

- Assumptions about aperture and mask sizes:
 - Aperture diameter: $D = 1\text{ m} = 2048\text{ pix}$
 - Mask size = Pixel size = 0.488 mm
- FF = Fill-Factor

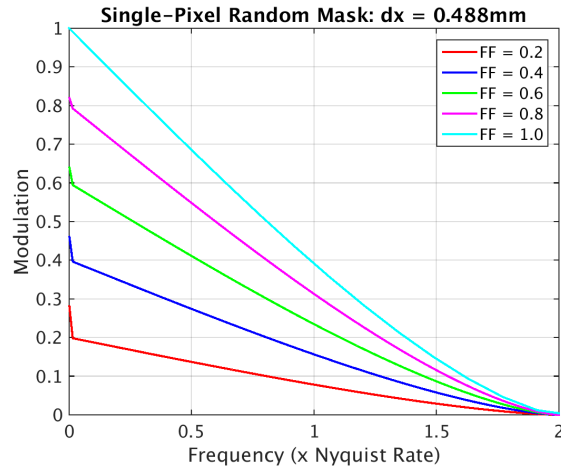


Figure 83. Single pixel random mask.

2x2 Pixels Random Masks

AGranular / pr0_masksize.m

- Assumptions about aperture and mask sizes:
 - Aperture diameter: $D = 1\text{ m} = 2048\text{ pix}$
 - Mask size = $2 \times \text{pixSize} = 2 \times 0.488\text{ mm}$
- FF = Fill-Factor

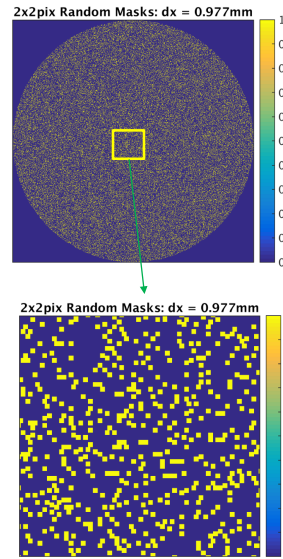
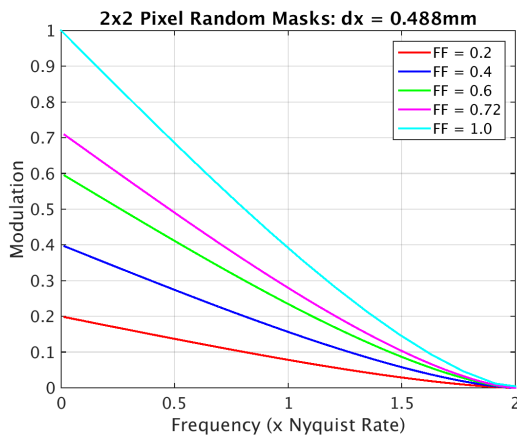


Figure 84. 2x2 pixel random mask.

3x3 Pixels Random Masks

AGranular / pr0_masksize.m

- Assumptions about aperture and mask sizes:
 - Aperture diameter: $D = 1\text{ m} = 2048\text{ pix}$
 - Mask size = $3 \times \text{pixSize} = 3 \times 0.488\text{ mm}$
- FF = Fill-Factor

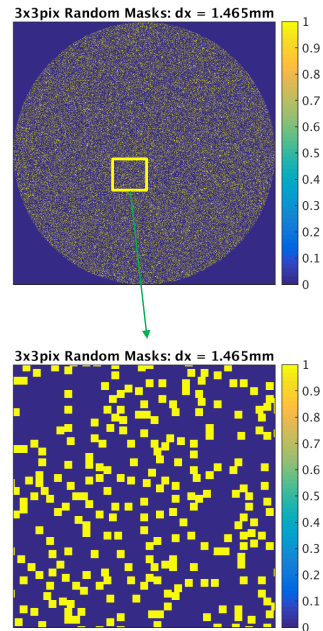
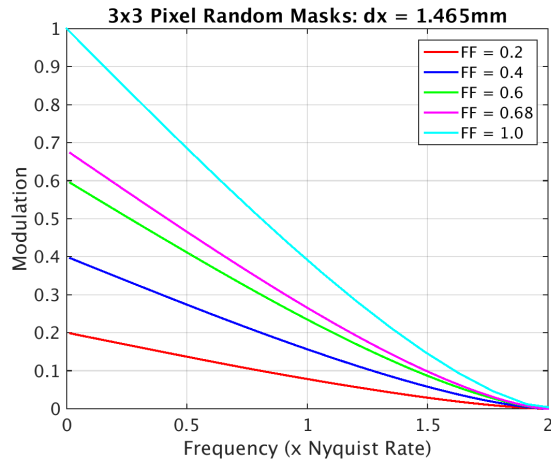


Figure 85. 3x3 pixel random mask.

4x4 Pixels Random Masks

AGranular / pr0_masksize.m

- Assumptions about aperture and mask sizes:
 - Aperture diameter: $D = 1\text{ m} = 2048\text{ pix}$
 - Mask size = $3 \times \text{pixSize} = 4 \times 0.488\text{ mm}$
- FF = Fill-Factor

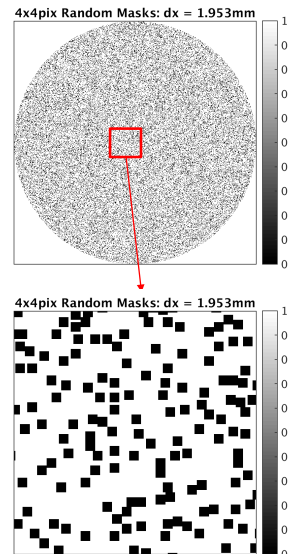
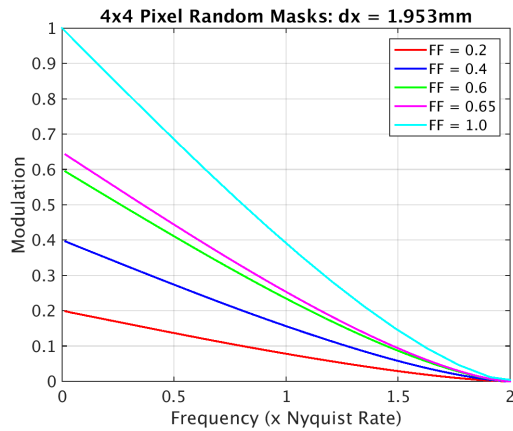


Figure 86. 4x4 pixel random mask.

5x5 Pixels Random Masks

AGranular / pr0_masksize.m

- Assumptions about aperture and mask sizes:
 - Aperture diameter: $D = 1\text{m} = 2048\text{ pix}$
 - Mask size = $3 \times \text{pixSize} = 4 \times 0.488\text{ mm}$
- FF = Fill-Factor

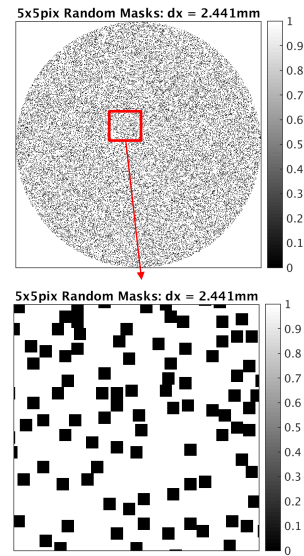
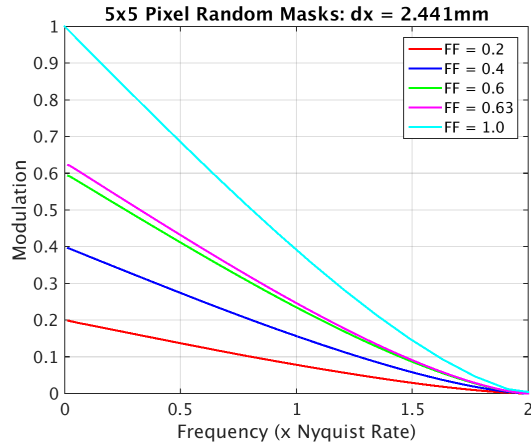


Figure 87. 5x5 pixel random mask.

5x5 Pixels Random Masks: Edge-Rounded

AGranular / pr0_masksize3.m

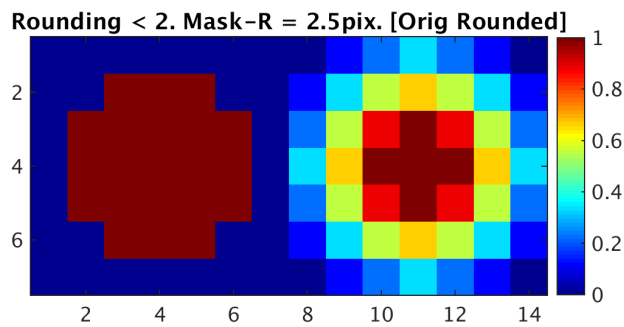


Figure 88. Rounding edges in single grain.

5x5 Pixels Edge-Rounded Masks

AGranular / pr0_masksize.m

- Assumptions about aperture and mask sizes:
 - Aperture diameter: $D = 1\text{m} = 2048\text{ pix}$
 - Mask size = $5 \times \text{pixSize} = 5 \times 0.488\text{ mm}$
- FF = Fill-Factor

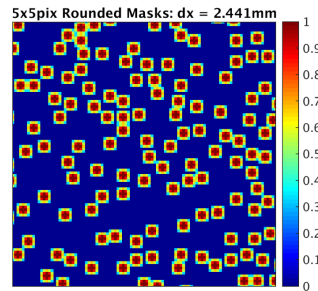
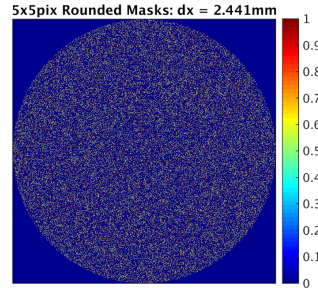
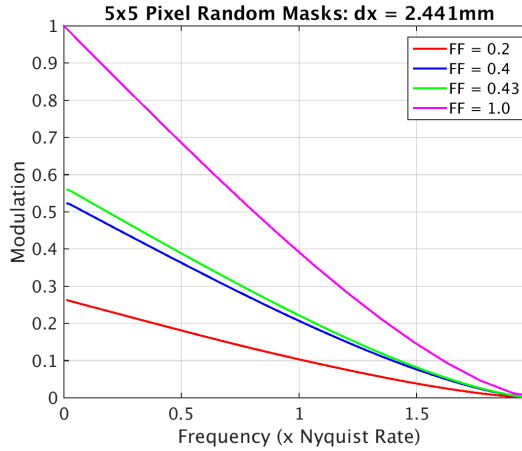


Figure 89. 5x5 pixel random mask with rounded edges.

7x7 Pixels Random Masks: Edge-Rounded

AGranular / pr0_masksize3.m

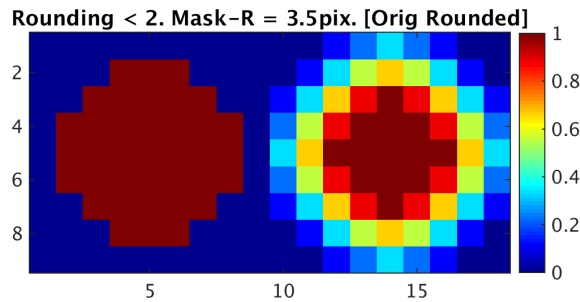


Figure 90. Rounded edges with more pixels.

7x7 Pixels Edge-Rounded Masks

AGranular / pr0_masksize3.m

- Assumptions about aperture and mask sizes:
 - Aperture diameter: $D = 1\text{m} = 2048\text{ pix}$
 - Mask size = $7 \times \text{pixSize} = 7 \times 0.488\text{ mm}$
- FF = Fill-Factor

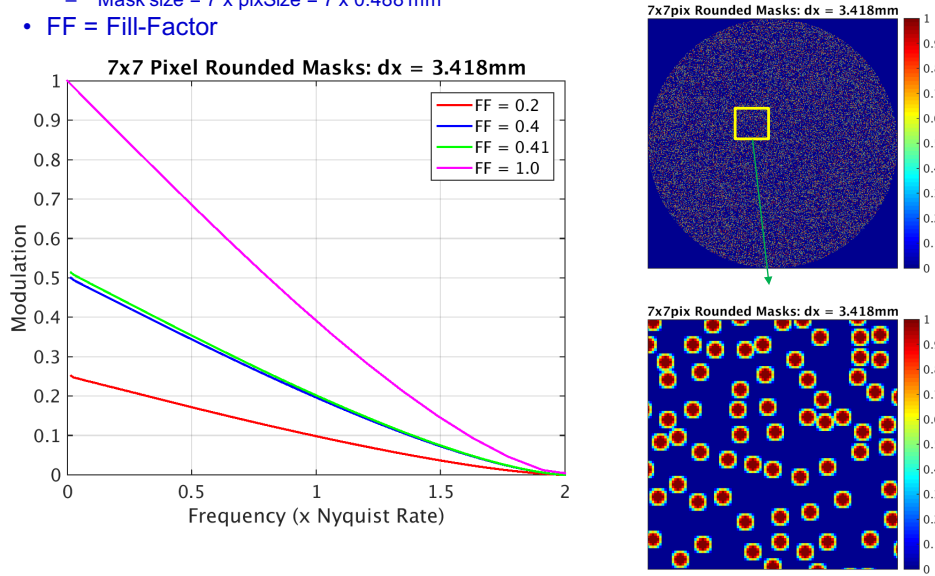


Figure 91. 7x7 pixel random mask with rounded edges.

Comparison of Fill-Factor = 0.4 Curves

AGranular / pr0_masksize3.m

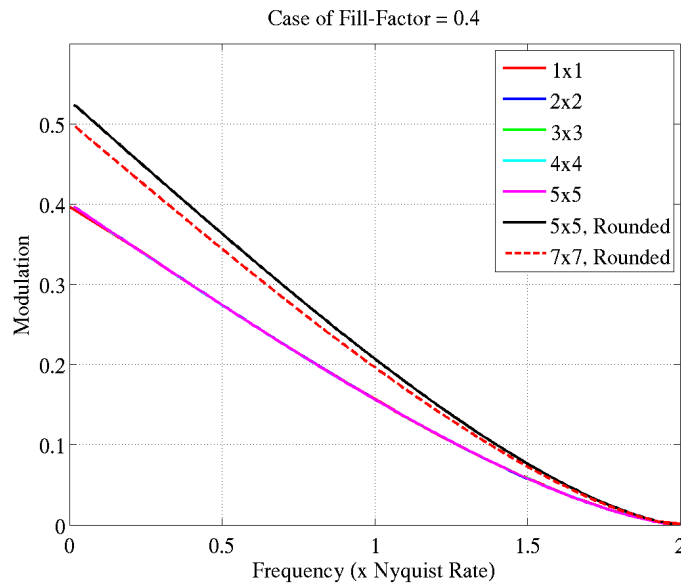


Figure 92. Effect of grain shape and pixel size on system MTF.

6.2 Imaging Properties of Granular Imager: Preliminary Experiment with Hexagonal Reflectors

Several implementations of the Granular Imager were examined experimentally. Figure 93 shows a few of the granular lenses that were tested.



Figure 93. Different granular lenses used in the experiments.

Figure 94 shows the schematic diagram of our experimental setup.

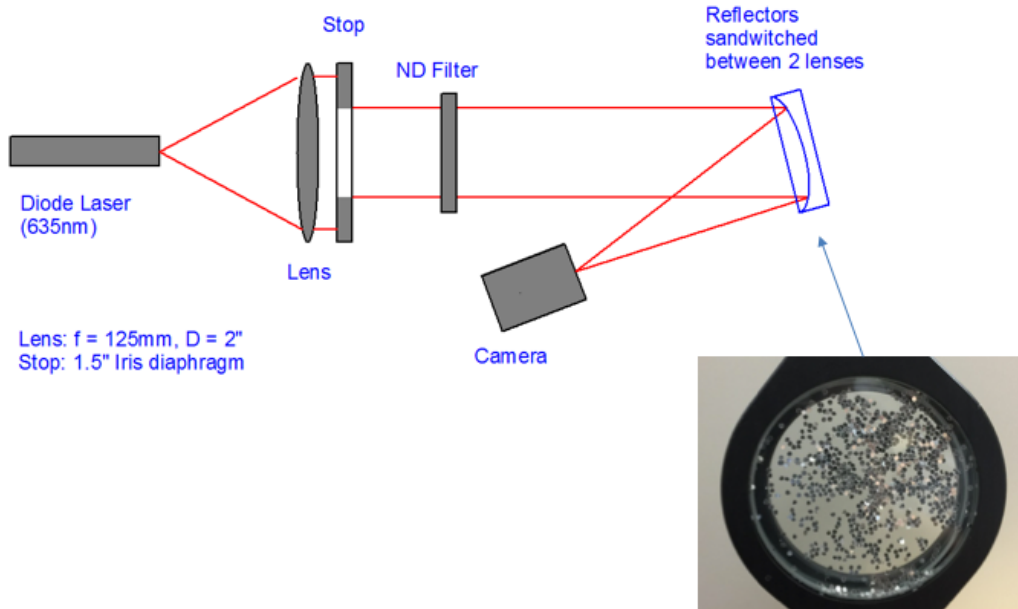


Figure 94. Schematic diagram of experimental setup to measure the Modulation Transfer Function of the Granular Imager.

Figure 95 shows two sets of images generated with the hexagonal reflectors and captured at different reflectors-camera distances. In this experiment, the camera was mounted on a free-standing post was moved by hand from a position to the next.

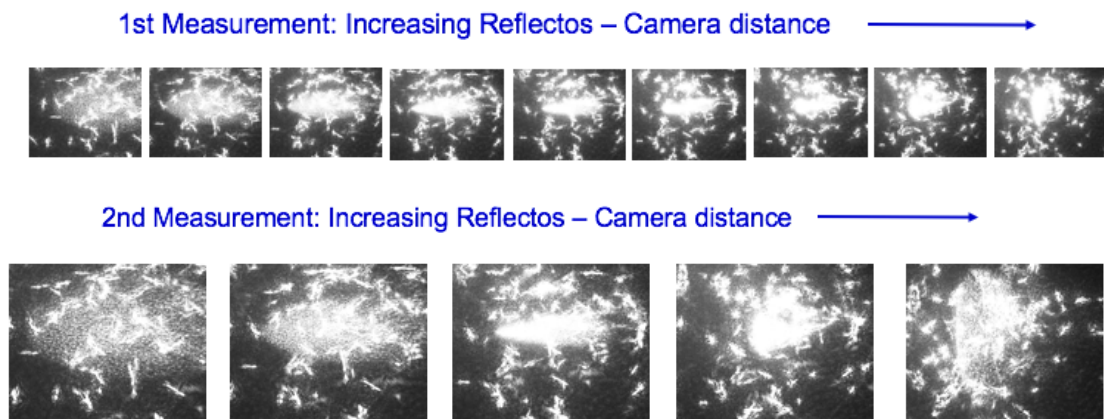


Figure 95. two sets of images generated with the hexagonal reflectors and captured at different reflectors-camera distances.

If we image a collimated light using an ideal lens, we obtain a PSF and MTF shown in Fig. 96.

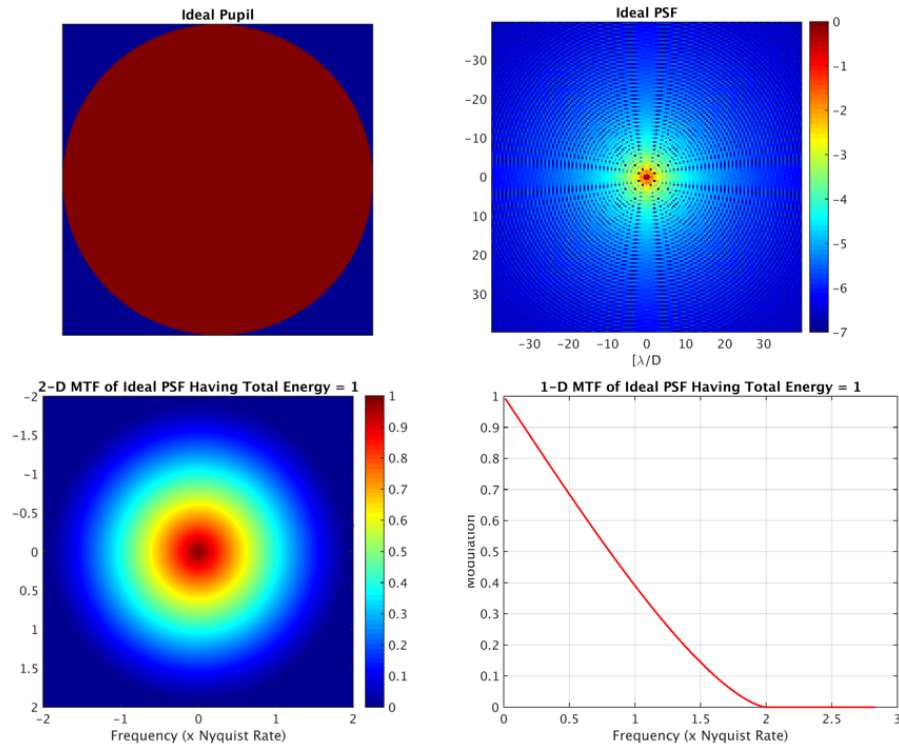


Figure 96. PSF and MTF of ideal lens.

However, in this experiment, we first imaged a collimated beam using a spherical mirror ($D = 25\text{mm}$, beam diameter $\sim 20\text{mm}$). Because of the limitations in hardware, space and time, we had to operate the spherical mirror at a large tilt angle (angle of incidence of ~ 20 degrees). This introduced severe aberration in the measured PSF image, and also resulted in a poor MTF characteristics (see Fig. 97, two left plots).

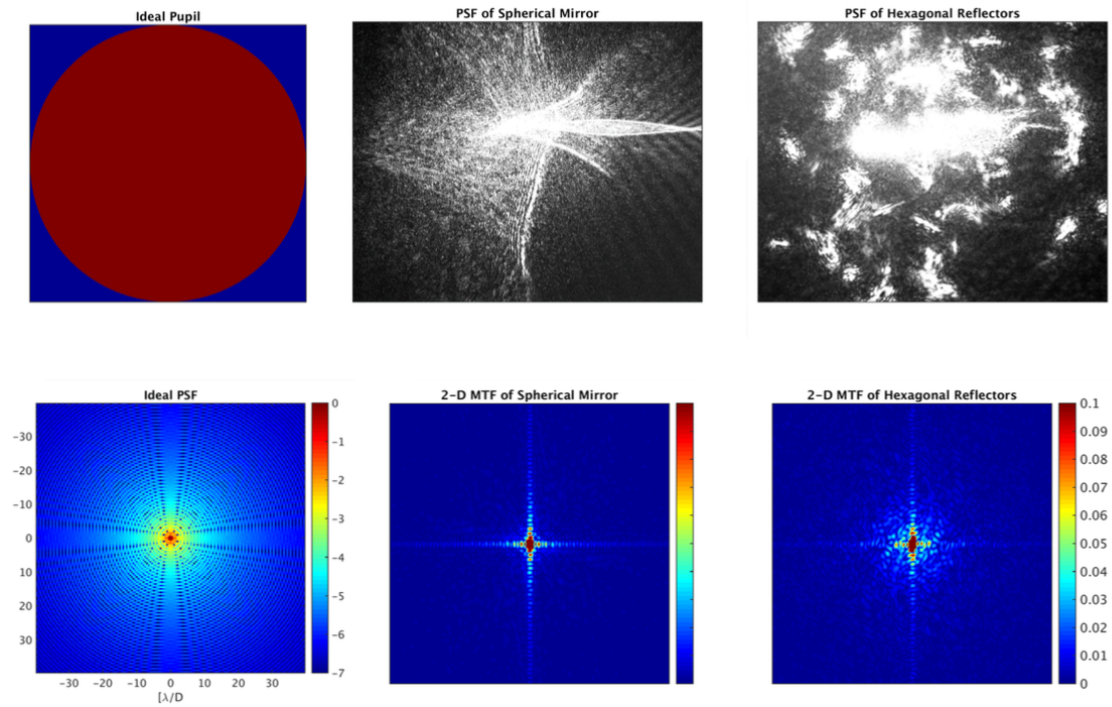


Figure 97. Comparison of MTF of ideal lens, spherical mirror, and granular hexagonal mirror.

Next, we sandwiched small, hexagonal reflectors between a concave and a convex lens having the same radius of curvature, as shown in Fig. 93, bottom left. By reflecting a collimated beam from that reflecting sub-assembly, we produced an image, as shown in the top-right plot of Fig. 97. We also calculated its MTF. Figure 98 compares the 1-D MTF curves of an ideal PSF, the image obtained with the spherical mirror, and the image obtained with the hexagonal reflectors. As we can see, the MTF of the hexagonal reflectors is comparable to that of the spherical mirror.

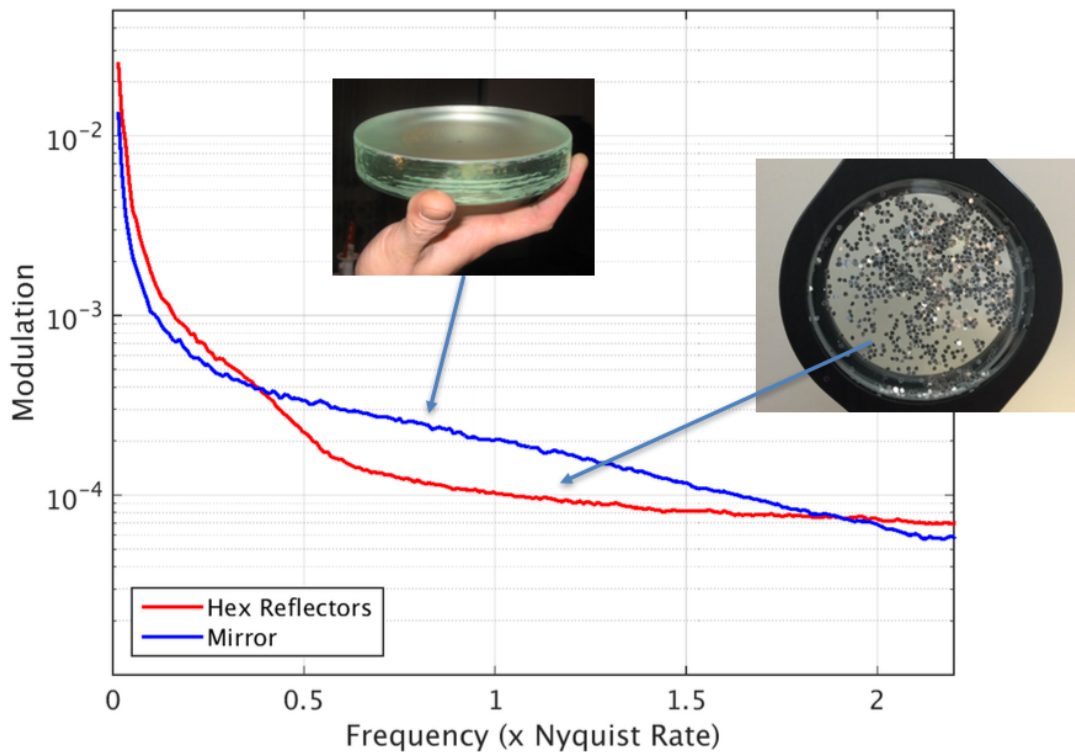


Figure 98. Comparison of experimental modulation transfer function (MTF) of continuous mirror with granular mirror with hexagonal elements.

6.3 T-matrix modeling approach

The optical forces and torques that allow trapping and manipulation of micron sized particles in beams of light result from the transfer of momentum and angular momentum from the electromagnetic field to the particle—the particle alters the momentum or angular momentum flux of the beam through scattering. Thus, the problem of calculating optical forces and torques is essentially a problem of light scattering. In some ways, it is a simple problem: the incident field is monochromatic, there is usually only a single trapped particle, which is finite in extent, and speeds are so much smaller than the speed of light that we can for most purposes neglect Doppler shifts and assume we have a steady-state monochromatic single scattering problem. Although typical particles inconveniently are of sizes lying within the gap between the regimes of applicability of small-particle approximations (Rayleigh scattering) and large particle approximations (geometric optics), the particles of choice are often homogeneous isotropic spheres, for which an analytical solution to the scattering problem is available—the Lorenz–Mie solution. The source of the difficulty lies in the usual paraxial representations of laser beams being solutions of the scalar paraxial wave equation rather than solutions of the vector Helmholtz equation. Our method of choice is to use a least squares fit to produce a Helmholtz beam with a far field matching that expected from the incident beam being focused by the objective. At this point, we can write the incident field in terms of a discrete basis set of functions $\psi_n^{(inc)}$,

where n is the mode index labelling the functions, each of which is a solution of the Helmholtz equation,

$$U_{inc} = \sum_n^{\infty} a_n \psi_n^{(inc)}, \quad (12)$$

where a_n are the expansion coefficients for the incident wave. In practice, the sum must be truncated at some finite n_{max} , which places restrictions on the convergence behavior of useful basis sets. A similar expansion is possible for the scattered wave, and we can write

$$U_{scat} = \sum_k^{\infty} p_k \psi_k^{(scat)}, \quad (13)$$

where p_k are the expansion coefficients for the scattered wave. As long as the response of the scatterer—the trapped particle in this case—is linear, the relation between the incident and scattered fields must be linear, and can be written as a simple matrix equation

$$p_k = \sum_n^{\infty} T_{kn} a_n \quad (14)$$

or, in more concise notation, $\mathbf{P} = \mathbf{T}\mathbf{A}$, where T_{kn} are the elements of the T -matrix. This is the foundation of both GLMT and the T -matrix method. In GLMT, the T -matrix \mathbf{T} is diagonal, whereas for non-spherical particles, it is not. The T -matrix depends only on the properties of the particle—its composition, size, shape, and orientation—and the wavelength, and is otherwise independent of the incident field. This means that for any particular particle the T -matrix only needs to be calculated once, and can then be used for repeated calculations of optical force and torque. This is the key point that makes this a highly attractive method for modelling optical trapping and micromanipulation, since we are typically interested in the optical force and torque as a function of position within the trap, even if we are merely trying to find the equilibrium position and orientation within the trap. Thus, calculations must be performed for varying incident illumination, which can be done very easily with the T -matrix method. This provides a significant advantage over many other methods of calculating scattering, where the entire calculation needs to be repeated. This is perhaps the reason that optical forces and torques have been successfully modelled using methods such as the finite-difference time domain method (FDTD), the finite element method (FEM), or other methods. Since, as noted above, the optical forces and torques result from differences between the incoming and outgoing fluxes of electromagnetic momentum and angular momentum, calculation of these fluxes is required. This can be done by integration of the Maxwell stress tensor, and its moment for

the torque, over a surface surrounding the particle. Fortunately, in the T -matrix method, the bulk of this integral can be performed analytically, exploiting the orthogonality properties of the VSWFs. In this way, the calculation can be reduced to sums of products of the expansion coefficients of the fields.

For spherical particles, the usual Mie coefficients can be rapidly calculated. For non-spherical particles, a more intensive numerical effort is required. We use a least squares overdetermined point-matching method. For axisymmetric particles, the method is relatively fast. However, as is common for many methods of calculating the T -matrix, particles cannot have extreme aspect ratios, and must be simple in shape. Typical particle shapes that we have used are spheroids and cylinders, and aspect ratios of up to four give good results. Although it can take a long time to calculate the T -matrix for general non-axisymmetric particles, it is possible to make use of symmetries such as mirror symmetry and discrete rotational symmetry to greatly speed up the calculation. We include a symmetry-optimized T -matrix routine for cubes. Expanding the range of particles for which we can calculate the T -matrix is one of our current active research efforts, and we plan to include routines for anisotropic and inhomogeneous particles, and particles with highly complex geometries. Once the T -matrix is calculated, the scattered field coefficients are simply found by a matrix–vector multiplication of the T -matrix and a vector of the incident field coefficients.

As noted earlier, the integrals of the momentum and angular momentum fluxes reduce to sums of products of the expansion coefficients. It is sufficient to give the formulae for the z -components of the fields, as given, for example, by [Crichton2000]. We use the same formulae to calculate the x and y components of the optical force and torque, using 90° rotations of the coordinate system. It also possible to directly calculate the x and y components. The axial trapping efficiency Q is

$$Q = \frac{2}{P} \sum_{n=1}^{\infty} \sum_{m=-n}^n \frac{m}{n(n+1)} \operatorname{Re}(a_{nm}^* b_{nm} - p_{nm}^* q_{nm}) - \frac{1}{n+1} \left[\frac{n(n+2)(n-m-1)(n+m+1)}{(2n+1)(2n+3)} \right]^{1/2} \times \operatorname{Re}(a_{nm} a_{n+1,m}^* + b_{nm} b_{n+1,m}^* - p_{nm} p_{n+1,m}^* - q_{nm} q_{n+1,m}^*) \quad (15)$$

in units of $n\hbar k$ per photon, where n is the refractive index of the medium in which the trapped particles are suspended. This can be converted to SI units by multiplying by nP/c , where P is the beam power and c is the speed of light in free space. The *torque efficiency*, or normalized torque, about the z -axis acting on a scatterer is

$$\tau_z = \sum_{n=1}^{\infty} \sum_{m=-n}^n m (|a_{nm}|^2 + |b_{nm}|^2 - |p_{nm}|^2 - |q_{nm}|^2) / P \quad (16)$$

in units of h per photon, where

$$P = \sum_{n=1}^{\infty} \sum_{m=-n}^n |a_{nm}|^2 + |b_{nm}|^2$$

(17)

is proportional to the incident power (omitting a unit conversion factor which will depend on whether SI, Gaussian, or other units are used). This torque includes contributions from both spin and orbital components, which can both be calculated by similar formulae [Crichton2000]. Again, one can convert these values to SI units by multiplying by P/ω , where ω is the optical frequency.

6.3.1 Trapping of a cube

We did the simulation of the optical trapping of a cube using the T-matrix approach. The cube has faces of $2\lambda/n_{\text{medium}}$ across, and has a refractive index of $n = 1.59$, and is trapped in water. Since the force and torque depend on the orientation as well as position, a simple way to find the equilibrium position and orientation is to ‘release’ the cube and calculate the change in position and orientation for appropriate time steps. The cube can be assumed to always be moving at terminal velocity and terminal angular velocity. The cube begins face up, centred on the focal plane of the beam, and to one side. The cube is pulled into the trap and assumes a corner-up orientation. The symmetry optimizations allow the calculation of the T -matrix in 20 min; otherwise, 30 h would be required. Once the T -matrix is found, successive calculations of the force and torque require far less time, on the order of a second or so. (Figure 99).

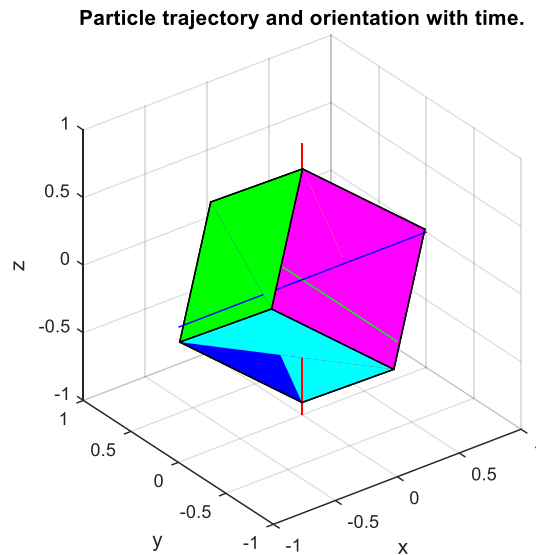


Figure 99. The cube has faces of $2\lambda/n_{\text{medium}}$ across, refractive index $n = 1.59$, and is trapped in water. Force and torque depend on orientation and position, to find equilibrium – we “release” the cube and calculate the change in position and orientation for appropriate time steps

6.3.2 Trapping of an ellipsoid

The same simulation was repeated for an ellipsoid trapped in water with refractive index $n = 1,59$ of particle itself and $n = 1,33$ of the medium (water). This dynamics simulation simulates the trap in some hypothetical substance. It does not represent any physical system except that it displays the same kind of dynamics as a trapped particle capable of rotation. Given the initial values, the normalization factors were chosen empirically to give a more interesting simulation. We assume big rotations. This corresponds to low resistance. The change of coordinates of the old particle position from xyz to spherical polar coordinates was implied. The ellipsoid simulation is generating vectors i,j , each consisting 21 points. Force and torque depend on orientation and position, in order to find equilibrium – we “release” the ellipsoid and calculate the change in position and orientation for appropriate time steps. (Figure 100). The initial vertex from where it starts to rotate is $k = [-1,-1,-1]$, it is the reference point from where rotational matrix R_{total} starts to rotate, this parameter varies with rotational matrix for different geometries. A Matlab routine generates radii and normals to the surface for a range of shapes for which the surface is a function of angle (θ,φ) . With respect to the cube, the number of shape parameters was changed from 1 to 3. The surface is defined by spherical coordinates $r = r(\theta,\varphi)$. The surface area element and normal are $dS n = r^2 \sin(\theta) \sigma(\theta,\varphi) \hat{\theta} \hat{\varphi}$, where $\sigma(\theta,\varphi) = \hat{r} - \frac{1}{r} \frac{dr}{d\theta} * \hat{\theta} - \frac{1}{r \sin(\theta)} * \frac{dr}{d\varphi} * \hat{\varphi}$. It takes from 72,9131 to 86,512 seconds to calculate the T-matrix for the ellipsoid.

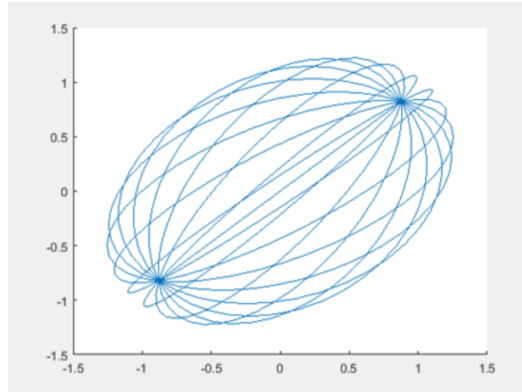


Figure 100. The ellipsoid, with refractive index $n = 1.59$, trapped in water

Future work would include the investigation of a Multiple sphere T-matrix analysis for calculation of the electromagnetic scattering and absorption properties of a system of spherical surfaces and arbitrary configurations of spherical surfaces.

6.4 Laser confinement subsystem

We conducted a preliminary assessment of laser subsystem characteristics, and used laser system performance models to determine sizing parameters such as distance to beam waist and relation to granular patch area to apply pressure effectively (Fig. 101, Fig. 102). The Laser Acquisition, Tracking and Point Assembly would include: Beacon Transmit Module to scan for cloud; Beacon Receive Module to acquire and confirm link; Processor Module to establish and maintain link to cloud. It would also include: Optical Assembly with a Telescope Module, with Telescope, aperture, gimbal, and mounting support; Jitter Control Module, with Fast steering mirror, adaptive optics; Vibration-isolation stage to cancel noise, and an Optical Pathway Module with Polarizers, filters, beam formers, and fiber optic cable. Technical challenges include: precise laser beam pointing, stray illumination from solar background light, the need for low-cost large diameter telescopes, and the line of sight pointing and stabilization requirements. See Figures 101 and 102.

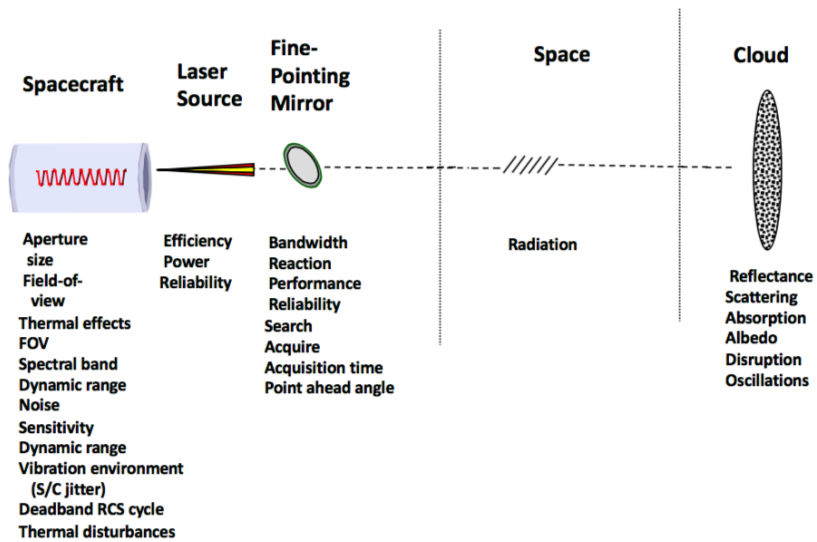


Figure 101. Laser confinement subsystem drivers.

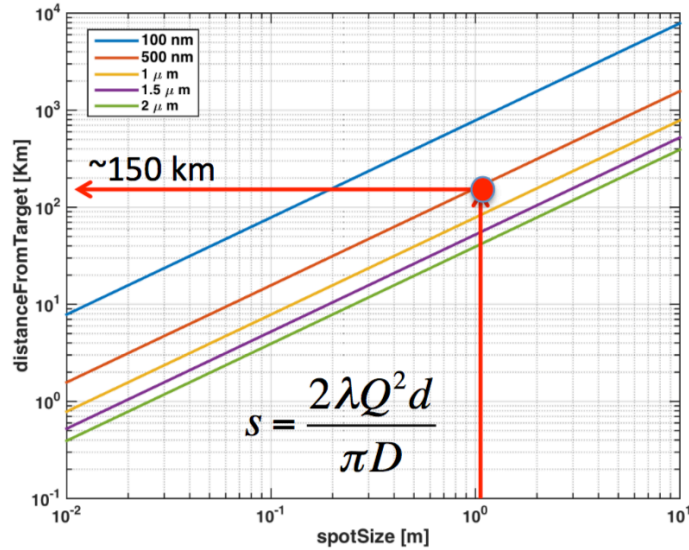


Figure 102. Calculation of laser spot size and distance from cloud.

6.6 Experimental tests of Radiation Pressure

Radiation pressure experiments were conducted in liquids to lessen the effects of gravity and surface forces. Experience shows that the motion and orientation of large millimeter scale objects is easier to discern than small micrometer scale ones. We placed glass hemispheres of diameter ~1mm in a nearly saturated solution of sodium polytungstate (also called sodium metatungstate), which has a density that can be matched to that of glass. By adding or removing water from the solution we can made the hemispheres near the neutral buoyancy condition. The refractive index of the solution of nearly identical to that of glass too, so the index contrast in the experiment was low. An index contrast is needed to achieve radiation pressure and torque. As the frames of recorded video show below, the hemisphere is attracted toward the beam (compare t=4s and 8s). The hemisphere stops moving when the beam is turned off (see t=12s and 16s). Motion is resumed when the laser beam is turned back on (t=20s). As the hemisphere enters the beam, it also changes its attitude (orientation). Initially the front face of the hemisphere is facing the viewer. At t > 28s the face clearly rotates. This is evidence of laser-induced torque on the hemisphere. See Fig. 103.

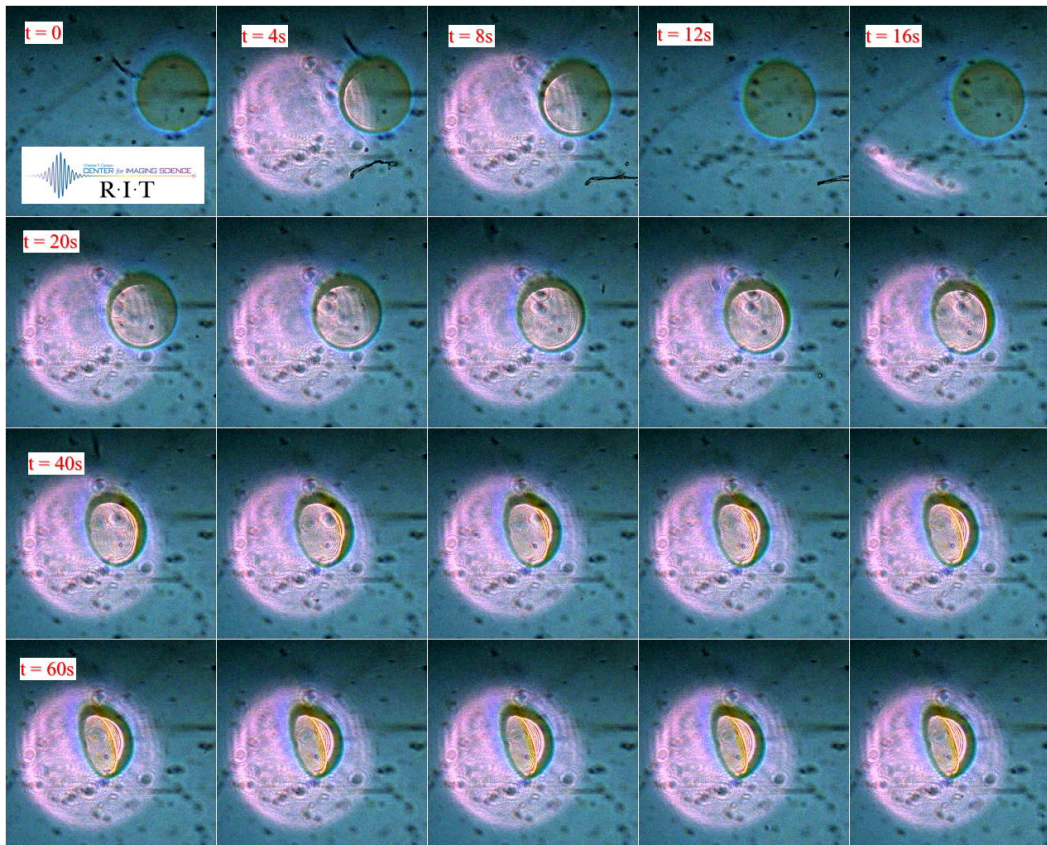


Figure 103. Glass hemisphere in sodium polytungstate solution to achieve near-neutral buoyancy. Frames separated by 4 second intervals, advancing left to right starting from the top: $t = 0, 4, 8, \dots$ [sec]. Laser is turned on at 4sec, off at 12sec, on again at 20 sec. Hemisphere moves toward beam center and flips from bottom side down, to bottom side at $\sim 60^\circ$.

Two mechanisms can give rise to the observations described above: Radiation pressure or Laser-induced flow. The latter occurs when the laser heats a liquid along a column defined by the laser beam. The density of the heated liquid experiences a buoyant effect. A viscous liquid can entrain a volume of liquid flow that is larger than that of the laser beam volume. To determine the severity of liquid heating from the laser we borrowed a spectrophotometer from a colleague, and using a white light source, we measured the transmission spectrum below. Our radiation pressure laser operates at 532 nm, and thus, the transmission of the sodium polytungstate solution was $\sim 90\%$. Nevertheless, a 10% absorption value is significant, and thus, we cannot easily rule out thermal effects (Figure 104).

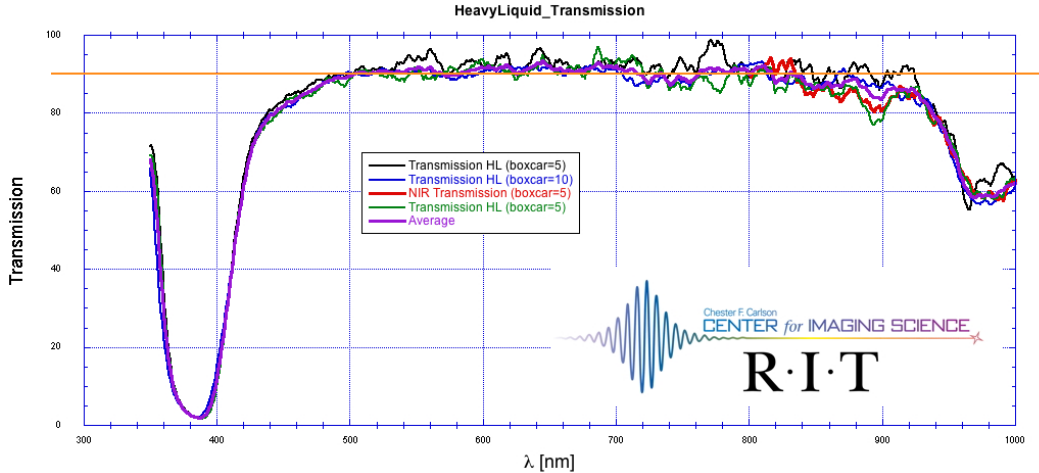


Figure 104. Measured transmission spectrum of near-saturated aqueous solution of sodium polytungstate.

The refractive index of the sodium polytungstate varies with density (e.g., water content). We had sent a sample of the solution to NIST to obtain a refractive index and absorption spectrum, but they were unable to honor the request because their apparatus was designed for solids, rather than liquids. After time consuming searches and email exchanges, we finally obtained the refractive index vs density plot (see below) from another source: Dr. Rainer Kamps, Germany. BK-7 glass has an index of 1.52, which is clearly in the range of the solution. Further, BK-7 has a density of 2.51 g/cm³. To achieve a significant refractive index contrast, we adjusted the solution density to be lower than that of glass. In this case the hemisphere slowly sank to the bottom of our sample chamber. This also lessened the viscosity of the solution (Fig. 105).

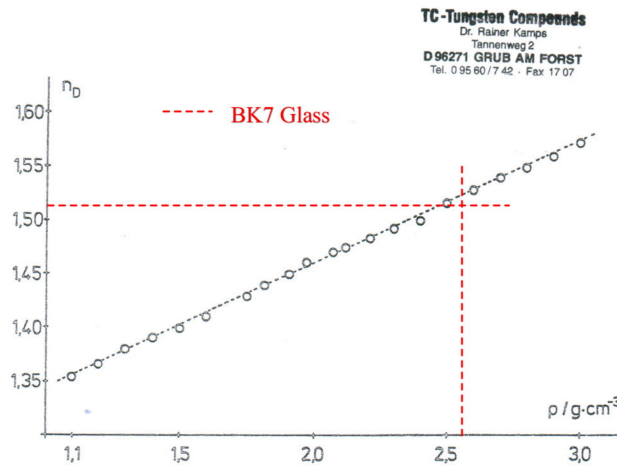


Abb.4. Brechungsindex n_D als Funktion der Dichte ρ
wäßriger Natriummetawolframatlösungen bei 20 °C.

Figure 105. Refractive index of sodium polytungstate as a function of density at 20°C. Source: Dr. Rainer Kamps, TC-Tungsten-Compounds, Germany. Red dashed lines have been added to indicate the refractive index and density of BK7 glass.

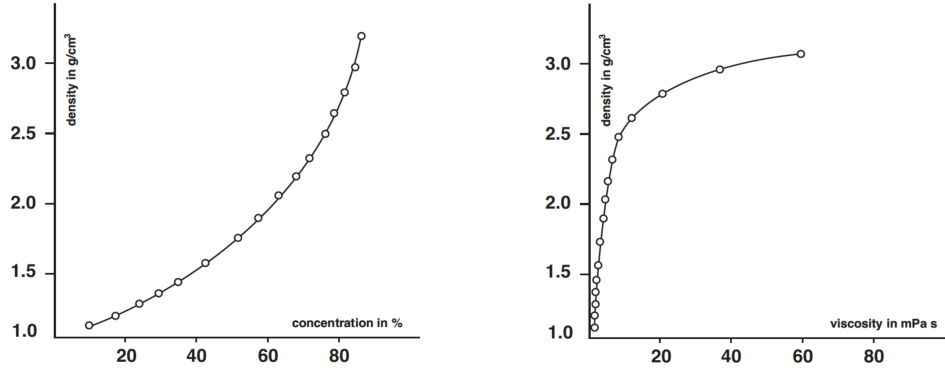


Figure 106. Density (left) and viscosity (right) of sodium polytungstate. Source: GEOLiquids Inc.

Using our ray-tracing model for calculating the force and torque on a hemisphere (see below), we find that a modest refractive index contrast ($n_{BK7}/n_{solution} \sim 1.1$) will cause the hemisphere to change its attitude by $\sim 60^\circ$, which is in good agreement with our observation. What is more, the particle experiences a force along the axis of the beam, which is necessary to help raise the center of mass as the hemisphere rolls to a new orientation. The hemisphere also is expected to experience a significant force perpendicular to the beam. These results are consistent with the observation (Fig. 106 and Fig. 107).

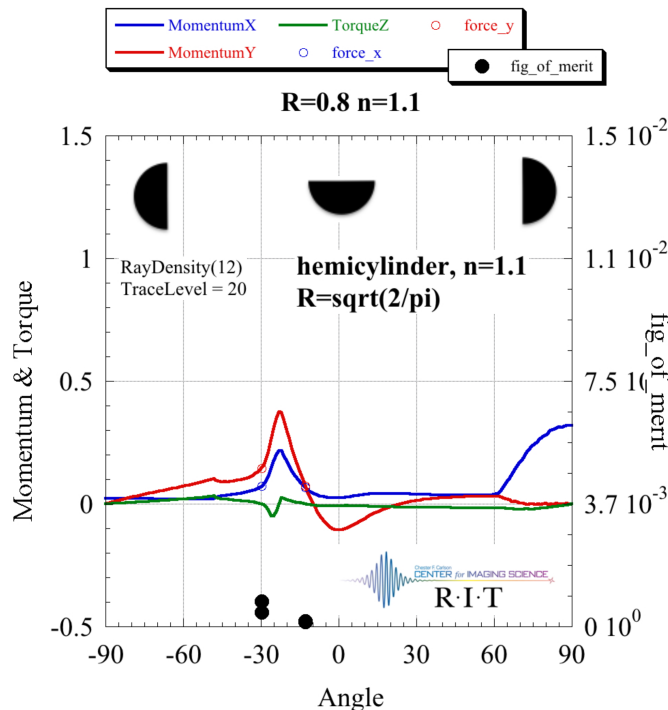


Figure 107. Raytracing model of the predicted forces (x is along the beam and y is transverse) and torque on a hemisphere having a relative refractive index of 1.1. The inset hemispheres show the orientation of the hemisphere that corresponds to the values along the abscissa. Light is assumed to strike those hemispheres from a source on the left hand side of the figure (light travels from left to right).

7. Granular Imager Optical System Design

In this section, we present some ideas regarding the optics and imaging aspects of granular spacecraft. Granular spacecraft are complex systems composed of a spatially disordered distribution of a large number of elements, for instance a cloud of grains in orbit. An example of this application is a spaceborne observatory for exoplanet imaging, where the primary collecting aperture is a cloud of small particles instead of a monolithic aperture.

7.1 Reflective Optical Designs

We developed concepts for refractive, reflective and holographic systems and designed optical correction and collection systems. We designed an optical imaging system for multiple aerosol optics that combines several layers of sensing and control to adapt to possible misalignments and shape errors in the aerosol. The design also combines the light from several of these “clouds” to synthesize a large, multiple-aperture system to increase light throughput and resolution. A two-dimensional version that includes two separate Granular Telescope, is shown in Fig. 108. The entire system is represented in the diagram on the right. Starlight enters from the left, reflects off the two separate patches, and is slowly focused toward the formation-flying spacecraft that collects, corrects, and combines the light from individual patches to a single detector. The diagram on the left is an enlarged drawing of the separate spacecraft/optical “bench” that contains all the optics to perform line-of-sight and mid- to low-spatial frequency wavefront sensing and control for the optical system. The sequence of optics is as follows: the starlight is focused by granular spacecraft optical “patch”, creating a spherical wavefront. Light from all patches converges at an intermediate focus, which can be seen in the left side of Figure 108. The light reflects off secondary mirror (Gregorian) and the light from each patch is collimated (Fig. 109).

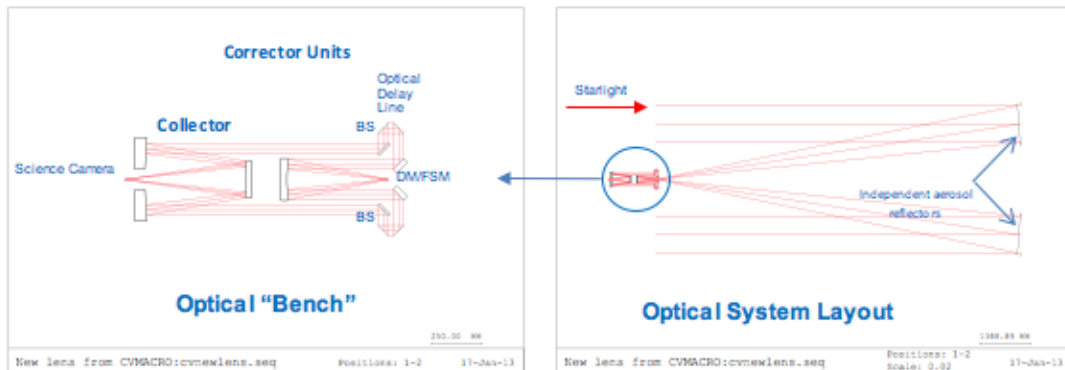


Figure 108. A two-dimensional slice of a multi-patch reflective system, with optical rays shown in red, is displayed on the right. An expanded view of the Optical “Bench” is displayed on the left

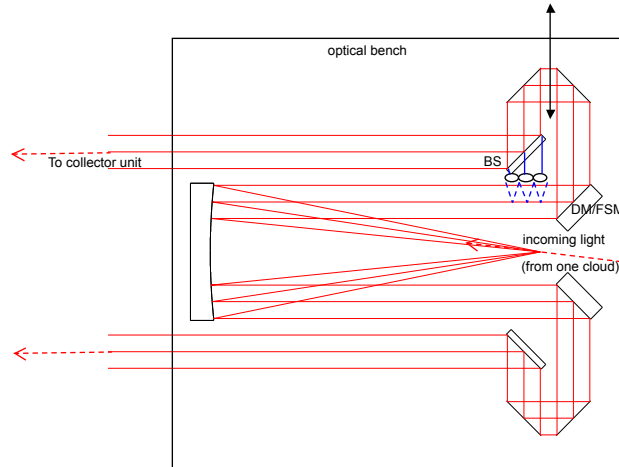


Figure 109. An expanded view of the corrector part of the optical “bench” that explicitly show the Shack-Hartmann wavefront sensor in blue. The SH sensor will be below the main optical path to avoid vignetting.

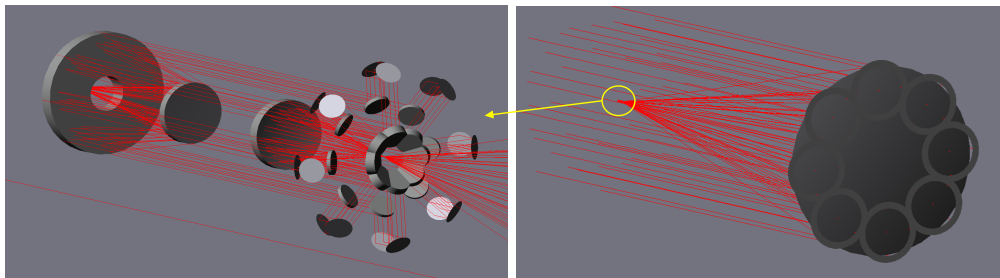


Figure 110. 3D solid optics view of the reflective imaging system concept design with 8 cloud patches forming the aperture.

The collimated light from each patch then continues to a separate adaptive optics system. A combined fast steering mirror and deformable mirror correct pointing and low to mid-spatial frequency aberrations. An optical delay line is used to correct phasing difference between the patches and enables Fourier transform spectroscopy. A beam-splitter is included to allow some of the light to go a Shack-Hartmann sensor to measure aberrations in the system and provides a feedback mechanism to the deformable mirror. The Shack-Hartmann placement can be seen in Figure 109 in blue. The light continues to the collector system, which consists of a Cassegrain telescope that combines and focuses the light from all the patches onto the science detector. Figure 110 shows a 3D solid picture of the optics, including 8 optical “patches”.

For this system, the selected approach for cloud management/sensing/control is multistage, with an outer stage for formation stabilization, and an inner stage for telescope wavefront sensing and correction, relegating fine adaptive optics to a deformable/fast steering mirror stage in the optical bench. The system’s relative range/bearing sensing and metrology is based on virtual telescope formation flying, in which distributed relative sensing is accomplished using Ka-Band transceivers/patch antennas, and a centralized laser

metrology system, relying on a single laser source on the main light-collecting spacecraft, while single reflecting target are on other free-flying elements except granular spacecraft.

For the reflective optical system, height variations of the optical surface must be less than $\lambda^2/\Delta\lambda$, where $\Delta\lambda$ is the bandwidth of light, to achieve meaningful imagery. Longer wavelengths (e.g. >10 μm) and smaller optical bandwidths make this requirement achievable with micron-sized particles for the cloud. Creating and maintaining a perfectly continuous surface is not likely to be achieved using the techniques we are considering in our approach, therefore sophisticated image processing algorithms will be required to synthesize an astronomical image. For example, taking several short exposures and using speckle imaging techniques would allow for weaker tolerances on the reflective surface. Instead of correcting for atmospheric instabilities, as is typical for speckle imaging, we would correct for the small changes of the mirror surface due to particles being constantly in motion [Labeyrie1970], [Beavers1989]. Multiframe blind deconvolution [Ayers1988] is a related technique to process multiple imperfect images to obtain a better estimate of the object. Utilizing multiple clouds would be a natural extension that would be applicable to speckle interferometry and increase the effective resolution of the system inversely proportional to the separation of clouds [Weigelt1977, Fienup1980]. In addition to the techniques mentioned above, the addition of a diversity mechanism to the optical path would allow for phase diversity [Paxman1992] techniques to be used. We plan to use a MEMS-based microshutter array as a programmable coded aperture in a pupil plane. Using optimized patterns in the coded aperture, and taking multiple images, would allow phase diversity to reconstruct the “phase” of our reflective surface as well as obtain an enhanced estimate of the “object”.

7.2 Refractive Optical Designs

In addition to the system design we created for treating the cloud as reflective optical surface, we also designed an optical system for treating the cloud as a refractive optic, or lens, to maintain maximum flexibility of the cloud physics for future work. One such system design is shown below in Figure 111. The diagram on the left shows light from an object passing through a medium (our cloud). The cloud causes the light to come to a focus and is then relayed to our separated spacecraft that contains the rest of the optical system, shown on the diagram on the right. The corrector/collector design is identical to the reflective system. The solid optics view on the bottom left shows 8-apertures, each consisting of one aerosol optic, forming an equivalent lens. The solid optics view on the bottom right shows a three-dimensional view of the corrector/collector system.

7.3 Bruggeman Effective Medium

One approach for creating a refractive optic using aerosols is to assume very small particles dispersed evenly throughout a volume and use Bruggeman effective medium theory to compute the focusing power of the volume of particles. The containment mechanism of the particles could be as simple as a thin transparent bladder that is released and filled in space. Other approaches could include a laser containment system. The following computations assume particles with a refractive index approximating that of glass, for example, $n = 1.5$. According to Bruggeman effective medium theory, the focal length is:

$$f = \frac{2R}{(n_e - 1)}$$

(18)

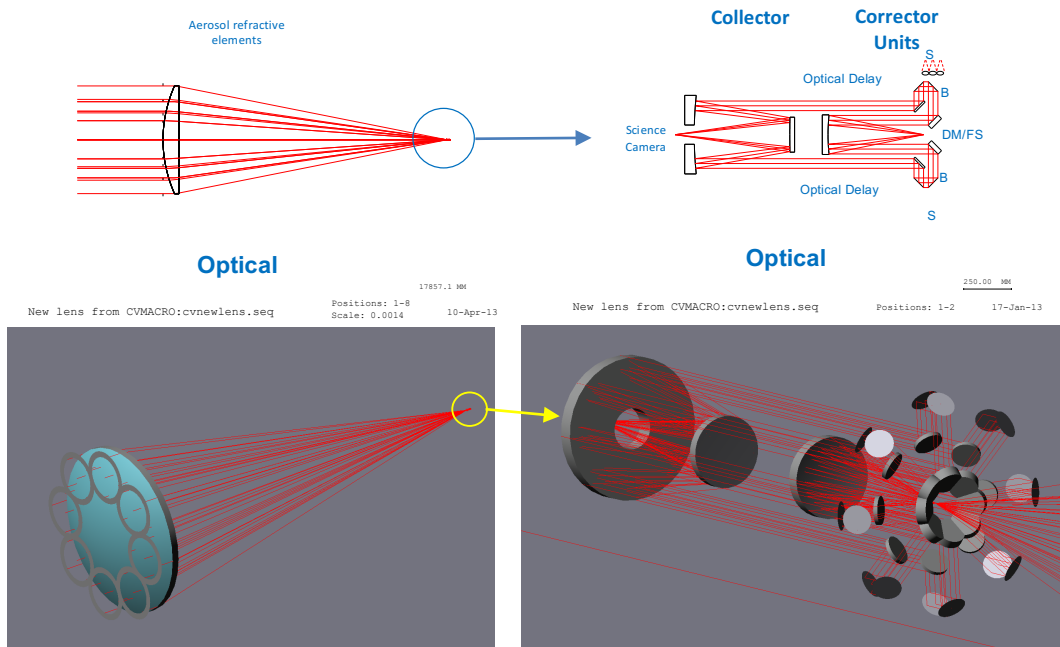


Figure 111. Refractive optical system design, both 2-D and solid optics views.

where

$$(n_e - 1) = \frac{3}{2} F \frac{(n^2 - 1)}{(n^2 + 2)}$$

(19)

F is the fill fraction, and n is the refractive index of the particles. If we have cloud of diameter $2R = 10$ meters, a fill fraction of 10^{-3} , and particles with an index of refraction of $n = 1.5$ then the focal length of the cloud is $f = 23$ km. The f-number is $f/D = 2.3 \times 10^3$. The Airy disk ($1.22 \lambda / D$) is then 1.4 mm (at $D = 0.5$ micrometers), where the camera pixels would ideally be about this size to have a reasonable Q . The f-number is inversely related to the fill fraction as can be seen from

$$f / D = f / 2R = \frac{1}{(n_e - 1)}.$$

(20)

The angular resolution (λ/D) is independent of the fill fraction. If $n = 1.5$ is replaced with $n \approx 1$, the focal length tends toward infinity. This represents a very “slow” optical system, however, since our plan is to have a separate spacecraft to collect the light, separation of several kilometers is not unreasonable.

7.4 Diffractive Optical Design

Another application of our orbiting rainbow that we considered is to create a holographic, or diffractive, optic for our system (Fig. 112). Projects such as DARPA’s Membrane Optic Imager Real-Time Exploration (MOIRE) [MOIRE, Ball] are striving to create a “Fresnel Lens” in space using a thin membrane. The goals of that program are similar to ours, to develop a space-based telescope with apertures larger than 10 meters. It would rely on a separate spacecraft for with a chromatic corrector. Laboratory demonstrations of a 50 cm class diffractive primary mirror with long f-numbers ($f/50$) have been published [Barton2001]. Lawrence Livermore National Laboratory, through the “Eyeglass” program, has created a 5 meter diameter $f/50$ transmissive diffractive optic composed of 50 cm segments [Hyde2003].

Palmer [Palmer1983] considered using the nonlinear optical index of glass beads or aerosol droplets to organize the particles and trap them into Fresnel-like three-dimensional holographic gratings. Extrapolating from this concept, we have designed a third optical system that has a diffractive optical element (DOE) as its primary lens. The system design is nearly identical to the other two systems we designed, but with the primary optics replaced by a thin holographic lens.

A diffractive lens is inherently monochromatic, it only brings light to a focus for the wavelength it was designed for. However, it is straightforward to design an all-refractive chromatic correction system that provides a diffraction limited system with a 10% bandwidth. Meinel and Meinel published a basic design for such a system [Meinel2002a, Meiner2002b]. M. Rud at JPL created the design pictured below (Fig. 116) for a concept for the MOIRE project. More complex correctors that include a reverse Fresnel lens have also been proposed for space telescope applications [Lo2006].

Table 7 compares the three optical systems considered, and Table 8 compares the granular imager to the state of the art in mirror technology.

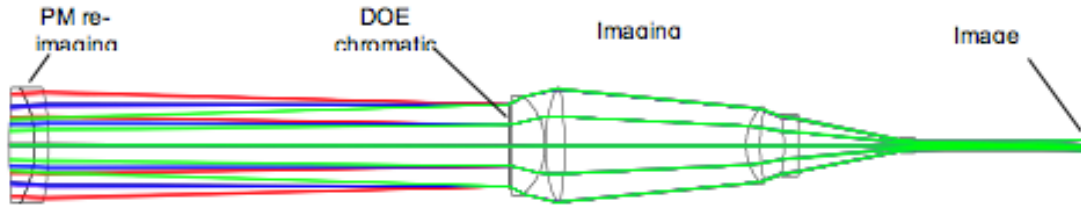


Figure 112. Diffractive Optical system chromatic corrector.

Table 7. Comparison of three optical systems

Characteristic	Reflective	Refractive	Diffractive
Each particle needs to be precision controlled	Yes	No	Yes
Optical Bandwidth	Very high	Constrained	Very constrained

Table 8. Comparison to state of the art.

Metric	Conventional Mirror <u>SoA</u>	Light-Weight Mirror <u>SoA</u>	Aerosol Objective
Mass Areal Density	40-100 kg/m ²	10-20 kg/m ²	<1 g/m ²
Surface Figure Error	10 nm RMS	14 nm RMS	100 nm RMS
Surface microroughness	<5Å	<10Å	<100Å
First free-free mode	>100Hz	>100Hz	TBD
Size	0.1 to 2.4m and larger	0.3 to 1.35m and larger	1 to 10m
Deployable	No	No	Yes
Thermal stability	Low CTE	Thermally controlled	TBD

8. Granular Imager Multi-stage Sensing and Control

A granular imager is a space-borne imaging system that makes use of a collection of small reflective grains to form a sparsely filled primary mirror. The concept is depicted graphically in Fig. 3, where a cloud of reflective grains is constrained by a space-borne optical trap into the parabolic shape of a primary mirror. Light reflected from each grain is then focused into a back-end system consisting of a control system and detector. However, to be an effective imager with a useful point spread function, the wavefronts reflected from the parabolic surface of the cloud must be corrected. This section details a control system that may be used in conjunction with the optical trapping system to correct the wave-fronts so that the granular imager will generate high resolution image that fully realize the potential of larger aperture sizes.

The challenge of a wavefront control system for a granular imager is to correct for the scattered speckle field when the effective surface roughness of the granular media is on the order of microns. It is unlikely that a single deformable optic will have both the range and control accuracy to correct for such roughness. Therefore, we opted for a staged control architecture as depicted in Fig 113.

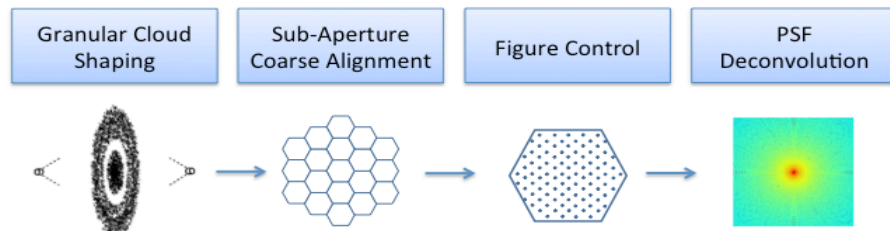


Figure 113. Wavefront Control Architecture

The wavefront control process follows the following steps:

1. **Granular Cloud Shaping** – Grains are trapped in an optical trap, where they are shaped into a parabola
2. **Sub Aperture Coarse Alignment** – The trapped grains may be broken into regions or sub-apertures. Correcting for coarse misalignments between sub-apertures, corrects the low spatial frequency surface roughness of our granular imager, thereby making the PSF of the granular imager more compact.
3. **Figure Control** – Now that each sub-aperture is controlled globally with respect to each other, we can control the figure of each sub-aperture.
4. **Computational Imaging**. A combination of PSF deconvolution techniques and computational imaging will be used to compensate for less-than-ideal imaging as a result of the granular nature of the primary mirror.

An optical design that implements the above described wavefront control architecture is depicted in Fig. 109. In this design, the cloud of grains is re-imaged onto an array of fast steering deformable mirrors (DM/FSM). The tip/tilt of each cloud sub-aperture are

controlled so that the entire collections of clouds fit onto a curved surface. A Shack-Hartmann wavefront sensor is used to sense the figure error that the DM/FSM must correct. In addition, there is an optical delay line that can be used to phase multiple granular telescopes together as a hybrid segmented granular imager design as depicted in Fig. 109.

To detect exoplanets requires near perfect optical systems that are figure controlled to the sub-nanometer level. To achieve this goal one must have excellent control hardware but also must employ control algorithms that can command the control system appropriately. The development of wavefront control algorithms that can meet such demand is a topic of intense research. In 2007, Give'on et al [Giveon2006, Giveon2007] proposed a general correction methodology called electric field conjugation (EFC) to control a coronagraph's residual scattered speckle field. This technique is applicable to a granular imager because it is a method for controlling coherent scatter, which we know will be the limiting factor on performance. With EFC the electric field in an image plane is corrected by applying the conjugate electric field as the correction, as opposed to phase conjugation techniques that try to correct for phase errors in the pupil plane [Giveon2007]. The EFC correction process is outlined in Fig. 114. The most challenging aspect of the control process is the inversion of the G matrix, where several techniques have been proposed [Giveon2007].

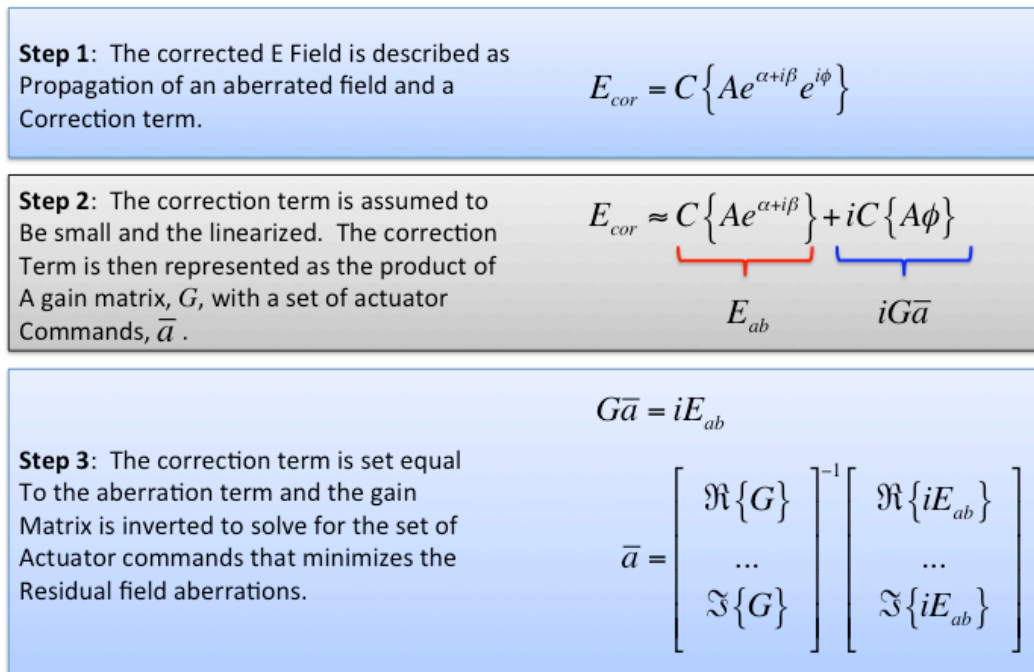


Figure 114. Electric Field Conjugation Correction.

We may also use EFC to sense the electric field in the image plane by using the conjugate field as a method to probe the wavefront. Give'on et al [Giveon2007] demonstrated that it is possible to derive the electric field in the image plane by applying sets of opposite probe patterns. An example of a set of probe patterns and their responses are depicted in Fig. 116 and Fig. 117, respectively. The estimated image plane electric

field is compared to the actual field in Fig. 118.

By Setting the DM in pairs of opposite patterns the real and imaginary components of the pupil aberrations may be determined without the use of a separate wave front sensor. This is highly desirable for low-light imaging

$$I_{probe} \approx \left| E_{ab} + iC \{ A\varphi_{probe} \} \right|^2$$

$$\begin{bmatrix} \Re\{E_{ab}\} \\ \Im\{E_{ab}\} \end{bmatrix} = \frac{1}{4} \begin{bmatrix} \Re\{iC\{A\varphi_1\}\} & \Im\{iC\{A\varphi_1\}\} \\ \vdots & \vdots \\ \Re\{iC\{A\varphi_k\}\} & \Im\{iC\{A\varphi_1\}\} \end{bmatrix} \begin{bmatrix} I_1^+ - I_1^- \\ \vdots \\ I_k^+ - I_k^- \end{bmatrix}$$

Figure 115. EFC probing.

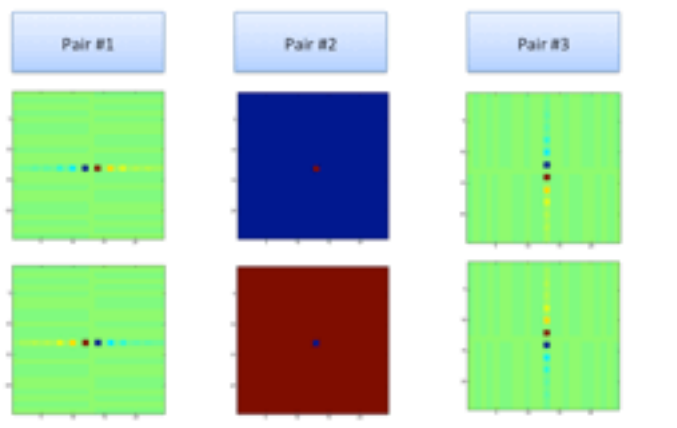


Figure 116. EFC probe pattern.

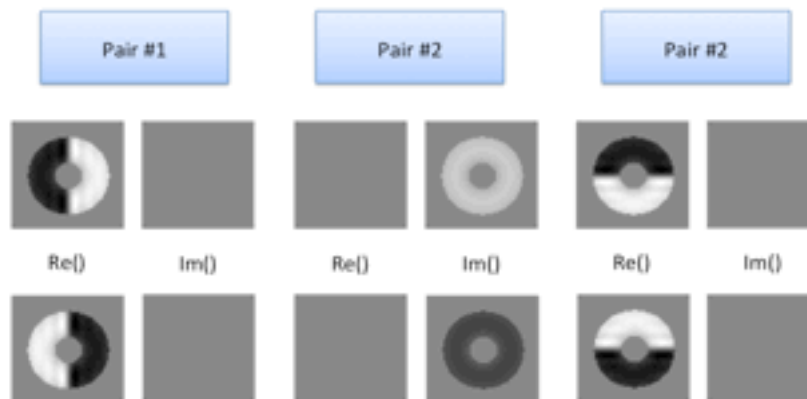


Figure 117. EFC probe responses.

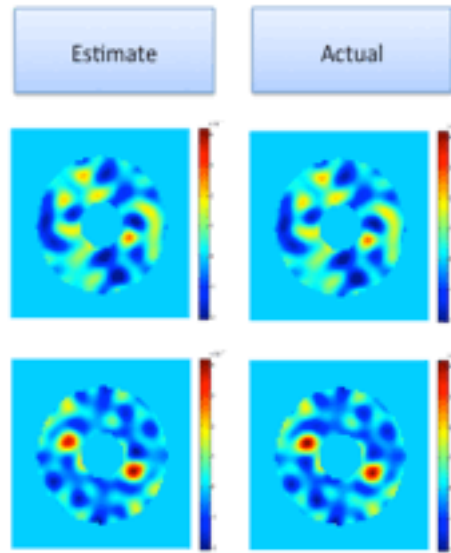


Figure 118. Comparison of the actual and estimated pupil fields.

8.1 Wavefront Sensing

Wavefront Sensing (WFS) is the measurement of the overall effect of the optical aberrations in an imaging system, such as a space telescope. Phase Retrieval is an image-based WFS tool, taking as its input data defocused images of an unresolved object such as a star or an optical pinhole or fiber. It computes a WF map – a 2-dimensional array of Optical Path Difference values – showing the deviation of the actual wavefront from its spherical ideal. For telescopes equipped with actuated optics, such as deformable or movable mirrors, this WF map provides the information needed for control of WF errors, and it does so in the actual science cameras, without requiring a dedicated WFS instrument

Phase Diversity is a superset of Phase Retrieval that attempts not only to estimate phase errors in a system, but also the object that forms an image. Therefore, it is not limited to an unresolved point source, but utilizes an extended scene. There are many methods for performing phase diversity, one of which, multiframe blind deconvolution, is described in detail in the following section.

Shack-Hartman wavefront sensing utilizes a dedicated instrument, which includes a lenslet array at a pupil to convert wavefront slope to centroid offsets on a separate detector. Therefore, part of the light from the science path must be “picked off”, typically using a beamsplitter, for this instrument. The advantage of a Shack-Hartman wavefront sensor is that it has a relatively high dynamic capture range and the image processing requirements are low. Therefore it can make rapid phase estimates (typical systems run at 500 Hz or greater, including corrections on a deformable mirror). However, the spatial frequencies that it can measure are limited to the number of lenslets and it does not work across discontinuities, such as a segmented telescope system will have. Our system is not

segmented, and therefore we would use this kind of wavefront sensor to interrogate and keep aligned individual aerosol clouds. When combining imagery from multiple apertures, or clouds, we plan to investigate using phase diversity.

8.2 Multiframe Blind Deconvolution

Technique such as “blind deconvolution” [Kundur1996] are used if the diversity terms between images is not known or not well known. Multi-frame Blind Deconvolution [Schulz1993] was developed for speckle imaging, where a precise measurement of a stellar object from the ground is not possible due to the changing index of refraction caused by the Earth’s atmosphere. Schulz developed the technique for ground-based imaging of finite extent objects and Van Kampen and Paxman extended the technique to infinite extent objects, or objects that extend beyond the field of view [vanKampen1998].

In general, multi-frame blind deconvolution works by taking multiple images through the optical system. Ground-based techniques assume that the effect of the atmospheric effects are not known exactly, or not measured. However, certain information, such as measuring the Fried parameter (r_0) and relying on Kolmogorov statistics, are used in the algorithm. Recent work [Scharmer2010] has shown that high-order aberrations can be estimated and compensated for computationally. In our Phase 2 work, we simulated the cloud physics, and explored using multi-frame blind deconvolution to determine the quality of imagery that can be reconstructed using these advanced computational optics techniques. Another form of diversity that can be exploited for post-processing of multiple images to better estimate the object is wavelength diversity. This was discussed by Gonsalves [Gonsalves1982] and a blind-image deconvolution approach was developed and tested more recently by Ingelby et al [Ingelby2005]. Assuming our system is polychromatic, we plan to pursue this technique as well.

8.3 Sequential Control Steps

In the following, we outline the modeling and control architecture we envision to realize a closed loop control system that makes use of the granular primary shape estimation scheme. We divide this control architecture into an acquisition step, a trapping step, a rigidification step, a static step, and a dynamic step.

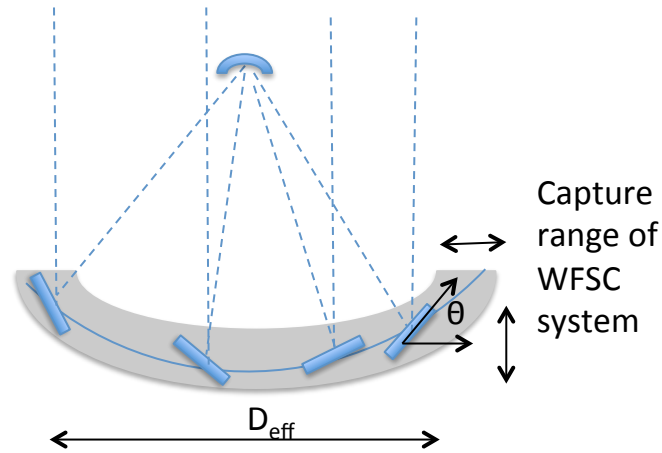
8.3.1 Acquisition Step

The acquisition step begins when the cloud, previously ejected from a canister, is detected and its position and attitude are acquired by a lidar system.

8.3.2 Trapping Step

Once acquired, the trapping step involves the capture and stabilization of the cloud inside a capture volume. See Figure 119. The capture volume is defined as the volume in space where a granular patch needs to be placed as an element of a sparse

aperture system. The cloud is trapped by an external trapping mechanism of an electrostatic or magnetostatic type. The external confinement mechanism is based on the principle of the Optical Tweezer. It relies on a combination of the scattering and gradient optical force on the grains to trap them into equilibrium states.



→ Seen from detector,
becomes equivalent to
monolithic aperture D_{eff}
once aberrations have
been compensated

Figure 119. Cloud inside capture volume.

8.3.4 Rigidification step

The rigidification step assumes that the trapped cloud is first driven to crystallization inside the capture volume by the external confinement mechanism. Once rigidified inside the capture volume, the cloud takes the form of a thin compressed carpet, and is kept stably in that form. Low frequency oscillations can and will occur, due to long period perturbations such as gravitational harmonics, but essentially, the cloud behaves like a rigid body inside the capture volume.

8.3.5 Shaping step

In the shaping step, the rigidified granular layer is now gradually shaped into a spherical surface by differentially actuating the confinement mechanism to produce the resulting shape. It involves sensing of the cloud's position and three-dimensional shape via a lidar system, and actuating the cloud by a modulated electric field distribution from the confining electrodes.

8.3.6 Static step

Once shapped, the cloud behaves like an equivalent rigid reflector. Once a model is developed of a shaped granular layer, the capability is available to model the entire spherical mirror surface undergoing static deformations. The static solution for the

mirror displacement is used to optimize the electrode potential distributions so that the resulting aberrations are gone. Therefore, an iterative process is required to optimally distribute the electrode potentials. To do this, we propose a quasi-static modal control approach for the granular mirror shape control. For reference, Figure 120 shows the modal shapes for a segmented mirror, obtained from modal analysis. In this approach, the shape of the mirror is given in terms of orthonormal polynomials defined on a unit disk, which are known as Zernike polynomials [Tyson1997]. Then, an algorithm that computes the required boundary actuation will adjust the coefficients in these series in order to establish the desired spherical mirror shape. The general two dimensional Zernike series is given in the following form:

$$z(\rho, \theta) = A_{00} + \frac{1}{\sqrt{2}} \sum_{n=2}^{\infty} A_{n0} R_n^0 \left(\frac{\rho}{R} \right) + \sum_{n=1}^{\infty} \sum_{m=1}^n \{A_{mn} \cos m\theta + B_{mn} \sin m\theta\} R_n^m \left(\frac{\rho}{R} \right) \quad (21)$$

where z represents the surface elevations, R is the radius over which the polynomials are defined, χ and Θ are the polar coordinates defined on the mirror plane, $n-m$ is even with R_n^m defined as

$$R_n^{\pm m} \left(\frac{\rho}{R} \right) = \sum_{k=0}^{\frac{n-m}{2}} (-1)^k \frac{(n-k)!}{k! \left(\frac{n+m}{2} - k \right)! \left(\frac{n-m}{2} - k \right)!} \left(\frac{\rho}{R} \right)^{n-2k} \quad (22)$$

and A_{nm} are Zernike coefficients. Figure 121 (right), shows the Zernike polynomials used to describe the wavefront. Consequently, the surface deformations for the mirror can be effectively described by using these polynomials, and there are techniques available to extract the coefficients of these polynomials from sensed information. Our approach is to define a desired shape for the mirror, and then to describe the deviation from this shape in terms of Zernike series, and to adjust the Zernike coefficients with a control actuation. At the Sun-Earth L2 point, the large mirror will be exposed to disturbance forces, which vary extremely slowly, such as solar pressure. Therefore, we can treat the shape control of the large mirror as finding the control forces to correct the static deformations at a given time. The dynamics of the mirror are ignored in this approach, so the approach is static in nature. But, since this correction is done frequently, and the external control actuation can be applied very rapidly, this is a reasonable simplification.

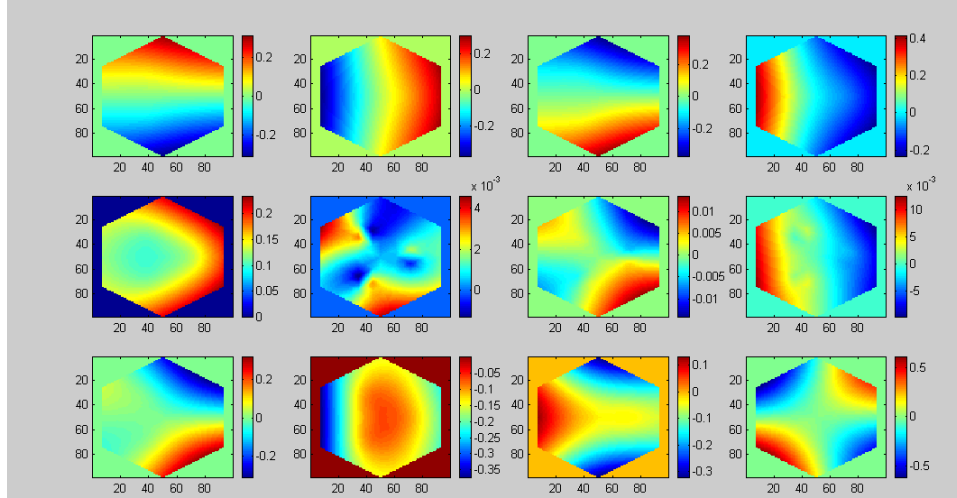


Figure 120. Modal shapes of hexagonal segment.

8.3.7 Dynamic step

Once this initial static step is completed, the system dynamics can be computed, and the system modal data evaluated. This is the beginning of the dynamics loop.

An integrated modeling approach previously considered for high-precision space telescopes is followed in the development of the system model for control design [Moser1998]. The granular aperture dynamic model is a model of the system in modal space, obtained from the mass and stiffness (M,K) set. The solution is based on a continuous to discrete transformation in 2nd order form

$$\ddot{\eta}_k + 2\Sigma\Lambda\dot{\eta}_k + \Lambda^2\eta_k = \Phi^T f_k, \quad (23)$$

where Λ , Φ are diagonal ($n \times n$) and η_k is ($n \times 1$), and n is the number of retained modes. In state-space form, where A is ($2n \times 2n$) and B is ($2n \times n$), this system becomes:

$$\dot{z}_k = Az_k + Bf_k \quad (24)$$

$$z = \begin{bmatrix} \eta_1 \\ \vdots \\ \eta_n \\ \dot{\eta}_1 \\ \vdots \\ \dot{\eta}_n \end{bmatrix}$$

(25)

From the global stiffness matrix of the cloud, we can derive the generalized compliance, i.e. the influence functions. Influence functions are the mappings $\frac{\partial u_{Ki}}{\partial f_{Nj}}$, where u_{Ki} is the displacement at location K in the i-th direction, and f_{Nj} is the control action at location N in the j-th direction. For reference, Figure 122 (left) shows influence functions for a hexagonal segment, obtained by applied unit actuator inputs circumferentially around the mirror.

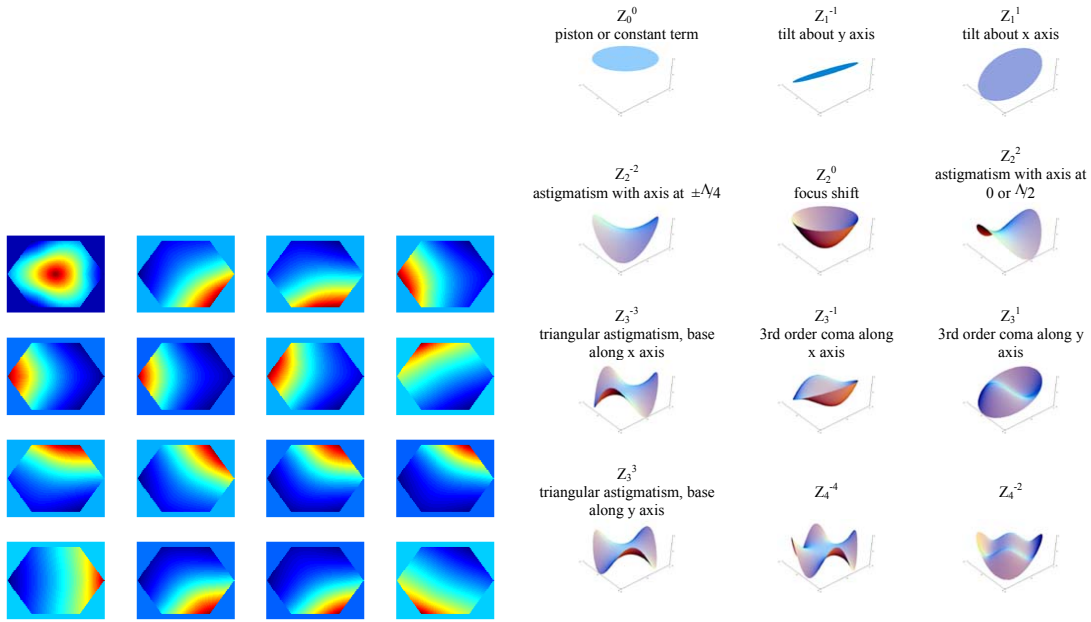


Figure 121. Influence functions for hexagonal segment (left), and Zernike polynomials used to describe wavefront aberrations (right).

Mirror surface deformations are then computed at each time step given the external perturbation sources and the actuator inputs. With these mirror surface deformations, the deformed granular reflector shape can be synthesized. The coefficients of the Zernicke polynomials are then identified, and the corresponding control inputs are then computed. These voltages are compared with the static voltages required to attain the ideal spherical surface, and a corrective control action is requested with an additional voltage correction.

8.4 Wavefront Sensing and Control System Performance

In this section, we examine the optical imaging performance of a granular imager for two types of systems: a high-resolution imager and a high-contrast coronagraph. The first system is depicted graphically in Fig 122. In this case the most important metric of

performance is resolution. The modulation transfer function measures how the modulation of a sinusoidal intensity variation in the image plane will vary as a function of spatial frequency. An ideal system will pass the zeroth spatial frequency perfectly but the modulation slowly decreases with spatial frequency until it reaches the cutoff frequency, $2 \times \text{Nyquist Rate}$, where the modulation falls to zero. Traditionally, an object is considered resolvable if it modulates the intensity by greater than 10%. It has also been shown that low contrast images are able to be boosted back to nominal using a Wiener filter as long as the signal to noise (SNR) of the system is sufficiently high [Pratt1972], which often correlates with a 10% spatial frequency cutoff.

In the simulations presented in this section, the parabolic primary mirror of the granular imager was filled randomly with small, unresolved grains (grain size \ll granular imager focal length). The fill factor, or the fraction of the aperture that is filled with grains, was allowed to vary from 0.2 to 1.0. In addition, the wavefront phase aberrations were allowed to vary from 0 – 1 waves of rms error.

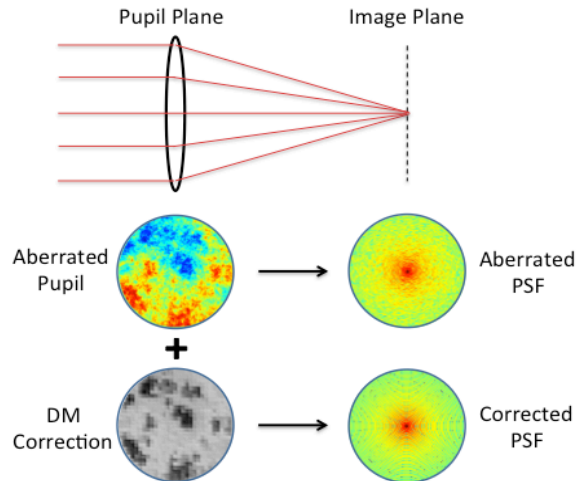


Figure 122. High-resolution imager with WFS&C

In the first simulation, the fill factor of the granular imager is allowed to vary but the wavefront phase had no phase aberrations in the pupil (0 waves rms). Fig. 123 is a plot of the granular imager MTF vs. spatial frequency for several fill factor values. As expected the modulation decreases as a function of fill factor. However the resolution doesn't change appreciably until the fill factor is below 0.3. The 10% resolution cutoff for a perfect system occurs at approximately $1.6 \times \text{Nyquist}$ rate, even with a fill factor of 0.4, the resolution cutoff has only degraded to $1.4 \times \text{Nyquist}$ or approximately 12%. Although the contrast suffers as we decrease the fill factor, we may still be able to recover $\sim 90\%$ of the image in post processing using standard Wiener filtering techniques.

In the second simulation, the fill factor of the granular imager is now kept constant at fill factor = 1.0 and wavefront phase error (WFE) was allowed to be vary from 0.1 – 0.5 waves rms aberration. Fig. 128 is a plot of the granular imager MTF vs. spatial frequency for several WFE cases. These plots reveal, that even with a fully filled aperture, the WFE limits the performance of the system severely when the WFE is greater than approximately

0.2 waves. Therefore, it's important to correct the optical figure at least to this level for high-resolution imaging.

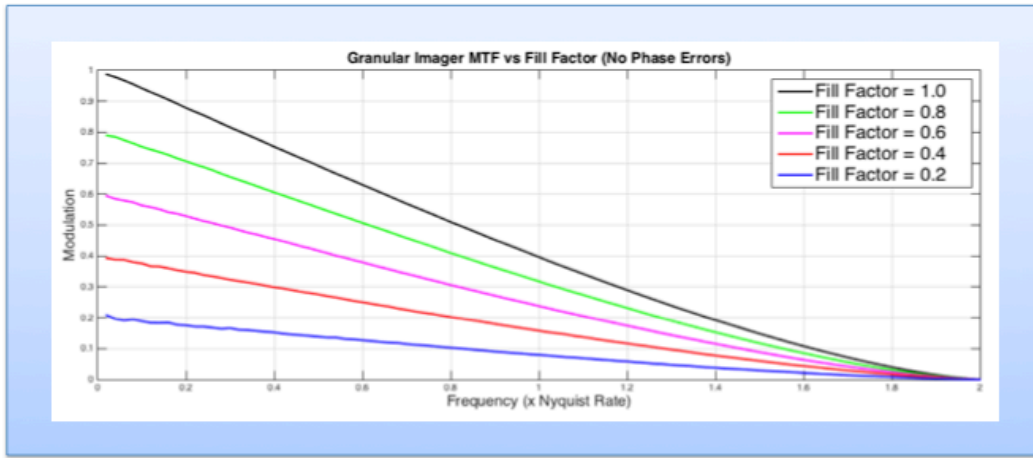


Figure 123. Granular Imager MTF vs. fill factor.

8.5 Contrast Analysis

High Contrast coronagraphy is a more challenging case for the granular imager and the wavefront control system is critical. The granular imager was modeled in conjunction with a hybrid Lyot coronagraph (HLC) [Trauger2014] as depicted in Fig 125. In the results presented here, the grains were small, unresolved spheres that scattered light equally in all directions and the entrance pupil limited the surface roughness of the coronagraph to a simple power law power spectral density function with an peak-to-valley phase error of 200nm (30 nm rms), and an amplitude uniformity error of 8% peak-to-valley (1.2% rms). The coronagraph acts as a high-pass spatial filter, suppressing the light from an on-axis star, but leaves the light from nearby objects such as planets relatively intact. The difficulty of using a granular imager for this application lies in the fact that the grains will scatter light from the star into the mid-spatial frequencies where they will drown out the light from nearby objects, rendering the coronagraph ineffective. However, the use of a wavefront control system can help mitigate this issue. A wavefront control system was placed before the entrance aperture of the coronagraph as shown in Fig 125. In this configuration, two deformable mirrors (DM1 & DM2) are used to control the electric field at the occulter. One is placed in a pupil plane and another is placed outside the pupil plane. At least two DMs are required because a single DM located at the Coronagraph pupil could not control both phase and amplitude errors originating in the same plane simultaneously.

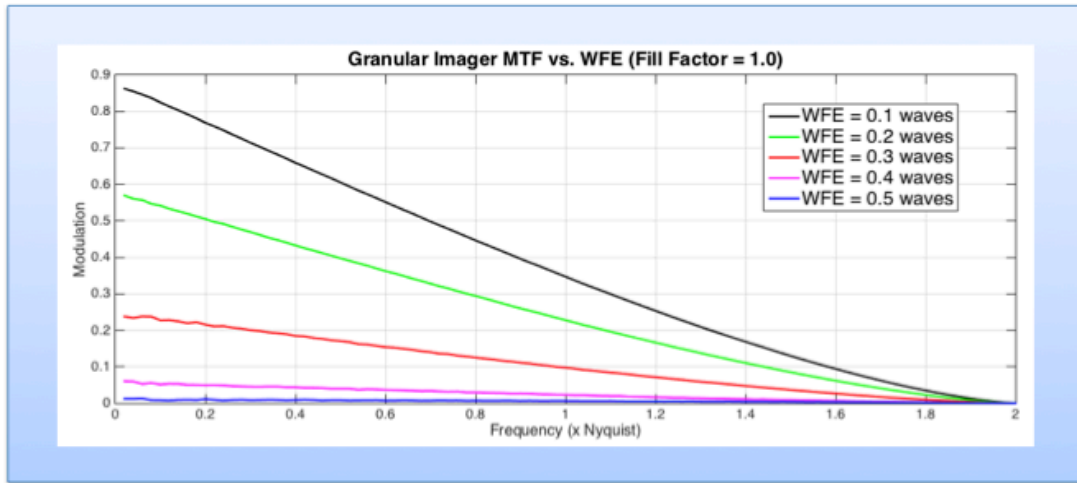


Figure 124. Granular Imager MTF vs. wavefront error.

Contrast is a measure of how much the light from the on-axis star has been reduced as compared to nearby objects. The greater the contrast, the fainter an object can be and still be detected. Simulations of the contrast provided by the system above were run for a fill factor of 1.0 (normal aperture) and a fill factor of 0.5 (sparse aperture) are shown in Fig 130. As we expect when the fill factor is reduced from 1.0 to 0.5, light is scattered in all directions to form a speckle field. Note that in the normal aperture case (fill factor = 1.0) the scattered light rolls off as a power law as we defined it. However in the sparsely filled case (fill factor = 0.5) the light is scattered in all directions as expected. The control system allows us to dig a dark hole in the scattered light as shown in the zoomed in insets in the lower half of Fig 126. Although the contrast in the dark hole has decreased from 10^{-10} to 10^{-8} , we are still able to control the majority of the scattered light from the grains using the EFC algorithm in conjunction with two deformable mirrors (DM). See Fig. 126. If the wavefront control system were not able to control the scattered light, no dark hole would form. Two DMs gives you more controllability than one because we are increasing the number of degrees of freedom that we can use to control each point in the image plane. Therefore, it may be possible to increase the contrast by increasing the number of DMs used.

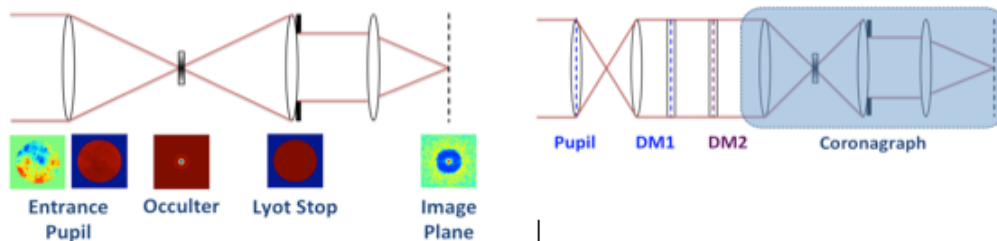


Figure 125. HLC Control system.

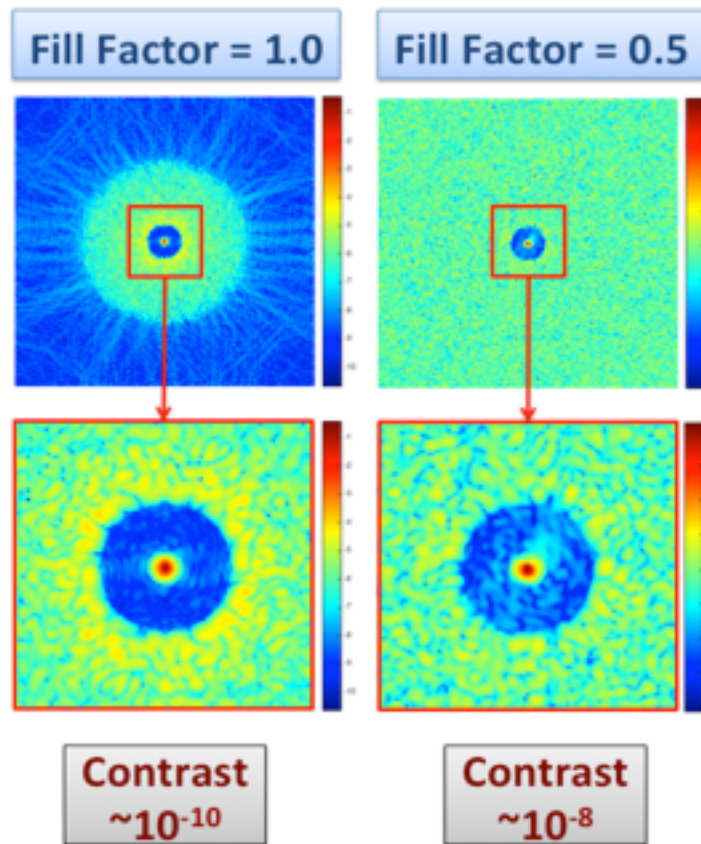


Figure 126. Granular Imager HLC Contrast vs Fill Factor.

Now we ask the question: How sparse can an aperture be before we lose all controllability? To answer the question for the case of 2 DMs, we performed simulations where the fill factor was allowed to vary from 0.1 to 1.0. The mean contrast in the dark hole was plotted as a function of fill factor in Fig 127. As can be seen, the contrast in the dark hole increases for fill factors greater than 0.3 regardless of whether or not phase errors were present. This suggests that the granular cloud does not have to be perfectly shaped into a parabola but rather just needs to be shaped with an RMS surface roughness that is within the capture range of the wavefront control system. This allows one to trade between grain trapping error and the wavefront control capture range.

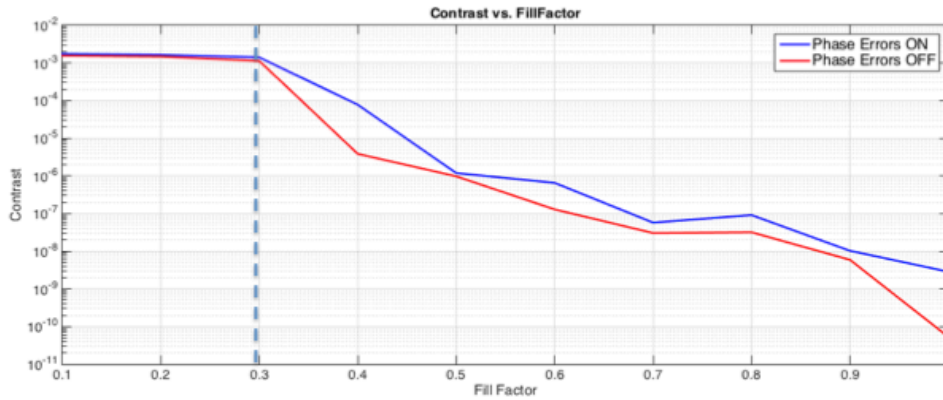


Figure 127. Granular Imager contrast vs. phase errors.

9. Granular Imager Integrated Modeling

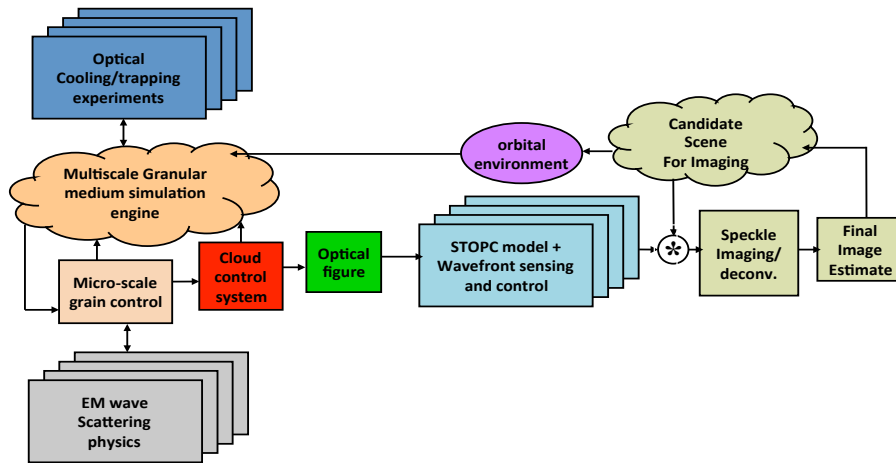


Figure 128. Granular Telescope Integrated Modeling Diagram.

Figure 128 describes the overall control architecture for the system model that we considered in Phase II. It follows the task flow described in Figure 9, and will be described again in this section for clarity purposes. It starts in the upper left corner with the particle simulation engine, which was developed in Phase I. This engine computes the motions of the particles that make up the primary optic at the granular level. The orange rectangles represent the microscale control system of the particles. Its purpose is to “corral” the particles, keep them functioning as a unit, and ensure the optical properties of the conglomerate meet the requirements for the next stages of control. From the position and orientation of the particles, a complex electromagnetic pupil function is computed, from which the optical figure and pupil can be determined (green box). The red boxes represent the next stage of control, which is the relative position and orientation of the separate spacecraft imaging system. The spacecraft has its own thrusters and reaction wheels to maintain precision optical alignment

using a laser metrology truss developed at JPL as a precision sensor. The light blue boxes represent the mid-level control systems. A STOP integrated model was created for a single patch/cloud and its corresponding correction/collections system. Drivers to the STOP model include thermal variations (purple circle) based on the trajectory of the system relative to the Sun and other thermal sources. The STOP model has two main control systems, one for LOS correction and an adaptive optics control system that uses a Shack-Hartmann sensor to control a deformable mirror. Combining information from multiple STOP models (one for each patch), a time-varying PSF is computed (green box). The relative positions of each cloud may vary with respect to each other; therefore, an outer control system for maintaining precision phasing between the patches is necessary (shown in yellow). An IPO (In-focus PSF Optimizer) is another WFS&C algorithm developed at JPL for segmented optical systems. This algorithm will drive the optical delay lines to maintain the relative phase of each patch and will also provide feedback information to the LOS control to maintain pointing. Finally, the time-varying PSF is convolved with an image (or “scene”). Speckle imaging and multiframe blind deconvolution algorithms were investigated to “clean up” the imagery to get an accurate estimate of the original scene.

The integrated modeling simulation is needed to provide a simulation environment with which to assess the system performance. This simulation leverages the preliminary simulation engine initially developed in Phase I. The simulation flow starts in the upper left corner with data provided by the optical manipulation experiments. This engine computes the motions of the particles that make up the PMC. It was modified as necessary as data from the planned laboratory experiments becomes available. The orange rectangle in the left represents the microscale control system of the particles. Its purpose is to “corral” the particles, keep them functioning as a unit, and ensure the optical properties of the conglomerate meet the requirements for the next stages of control. Assuming now that the system is successfully contained and trapped in space, from the known position and orientation of the particles, a complex electromagnetic pupil function is computed, from which the optical figure and pupil can be determined (green box). The red box in Figure 128 represents the next stage of control, which is the relative position and orientation of the separate spacecraft imaging system. Each spacecraft in the formation has its own thrusters and reaction wheels to maintain precision optical alignment with the equivalent “virtual truss”. The light blue boxes in Figure 128 represent the mid-level control systems involving the wavefront sensing and control. A STOP integrated model was created for a single patch/cloud and its corresponding correction/collections system. Drivers to the STOP model include thermal variations (purple circle) based on the trajectory of the system relative to the Sun and other thermal sources. The STOP model has two main control systems, one for LOS correction and an adaptive optics control system that uses a Shack-Hartmann sensor to control a deformable mirror. Combining information from multiple STOP models (one for each patch), a time-varying PSF is computed (green box). The relative positions of each cloud may vary with respect to each other; therefore, an outer control system for maintaining precision phasing between the patches is necessary. Finally, the time-varying point spread function (PSF) is convolved with an image (or “scene”), at the right of Figure 128. Speckle imaging and multiframe blind

deconvolution algorithms were investigated to “clean up” the imagery to get an accurate estimate of the original scene.

9.1 Granular Imager Dynamics and Control

This section follows the approach for formation dynamics and control presented in Fig [Mettler2005] and in the Phase I Final Report. Also see Fig. 129 for reference. The Granular Telescope formation most basic active elements are five free-flying optical modules. The free flyers are

- S0, the primary mirror cloud (PMC)
- S1, the free flying mirror (FFM)
- S2, the Focal Plane Assembly (FPA)
- S3, The Primary Figure Sensor (PFS)
- S4, the Laser Containment/Trapping System (LCTS)
- S5, the co-orbiting sunshade (OSS)

The following assumptions are used in this report:

- The formation is composed of five rigid bodies (sunshade dynamics is neglected).
- The orbit is circular.
- The formation dynamics is described (and numerically integrated) with respect to the Orbiting Reference Frame, to be described next.

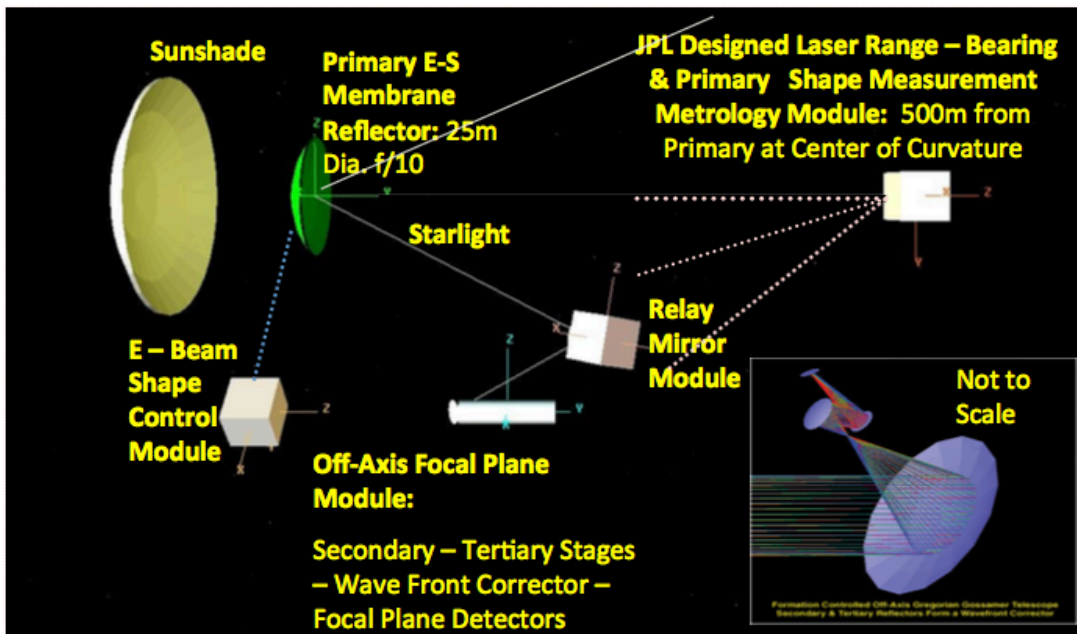


Figure 129. JPL's super-precision formation flying telescope [from Mettler2005].

9.1.1 Reference Frames

- F_I - Inertial Frame F_I taken as J2000
- F_C - Define the PMC frame F_C by 3 fiducial points at the periphery of the PMC membrane. The z axis is defined normal to the fiducial plane, and in the direction of the nominal LOS of the telescope. The F_C frame is located at the “mechanical center” of the PMC, defined by the mean location of the three fiducial points.
- F_O - Define the Orbital frame F_O of the PMC for a geosynchronous or heliocentric orbit. The orbital frame is defined with x_O axis along positive radial vector r from Sun center to the mechanical center of the PMC, and z_O=rXv, where v is the orbital velocity vector. The orbital frame is assumed to be located at the mechanical center of the PMC.
- F_T - Telescope Formation Frame F_T, is an inertial frame located at center of PMC, which specifies the desired attitude of the telescope (this points the telescope LOS to a desired J2000 location, and maintains acceptable twist angle of the formation). Thus defined, the z axis of F_T, is labelled as the axis of the desired telescope LOS.
- Define body frames F_fpa, F_pfs, and F_lcts for the free flying elements FPA, FPS, LCTS, respectively.
- q_A - Define the formation attitude q_A as the quaternion (or equivalent direction cosine matrix A) which maps the F_I frame into the F_T frame, i.e., $F_T = A F_I$
- q_R - Define the PMC alignment as the quaternion q_R (or equivalent direction cosine matrix R) which maps the F_T frame into the F_C frame, i.e., $F_C = q_R F_T$

9.1.2 Kinematics and Kinetics of System in Orbit

The assumptions we used to model the dynamics follows [Quadrelli2003], and are as follows: 1) The inertial frame F_I is fixed at Earth’s center. 2) The orbiting Frame (ORF) F_O follows a Keplerian orbit. 3) the cloud system dynamics is referred to F_O. 4) the attitude of each grain uses the principal body frame as body fixed frame. 5) the atmosphere is assumed to be rigidly rotating with the Earth. Regarding the grains forming the cloud: 1) each grain is modeled as a rigid body; 2) a simple attitude estimator provides attitude estimates, 3) a simple guidance logic commands the position and attitude of each grain, 4) a simple local feedback control of local states is used to stabilize the attitude of the vehicle. Regarding the cloud: 1) the cloud as a whole is modeled as an equivalent rigid body in orbit, and 2) an associated graph establishes grain connectivity and enables coupling between modes of motion at the micro and macro scales; 3) a simple guidance and estimation logic is modeled to estimate and command the attitude of this equivalent rigid body; 4) a cloud shape maintenance controller is based on the dynamics of a stable virtual truss in the orbiting frame. Regarding the environmental perturbations acting on the cloud: 1) a non-spherical gravity field including J0 (Earth’s spherical field) zonal component, J2 (Earth’s oblateness) and J3 zonal components is implemented; 2) atmospheric drag is modeled with an exponential model; 3) solar pressure is modeled assuming the Sun is inertially fixed; and 4) the Earth’s magnetic field is model using an equivalent dipole

model. The equations of motion are written in a referential system with respect to the origin of the orbiting frame and the state is propagated forward in time using an incremental predictor-corrector scheme.

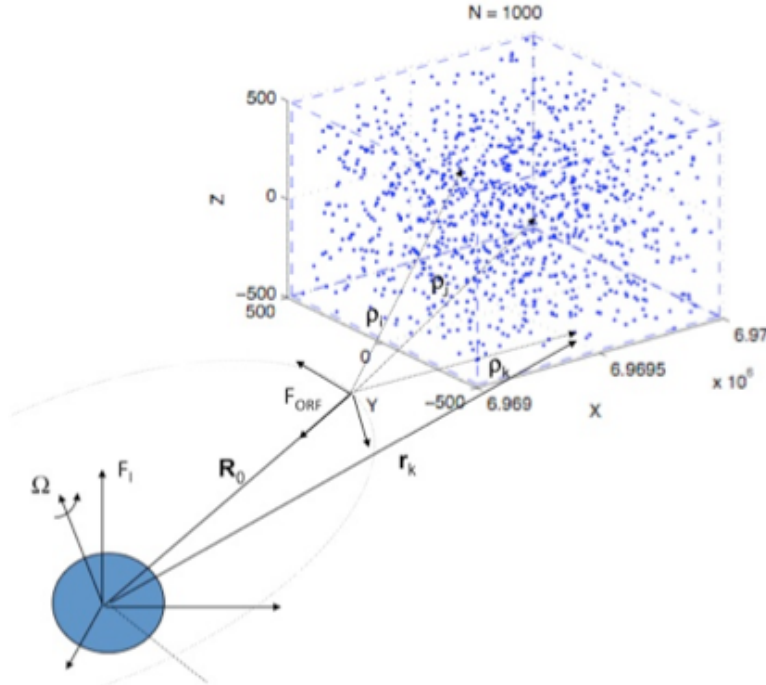


Figure 130. Geometrical description of orbiting cloud in orbit.

Figure 130 shows the kinematic parameters of a 1000 element cloud in orbit. The motion of the system is described with respect to a local vertical-local horizontal (LV-LH) orbiting reference frame $(x,y,z)=F_{ORF}$ of origin O_{ORF} which rotates with mean motion Ω and orbital semi-major axis R_0 . The orbital geometry at the initial time is defined in terms of its six orbital elements, and the orbital dynamics equation for point O_{ORF} is propagated forward in time under the influence of the gravitational field of the primary and other external perturbations, described below. The origin of this frame coincides with the initial position of the center of mass of the system, and the coordinate axes are z along the local vertical, x toward the flight direction, and y in the orbit normal direction. The inertial reference frame $(X,Y,Z)=F_I$ is geocentric inertial for LEO (X points toward the vernal equinox, Z toward the North Pole, and Y completes the right handed reference frame), and heliocentric inertial for other applications. The orbit of the origin of F_{ORF} is defined by the six orbital elements a (semimajor axis), e (eccentricity), i (inclination), Ω_L (longitude of ascending node), ϖ (argument of perigee), v (true anomaly), and time of passage through periapsis. From Figure 130, the position vector of a generic grain with respect to O_{ORF} is denoted by ρ_i , and we have $\mathbf{r}_i=\mathbf{R}_0+\rho_i$. We define the cloud state vector as

$$\mathbf{X} = (\mathbf{r}_E, \dot{\mathbf{r}}_E, \mathbf{R}_0, \dot{\mathbf{R}}_0, \dots, \rho_i, \mathbf{q}_i, \dot{\rho}_i, \dot{\mathbf{q}}_i, \omega_i, \mathbf{R}_s, \dot{\mathbf{R}}_s, \rho_s, \dot{\rho}_s, \mathbf{q}_s, \dot{\mathbf{q}}_s, \omega_s)$$

(26)

where \mathbf{q}_i and $\boldsymbol{\omega}_i$ represent the quaternion and angular velocity vector of the i -th grain with respect to F_1 . The translation and rotation kinematics at the grain level are:

$$\begin{array}{l} \text{grain} \\ \text{cloud} \end{array} \left\{ \begin{array}{l} \mathbf{V}_0 = \dot{\mathbf{R}}_0 \\ \mathbf{v}_i = \dot{\boldsymbol{\rho}}_i \\ \dot{\mathbf{R}}_{bi} = -\boldsymbol{\omega}^\times \mathbf{R}_{bi} \end{array} \right. \quad \begin{array}{l} \text{cloud} \\ \text{cloud} \end{array} \left\{ \begin{array}{l} \mathbf{V}_s = \dot{\mathbf{R}}_s \\ \mathbf{v}_s = \dot{\boldsymbol{\rho}}_s \\ \dot{\mathbf{C}}_{si} = -\boldsymbol{\omega}_s^\times \mathbf{C}_{si} \end{array} \right. \quad (27)$$

The angular momentum balance is:

$$\begin{array}{l} \text{grain} \\ \text{cloud} \end{array} \left\{ \begin{array}{l} \mathbf{J}_i \dot{\boldsymbol{\omega}}_i + \boldsymbol{\omega}_i^\times \mathbf{J}_i \boldsymbol{\omega}_i = \sum_{j=1}^{N_{pert}} \boldsymbol{\tau}_j \\ \mathbf{J}_s \dot{\boldsymbol{\omega}}_s + \boldsymbol{\omega}_s^\times \mathbf{J}_s \boldsymbol{\omega}_s = \boldsymbol{\tau}_s \end{array} \right. \quad (28)$$

and the linear momentum balance is:

$$\begin{array}{l} \text{grain} \\ \text{cloud} \end{array} \left\{ \begin{array}{l} \dot{\mathbf{V}}_0 = -\mu_E \frac{\mathbf{R}_0}{|\mathbf{R}_0|^3} + \frac{\sum_{j=1}^{N_{pert}} \mathbf{f}_j}{m_{total}} \\ \dot{\boldsymbol{\rho}}_i = -\dot{\mathbf{V}}_0 - \dot{\boldsymbol{\Omega}}^\times \boldsymbol{\rho}_i + \boldsymbol{\Omega}^\times \boldsymbol{\Omega}^\times \boldsymbol{\rho}_i - 2\boldsymbol{\Omega}^\times \dot{\boldsymbol{\rho}}_i + A_i \ddot{\mathbf{r}}_i \\ \ddot{\mathbf{r}}_i = -\mu_E \frac{\mathbf{r}_i}{|\mathbf{r}_i|^3} + \frac{(\mathbf{f}_a + \mathbf{f}_e)_i}{m_i} \end{array} \right. \quad \begin{array}{l} \text{cloud} \\ \text{cloud} \end{array} \left\{ \begin{array}{l} \dot{\mathbf{V}}_s = -\mu_E \frac{\mathbf{R}_s}{|\mathbf{R}_s|^3} + \frac{(\mathbf{f}_{J2} + \mathbf{f}_{J3})_s}{m_s} \\ \dot{\boldsymbol{\rho}}_s = -\dot{\mathbf{V}}_s - \dot{\boldsymbol{\Omega}}^\times \boldsymbol{\rho}_s + \boldsymbol{\Omega}^\times \boldsymbol{\Omega}^\times \boldsymbol{\rho}_s - 2\boldsymbol{\Omega}^\times \dot{\boldsymbol{\rho}}_s + C_s \frac{\mathbf{f}_s}{m_s} \end{array} \right. \quad (29)$$

where: A_i = rotation matrix of i -th body frame wrt. Inertial; \mathbf{R}_0 = orbital radius vector to origin of ORF; $\boldsymbol{\Omega}$ = orbital rate; \mathbf{C}_{si} = rotation matrix of cloud body frame wrt. Inertial; $\mathbf{f}_{a,e}$ = actuation + external forces (gravity, aerodynamics, magnetic, solar); $m_{i,s}$ = grain/cloud mass; $\boldsymbol{\omega}_{i,s}$ = body, cloud angular rate; $\boldsymbol{\tau}_{a,e}$ = actuation + external torques; $\mathbf{J}_{i,s}$ = grain/cloud moment of inertia. Finally, the translation kinematics and dynamics equations of a grain of mass m in a general orbit can then be summarized as:

$$\ddot{\boldsymbol{\rho}} = -\ddot{\mathbf{R}}_0 - \dot{\boldsymbol{\Omega}}^\times \boldsymbol{\rho} - \boldsymbol{\Omega}^\times \boldsymbol{\Omega}^\times \boldsymbol{\rho} - 2\boldsymbol{\Omega}^\times \dot{\boldsymbol{\rho}} + \ddot{\mathbf{r}} \quad (\text{near field}) \quad (30)$$

$$\ddot{\mathbf{r}} = -\mu_E \frac{\mathbf{r}}{|\mathbf{r}|^3} + \frac{\mathbf{f}_a + \mathbf{f}_s + \mathbf{f}_3}{m} \quad (\text{far field}) \quad (31)$$

$$\ddot{\mathbf{R}}_0 = -\frac{\mu_E}{|\mathbf{R}_0|^3} \mathbf{R}_0 + \frac{\mathbf{f}_{pert} + \mathbf{f}_{J_2} + \mathbf{f}_{J_3}}{m} \quad (\text{ORF orbital dynamics}) \quad (32)$$

where: \mathbf{x}_ρ = relative position vector of mass with respect to ORF, \mathbf{R}_0 = orbital radius vector to origin of ORF, Ω = orbital rate, μ_E = gravitational parameter, \mathbf{f}_a = thruster actuation force vector, \mathbf{f}_s = solar pressure force vector, \mathbf{f}_3 = third-body forces vector, m = spacecraft mass with rotors added, and \mathbf{f}_{pert} , \mathbf{f}_{J_2} , \mathbf{f}_{J_3} = resultants of higher order gravitational terms from the primary acting on the entire system as an extended body. The rotational dynamics equations of a spacecraft with a gyroscopic distribution about its center of mass (for example, reaction wheels or control moment gyros) are:

$$\mathbf{J}\dot{\omega} + \sum_i \dot{\mathbf{H}}_i^w + \omega \times \left(\mathbf{J}\omega + \sum_i \mathbf{H}_i^w \right) = \mathbf{g}_e + \mathbf{g}_a \quad (33)$$

$$\dot{\mathbf{H}}_i^w = -\mathbf{g}_{w_i} \quad (i=1, \dots, \text{number of rotors}) \quad (34)$$

where ω = spacecraft's body angular rate, \mathbf{g}_e = external perturbation torques (solar pressure, gravity gradient, J_2 , etc.), \mathbf{g}_a = thruster actuator torques, \mathbf{g}_w = rotor control torque, \mathbf{J} = spacecraft moment of inertia, \mathbf{H}_i^w = angular momentum of the i -th rotor.

An integrated modeling approach previously considered for high-precision space telescopes is followed in the development of the system model for control design [Mosier1998, Mosier2000]. The vehicle plant model is a model of the system in modal space, obtained from the system mass and stiffness matrix set. After solving the eigenvalue problem $K_a \Phi_a = \Lambda_a M_a \Phi_a$ with $\Phi_a^T M_a \Phi_a = 1$, and introducing the canonical transformation $X_a = \Phi_a \eta_a$, where Φ_a is the matrix of modal shapes, with $n < N$ retained modes, we obtain the modal equations. Introducing now the structural damping matrix Σ , we may write the modal dynamics equations as:

$$\dot{Z}_a = \begin{bmatrix} 0 & 1 \\ -\Lambda_a^2 & -2\Sigma\Lambda_a \end{bmatrix} \begin{bmatrix} \eta_a \\ \dot{\eta}_a \end{bmatrix} + \begin{bmatrix} 0 \\ \Phi_a^T D_a \end{bmatrix} U_a = A_a Z_a + B_a U_a \quad (35)$$

where Σ , Λ are diagonal ($n \times n$) and η_k is the modal displacement, and n is the number of retained modes. In state-space form, where A is $(2n \times 2n)$ and B is $(2n \times n)$, this system becomes:

$$\begin{aligned} \dot{x}_k &= A x_k + B_u u_k + B_w w_k \\ y_k &= C_y x_k + D_y u_k + v \\ z_k &= C_z x_k \end{aligned} \quad (36)$$

where u_k is the actuator input, w_k is a disturbance input, and v is sensor noise, representative of the spacecraft gyro noise. B_w defines how the disturbances are input

into the system, B_u defines how the actuator commands are input to the system, C_y relates the sensor outputs to the states, z are the performance outputs, C_z relates the performance outputs to the states, D_y relates the performance outputs to the control inputs, and y are the sensor outputs. The inputs and outputs of the model are defined based on the desired disturbances, performance outputs, and control systems. The equations of motion for the flexible spacecraft in global coordinates can be written in terms of the configuration vector \mathbf{q} (of length n_g+1), which contains the nodal displacements and rotations of each node in global coordinates plus the rotor rotation angles plus the rigid body degrees of freedom. The global equations need to be reduced from the global set n_g of dependent configuration variables to a set of independent degrees of freedom n_e , and this is done by a transformation $\mathbf{q}=\mathbf{T}\mathbf{q}_e$, where \mathbf{T} is of dimension $n_g \times n_e$. Splitting the equations in elastic (e) and rigid (r) coordinates, we have:

$$\begin{aligned} \mathbf{M}_{ee}\ddot{\mathbf{q}}_e + \mathbf{M}_{er}\dot{\mathbf{\Omega}} + (\mathbf{G}_{ee} + \mathbf{D}_{ee})\dot{\mathbf{q}}_e + \mathbf{K}_{ee}\mathbf{q}_e &= \mathbf{f}_e \\ \mathbf{M}_{re}\ddot{\mathbf{q}}_e + \mathbf{M}_{rr}\dot{\mathbf{\Omega}} &= \mathbf{f}_r \end{aligned} \quad (37)$$

where now $\mathbf{M}_{ee}=\mathbf{T}^T\mathbf{M}_g\mathbf{T}$, and similarly for the other matrices.

9.2 Confined Aperture Pointing Control

Robust and realistic control, sensing, estimation, and system identification methodologies and algorithms are common to most of the gossamer spacecraft envisioned in NASA missions. This commonality stems from the fact that their control design and performance is very sensitive to modeling errors. These may arise from unmodeled flexibility in large structures, unmodeled sensor and actuator dynamics, and uncertainties in the interaction with the environment. The long life expectancy of these envisioned missions (3 to 5 years) requires a sensing and actuation scheme, which must be robust to uncertainties in the plant model. There are a variety of dynamics and control issues associated with gossamer-like spacecraft, which have only begun to be addressed. Some are common to other spacecraft as well, but in general they present additional problems.

The Granular imager aperture would be light, possibly very large, and hence simultaneously quite flexible. The pointing issues of large flexible spacecraft cannot be addressed as if they were more traditional structures. The problem is difficult because a high control bandwidth is necessary for tight requirements, relative to the low frequency structural modes. One issue related to the momentum control of the Granular imager is that solar torques will be large because the surface is large and opaque, and the center of pressure to center of mass offset is also large. This can lead to substantial propellant requirements to maintain pointing. For very large reflectors, the propellant mass alone could be prohibitive.

In general, the control problem for gossamer spacecraft is multifaceted. There exist problems arising from shape errors originating in manufacturing errors,

fabrication errors, and errors deriving from dynamic noise and ageing. In terms of attitude control, as structures get larger, and more flexible, control-structure interaction becomes the dominant cause for possible instability. Translational control becomes necessary if the gossamer spacecraft must fly in a formation. Pointing control is very demanding when inflatable apertures are used in interferometric instruments. Momentum control becomes necessary to compensate for solar pressure disturbances. Shape control represents a challenge for maintenance of surface accuracy. Deployment control is advisable, since inflatable structures are tightly packaged with tendency to crease formation in the film material, which has an influence on the deployment trajectory.

Based on the Hubble Space Telescope test data, also used for the James Webb Telescope [Mosier1998, Mosier2000], the disturbance forces and torques can be modeled as consisting of discrete harmonics of the reaction wheel speed, f_{rwa} , with amplitudes proportional to the square of the wheel speed:

$$m(t) = \sum_{i=1}^n C_i f_{rwa}^2 \sin(2\pi h_i f_{rwa} t + \phi_i) \quad (38)$$

where $m(t)$ is the disturbance torque or force, C_i is an amplitude coefficient, h_i is the harmonic number, and ϕ is a random phase (uniform over $[0; 2\pi]$). Using this model, estimating the amplitude coefficient and the harmonic number is equivalent to determining the amplitude and frequency of each component as a function of wheel speed. The disturbances that can be measured are forces in the plane of the wheel (radial forces), force along the wheel's axis of rotation (axial force), and wobble torques (radial torques). Experimentally, torque about the axis of rotation (torque ripple and motor cogging) was found to be insignificant. With standard sensing equipment located on board the bus, i.e. three-axis accelerometers, gyro unit, and a global attitude determination system such as an on-board star tracker, both inertial position (in inertial coordinates), inertial attitude (with respect to the inertial reference frame, which is being propagated through ephemeris in the on-board computer) and their rates can be determined. Some estimation procedure is necessary when the full dynamic state cannot be measured. With this information, the nonlinear gyroscopic terms in the equations of motion can be cancelled from the equations. This cancellation results in a feedback linearized equation of motion in the direction of the controlled axes, namely we achieve near perfect state decoupling, and we can design the local controllers assuming independent control loops. The pointing control algorithms would rely on a feedback linearization of the dynamics to derive a globally, exponentially stable controller for the pointing dynamics. An attitude estimator on board the bus provides real-time estimates of the attitude quaternion and angular velocity. A command profiler specifies the command to be tracked, in the form of a constant or a step versus time. These commands are provided to the controller in the form of desired attitude, angular velocity, and angular acceleration. It is desired to cancel all possible dynamic nonlinearities arising from gyroscopic and

centrifugal terms, as derived from the equations of motion. The rotational control torque vector $\boldsymbol{\tau}$ is then of the following form

$$\boldsymbol{\tau} = \boldsymbol{\Gamma}_{pi} [\boldsymbol{\lambda}(\boldsymbol{\theta}_{err})_{Cmd} - \boldsymbol{\lambda}(\boldsymbol{\theta}_{err})_{Est}] + \boldsymbol{\Gamma}_{vi} ({}^N\boldsymbol{\omega}_{Cmd}^P - {}^N\boldsymbol{\omega}_{Est}^P) + \mathbf{J}_P {}^N\boldsymbol{\alpha}_{Cmd}^P + \mathbf{h}_{cancel} \quad (39)$$

where $\boldsymbol{\Gamma}_{pi}$ and $\boldsymbol{\Gamma}_{vi}$ are rotational control gain matrices, \mathbf{J}_P is the payload moment of inertia matrix, $\boldsymbol{\lambda}$ is the unit eigenaxis of rotation, $\boldsymbol{\theta}_{err}$ is the magnitude of rotation corresponding to the difference between the commanded ($(\cdot)_{Cmd}$) and the estimated ($(\cdot)_{Est}$) quaternion, \mathbf{h}_{cancel} is the vector of the centrifugal and Coriolis nonlinear terms to be cancelled, which can be obtained from the appropriate terms in the equation of motion, and ${}^N\boldsymbol{\omega}^P$ and ${}^N\boldsymbol{\alpha}^P$ are the angular velocity and acceleration vectors of the payload respectively. The desired control forces and torques are subsequently fed to the thruster selection logic and to the reaction wheel selection logic. The thruster selection logic features a nonlinear programming logic, which computes the desired on-time durations of all thrusters such that a weighted combination of force and torque errors (as differences between achievable and commanded) is minimized with the constraints of positive on-time. In a similar way, the torque command is distributed on the reaction wheels depending on their orientation in the spacecraft body frame.

9.3 Formation Control, Sensing, and Estimation

The Granular Imager Formation Control diagram is shown in Figure 131. The translation control actually implemented on the i -th spacecraft is of the form

$$\mathbf{f}_i = \mathbf{K}_p^i (\mathbf{q}_{Cmd}^i - \mathbf{q}_{Est}^i) + \mathbf{K}_v^i (\mathbf{v}_{Cmd}^i - \mathbf{v}_{Est}^i) + \mathbf{M}^i \mathbf{a}_{Cmd}^i \quad (40)$$

where \mathbf{K}_p^i and \mathbf{K}_v^i are translation control gain matrices, \mathbf{M}^i is the spacecraft mass matrix, \mathbf{q}_{Est}^i and \mathbf{q}_{Cmd}^i represent the estimated and commanded translation state, respectively. The rotational control instead is of the following form

$$\boldsymbol{\tau}_i = \boldsymbol{\Gamma}_{pi} (\boldsymbol{\lambda}(\boldsymbol{\theta}_{err})_{Cmd}^i - \boldsymbol{\lambda}(\boldsymbol{\theta}_{err})_{Est}^i) + \boldsymbol{\Gamma}_{vi} ({}^N\boldsymbol{\omega}_{Cmd}^i - {}^N\boldsymbol{\omega}_{Est}^i) + \mathbf{J}^i {}^N\boldsymbol{\alpha}_{Cmd}^i \quad (41)$$

where $\boldsymbol{\Gamma}_{pi}$ and $\boldsymbol{\Gamma}_{vi}$ are rotational control gain matrices, \mathbf{J}^i is the spacecraft moment of inertia matrix, $\boldsymbol{\lambda}$ is the eigenaxis of rotation, $\boldsymbol{\theta}_{err}$ is the magnitude of rotation corresponding to the difference between the commanded and the estimated quaternions, and ${}^N\boldsymbol{\omega}$ and ${}^N\boldsymbol{\alpha}$ are the angular velocity and acceleration respectively.

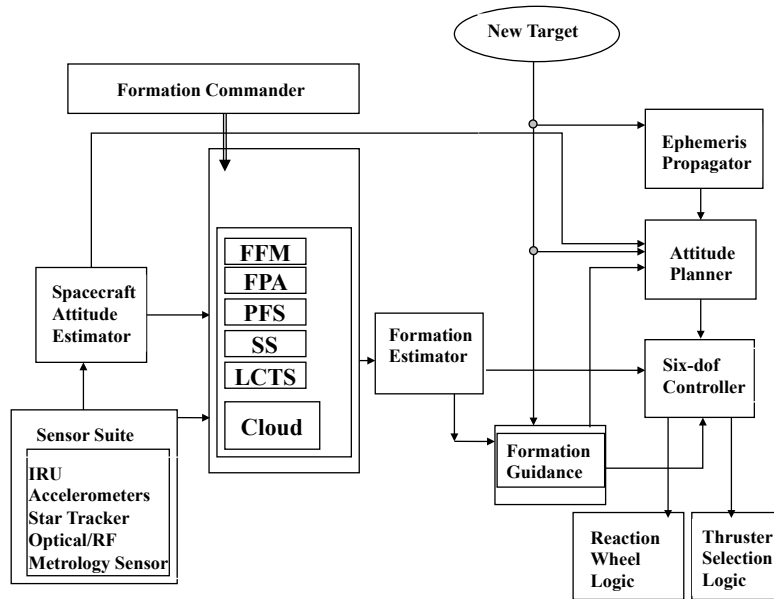


Figure 131. Proposed Formation Command & Control Functional Diagram.

Figure 132 shows a proposed architecture for the Granular Imager Formation Laser and RF Metrology Systems. The RF metrology subsystem collects from each formation element receiver data of range and phase, at each of 3 antennae, of signals from a transmitter on each other element. This is a set of 6 one-way links for each element pair. The 6 links provide an RF “truss” to determine the relative position and attitude of the two elements. Assuming that all the common errors in the system have been calibrated (or solved for) and attitude is known accurately from Attitude Estimation, each “truss” can be viewed as an independent measurement of the relative position of the two elements. Previous analysis has shown that the measurement accuracy can be characterized by independent range (along the LOS) and bearing (2 dof pointing normal to the LOS) errors. Simulation of the RF metrology subsystem can be carried out on two levels, simulating individual RF links as input to an extensive processing algorithm or simulating the outputs of the process, the equivalent “truss” measurements. The latter is more suitable for a higher level system functional simulation where the subsystem low level detail is not important.

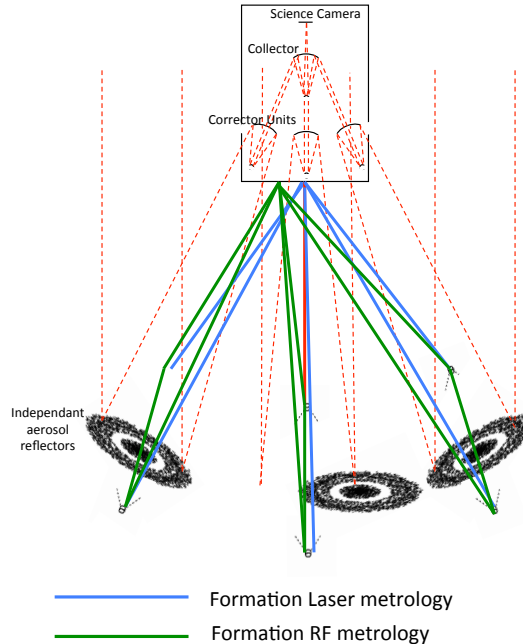


Figure 132. Proposed architecture for Formation Laser and RF Metrology Systems.

A proposed block diagram for the Granular Imager Formation Estimator is shown in Figure 133. An estimator of the formation relative state is needed both in simulations as well as in real life because the control of the formation rigidity demands an accurate acknowledge of the relative range and range rate between adjacent spacecraft. In this section we deal with the relative translation estimator only. The current implementation of the translation estimator estimates only the relative position and velocity of adjacent spacecraft. This implies that the measurements used depend only on relative position and are not correlated to other system variables such as the attitude estimates of the spacecraft, or the misalignments between various subsystems. This assumption is acceptable only as long as the effects of these secondary disturbances are small compared to the errors in the relative position measurements (e.g. attitude estimate error is much less than metrology bearing measurement uncertainty). The metrology measurements are also assumed to be independent and uncorrelated between measurements, which implies that any common factor within the metrology subsystem have been removed, by calibration or estimation, in the internal processing. The radio-frequency metrology subsystem collects from each formation element receiver data of range and phase, at each of three antennae, of signals from a transmitter to three receivers on each element. This represents six one-way links for each element pair. Thesesix links provide an RF “truss” to determine the relative position and attitude of the two elements. After measurement and estimation, the following input data is available to the Commander/Controller of the formation. For each spacecraft, we have: linear position, velocity, acceleration vectors, quaternions, angular velocity, angular acceleration vectors in relative bearing and bearing rate, relative range and range rate, all measured with respect to the vehicle’s body frame, the neighbor spacecraft body frame, and the inertial frame. The estimation of the attitude of each spacecraft

is decentralized. Star tracker and gyro measurements are each spacecraft are processed to give the spacecraft attitude relative to an inertial frame. Accelerometer and relative position measurements in the form of an RF metrology sensor are also available.

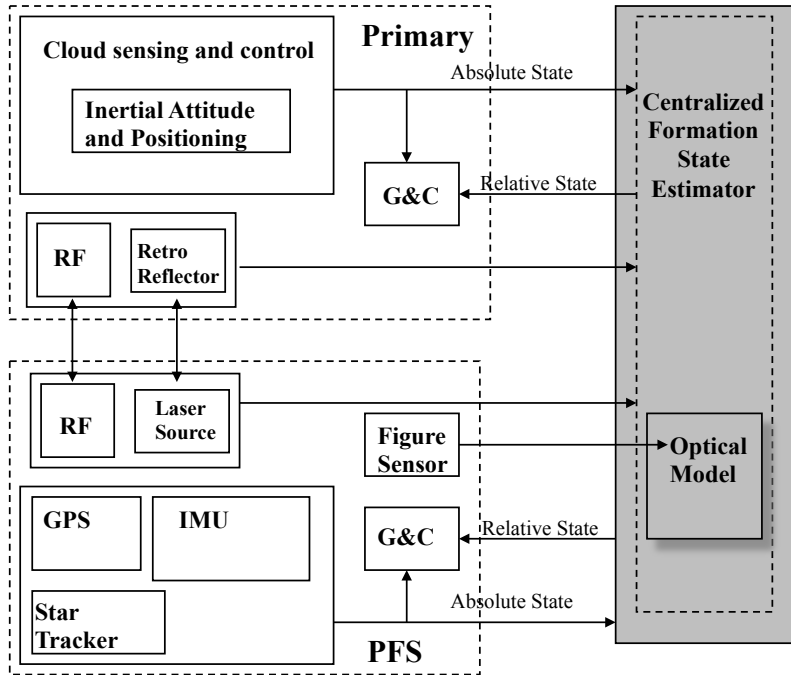


Figure 133. Proposed Formation Estimator

9.4 Granular Media/Molecular Dynamics Simulation Effort

Using the formulation described in Section 9.1, a molecular dynamics simulation effort was carried out. The problem is treated as a coupled set of semi-discrete differential equations for each grain. Given the position and velocity of each particle at one time step, the algorithm estimates these values at the next time step. To compute the next position of each particle requires the evaluation of the right hand side of its corresponding differential equation. Since each of these calculations is independent, there is a potential speedup if the program can take advantage of parallel computing. A Gaussian random process generator generates an initial distribution of grains. The “cloud” is placed in an orbit identified by the six classical orbital elements. The cloud is subject to gravitational harmonics from the Earth (JGM3 Earth gravity model, with 20 harmonic components). Currently, we are adding third-body disturbances from the Sun and the Moon, solar radiation pressure, and atmospheric drag. Figure 134 shows a couple of snapshots from the simulation of 1000 grains. Since there is no control, the cloud evaporates within a fraction of the orbital period. This simulation was used as the basis for modeling the levitated clouds

discussed in a later section, and also for the integrated model used for simulations in the radar band, discussed in Section 5.

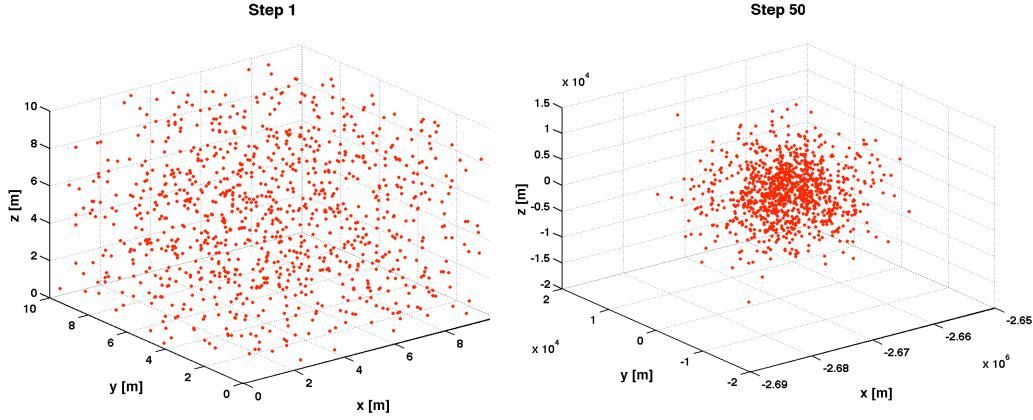


Figure 134. Snapshots of molecular dynamics simulation with $N=1000$.

9.5 Stochastic Guidance of Granular Medium using Optimal Transport

Optimal transport (OT) is an optimization approach that is used to find the optimum transference plan from an initial distribution μ to the desired distribution ν with respect to the given cost function [Villani2008]. OT has been previously used for the formation control of swarms of spacecraft [Bandyopadhyay2014]. Since the cloud of particles can be modeled as a distribution over the state space, OT is applicable for this problem. As shown in Fig. 135, the initial distribution of the swarm μ_0 is a uniform distribution over the state space. The desired distribution ν is a parabolic telescope shape. The objective of our control law is to drive the distribution of the particles to the desired distribution.

A further complication arises due to the fact that the particles do not have any onboard actuators, and external electric fields are used to control all the particles simultaneously. Moreover, the number of actuators are significantly smaller than the number of particles and the effect of the particles due to each actuator depends on the strength of the control input and the distance from the actuator. Therefore, the time-varying nature of the swarm distribution is given by:

$$\mu_{k+1} = \mu_k + \mathbf{f}_k(\mu_k)u_k, \quad \forall k \in \mathbb{N}, \quad (42)$$

where u_k is the control input at the k^{th} time instant and $f_k(\mu_k)$ is a deterministic linear function of μ_k . Therefore, the OP problem at the k^{th} time instant is given by:

$$\begin{aligned}
 & \min_{u_k} D_{L_1}(\mu_{k+1}, \nu) \\
 & \text{subject to } \mu_{k+1} = \mu_k + \mathbf{f}_k(\mu_k)u_k, \\
 & \mu_{k+1} \geq 0, \\
 & u_k \geq 0.
 \end{aligned}
 \tag{43}$$

Here D_{L_1} is the L_1 distance between the two distributions. The same OT problem is executed at each time step till the swarm satisfactorily converges to the desired distribution. Simulation results shown in Fig. 136 demonstrate that this OT-based approach indeed makes the swarm converge to the desired distribution.

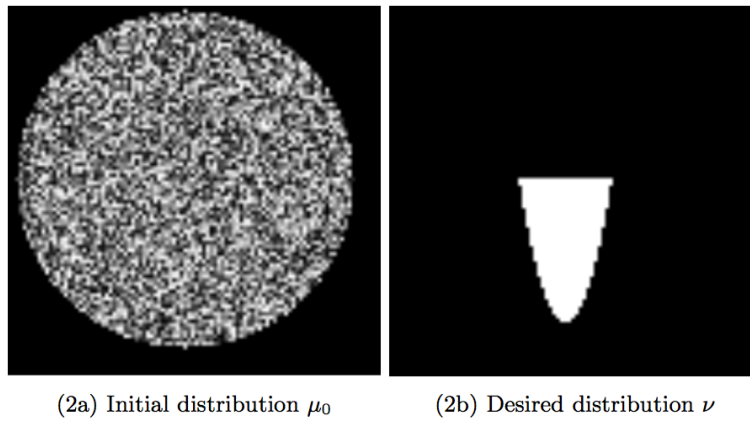


Figure 135. The inputs to the optimal transport optimization problem.

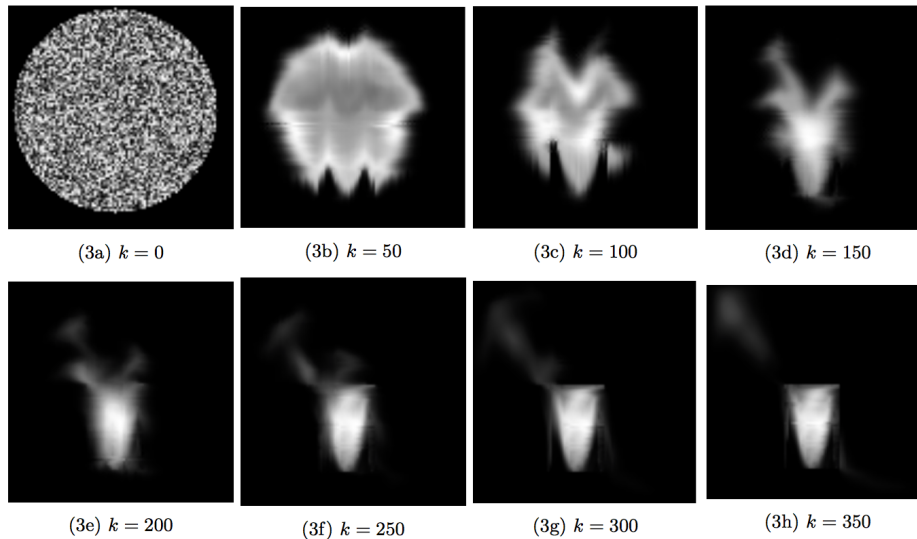


Figure 136. Evolution of the granular medium distribution under the optimal transport guidance policy.

10. Granular Medium Trapping and Confinement

We developed techniques for the modeling and simulation of trapped granular media, within the context of the Granular Imager project. After describing the physics of trapped granular media in space, we discussed the methodologies used to stably confine and shape such a medium using electromagnetic fields. The numerical models have also been validated with results in the literature, obtaining excellent agreement. The results of the numerical tests indicate that it is possible, with structural arrangements of rings and plates at different levels of electrostatic potential, to stably confine one or more charged particles, when driven by voltages that can be modulated in time and space.

10.1 Trapping and Confinement Techniques

We have been exploring options for trapping and confinement based on techniques being used to contain and levitate atmospheric aerosols (clouds of ice crystals) in ground laboratories. Some of these include aerodynamic levitation, acoustic levitation, optical levitation, electric levitation, magnetic levitation, radio-frequency levitation and superconducting levitation. The most promising techniques are based on electro-dynamic trapping using electrodynamic balances [Major2005], [Davis2012]. There are different possibilities that are relevant to the Orbiting Rainbows task (i.e., levitation in vacuum). Some of these options are shown in Figure 137, taken from [Davis2012]. These are:

- Electrodynamics levitation: Small particles can be confined by electrodes in an electrostatic trap (Penning trap). A Paul trap includes a lateral magnetic confinement field, which adds stability. A major issue in levitation is particle stability, and stability requires that the suspended object have forces exerted on it, which return it to its initial position when it is slightly displaced from that position.
- Parallel plate capacitor. Since the parallel plate Millikan condenser cannot exert a restoring force on a charged droplet in either vertical or horizontal directions, the particle drifts.
- Electrostatic balances. Although the electrostatic balance of Millikan does not provide stable suspension, the use of electro-optic feedback control allows for a weak restoring force in virtue of the electrode shape.
- Electrodynamic balances. By inserting a ring electrode at the center plane between the plates of a Millikan condenser and by applying an AC potential to the ring electrode, the charged particle can be focused at the center of the balance.
- Lorentz coupling with the planetary magnetic field, assuming that the grain is electrically charged.
- Optical levitation. In a three-dimensional gradient-force optical trap for microscopic dielectric particles was demonstrated in 1986. They showed that low-absorbing, dielectric spherical particles with an index of refraction higher than that of a surrounding liquid could be trapped in three dimensions by use of

a strongly focused Gaussian laser beam. This phenomenon was suggested earlier for moving atoms and more recently has led to biomedical and related applications involving micromanipulation of living cells, chromosomes, and motor proteins. However, the conventional gradient-force trap based on the design of Ashkin [Ashkin1970] has some limitations. Trapped particles are susceptible to optical damage by absorptive heating because the center of the trap is located in the high-intensity focal region of the beam. Another limitation is that multiple particles may be attracted into the same trap; thus isolating a single particle requires dilute samples. Furthermore, the trapping of low-index particles such as bubbles and droplets or of absorbing particles such as metallic fragments requires a rotating beam when a conventional gradient-force trap is used. There are probably other options, involving multi-physics coupling at different levels.

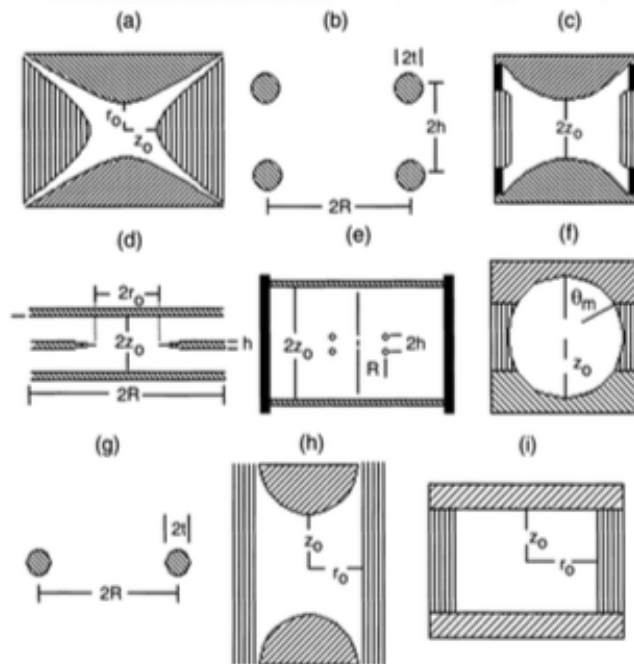


Figure 137. Various types of electrodynamic traps (from [Davis2012])

Two or more atoms stripped of their outer electrons, trapped by electric fields array themselves in structures that behave like both liquids and solids. The possibility of achieving a regular structure of a plasma and the ability of this plasma to be controlled remotely by the direct control of electric and magnetic fields lead us to the concrete realization of an adaptive and re-configurable lens.

Employing the control over the temperature and position of ions (atoms stripped of one or more of their electrons) it is possible to obtain a particular state of matter called microplasma by extension from the large groups of ions and electrons known as plasmas. A microplasma is made by applying electric fields in order to confine a

certain amount of ions in a specified region of space. Consequently a cooling process called laser cooling cools the ions near to zero kelvin. The final temperature is related to the behavior of the ions as a whole entity. As it is explained below, the lower is the temperature, the more solid-like the behavior of the plasma will be. Microplasmas can serve as models for the dense plasmas in stellar objects. Like the atoms in liquids, the ions in some cold microplasmas can diffuse through a somewhat ordered state. In other cases, the ions can resemble the atoms in solids, diffusing very slowly through a crystal lattice. The nature of microplasmas is quite different from that of conventional liquids and solids. Whereas common liquids and solids have densities of about 10^{23} atoms per cubic centimeter, microplasmas have concentrations of about 10^8 ions per cubic centimeter. Furthermore, whereas internal attractive forces between the atoms hold conventional liquids or solids together, external electric fields hold the trapped ion microplasmas together. Indeed, the ions, which all have the same charge, actually repel each other and tend to disperse the microplasma.

The specific heat, melting point and other thermodynamic properties of a one-component plasma depend greatly on the density and the temperature of the mobile particles; This explains why the electromagnetic confinement is essential in order to obtain and manipulate the physical properties of a one-component plasma. The dimensionless parameter, which expresses the structural behavior of the plasma is called the coupling. It can be derived from the temperature and the particle density, and it provides a measure of how strongly the neighboring ions interact. The coupling is defined as the Coulomb potential energy between nearest neighboring ions divided by the kinetic energy of the ions:

$$Coupling = \frac{V_{C_{ij}}}{E_{K_i}} \quad (44)$$

The Coulomb potential energy V_C depends on both the average distance between the ions (a function of density) and the charge of the ion species

$$V_{C_{ij}} = \frac{1}{4\pi\epsilon_0} \frac{q_i q_j}{|r_{ij}|} \quad (45)$$

in which q_i and q_j are multiple of the elementary charge (the smallest conventional charge) $e = 1.602 \times 10^{-19}C$. The kinetic energy E_K is simply the temperature (T) multiplied by a physical constant known as the Boltzmann constant $K_B = 1.3806 \times 10^{-23}m^2kg^{-1}s^{-2}K^{-1}$

$$E_K = T K_B$$

(46)

Hence the value of the coupling parameter describes the global behavior of this particular plasma (Table 9). When the Coulomb potential energy is less than the kinetic energy (Coupling < 1) the one-component plasma should have no obvious structure and should behave like a gas. But a one-component plasma whose coupling is greater than one (Coupling > 1) should show some spatial order. In such strongly coupled one-component plasmas, the ions should stay away from each other because the repulsive Coulomb forces are greater than the thermal forces. At couplings of two or more, a plasma should exhibit liquid behavior. At Coupling ≈ 180 , a one-component plasma should change from a liquid to a solid phase, in which the ions are arranged in a body-centered cubic crystal.

The predictions are valid as long as the ions in the plasma behave classically and the number of ions is sufficiently high (for one-component plasmas the theory pertains “infinite” systems), that is, as long as the effects of quantum mechanics can be neglected. Under conditions of high density and low temperature, quantum mechanics can be important.

Table 9, Different behaviors of component plasma depending on the coupling value.

Coupling value	Physical characteristics
$C < 1$	<i>Gas</i>
$C > 1$	<i>Gas-Liquid transition</i>
$C > 2$	<i>Liquid</i>
$C > 180$	<i>Solid lattice</i>

Table 10. Values of the distance within the ions in order to obtain a given structural behavior.

Coupling value	Value of r	Physical characteristics
$C < 1$	$r > 2.1709 \times 10^2 m$	<i>Gas</i>
$C > 1$	$r < 2.1709 \times 10^2 m$	<i>Gas-Liquid transition</i>
$C > 2$	$r < 1.0854 \times 10^2 m$	<i>Liquid</i>
$C > 180$	$r < 1.2061 m$	<i>Solid lattice</i>

Let us consider a one-component plasma made of dissipative particles in a controlled outer space environment. These particles behave like ions once they are hit by space radiations. The hypotheses are $T_{eq} = 300K$, $Q = 10-14C$, hence we obtain

$$E_K = T K_B = 4.14 \times 10^{-21} J$$

$$V_{C_{ij}} = \frac{1}{4\pi\epsilon_0} \frac{q_i q_j}{|r_{ij}|} = \frac{1}{r} 8.9877 \times 10^{-19} J$$

$$Coupling = \frac{V_{C_i}}{E_{K_i}} = \frac{1}{r} 2.1709 \times 10^2$$

(47)

in which r could be considered an evaluation variable in order to obtain all the possible plasma structures. Hence we can achieve a different global behavior simply by varying the average distance that separates ions (Table 10). One method is the electrode active-control that acts on the VC parameter by varying the electromagnetic field intensity, otherwise the other parameter we can change is the temperature (EK) by heating or cooling the one-component plasma.

Because the thermodynamic properties of a one-component plasma depend only on the coupling, a one- component plasma that is cool and diffuse can have the same properties as a one-component plasma that is hot and dense.

The configuration of the Paul trap and the Penning trap are the same; they both consist of a cylindrical symmetrical structure composed by three electrodes. one is ring electrode and the other two are end-cap electrodes. The difference between the two type of trap regards the nature of the inside fields.

In the Paul trap there is a combination of DC and radio-frequency voltages applied to the electrodes. The equations of motion of an ion inside the this type of trap are Mathieu differential equations, which lead to both stable and unstable solutions depending on the operating parameters. By controlling these parameter, ions of a desired m/e range can be confined, other ions which are intrinsically unstable or have large amplitudes collide with the trap or are lost. All the traps here described are used to confine any charged particle, so we refer to these charges calling them ions.

The Penning trap uses an axial magnetic field and in addition an electric field with both the end-cap electrodes at positive potential (for positive ions/charges) with respect to the ring electrode. The associated radial electric field is repulsive and tends to push ions out of the trap. It is the axial magnetic field which forces the ions into stable epicyclic trajectories resulting in their confinement.

10.1.1 Paul Trap

We will now provide a conceptual explanation of how and why the Paul trap works. In order to understand the operation of Paul trap we firstly start considering the ion motion in a two- dimensional quadrupole device and then extend the concept to a three-dimensional quadrupole field which is the basic form of Paul trap concept. It is also useful to consider firstly the form of the electromagnetic potential of the quadrupole field and then move to the single ion motion in the two-dimensional and three- dimensional field.

In three-dimensional space the quadrupole field potential is given by

$$\phi = \frac{\phi_0}{2r_0^2}(\lambda x^2 + \sigma y^2 + \gamma z^2) \tag{48}$$

where ϕ_0 is an externally applied electric potential, λ, σ, γ , are constants that depend on the nature of the field, and r_0 depends on the physical structure of the field. To satisfy the Laplace equation we write

$$\nabla^2 \phi = \frac{\phi_0}{2r_0^2} (2\lambda + 2\sigma + 2\gamma) = 0 \quad (49)$$

In the two-dimensional quadrupole field (Fig.138) the coordinate $z = 0$. In the specific case of constants equal to 1, the potential equation is a function of x and y assumes the following form:

$$\phi(x, y) = \phi_0 \frac{(x^2 - y^2)}{r_0^2} \quad (50)$$

This is possible if the potentials on the surfaces of the four rods are

$$\phi(x, y, t) = (U - V \cos \Omega t) \frac{(x^2 - y^2)}{2r_0^2} \quad (51)$$

The result is that the equations of motion of a charged particle characterized by a given m/e are

$$\begin{aligned} \ddot{x} + \frac{e}{mr_0^2} (U - V \cos \Omega t) x &= 0 \\ \ddot{y} + \frac{e}{mr_0^2} (U - V \cos \Omega t) y &= 0 \\ \ddot{z} &= 0 \end{aligned} \quad (52)$$

In this case, the particle will move along z -axis with constant velocity due to 2D simplifications. Introducing the following substitutions

$$\begin{aligned} \frac{4Ue}{mr_0^2 \Omega^2} &= a \\ \frac{2Ve}{mr_0^2 \Omega^2} &= q \\ \Omega t &= 2\zeta \end{aligned} \quad (53)$$

the equations along x-axis and y-axis become

$$\begin{aligned} \frac{d^2x}{d\zeta^2} + (a - 2q \cos 2\zeta)x &= 0 \\ \frac{d^2y}{d\zeta^2} - (a - 2q \cos 2\zeta)y &= 0 \end{aligned} \tag{54}$$

that are the so called Mathieu differential equations for x and y. Depending on the parameters a and q the Mathieu equation has stable or unstable solutions. The symmetry properties along a-axis (Fig.139) means that if a stable solution is found for a couple of a,q then the same stable solution must be found for the couple a, 160q. In order to achieve a stable motion of the ion both solutions of the two Mathieu equations must be stable, so if we compute the results we can define the stability values for the parameters a and q, and then x and y. In three-dimensional space the quadrupole field potential is given by

$$\phi = \frac{\phi_0}{2r_0^2}(\lambda x^2 + \sigma y^2 + \gamma z^2) \tag{55}$$

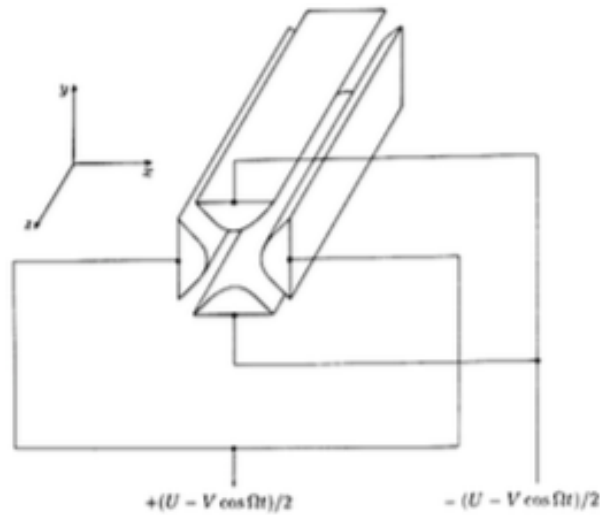


Figure 138. Electrode structure of a 3D quadrupole field.

In the symmetric geometry case, the potential has the form

nce the potential has the f

$$\phi = \phi_0 \left(\frac{x^2 + y^2 - 2z^2}{2r_0^2} \right) \quad (56)$$

and leads to the following equation of motion:

$$\begin{aligned} \frac{d^2 r}{dt^2} + \frac{e}{mr_0^2} (U - V \cos \Omega t) r &= 0 \\ \frac{d^2 z}{dt^2} + \frac{e}{mr_0^2} (U - V \cos \Omega t) z &= 0 \end{aligned} \quad (57)$$

Introducing the following substitutions

$$\begin{aligned} \frac{8Ue}{mr_0^2 \Omega^2} &= a_z = -2a_r \\ \frac{4Ve}{mr_0^2 \Omega^2} &= q_z = -2q_r \\ \Omega t &= 2\zeta \end{aligned} \quad (58)$$

the Mathieu equations become

$$\begin{aligned} \frac{d^2 r}{d\zeta^2} + (a_r - 2q_r \cos(2\zeta)) r(\zeta) &= 0 \\ \frac{d^2 z}{d\zeta^2} - (a_z - 2q_z \cos(2\zeta)) z(\zeta) &= 0 \end{aligned} \quad (59)$$

Some typical Paul trap trajectories are shown in Figure 140. One can notice a high-frequency micro-motion and a secular low-frequency motion.

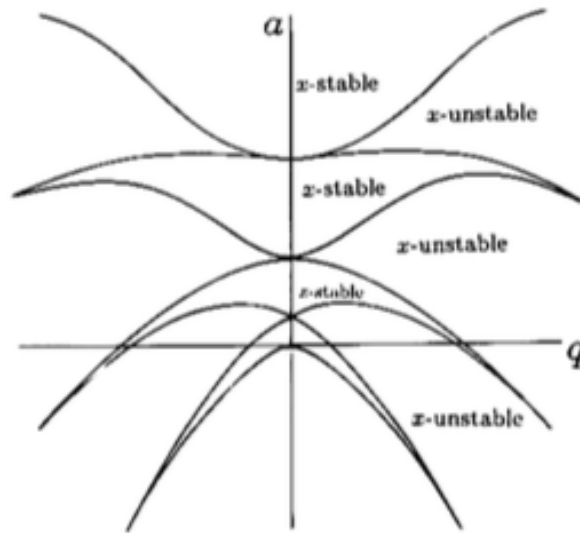


Figure 139. Stability diagram for Mathieu equation.

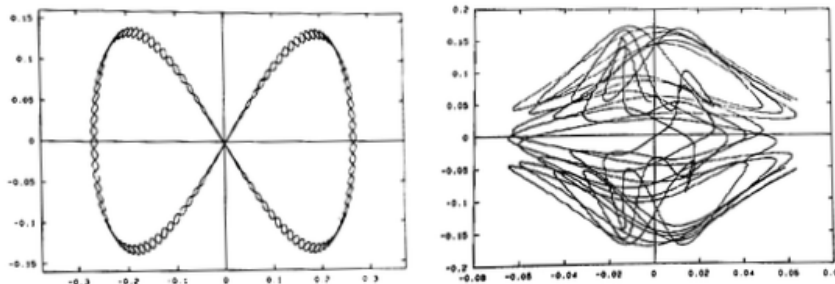


Figure 140. Typical trajectories in Paul trap (from [Gosh1995]).

10.1.2 Penning Trap

The structure of this trap is identical to the previous one: three electrodes, two end-caps and one ring electrode. What that makes this trap different from the Paul trap is that this doesn't use the radio-frequency field, but it uses a uniform magnetic field along z -axis. The end-caps electrodes have positive charge if the ions confined are positive. The main effect of the electric field is the shift of the ions toward the center of the trap; the force that acts toward the ion is proportional to the displacement of the ion in respect of the origin. This interaction results in harmonic oscillations of the ion along the axial direction. Due to the repulsive electric field along x - and y -direction the ion tends to be pushed out from the trap in the radial direction. As soon as the motion of the ion takes the radial direction, due to the presence of the magnetic field, it is turned back along a cyclotron-type orbit. Studying the overall motion of the particle we can assume that the main motion is given by the harmonic

component along the z-axis and the other two components of motion given by the cyclotron and magnetron drift motion (caused by the crossing of electric and magnetic field $E \rightarrow B$) again along z-axis. The result is a precessional motion in the equatorial plane around the z-axis.

The motion of an ion in a Penning trap is induced by the combination of the magnetic and electric field. For a constant electromagnetic field the vector potential A and the scalar potential can be chosen for a constant electric field as

$$\begin{aligned} A &= 0 \\ \phi &= \phi \end{aligned} \tag{60}$$

and for a constant magnetic field

$$\begin{aligned} A &= \frac{1}{2}B \times r \\ \phi &= 0 \end{aligned} \tag{61}$$

For a mass m of the particle we obtain the Lagrangian

$$\begin{aligned} L &= \frac{m}{2}\dot{r}^2 + \frac{e}{2c}[r, r, B] - e\dot{\phi} + \int dV L_0 \\ &= \frac{m}{2}(\dot{x}^2 + \dot{y}^2 + \dot{z}^2) + \frac{eB}{2c}(xy - yx) - e\dot{\phi} + \int dV L_0 \end{aligned} \tag{62}$$

where

$$\phi = \frac{U}{2z_0^2 + r_0^2}(-x^2 - y^2 + 2z^2) \tag{63}$$

and B points toward the positive direction of z-axis. The $dV L_0$ term is the field-free Lagrangian and can be neglected. Applying the Euler-Lagrange equation, we obtain the equations of motion:

$$\begin{aligned} \ddot{x} &= \omega_c \dot{y} + \frac{1}{2}\omega_{0z}^2 x \\ \ddot{y} &= -\omega_c \dot{x} + \frac{1}{2}\omega_{0z}^2 y \\ \ddot{z} &= -\omega_{0z}^2 z \end{aligned} \tag{64}$$

where we can define the axial frequency as

$$\omega_{0z} = \sqrt{\frac{4eU}{m(2z_0^2 + r_0^2)}} \quad (65)$$

and the cyclotron frequency as

$$\omega_c = \frac{eB}{mc} \quad (66)$$

As said above the motion of each ion for this type of trap is the result of three different motions: axial, cyclotron motion and magnetron motion. These three motions are uncoupled and completely independent. Figure 141 shows a typical trajectory of a particle inside a Penning trap.

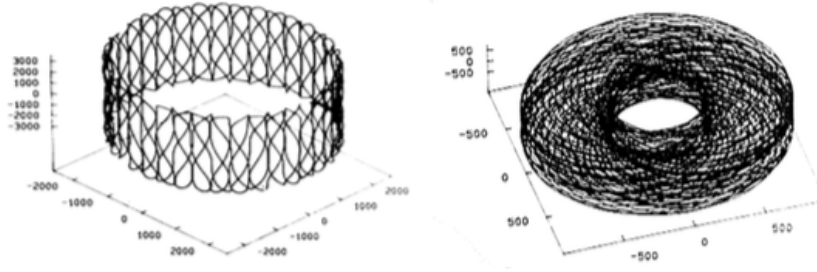


Figure 141. Typical trajectories in Penning trap (from [Gosh1995]).

10.1.3 Trapping simulations with rings and plates

In the following, we analyze the two-dimensional and three-dimensional electrostatic stability of the cloud of granular matter, floated between the electrode rings.

The two-dimensional geometry is a simplified trap model that is not sensitive to the stability problems due to the fact that it ignores the Earnshaw's theorem. Despite it doesn't have a strong correspondence to the real behavior of the charges/ions, it is still useful to understand how and why the charge moves along a given trajectory and what we can do to influence it.

The geometry (Fig.142) consists of two electrodes, one ring and one plate, positioned along the symmetry axis (x-axis) and other two electrodes positioned

symmetrically with respect to the x-axis. The ring and the plate provide the constant electric field (DC) and the two others provide the radio frequency (RF). Due to the two-dimensional analysis the ring is substituted by two dimensionless charges of the same value, so they generate a radial electric field named E21 and E22. The plate is positioned in the origin (O) of the reference system and it generates an uniform electric field E1 acting only along the in x-axis. The other two electrodes generate also an uniform and constant electric field (Variable EF) along the y-axis. In each couple of coordinate x-y it is possible to define the local electric field direction and magnitude by summing all the local contributes from each electrode. The model assumptions are that the ring is substituted by two dimensionless charges of the same value, that the plate generates a uniform and constant electric field along the x-axis, and that all the edge effects are neglected. The three-dimensional geometry is a result of several improving steps that has been carried on during the trap design. The first tested trap was the two-dimensional one in which a z-axis was added. Working in a three-dimensional volume we decided to decouple the equations of motion organizing them in order to describe the resultant accelerations along each axis separately. The fixed points found in this configuration result to be unstable, so we decided to change it using firstly just two rings and then the classic Paul trap configuration with two flat electrodes and one ring in the middle.

Next, we summarize the design changes that have been made during the development:

- The first geometry correspond to a three-dimensional version of the two-dimensional design: it has a single fixed point located between the two electrodes. The fixed point coordinate depend on the charge value of both the ring and the plate; in this case we have it at $x \sim 0.25$ (see Fig. (143)) where the sum of each electric field sources is zero. This fixed point is characterized by an unstable equilibrium: in fact while the x-components are null in this particular coordinate, the y- and z-components are not zero and tend to repulse the charge toward radial direction.
- The second design is represented by two concentric ring electrodes positioned along the x-axis (Fig.(144)). Initially the tests were conducted using two rings with the same size but the only things that follows the size change is the electric field pattern and not the nature of the fixed point(s) stability. Having two identical electrodes both of them positively and equally charged the fixed point is located between them along the x-axis. Focusing on the electric field magnitude close to the center of the rings is well understood why the fixed point in the middle of the trap is unstable: the mutual influence between the two electrodes creates an y-z plane at a certain x-coordinate ($x = 0.25$) in which all the forces and accelerations are null. Even though the charged particle in this particular x-coordinate lacks motion in the x-component, it has acceleration components that make the particle leave the trap along a trajectory that lies on the y-z plane (Fig.144). By using an additional RF to overcome the Earnshaw's theorem it is possible to establish a dynamic stability similar to the one expressed by Mathieu equation, so this opportunity opens to new point of view regarding ion trapping. Focusing on the main purpose of this examination this design allows the

development and control of optic devices due to the lack of plates in the light trajectory.

- The third design is more similar to a regular electromagnetic trap. The introduction of a third electrode solves the stability problem recreating the same dynamics of a Paul trap. This trap is made by two end-caps electrodes or plates which can be shaped in order to obtain a particular electric field distribution, and a ring similar to what we used for the previous designs (Fig.(145)). This design is sensitive to the instability described by Earnshaw's theorem and its electric fields are controlled in the same way a regular trap is driven. The fixed point(s) is in this case kept successfully stable by a driven radio frequency (RF) and the position of this fixed point(s) can be changed by varying the electrodes parameters (gains, voltages, shape...). In Figure 145 the stable or unstable location of the fixed point(s) lies on the y-z plane. This marked customization lead us to the achievement of multiple cloud shapes in order to fit different purposes.

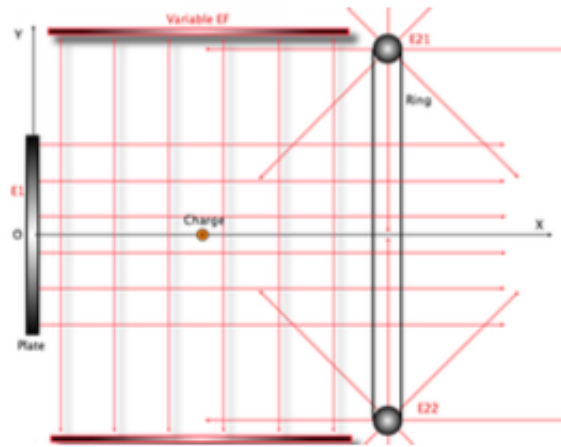


Figure 142. Two dimensional electrode geometry.

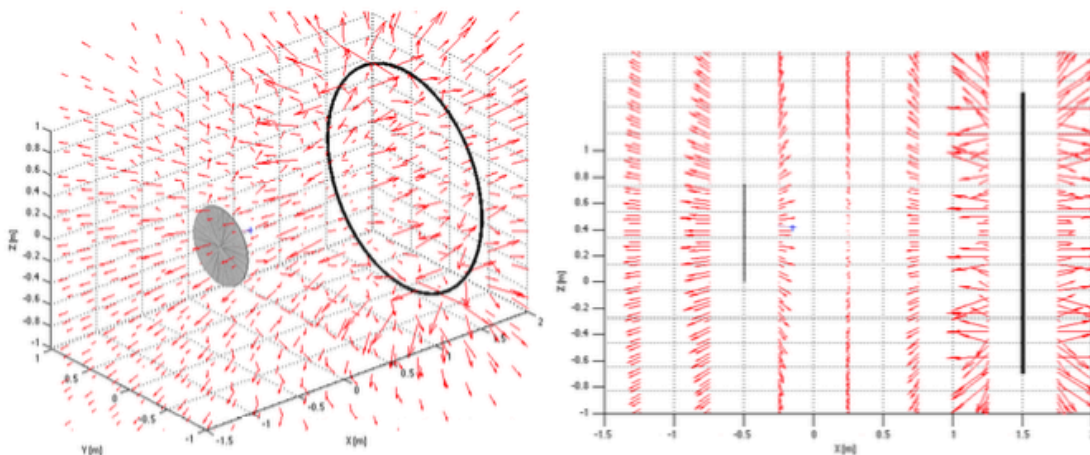


Figure 143. 3D geometry, case 1.

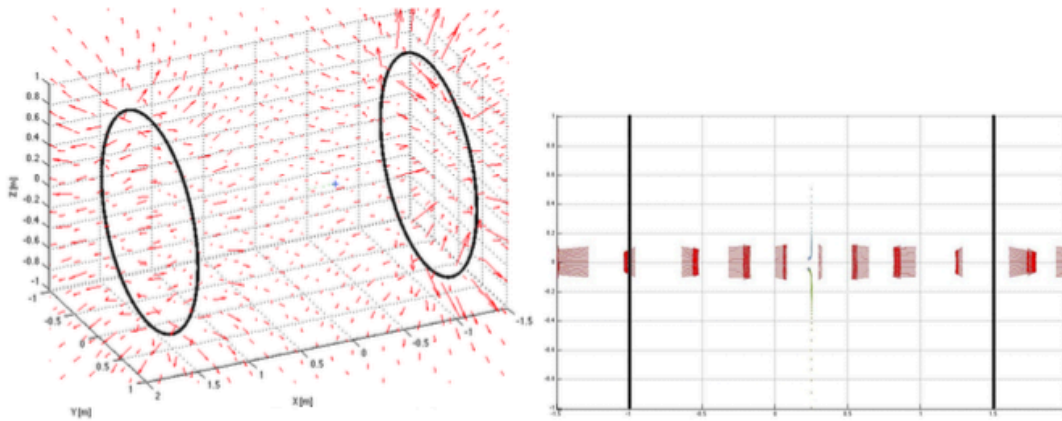


Figure 144. 3D geometry, case 2.

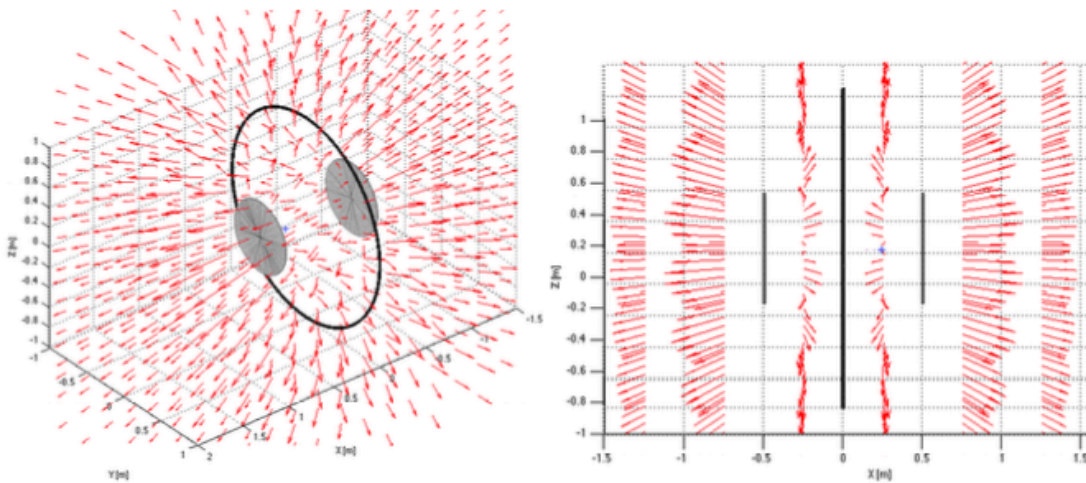


Figure 145. 3D geometry, case 3.

Configuration with two electrodes: one ring and one plate

Multiple tests confirm that the configuration with a plate and a ring tends to be unstable and the ions escape the trap. All the electric forces are in the same direction because there is no null force spot along the x-axis. The maximum electric field that comes from the ring is still lower than the one that comes from the plate, therefore there is no stability.

Configuration with two electrodes: two rings

This configuration gives a good stability margin when the RF is appropriately applied. Having two rings guarantees the location of the fixed point in the center of the trap if they have the same electrostatic charge. In Fig. 146, and Fig. 147 as well, we have two ring positioned respectively at $x = -1\text{m}$ and $x = 1\text{m}$, so the fixed point where the two potentials match and erase each other is on the center of the trap in $x = 0\text{m}$.

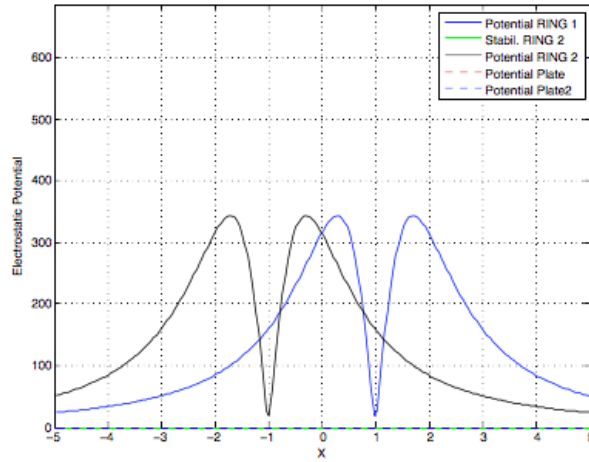


Figure 146. Electrostatic potential along x-axis. The two rings are at $x=-1\text{m}$ and $x=+1\text{m}$.

In order to maintain the charge in the center of the trap it is necessary to set the right parameters. If the conditions are not respected all the ions will leave the trap after a certain period (Fig.147) dependent on the potential value and the charge magnitude of the particle. The evolution of the x-, y-, z-components is reported in Figure 147 and shows how rapidly two of the three charges leave the trap increasing their velocity.

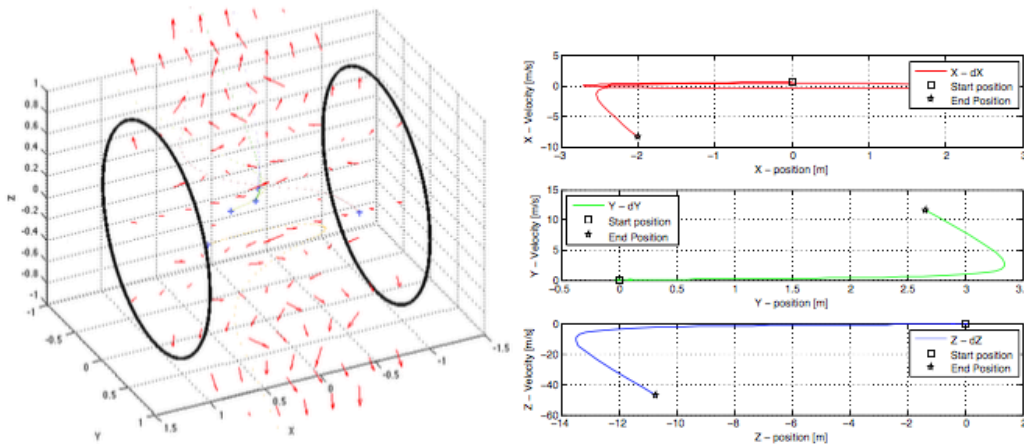


Figure 147. Two ring configuration, and components of particle position vs time.

A second simulation reports the trapping of three ions using the two-ring configuration. The resultant trajectories, as we will see, are similar to the ones

obtained with the Mathieu model and they can be easily controlled by change the ring parameters and the RF. The parameters used in the following simulation are described in Table 11. The result is shown in Figure 148 where all the particles tend slowly ($C = 0.1$) to reach the fixed point in the center of the trap. The phase planes are shown in Figure 148 and are again comparable with the Mathieu mathematical model. We can recognize two main frequencies: a high-frequency micro-motion and a secular low-frequency motion as the trapping theory predict. Sometimes the evolution in time is not perfectly regular due to the interference with the motion of the other particles. The Phase diagrams for the two given particles demonstrate the capability of the trap to maintain low average velocities and bounded x -, y -, z -positions.

Table 11. Simulation parameters for case with two rings, and case with one ring and two plates.

Description	Two-rings	One ring two plates 1	One ring two plates 2
Ring diameter [m]	2	2	2
Number of particles	3	3	5
Ring-plate distance [m]	2	-	-
Ring half thickness (radius) [m]	0.01	0.01	0.01
Plate 1 position [m]	-	[-0.25,0,0]	[-0.25,0,0]
Plate 2 position [m]	-	[+0.25,0,0]	[+0.25,0,0]
Ring position [m]	-	[0,0,1]	[0,0,1]
Hemispherical electrode radius 1 [m]	-	1	1
Hemispherical electrode radius 2 [m]	-	1	1
Plate 1 diameter [m]	-	0.7	0.7
Plate 2 diameter [m]	-	0.7	0.7
Plate charge [C]	3e-7	-	-
Plate 1 charge [C]	-	1e-7	1e-10
Plate 2 charge [C]	-	1e-7	1e-10
Ring 1 charge [C]	1e-7	1.5e-7	1e-7
Ring 2 charge [C]	1e-7	-	-
Particle charge [C]	1e-13	1e-13	1e-13
Particle mass kg]	1e-13	1e-13	1e-13
Main ring DC gain	0.1	0	0
Optional ring DC gain	0.1	0	0
Stabilizer ring DC gain	0	0.1	0.1
Plate 1 DC gain	0	0.1	0.1
Plate 2 DC gain	0	0.1	0.1
Frequency of ring RF voltage [rad/s]	65	35	35
Frequency of plate 1 RF voltage [rad/s]	0	35	39
Frequency of plate 2 RF voltage [rad/s]	0	35	39
Amplitude of ring RF voltage	1.75	0.75	0.75
Damping constant	0.1	10	0.1
Plasma temperature [K]	300	300	300

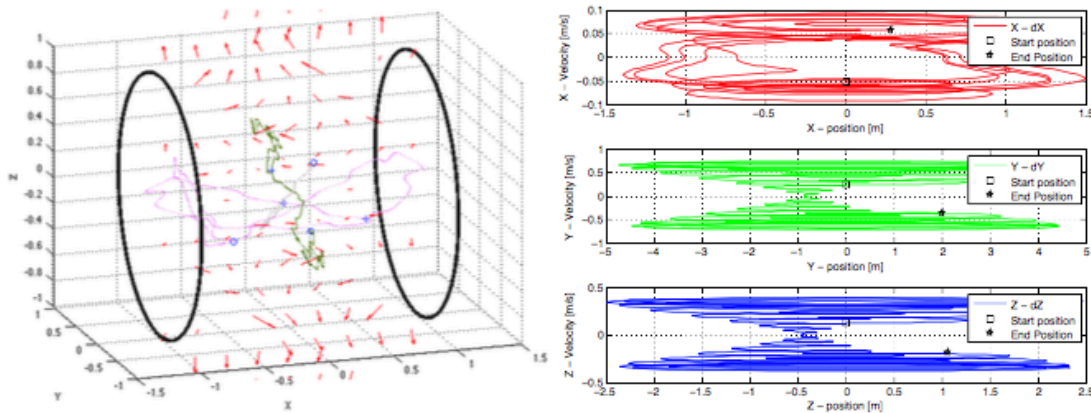


Figure 148. Trapped particle trajectories in two-ring configuration, and phase plane.

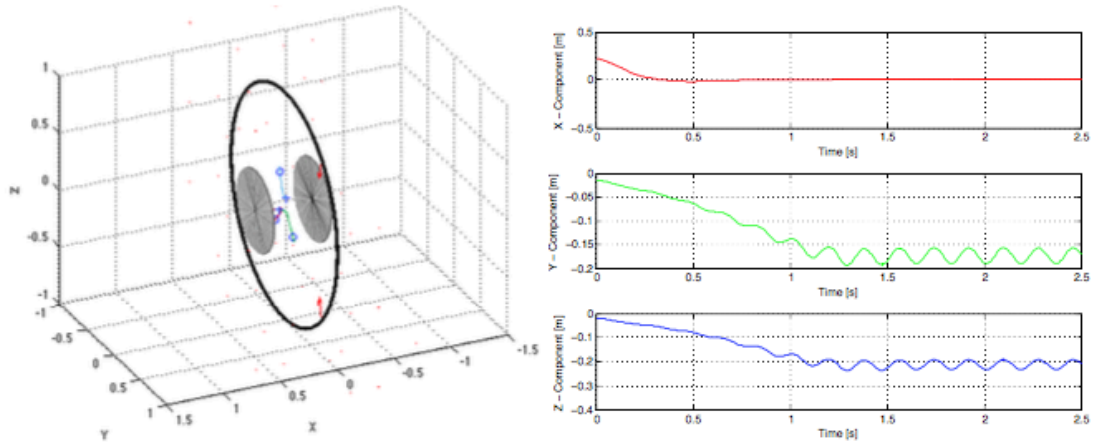


Figure 149. Paul trap configuration, and trajectory vs. time.

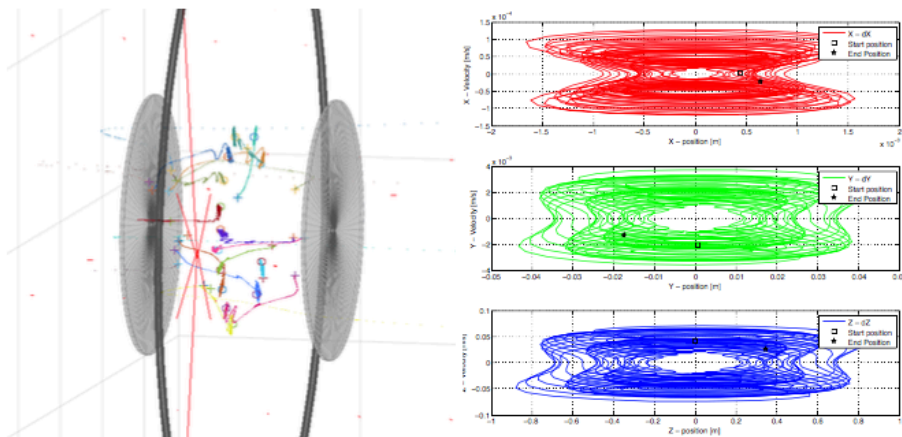


Figure 150. Close-up of confined particle trajectories, and phase plane.

Configuration with three electrodes: one ring, two plates (first parameter set)

The following configuration is similar to a classic Paul trap. The electrodes are set as hemispherical (see Table 11) and for certain conditions and parameters we can achieve different shapes of the final arrangement of the particles. Using specific conditions it is possible to achieve different particle distributions: two tests have been carried out using the settings reported in Table 11.

These settings lead to a final stable annulus pattern where the single particles keep moving just along the y- and z-axis in a limit cycle while their x-coordinate is constantly $x = 0$. For a better explanation can be useful to observe the phase plane

figures 149, where one can notice the quick response of the x-component that reach the equilibrium position with few oscillations, while a limit cycle is established along the other two axes. A better view is given by the figure 149 which shows in particular the frequency of the two cycles. More simulation results have been obtained getting the same results; when the number of particle rises it is more clear the final annulus shape as the figure 149 shows.

Configuration with three electrodes: one ring, two plates (second parameter set)

Changing some key parameters (see Table 11) it is possible to achieve the classic Paul trap ions trajectories, an example is shown in the figure 150. The final position of the ions in this case form a cusp-like shape that can be modified by varying parameters such RF or electrodes charge values. All the ions are trapped and tend to reach the fixed point at the center of the trap if there was no damping all the particles would move close to the fixed point achieving a dynamic equilibrium. Studying one of these trapped particles it is possible to notice again two frequency components on the trajectory (Fig 150), the high frequency micro-motion and the low-frequency motion. Looking at the phase diagrams the motion is well bounded and both velocity and position tend slowly to reach the designed position.

Example of particle trapped by fans

The next example is related to a first attempt to trap particles in an environment without gravity subjected to an initial random velocity. In order to do that six fans have been used, two per every direction and the particle whose behavior is under investigation is a sphere. The simulation tool called Chrono::Engine⁴ was used. In this case, even if the goal of the present work is to trap particles throughout electromagnetic force fields, they have been used fans since as a first attempt "rough" wind forces has been considered. One of those is present in one of the tutorial on projectchrono.org and explain well how to manage rotations and force field in Chrono::Engine. The force applied to each body is function of their velocity v_i and of two constants, the speed of the wind v_w and the density of the mean ρ .

$$F = (v_w - v_i) \rho \tag{67}$$

In the Chrono simulator, these forces can be treated as functions acting on the bodies, depending on their states. The most interesting things to notice in previous figures are that the particle reaches a steady-state condition, and in particular, the particle is stopped and fixed in the space by the force field. In one simulation set with 20 particles, with the same module for initial velocities and angular velocities, but different origin in the space, the same behavior is shown in Fig. 151. Considering

⁴ www.projectchrono.org

almost the same starting point for every simulation, it is interesting to analyze the distance covered by the particle before it is stopped by the force field. The most important parameter is Δ position, and it indicates how much space is needed to the force field generated by the fans to stop the particle movement. If one looks at the "Time Vs velocity vector" in Fig. 151, one can see that the system can be modeled as a first order dynamical system. They are characterized by a first order differential equation. In this case, x is equal to the velocity, the variable that actually is going to zero because of the force applied (as a consequence, position is going to asymptotically stabilize and acceleration is going to zero):

$$\dot{x} + \frac{1}{\tau}x = 0 \tag{68}$$

where τ is the time constant of the system. $T = 5\tau$ is the time needed for the state to reach the 67% of its initial condition, in this case defined by $v = 1$. The result is shown in Figure 152. In conclusion, it has been shown how force fields can be treated in Chrono::Engine and how increasing the number of the fans permits to obtain better performances in stopping the particles, acting in all the three principal directions. A "rough" expression of the force has been considered in this example, but it wants to show the potential of Chrono::Engine in treating this kind of problems. This can be the base simulation to develop a more complex one adding optical properties that can be managed by electromagnetic force fields and involving a greater number of particles with interactions between them.

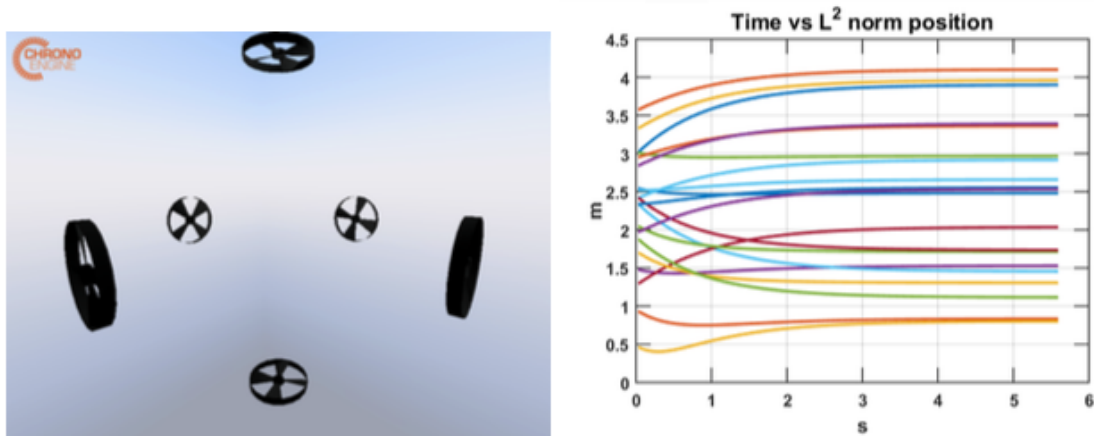


Figure 151. (left) Trapping system. (right) L2-norm of particles position

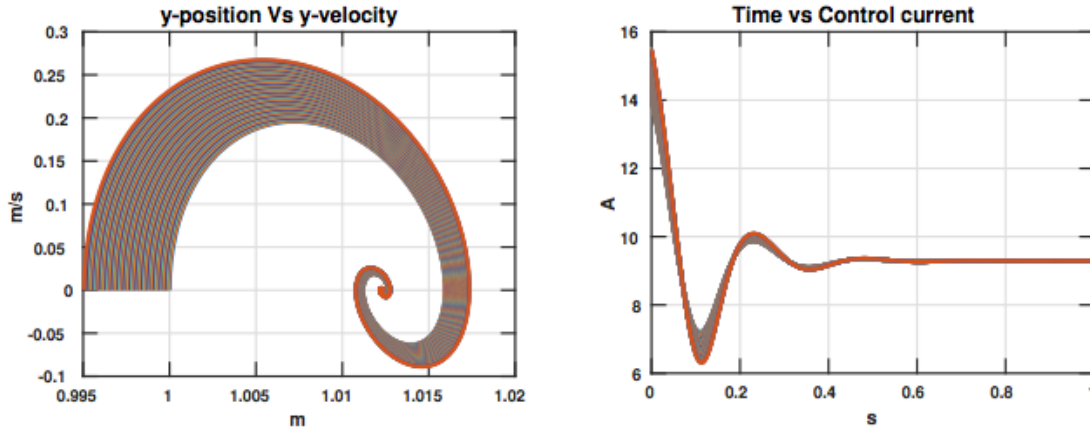


Figure 152. (left) y-position Vs y-velocity in the case of 100 spheres. (right) Time Vs current $I(t)$ in the case of 100 spheres

10.2 Inverse determination of electric and magnetic fields for confinement

A molecular dynamics simulation effort was also conducted. The problem is treated as a coupled set of semi-discrete differential equations for each grain. Given the position and velocity of each particle at one time step, the algorithm estimates these values at the next time step. To compute the next position of each particle requires the evaluation of the right hand side of its corresponding differential equation. Since each of these calculations is independent, there is a potential speedup if the program can take advantage of parallel computing. A Gaussian random process generator generates an initial distribution of grains. The “cloud” is placed in an orbit identified by the six classical orbital elements. The cloud is subject to gravitational harmonics from the Earth (JGM3 Earth gravity model, with 20 harmonic components). Currently, we are adding third-body disturbances from the Sun and the Moon, solar radiation pressure, and atmospheric drag. The simulation results shown in Figure 153 were obtained by commanding the grains to conform to a prescribed optical surface. The cloud is first shaped into a disk, then into a paraboloid of specified focal length and diameter. The numerical results indicate that the force required to shape 1 meter diameter disk into parabola is of the order of 10^{-8} N. Assuming a grain shape which is asymmetric to incoming light, the torque required to align 1 micron grain is of the order of 10^{-15} Nm.

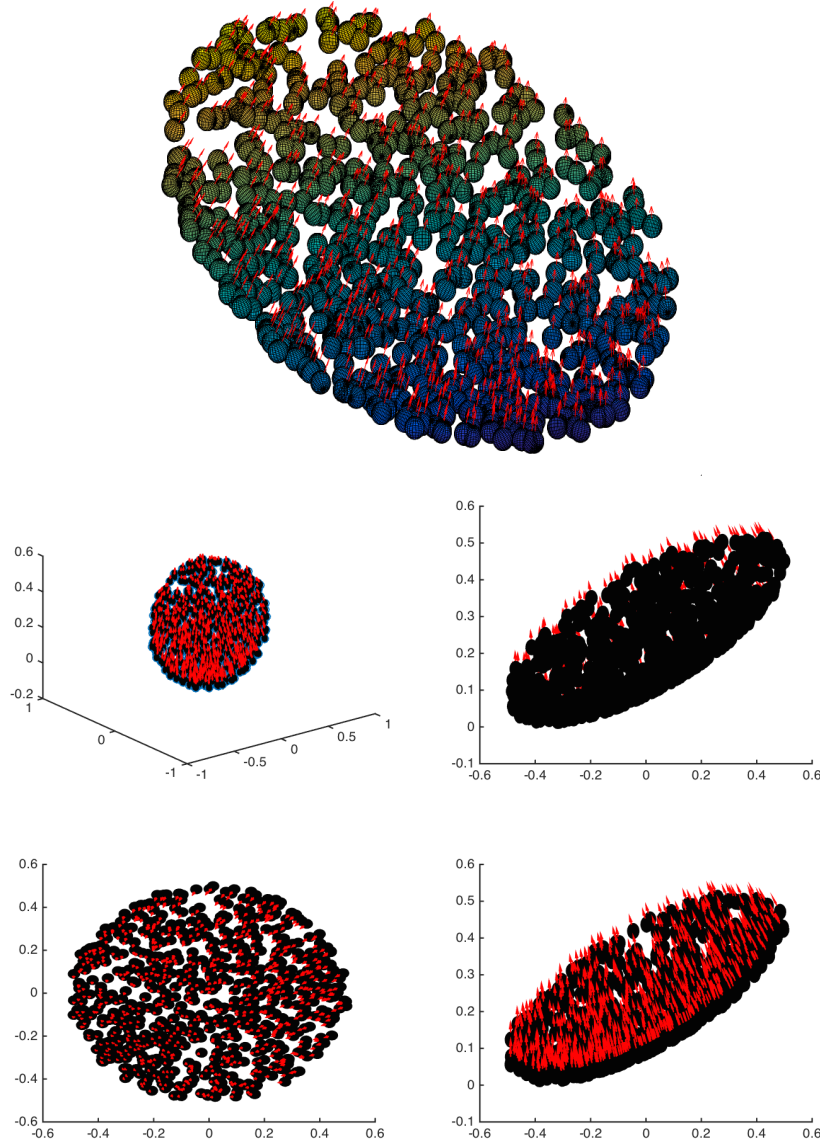


Figure 153. N=1000 grains aligned to wavefront.

We can derive a control law to track a desired surface as follows. Define the tracking error

$$e_z = q(x, y) - q_d(x, y) \quad (69)$$

where $q_d(x, y)$ describes the desired surface, and $q(x, y)$ the current position of the grain with respect to the origin of the orbiting reference frame. By imposing an exponentially stable error dynamics in the form:

$$\ddot{e}_z + 2\xi\omega\dot{e}_z + \omega^2 e_z = 0$$

(70)

where ω is the natural frequency, and ξ the damping ratio, we can make sure the error e_Z is driven to zero. Therefore, using the equations of motion expressed in the moving frame (the orbiting reference frame - ORF), the control law with components in ORF becomes:

$$u = -f_{pert} + f_{gyro} + m\ddot{q}_{des} - K_d\dot{e}_Z - K_p e_Z \quad (71)$$

where f_{pert} is the resultant of perturbation forces on the grain (gravity, solar pressure, etc), f_{gyro} are the Coriolis and centrifugal forces acting on the grain, K_d is a derivative gain, and K_p is a proportional gain. Once the control force to shape the cloud has been computed, the electric and magnetic field to produce that re-shaping can be computed as follows. A grain, of mass m and charge q , moving with inertial velocity v , and subject to an electric field E and to a magnetic field B , is subject to a Lorentz force given by:

$$f_L = q(E + v \times B) \quad (72)$$

In components in ORF, we obtain:

$$u = f_L = q(I_{33}E + v^\times B) = q \begin{pmatrix} I_{33} & v^\times \end{pmatrix} \begin{pmatrix} E \\ B \end{pmatrix} \quad (73)$$

where I_{33} is the 3×3 identity matrix, and the operator $(v)^\times$ denotes the skew-symmetric matrix operator associated with the vector product. Using the matrix pseudo-inverse operation $(v)^\dagger$, we obtain:

$$\begin{pmatrix} E \\ B \end{pmatrix} = q \begin{pmatrix} I_{33} & v^\times \end{pmatrix}^\dagger u \quad (74)$$

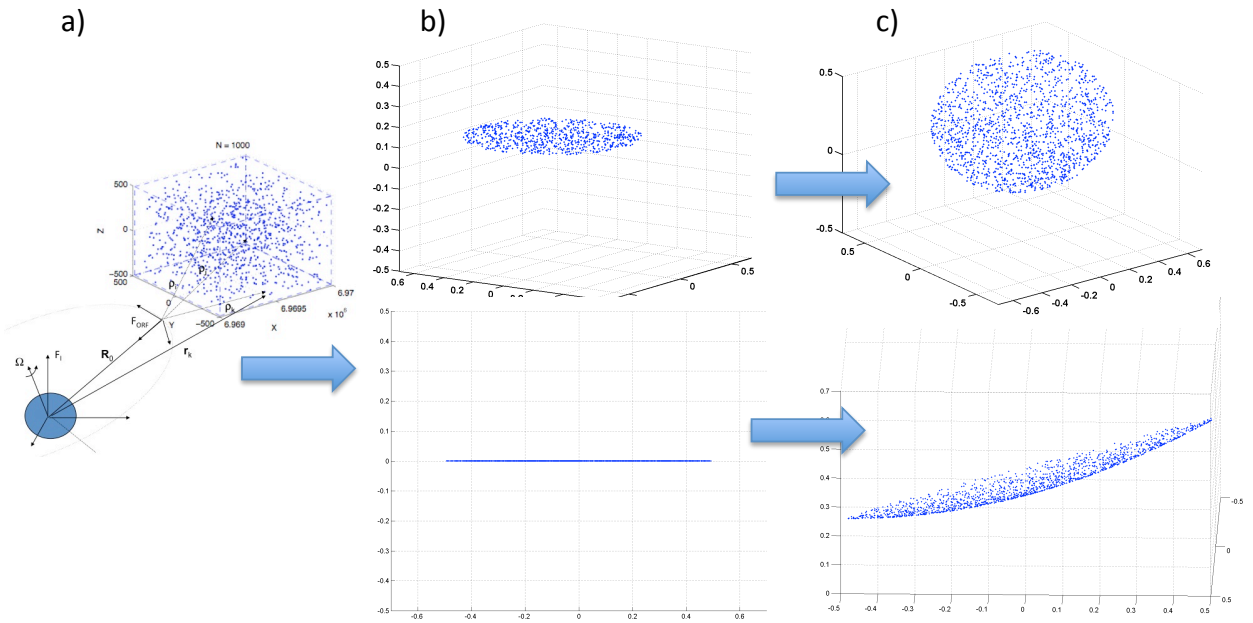


Figure 154. Re-shaping of a) amorphous cloud to b) disk and c) paraboloid.

Figure 154 shows the results of the integrated simulation of coherent and incoherent imaging of a growing cloud. Figure 155 and 156 show the components of the Electric and Magnetic field, as a function of Julian date, involved in the trapping mechanism required to rigidly retarget the parabolic shaped cloud of 60 degrees about the x-axis (in cloud body frame).

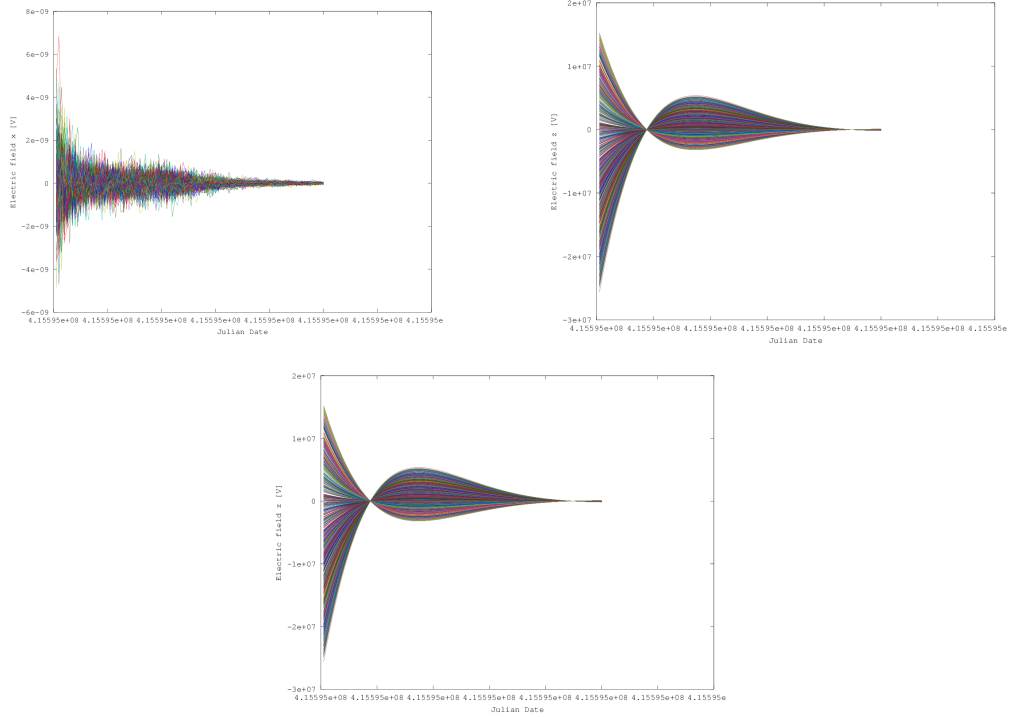


Figure 155. Components of Electric field, as a function of Julian date, involved in the trapping mechanism required to rigidly retarget the parabolic shaped cloud of 60 degrees about the x-axis (in cloud body frame).

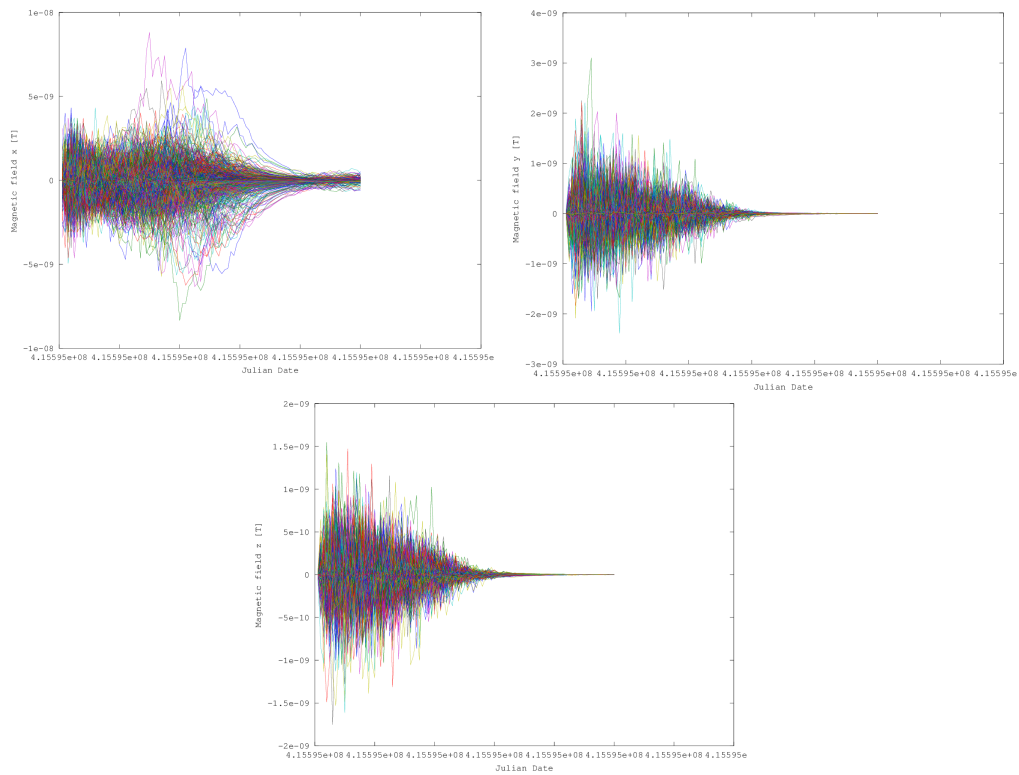


Figure 156. Components of Magnetic field, as a function of Julian date, involved in the trapping mechanism required to rigidly retarget the parabolic shaped cloud of 60 degrees about the x-axis (in cloud body frame).

10.3 Ion trap Levitation Experiments

We used an ion trap to test different configurations of levitated granular media. The ion trap was procured from Newtonian Labs, Inc., from Pasadena, CA⁵. The ion trap allowed us to conduct a broad range of qualitative and quantitative ion trapping experiments. Components of the ion trap include: a) Three plug-in ion traps (The Ring Trap, The Linear Trap, The Single Particle Trap); b) A High-Definition still+video camera, including live-view HDMI video; c) Macro and micro optics for video viewing of trapped particles; d) A steerable green laser for particle illumination, e) a HDMI TV screen. Figure 157 shows the installed ion trap set-up.

We have successfully stably levitated single particles and aggregates of multiple particles inside an ion trap. While the ion trap technique is very promising for the Granular Imager, we were able to levitate grains with a q/m ration comparable to that of 10-100 micron grains (mass of the order of the nanogram, and charges of the order of 10^5 electron charges). We were successful in stably trapping and levitating single particles and aggregates of particles in air. Once levitated, these clouds of grains displayed a remarkable regularity and stability over time, typical of Coulomb crystal behavior. This was expected. The particles used were in the 30-100 micron diameter range. The charge to mass ratio of the ion trap was tailored for optimal levitation of nanogram particles, so larger size grains could not be contained due to their excessive mass. Consequently, further work will require ion traps with larger electrostatic potentials, or particles with larger electron charge to compensate for the larger mass.

Figure 158 depicts the elements of ion trap used in tests (from Newtonian Labs). Figure 159 shows the schematics of ring trap (top), linear trap (middle) and single particle trap (bottom). (From Newtonian Labs). Figure 160 shows a top view of ion trap chassis, showing camera with zooming lens, illuminated laser, and trap. Figures 164 to 169 show photos of levitated cloud of silver coated hollow glass microspheres (100 micron diameter). Figures 161 to 166 show photos of levitated grain of silver coated hollow glass microsphere (100 micron diameter). Figure 167 shows a photo of levitated hexagonal grain (100 micron diameter). Figure 168 and Figure 169 show photos of stably levitated grains of silver coated hollow glass microspheres (100 micron diameter). Figure 170 shows the trapped cloud inside the double ring trap.

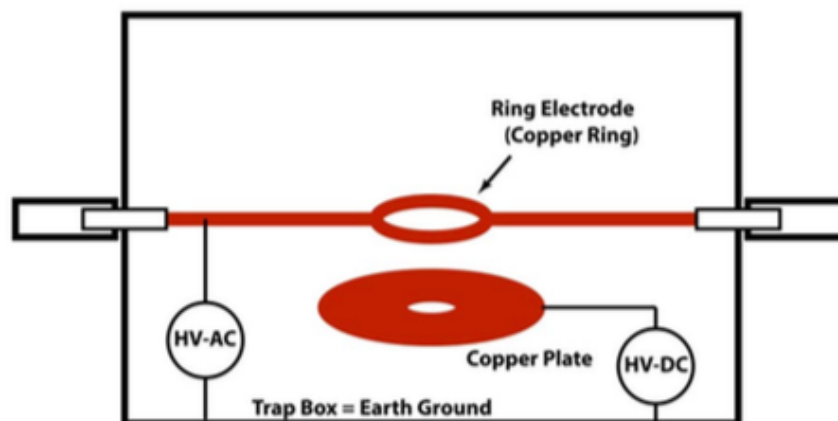
⁵ <http://newtonianlabs.com/eit/ElectrodynamiconTraps.html>



Figure 157. Installed ion trap set-up.



Figure 158. Elements of ion trap used in tests (from Newtonian Labs).



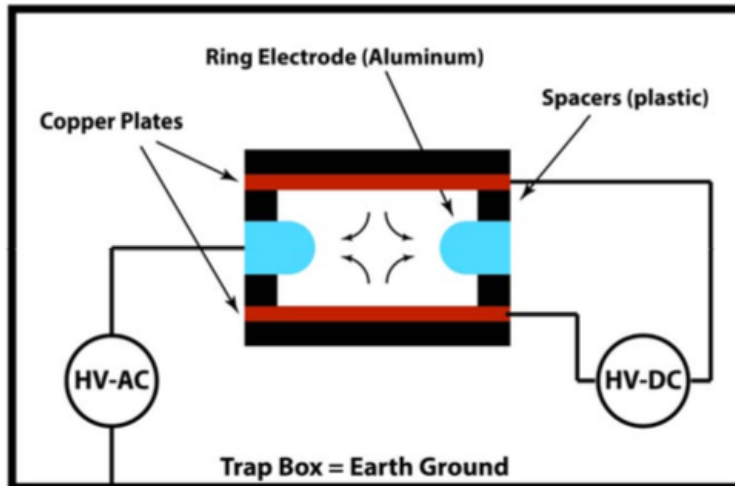
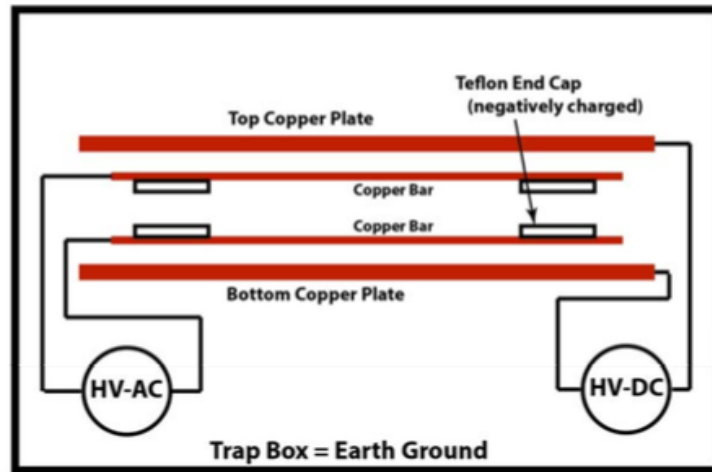


Figure 159. Schematics of ring trap (top), linear trap (middle) and single particle trap (bottom). From Newtonian Labs.



Figure 160. Top view of ion trap chassis, showing camera with zooming lens, illuminated laser, and trap.



Figure 161. Photo of levitated cloud of silver coated hollow glass microspheres (100 micron diameter).

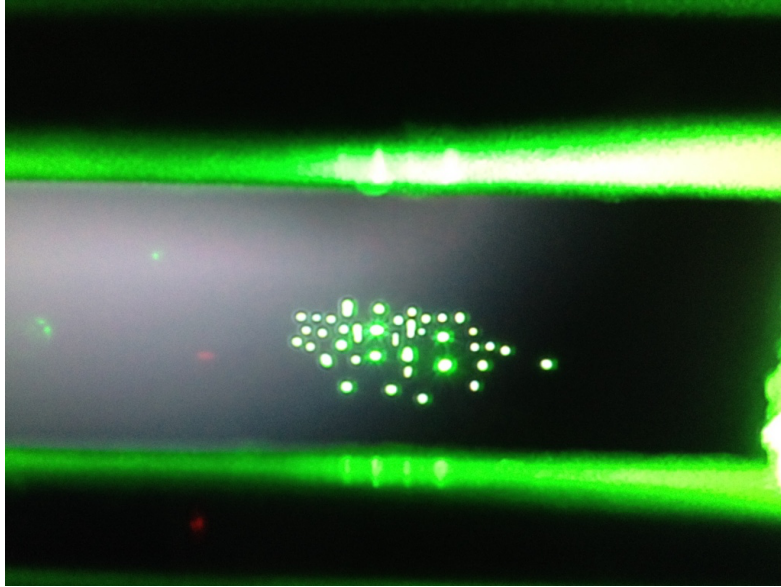


Figure 162. Photo of levitated cloud of silver coated hollow glass microspheres (100 micron diameter).

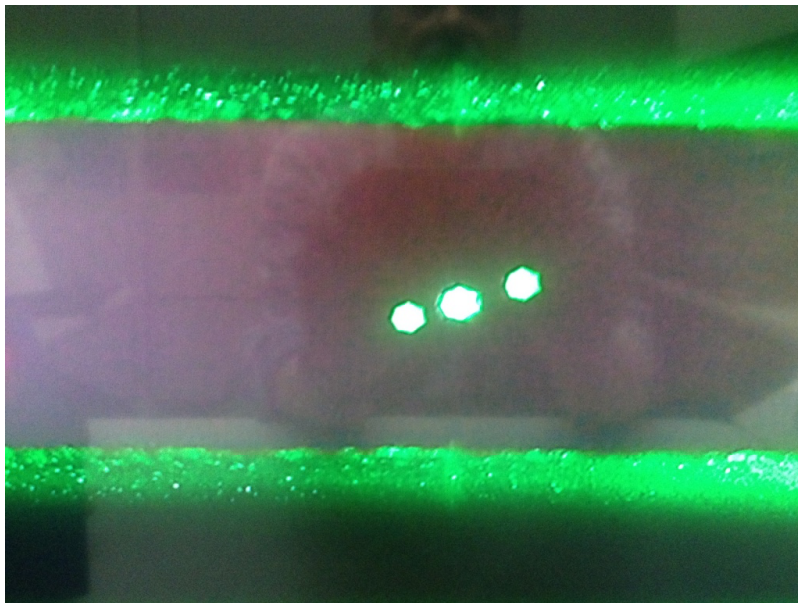


Figure 163. Photo of levitated cloud of silver coated hollow glass microspheres (100 micron diameter).



Figure 164. Photo of levitated cloud of silver coated hollow glass microspheres (100 micron diameter).

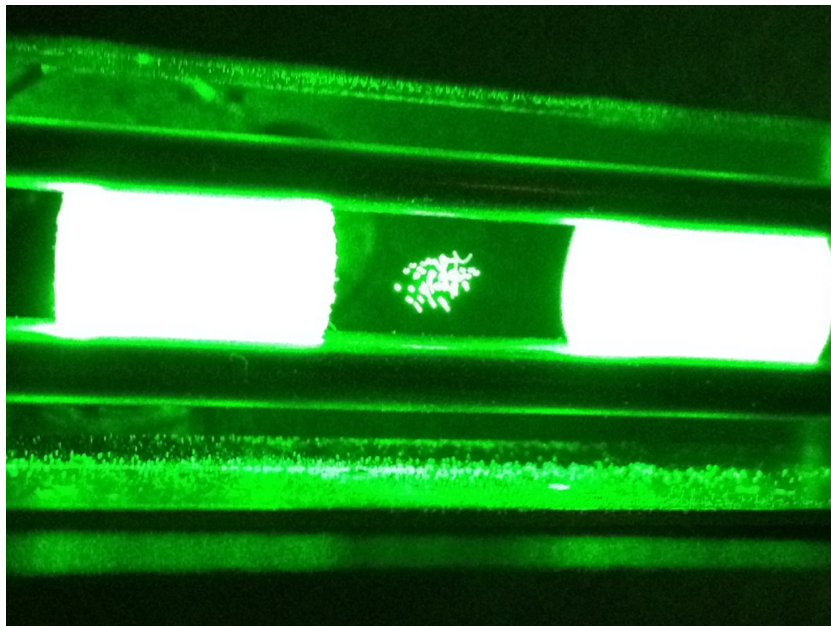


Figure 165. Photo of levitated cloud of silver coated hollow glass microspheres (100 micron diameter).

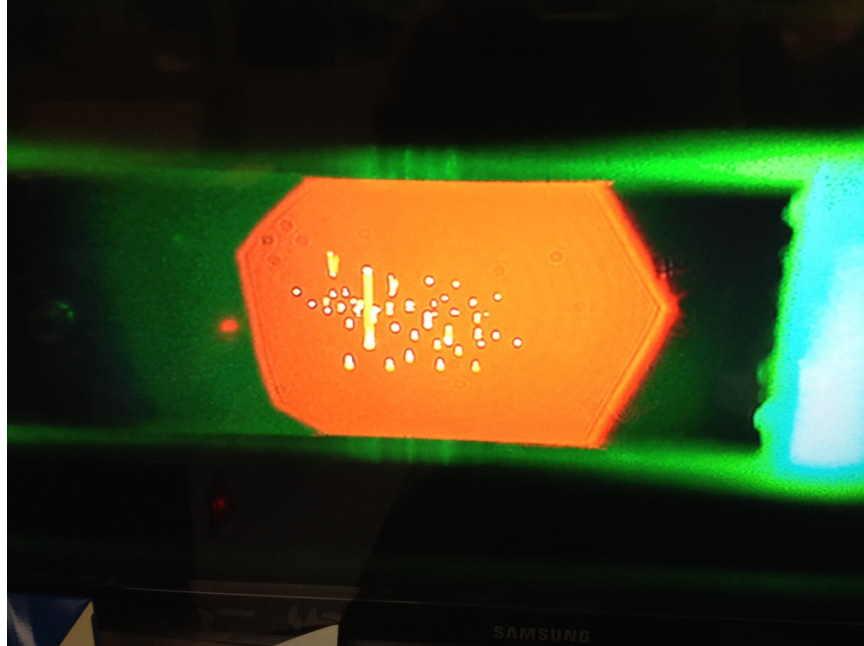


Figure 166. Photo of levitated cloud of silver coated hollow glass microspheres (100 micron diameter).

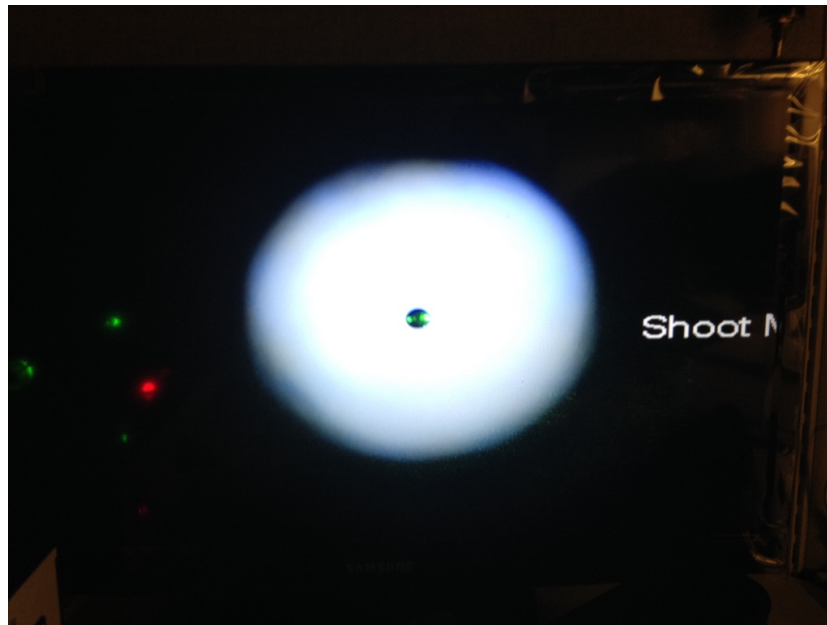


Figure 167. Photo of levitated grain of silver coated hollow glass microsphere (100 micron diameter).

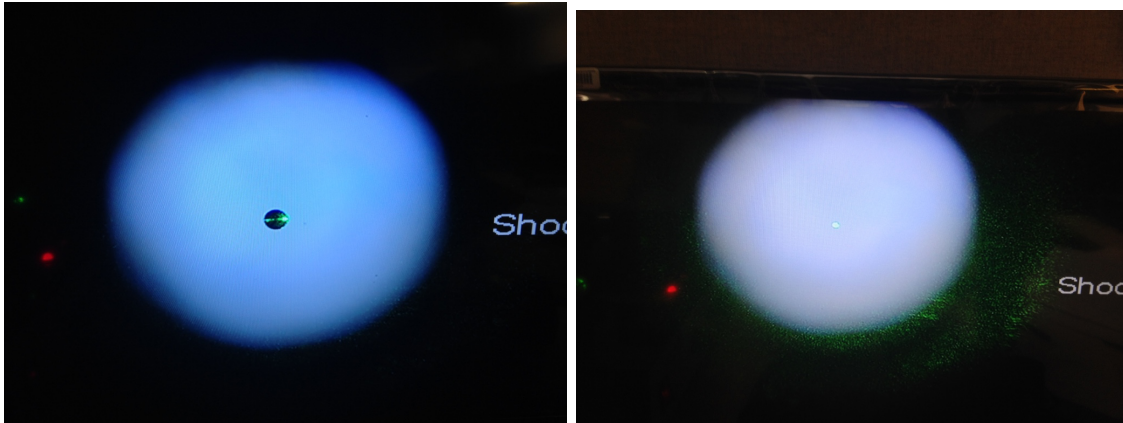


Figure 168. Photo of levitated grain of silver coated hollow glass microsphere (100 micron diameter).

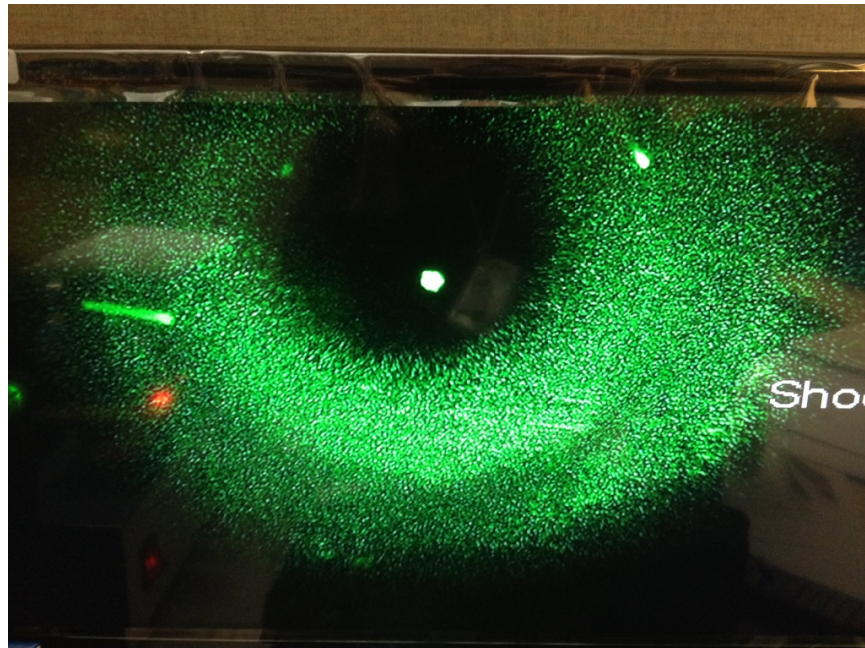


Figure 169. Photo of levitated hexagonal grain (100 micron diameter).

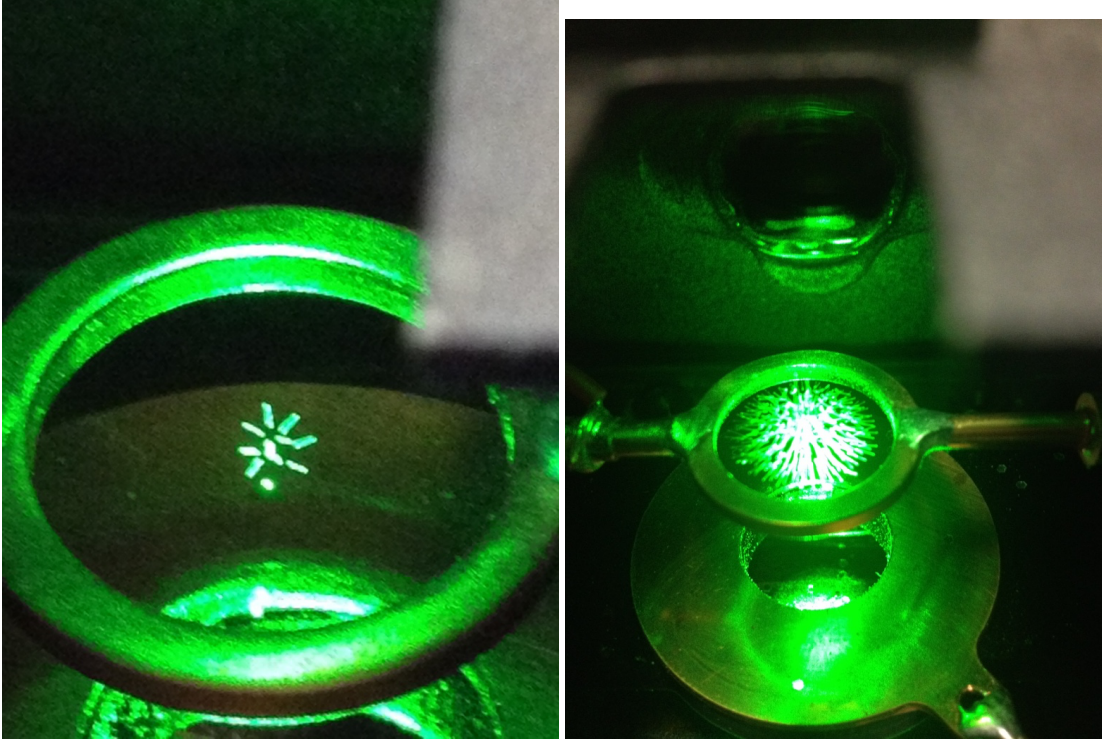


Figure 170. Photo of levitated grains of silver coated hollow glass microspheres (100 micron diameter).

10.4 Other Levitation Techniques

10.4.1 Magnetic Levitation for Radiation Pressure Experiments

Magnetic levitation was explored as a method of freeing an optical element from a surface so that radiation pressure forces could be used to affect a change in attitude and position. Such an element experiences overwhelming contact forces at a surface and confounding thermal and viscous forces when in a liquid. What is more, the refractive index contrast is a small value in a liquid that may also affect the radiation pressure force and torque on the object. The magnetic force on a small magnetic material of volume V and susceptibility χ depends on the gradient of the magnetic field:

$$\vec{F}_m = \frac{\chi V}{2\mu_0} \vec{\nabla} B^2 = \frac{\chi V}{\mu_0} \left(B_x \frac{\partial B_x}{\partial x} + B_y \frac{\partial B_x}{\partial y} + B_z \frac{\partial B_x}{\partial z} \right) \hat{x} + \dots \quad (75)$$

If we assign gravity along the z-direction, then we desire a magnetic force only the direction opposing the gravitational force. Thus, we have two conditions:

$$F_{m,z} = \frac{\chi V}{\mu_0} \left(B_x \frac{\partial B_z}{\partial x} + B_y \frac{\partial B_z}{\partial y} + B_z \frac{\partial B_z}{\partial z} \right) = -F_g \quad (76)$$

where F_g is the gravitational force. Further we desire a zero-valued transverse magnetic force:

$$\vec{F}_{m,\perp} = F_{m,x}\hat{x} + F_{m,y}\hat{y} = 0 \Rightarrow \vec{B} \cdot \vec{\nabla} B_x \hat{x} + \vec{B} \cdot \vec{\nabla} B_y \hat{y} = 0 \quad (77)$$

Setting the gradients in the last expression to zero would provide no transverse force, allowing levitation without trapping.

However, may be difficult, if not impossible to achieve since the magnetic field is governed by the Maxwell equation:

$$\nabla \cdot B = \partial B_x / \partial x + \partial B_y / \partial y + \partial B_z / \partial z = 0 \quad (78)$$

For example, the state $B_x = B_y = \text{const}$ violates Maxwell's equation unless B_z is also constant. The two desired condition are then satisfied:

$$F_{m,z} = \frac{\chi V}{\mu_0} \left(B_x \frac{\partial B_z}{\partial x} + B_y \frac{\partial B_z}{\partial y} + B_z \frac{\partial B_z}{\partial z} \right) = \frac{\chi V}{\mu_0} B_z \frac{\partial B_z}{\partial z} \quad \text{and} \quad \vec{B} \cdot \vec{\nabla} B_x \hat{x} + \vec{B} \cdot \vec{\nabla} B_y \hat{y} = 0 \quad (79)$$

but the magnetic force in the z-direction is zero valued. The above discussion assumes small particles (e.g., have a size much less than the characteristic distance over which the magnetic field changes). For larger particles, the force becomes very complicated because the magnetic field changes inside the diamagnetic material and Maxwell's equation require the boundary conditions must be satisfied to obtain a physical solution. The gradient of the magnetic field at the boundaries of the material are then largely responsible for the net magnetic force. Such calculations are beyond the scope of this project. In practice, magnetic trapping is typically achieved with current carrying coils in either a Helmholtz or quadrupole trap configuration. We numerically calculated the magnetic field and net force on a particle having mass for these two cases. This allowed us to determine both qualitative and quantitative characteristics of the trap, e.g., whether either configuration would allow free motion in the transverse direction (if even over a limited range) while levitating the particle against gravity. The magnetic and net force fields for a Helmholtz configuration are shown below in Figure 171 and Figure 172. The equilibrium positions (zero net force) are indicated by low (black) magnitudes of force. For a massless particle we see large unstable equilibrium point along the axis ($r=0$) half way between the planes of the coils ($z=0$). This is not suitable for our experiment. A stable equilibrium point

exists at $r=450$, but it is stiff. That is, there is a strong restoring force toward the equilibrium position. For a massive particle there is no practical stable equilibrium point. For a magnetic quad trap we see a stable trapping point at $(r,z)=(0,0)$ for a massless particle, and at $(r,z)=(0,-200)$ for a massive particle. The transverse stiffness of these trapping points appears to be non-negligible, but very small bodies (e.g., atoms or molecules) may experience little net force over a small volume centered at the trapping point.

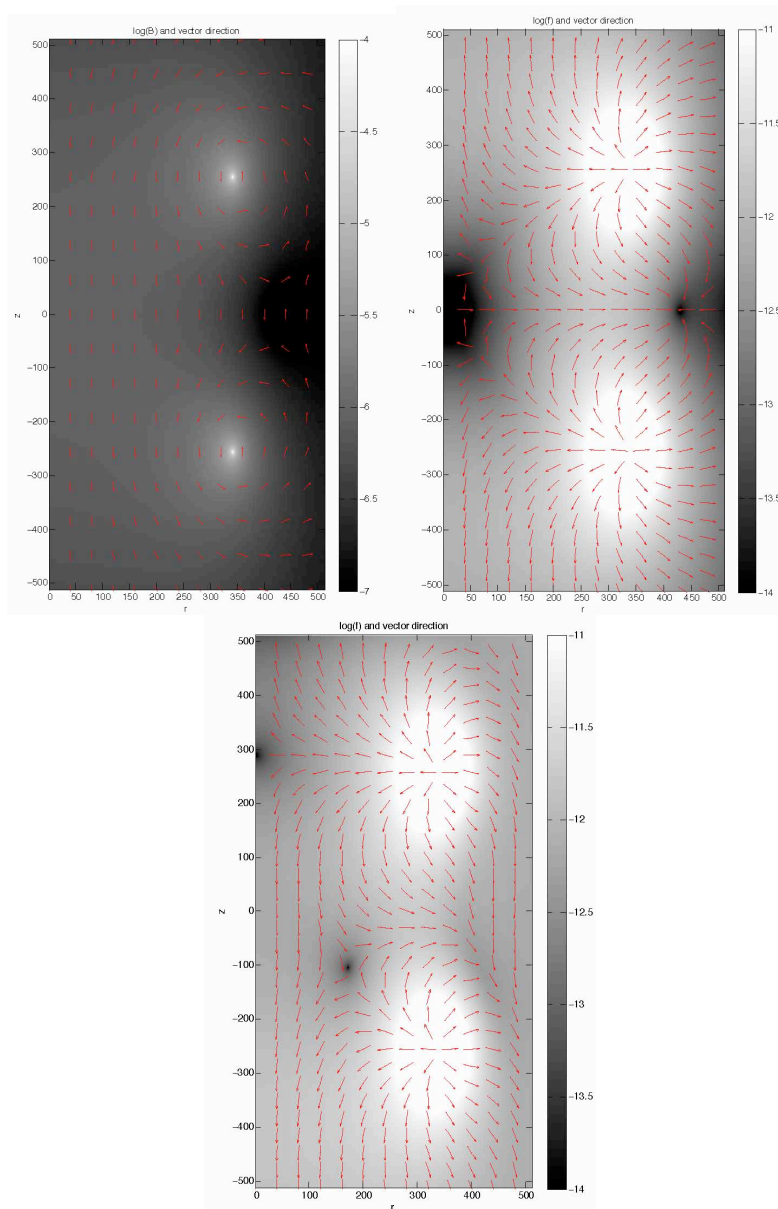


Figure 171. Helmholtz coils of unittless radius $r=350$. Left: Magnetic field strength (log grayscale) and field direction (red vectors). Center: Lines of force for a massless particle. Right: Lines of force for a massive particle.

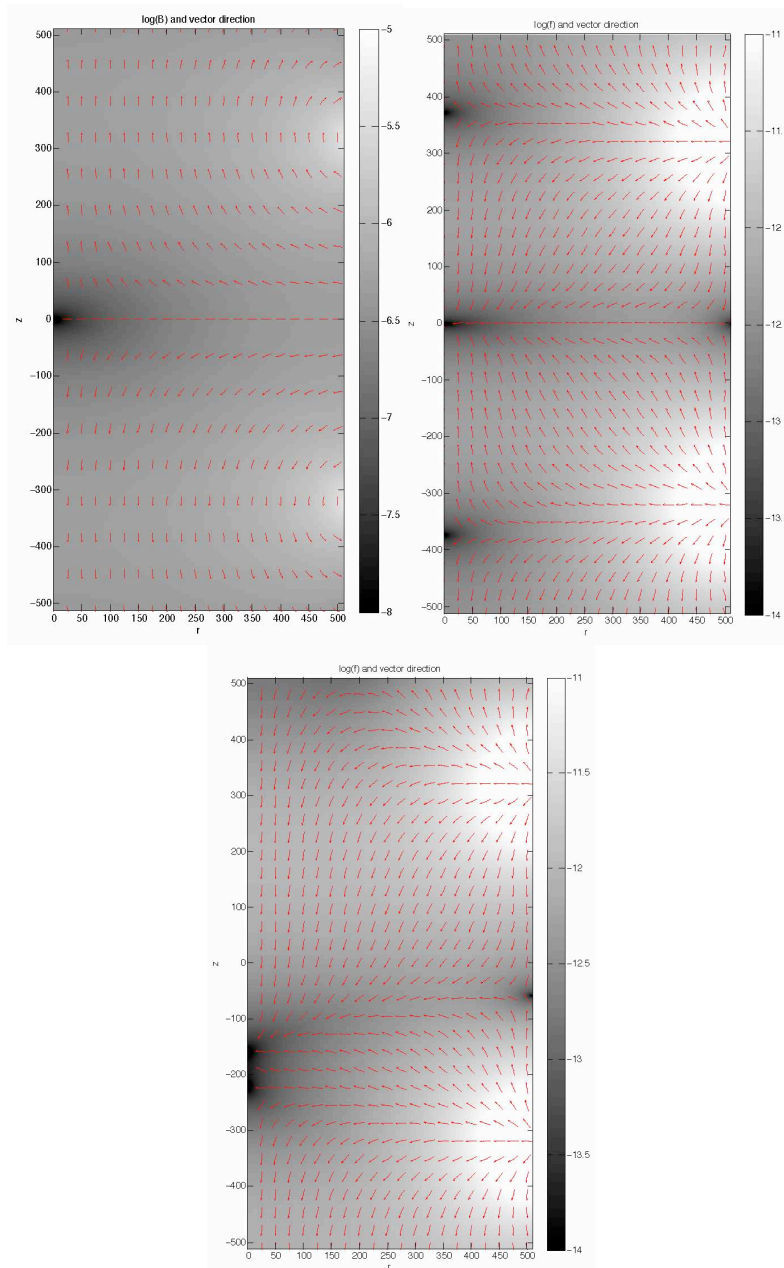


Figure 172. Two coils of radius $r=550$ in a quad trap configuration. Left: Magnetic field strength (log grayscale) and field direction (red vectors). Center: Lines of force for a massless particle. Right: Lines of force for a massive particle.

To explore the magnitude of the levitating and non-zero trapping (transverse) forces from an experimental point of view we purchased rare earth magnetics to create a large magnetic field. Stable levitation is possible with diamagnetic materials, and thus, we also purchased both graphite sheets and bismuth pellets that were melted to form a foil. We also obtained a piece thin silver wire. All three materials (Figure 173) have a negative magnetic susceptibility, as required for stable levitation. In short, we were able to achieve levitation with transverse trapping, but the transverse

force was too stiff to be useful for radiation pressure experiments. The levitation force was strong enough to support a glass hemisphere on top of a sheet of pyrolytic graphite (Figure 174). Using the principle of a driven harmonic oscillator, we explored whether it would be possible to set the body in motion by applying radiation pressure at the natural frequency of the magnetic trap. We found that the quality factor (Q) of the resonator was too low to achieve forces harmonic oscillation. We attribute the small value of the Q to the generation of eddy currents (magnetic breaking) within the diamagnetic material when the material moves through a field gradient (i.e., Faraday's Law of Induction). Convincing radiation pressure effects were not observed. Slight motion may have been caused by high power heating of the diamagnetic layer. The magnetic susceptibility is temperature dependent.

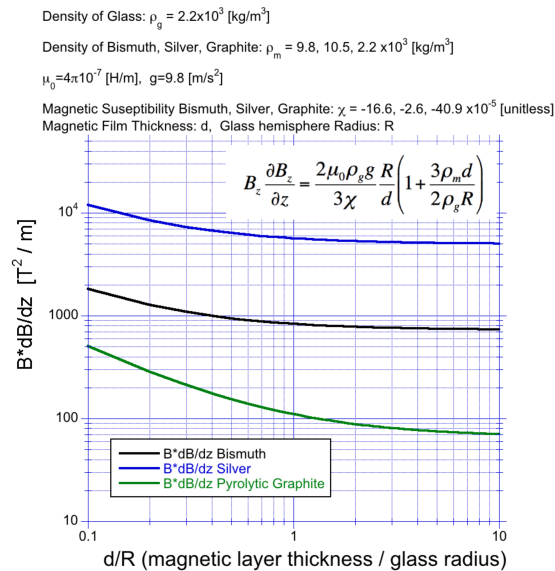


Figure 173. Calculated value of B_z (dB_z/dz) required to levitate (against gravity) a glass hemisphere of radius R atop a diamagnetic film of thickness d for silver, bismuth, and pyrolytic graphite.

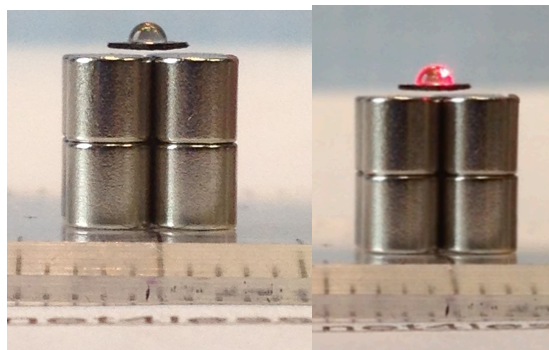


Figure 174. Stable magnetic levitation of glass hemisphere atop a sheet of pyrolytic graphite with (right) and without (left) exposure to red laser light.

10.4.2 Acoustic Levitation for Radiation Pressure Experiment

Acoustic levitation was explored as a method of freeing an optical element from a

surface so that radiation pressure forces could be used to affect a change in attitude and position. Such an element experiences overwhelming contact forces at a surface and confounding thermal and viscous forces when in a liquid. What is more, the refractive index contrast value is ~ 1 in a liquid -- this affects the radiation pressure force and torque on the object. In air or vacuum the refractive index contrast is significantly larger (~ 1.5). Sound waves are emitted from a source as a pressure wave that induces a velocity change of the air molecules, \mathbf{v} :

$$P(\mathbf{r},t) = P_0 + p(\mathbf{r},t). \quad (80)$$

The force per unit volume at a point on a surface is given by

$$\rho d\mathbf{v}/dt = -\nabla p = \rho(\partial\mathbf{v}/\partial t + (\mathbf{v}\cdot\nabla)\mathbf{v}) \quad (81)$$

where the perturbation $p(\mathbf{r},t)$ is generally much smaller than the ambient air pressure P_0 ($p/P_0 \ll 1$). To first order the sound pressure may be represented as a linear superposition for harmonic waves. A simple but suitable model is to assume a planar monochromatic wave of amplitude A propagating in one-dimension:

$$p(\mathbf{r},t) = A \sin(kz - \omega t) \quad (82)$$

where the frequency and wavenumber are related by the speed of the propagating wave $\omega/k = c$. For example, the wavelength ($\lambda = 2\pi/k$) at a frequency ($\nu = \omega/2\pi$) of 20 kHz is $\lambda = 1.73$ cm in air at standard temperature and pressure, where the speed of sound is $c = 343$ m/s. Weak laser heating of the air will shift the wavelength by a negligible amount. See Figure 175.

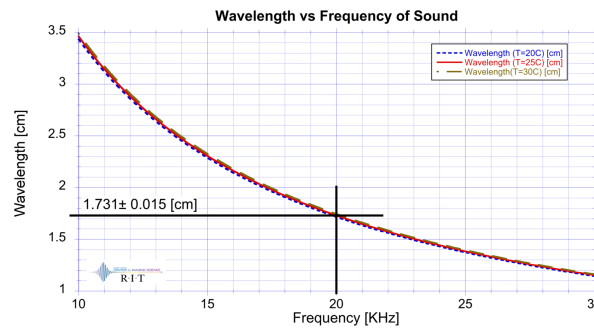


Figure 175. Wavelength vs. frequency of sound for acoustic levitation experiment.

The force per unit volume, \mathbf{f} , at a point on a surface is given by

$$\mathbf{f} = \rho d\mathbf{v}/dt = -\nabla p = \rho(\partial\mathbf{v}/\partial t + (\mathbf{v}\cdot\nabla)\mathbf{v}) \quad (83)$$

For theoretical convenience, the velocity may be expressed in terms of a velocity potential ϕ , assuming the velocity is irrotational ($\nabla \times \mathbf{v} = 0$): $\mathbf{v} = -\nabla\phi$. Note that \mathbf{f} has units of m^2/s . Equation (83) may be written:

$$(1/\rho)\nabla p = \nabla(\partial\phi/\partial t) - (1/2)\nabla(v^2) \quad (84)$$

The system is governed by a continuity equation (conservation of mass): $d\rho/dt = \partial\rho/\partial t + \nabla \cdot \rho\mathbf{v}$. To first order then density does not change explicitly with time ($\partial\rho/\partial t=0$) and thus Eq (84) may be written

$$(1/\rho)d\rho/dt = \nabla \cdot \mathbf{v} = -\nabla^2\phi \quad (85)$$

For materials where the density and pressure are linearly related: $dp/d\rho = c^2$. The potential may then be written as a differential equation:

$$(1/c^2) d^2\phi/dt^2 + (1/2c^2) d(v^2)/dt = -\nabla^2\phi \quad (86)$$

Neglecting the second term of order v^2/c^2 we see the potential is governed by a wave equation of speed c . For example, if $\phi = \phi_0 \sin(kz-\omega t)$, then $v_z = -\partial\phi/\partial z = -k\phi_0 \cos(kz-\omega t)$,

$$(1/\rho)\partial p/\partial z = -\partial^2\phi/\partial z\partial t - (1/2) \partial (v^2)/\partial z = k\omega\phi_0 \sin(kz-\omega t) + (1/2) k^3\phi_0^2 \sin(2kz-2\omega t) \quad (87)$$

Thus $p = \rho \omega\phi_0 \cos(kz-\omega t) + (1/4)k \phi_0^2 \cos(2kz-2\omega t)$. The first order force per unit volume (neglecting the ϕ_0^2 term) is then $f = \rho k\omega\phi_0 \sin(kz-\omega t)$. If a particle moves much less than the acoustic wavelength within a given temporal period, the effective force on the particle may be represented as a time average value. The expression in Eq. (87) therefore suggests that there is no net average force on the particle. To determine the acoustic radiation pressure force, one must therefore carry the above calculations to higher order. As in electromagnetic radiation pressure, the force depends on an intensity – in this case a rms squared value of the pressure or velocity. Doubling the magnitude of the pressure wave therefore increases the acoustic radiation pressure force by a factor of 4. At this point we skip the derivation and simply write the acoustic potential on a sphere of radius R_s , attributed to Gor'kov. The force on the sphere is given by $\mathbf{F} = -\nabla U$ where $U = 2\pi R_s^3(p_{rms}^2/3\rho c^2 - \rho v_{rms}^2/2)$, and where p_{rms} and v_{rms} are the root mean square values of the incremental pressure and air velocity, and ρ and c are the density and speed of sound in air. This expression assumes the sphere is much smaller than the wavelength of sound. Our first objective is to levitate an optically reflective element in a planar standing acoustic wave. See

Figure 176. In Figure 176, an acoustic compression driver (speaker) is driven at 20 kHz by means of a function generator and audio amplifier. A transparent plate above the speaker reflects sound, forming a standing wave. An optical element is levitated in a velocity nodal plane (i.e., pressure anti-nodal plane). A laser illuminates the element, providing an observable transverse force. We purchased a variety of compression drivers suitable for use in the high frequency audio end (~20 kHz). High frequency safeguarded against ear damage from the high power sound wave (on the order of 100 W). Earplugs and earphones were used as an additional safeguard. As shown in the diagram below, and audio amplifier was used to provide power to the speaker from a sine wave generator. An acoustic reflecting plate was used to create a standing wave. Fine tuning of the standing wave condition was achieved by varying the frequency from the function generator. Acoustic levitation requires significant power, and we destroyed 5 or 6 speaker diaphragms, including ones made from performance titanium. Acoustic levitation was achieved for various materials, including aluminum foil, styrofoam pellets, plastic sponge sheeting, and glass cover slips (Figure 177). In Figure 177, the frames were extracted from a video sequence captured at 15 frames per second. The blurring indicates that the disk was moving within the acoustic trap. Below the glass disk is a fine mesh screen that is used to catch the disk when it falls out of the trap. A PVC pipe was used as a waveguiding horn. Our secondary objective was to achieve an acoustic force against gravity, but little or no transverse restoring force. That is, we wanted levitation but not trapping. To achieve this, we tried using various horns to obtain to uniform planar standing wave across an extended area. The project ended before we could achieve this goal.

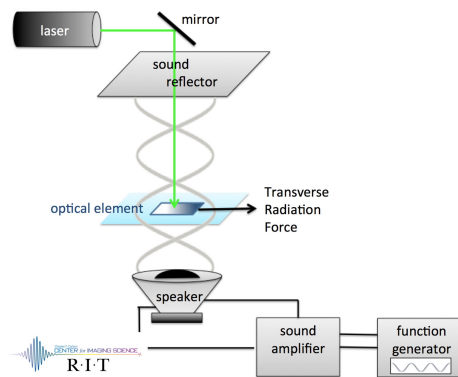


Figure 176. Acoustic levitation apparatus for measuring laser-induced radiation pressure.

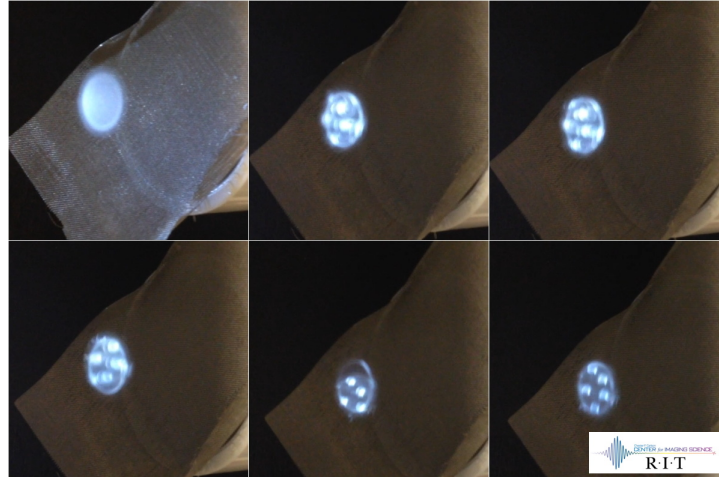


Figure 177. Demonstration of acoustic levitation of round glass disks. The front surface reflects light from a light emitting diode array.

10.5 Alignment Control of Grain under Uniform Illumination

Feedback control methodologies were examined that can enable the three-dimensional guiding and stabilization of a single grain illuminated uniformly by a collimated monochromatic beam from a single direction. Figure 178 and Figure 179 show the radiation pressure force and torque efficiency plots for a refractive hemisphere of refractive index 1.6 in vacuum. They were generated with a modified POV-Ray ray-tracing program.

Figure 180 shows the trajectory of a micron-scale hemisphere at three initial angles of attack (relative to the light source) showing two cycles pure precessional motion (2.8[s]) when illuminated with an irradiance of $10[\mu\text{W}/\mu\text{m}^2]$.

Preliminary results (see Figure 181 and 182) indicated that only one degree of freedom seemed to be fully controllable with arbitrary precision with a feedback plus feed-forward control architecture that senses the angle-of-attack of the grain (angle between the normal to the mirror plane and the illumination direction). This is similar to the optical-tweezer feedback, which however, is done in a medium. Therefore, we explored the options offered by control for optical tweezers and how much of the existing techniques can be extrapolated for operation in a vacuum, in the absence of a medium.

Since grain alignment is critical to enable a reflection from the granular mirror, more detailed analyses were then carried out on the nutation control of the spinning grains, and these analyses are described next.

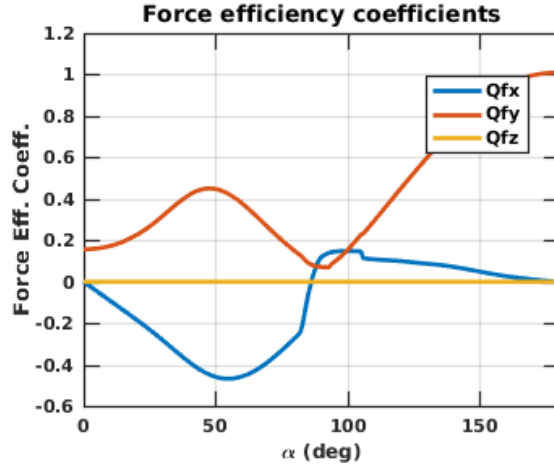


Figure 178. Radiation pressure force and torque efficiency plots for a refractive hemisphere of refractive index 1.6 in vacuum. Generated with a modified POV-Ray ray-tracing program.

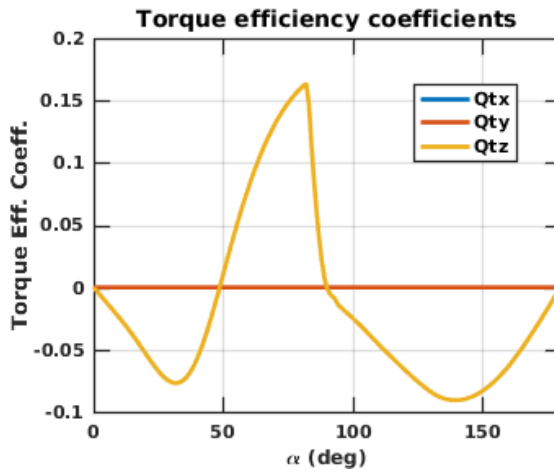


Figure 179. Radiation pressure torque efficiency plots for a refractive hemisphere of refractive index 1.6 in vacuum. Generated with a modified POV-Ray ray-tracing program.

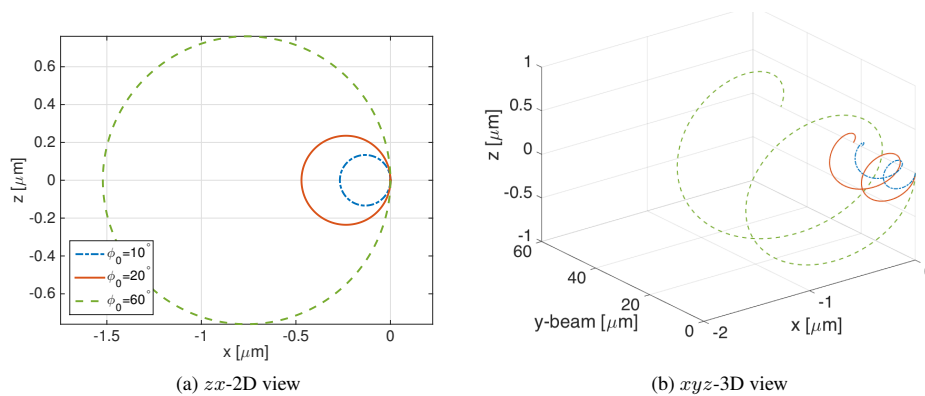


Figure 180. Trajectory of a micron-scale hemisphere at three initial angles of attack (relative to the light source) showing two cycles pure precessional motion (2.8[s]) when illuminated with $\Gamma = 10[\mu\text{W}/\mu\text{m}^2]$ irradiance. Generated using Matlab's ode45 differential equation solver.

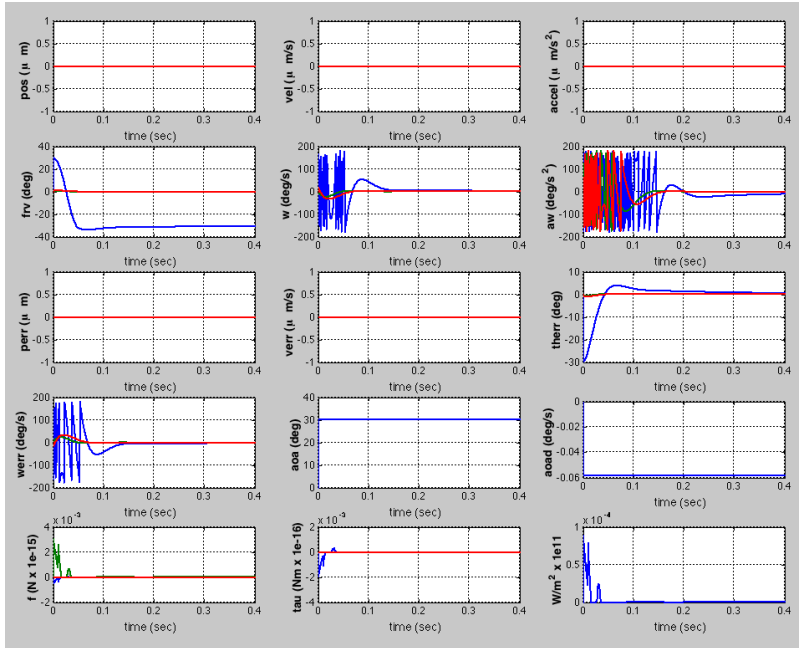


Figure 181. Results of simulated 3D attitude control of grain guided from +30 degrees to -30 degrees in pitch by one uniform collimated beam (frv= angles, therr=angular error, werr=angular rate error, aoa=angle of attack, aoad=rate of angle of attack, f=control force, tau = control torque, bottom right plot is irradiance).

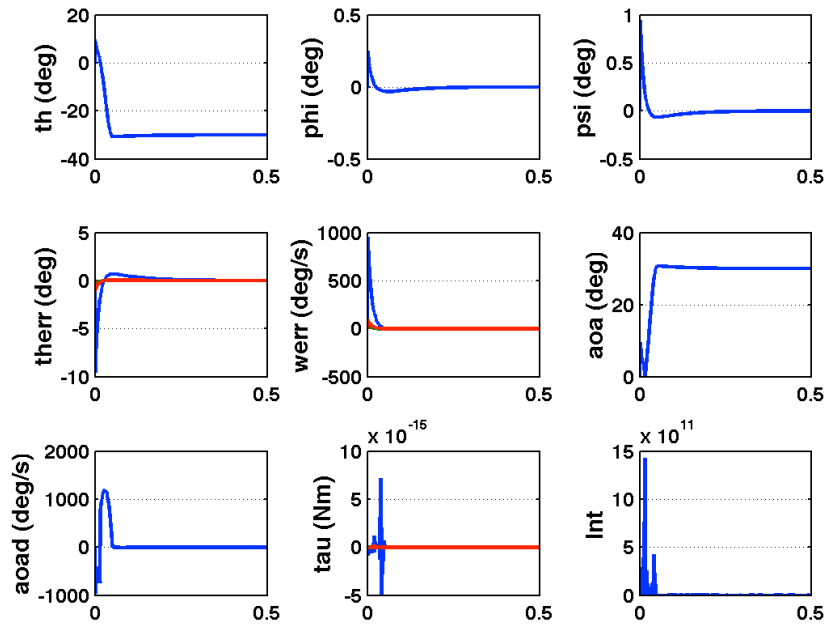


Figure 182. Results of simulated 3D attitude control of grain guided from +10 degrees to -30 degrees in pitch by one uniform collimated beam (theta, phi, psi=Euler angles, therr=angular error, werr=angular rate error, aoa=angle of attack, aoad=rate of angle of attack, f=control force, tau = control torque, bottom right plot is laser intensity).

The dynamic system under analysis can be expressed as:

$$\begin{aligned}
 m \ddot{\mathbf{x}} + k\mathbf{x} &= \mathbf{f} + \mathbf{U} \\
 \mathbf{J} \dot{\boldsymbol{\omega}} + \boldsymbol{\omega} \times \mathbf{J} \boldsymbol{\omega} &= \boldsymbol{\tau}
 \end{aligned}
 \tag{88}$$

Where \mathbf{f} and $\boldsymbol{\tau}$ are the expressions of forces meant as disturbances, such as gravity, aerodynamics, etc. \mathbf{U} instead, is the control force. If we define an error between the actual position of the particle and the desired one and their derivatives like

$$\begin{aligned}
 \mathbf{e} &= \mathbf{x} - \mathbf{x}_d \\
 \dot{\mathbf{e}} &= \dot{\mathbf{x}} - \dot{\mathbf{x}}_d \\
 \ddot{\mathbf{e}} &= \ddot{\mathbf{x}} - \ddot{\mathbf{x}}_d
 \end{aligned}
 \tag{89}$$

it is possible to define the control force \mathbf{U} in such a way that the dynamics of the error

$$m \ddot{\mathbf{e}} + k_v \dot{\mathbf{e}} + k_p \mathbf{e} = 0
 \tag{90}$$

tends to zero with time. In the previous equation, m is the mass of the particle, and k_v, k_p are gains for the control. The control force \mathbf{U} must have the form

$$\mathbf{U} = m \ddot{\mathbf{x}}_d - k_p \mathbf{e} + k\mathbf{x} - k_v \dot{\mathbf{e}} - \mathbf{f}
 \tag{91}$$

where k is defined as

$$k = k(-\mu, q, I, \dots)
 \tag{92}$$

which means that k is function of all the parameters that could be considered for the force fields applied, like the permeability of the material μ , the charge of the particle q , the intensity of the laser I , etc. Therefore, we have to consider the existing trapping systems (Paul trap, Penning trap, other Electromagnetic traps) and adapt them to the current situation in order to reduce as much as possible the displacement (and the rotation) of the particle when it is trapped. In particular, in this section we are interested in the dynamics and eventually the control of the attitude of the particles; that is why, intrinsic torque induced by a beam of light are studied and analyzed in this work. Other kind of trapping systems will be introduced in the model developed in the following in future works, in order to combine a more complete dynamics and control both under the translational and the rotational point of view. In addition, the most important consideration, is the one that derives from the Earnshaw's theorem, which states that charges cannot be maintained in a stable stationary equilibrium configuration by means of only an electrostatic field. This means that other type of forces, in particular electromagnetic and/or light pressure

forces has to be considered and added to keep the particle trapped in an "asymptotically" stable position.

10.5.1 Light pressure forces

We want study the dynamics and to control the attitude of a 3D hemisphere in vacuum through an incident wavefront as input force. First, a model for the specific system must be developed. The dynamical system is a rigid body, with the following equations of motion

$$\begin{aligned}
 \dot{\mathbf{v}} &= \frac{\mathbf{F}(t)}{m} \\
 \dot{\boldsymbol{\omega}} &= \mathbf{I}^{-1}(\boldsymbol{\tau}(t) - \boldsymbol{\omega} \times \mathbf{I} \boldsymbol{\omega}) \\
 \dot{\mathbf{r}} &= \mathbf{v} \\
 \dot{\mathbf{q}} &= \frac{1}{2} \mathbf{q}(0, \boldsymbol{\omega}_l)
 \end{aligned} \tag{93}$$

The rotational part is kept in fixed-body frame, but the translational one is considered in inertial frame. This is possible since translational and rotational part are decoupled having applied all the forces to the center of mass. In this way, the understanding and the representation is more intuitive in the inertial frame. As we will see, this is useful also because the forces and torque coefficients should be defined in the same way.

The different sets of reference frame are considered: $(\hat{i}_l, \hat{j}_l, \hat{k}_l)$ is the inertial frame (fixed in space and time), $(\hat{i}_l, \hat{j}_l, \hat{k}_l)$ is the light frame (fixed in space and time) and $(\hat{i}_b, \hat{j}_b, \hat{k}_b)$ is the body-fixed frame (it rotates according to the rotation of the body). \hat{n} is the direction perpendicular to the flat surface of the hemisphere and α is the angle between \hat{n} and the \hat{i}_l direction of light. The first thing to do is to set the initial condition for the components of velocity, angular velocity and position for the grain. In this analysis we do not want to work with rotation matrices and direction vectors, using the usual aircraft/spacecraft convention [Etkin2000, Stevens2016]. Therefore, the rotation for the body and for the incoming light must be defined according to the starting notation chosen for the orientation of a frame. In this case, we chose to use the "ZYX" order. It is needed just for calculating the angle of attack at each time, not for executing the kinematic part of the simulation. It is the one usually used in the aerodynamic field, since it refers to the "Yaw, Pitch and Roll" (Ψ, Θ, Φ) axis, with rotations applied in that order. Every initial orientation (body and light) must be converted into the equivalent quaternion. Every order of rotation has a different conversion vector. Therefore, once set the initial orientation for the body and for the light frames in terms of "Yaw, Pitch and Roll", we can obtain the equivalent

quaternion for each orientation. Once normalized the quaternion at each time of the simulation, the first step in the routine is to compute the relative rotation in 3D between the fixed-body frame and the light frame because the angle we need is the one between the normal direction to the hemisphere i_b and the light i_l . This can be done easily using the properties of the product between quaternions. Since that product is equivalent to the sum of consecutive rotations, we have $\mathbf{q}_i^b = \mathbf{q}_i^b \mathbf{q}_i^l$, where \mathbf{q}_i^b is the relative rotation between the light frame and the body frame, seen by the body frame. Therefore, $\mathbf{q}_i^b = \mathbf{q}_i^b (\mathbf{q}_i^l)^{-1}$.

The light and the inertial reference frame coincide; but we want to keep the model as general as possible. Once we have the relative rotation, we can compute the angles Ψ, Θ and Φ with the following relationships

$$\begin{cases} \Phi \\ \Theta \\ \Psi \end{cases} = \begin{cases} \text{atan2}((q_2 \cdot q_3 + q_0 \cdot q_1), (0.5 - (q_1^2 + q_2^2))) \\ \text{asin}(-2 \cdot (q_1 \cdot q_3 + q_0 \cdot q_2)) \\ \text{atan2}((q_1 \cdot q_2 + q_0 \cdot q_3), (0.5 - (q_2^2 + q_3^2))) \end{cases} \quad (94)$$

The angle of attack α we are interested into is equivalent to the "Pitch" angle Θ . At this point it is possible to interpolate the curve of the efficiency values using the absolute value of the angle of attack. It is useful to group the coefficients for forces and torques in two constants C_F and C_T

$$\begin{aligned} C_F &= \frac{A}{c} = \frac{\pi \cdot r_1^2}{c} \\ C_T &= \frac{A \cdot r_1}{c} = \frac{\pi \cdot r_1^3}{c} \end{aligned} \quad (95)$$

where A is the surface hit by the light, r_1 is the radius of the hemisphere and c is the speed of light. When all the previous steps have been done, the laser forces and torques can be computed, paying attention to the order of the components and of the efficiency coefficients [Shuster2014]:

$$F_{light} = \begin{cases} I \cdot C_F \cdot q_{f_y} \\ \text{sign}(\alpha) \cdot I \cdot C_F \cdot q_{f_z} \\ \text{sign}(\alpha) \cdot I \cdot C_F \cdot q_{f_x} \end{cases} \quad (96)$$

$$T_{light} = \begin{Bmatrix} I \cdot C_T \cdot q_{t_y} \\ sign(\alpha) \cdot I \cdot C_T \cdot q_{t_z} \\ sign(\alpha) \cdot I \cdot C_T \cdot q_{t_x} \end{Bmatrix} \quad (97)$$

where I is the intensity of the light, and q_{n_m} are the efficiency coefficients coming from the interpolation. After some simulation tests we discovered and verified that torques efficiency coefficients found by the POV-ray tracing systems are defined in the body-fixed frame. The force vector \mathbf{F}_{light} must be rotated from the the light to the inertial frame, since the scattering component has to be parallel to the \hat{i}_l direction, and the lift component perpendicular to that one. In this way it is applied in the inertial frame with the right orientation. For the rotational part, we remember that the current approach is in the fixed-body frame. Therefore, the torque vector \mathbf{T}_{light} , for what we wrote about the torque efficiency coefficients, has to be left directly in the fixed-body frame, without vector rotations. The rotation of the vector \mathbf{F}_{light} can be performed in an elegant and efficient way using quaternions. In order to do that, it must be converted into quaternions adding a zero as first element of the vector $\mathbf{q}_F = [0; \mathbf{F}_{light}]$. The rotation is $\mathbf{q}_{F_{rot}} = (\mathbf{q}_i^l)^{-1} \mathbf{q}_F \mathbf{q}_i^l$, where \mathbf{q}_F is the 4x1 vector in the *light* frame, $\mathbf{q}_{F_{rot}}$ is the same vector but expressed in the *inertial* frame and \mathbf{q}_i^l is the quaternion that allows to rotate a vector from the *inertial* to the *light* frame.

10.5.2 Stability analysis with 2D force plane

In order to predict the behavior of the system, and to apply a control law, we need to perform a stability analysis. In particular, we are interested in the rotational part, since it is the one that can be controlled through modulation of the light. This is because the forces and the torques are all dependent on the angle of attack α . In particular, at this point, we are performing simulations in 3D, but with a 2D force plane, the only state we are interested is the rotation $\Theta(F_{light_j} = T_{light_i} = T_{light_k} = 0)$. It is useful to remember that in these conditions, $\Theta = \alpha$ is valid. Therefore, the system under analysis is the following

$$J\dot{\omega} = T_{light}(\alpha) \quad (98)$$

which means, for the 2D case where $(p, q, r) = (\Phi, \Theta, \Psi)$, and $p = 0$ and $r = 0$, and substituting the formula of the torque:

$$I_{i_b} \ddot{\Theta} = \frac{Ar_1}{c} Iq_{t_z}(\Theta) \quad (99)$$

This expression is very close to the one used to perform the stability analysis for an airfoil, therefore we can use the same approach. Since the force could be non-linear in Θ we can expand it through a Taylor's series, ceasing it at the first order

$$q_{tz}(\Theta) = q_{tz}(\Theta_0) + \left(\frac{\partial q_{tz}}{\partial \Theta}\right)_0 (\Theta - \Theta_0) \quad (100)$$

Given $\Theta_0 = 0$, $q_{t_z}(\Theta_0) = 0$ from the torque curve and naming $\left(\frac{\partial q_{t_z}}{\partial \Theta}\right)_0 = k_{T_z}$, the linearized system is

$$I_{i_b} \ddot{\Theta} = \frac{Ar_1}{c} I k_{T_z} \Theta \quad (101)$$

It looks very similar to the equation of the simple harmonic oscillator, where $\frac{Ar_1}{c} I k_{T_z}$ is in this case an optical stiffness. If we substitute $\Theta = \Theta_0 e^{\lambda t}$ and therefore $\ddot{\Theta} = \lambda^2 \Theta_0 e^{\lambda t}$, we can find the eigenvalues of the system as

$$\lambda_{1,2} = \pm \sqrt{\frac{\frac{Ar_1}{c} I k_{T_z}}{I_{i_b}}} \quad (102)$$

Since A , r_1 , c , I and I_{i_b} are all greater or equal to zero, the value that determines if the rotational part of the system is stable or not is k_{T_z} :

- if $k_{T_z} > 0$ we have $\lambda_1 > 0$ and $\lambda_2 < 0$, therefore the system will be unstable since it has at least one eigenvalue with real part greater than zero.
- if $k_{T_z} < 0$ we have $\lambda_{1,2}$ complex conjugates. In this particular case the eigenvalues are purely imaginary, which means that the solution will oscillate around the equilibrium position.

The data used in the simulations are reported in Table 12. The only parameter that should be changed in every simulation is the initial condition for the orientation of the body.

In the following simulation, the initial rotation assumed by the body in terms of "ZYX (Ψ, Θ, Φ)" notation is $\mathbf{rot}_{0_{body}} = [0 \text{ deg}, 10 \text{ deg}, 0 \text{ deg}]$. The most interesting state variables are the displacement of the body in the k_i direction (lift) and the variation of Θ (angle of attack α) in time and in i_i direction (scattering). The angle of attack ($\alpha = \Theta$) oscillates uniformly in time around $\alpha = 0$, being that an equilibrium position. This kind of behavior was expected, since we are in a zero-damping environment, it should oscillate near an equilibrium position.

Table 12. Common data for the simulations of the 3D hemisphere

Parameter	Value	Unit
r_1	$2.5 \cdot 10^{-6}$	m
ρ	1060	$\frac{kg}{m^3}$
V	$\frac{2}{3} \pi r_1^3 = 3.2725 \cdot 10^{-6}$	m^3
m	$\rho V = 3.4688 \cdot 10^{-14}$	kg
I_{i_b}	$\frac{83}{320} m r_1^2 = 5.623 \cdot 10^{-26}$	$kg m^2$
I_{j_b}	$\frac{83}{320} m r_1^2 = 5.623 \cdot 10^{-26}$	$kg m^2$
I_{k_b}	$\frac{2}{5} m r_1^2 = 8.6721 \cdot 10^{-26}$	$kg m^2$
c	$3 \cdot 10^8$	$\frac{m}{s}$
\mathbf{v}_{b_0}	$[0, 0, 0]^T$	$\frac{m}{s}$
$\boldsymbol{\omega}_{b_0}$	$[0, 0, 0]^T$	$\frac{rad}{s}$
\mathbf{r}_{b_0}	$[0, 0, 0]^T$	m
$\mathbf{rot}_{0_{right}}$	$[0, 0, 0]^T$	deg

I	$1 \cdot 10^7$	$\frac{W}{m^2}$
t_i	0	s
t_f	10	s
dt	0.00001	

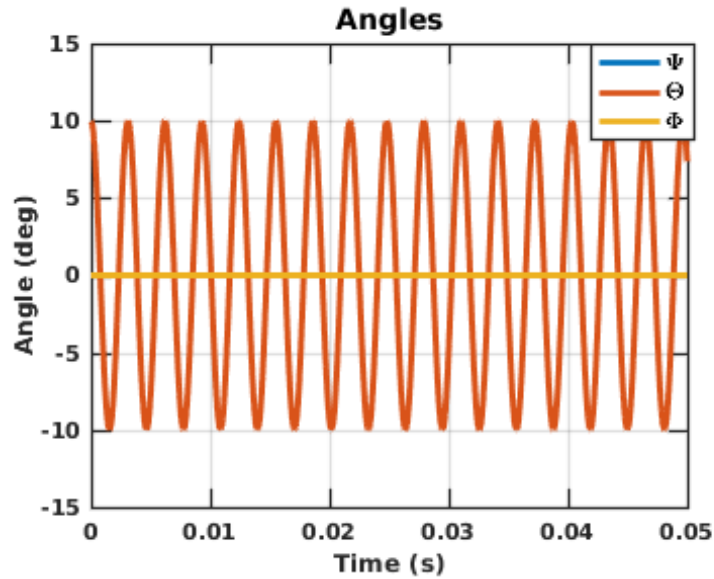


Figure 183. Angles with $\Theta_0 = 10$ deg

In Figure 183 and 184, the displacement in lift direction is shown. It oscillates at the same frequency of the angle of attack α , but not around zero, instead around another value, being the initial condition with $\Theta \neq 0$. The frequency domain response is shown in Figure 185, showing a clear single tone.

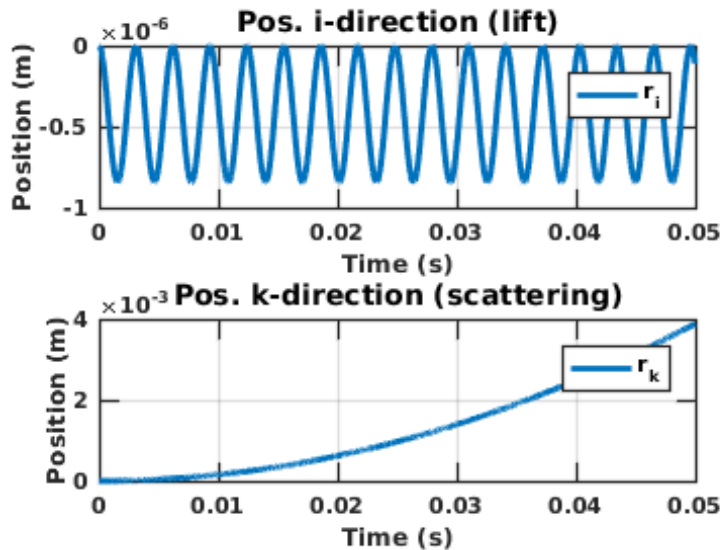


Figure 184. Displacements in scattering and lift directions with $\Theta_0 = 10 \text{ deg}$

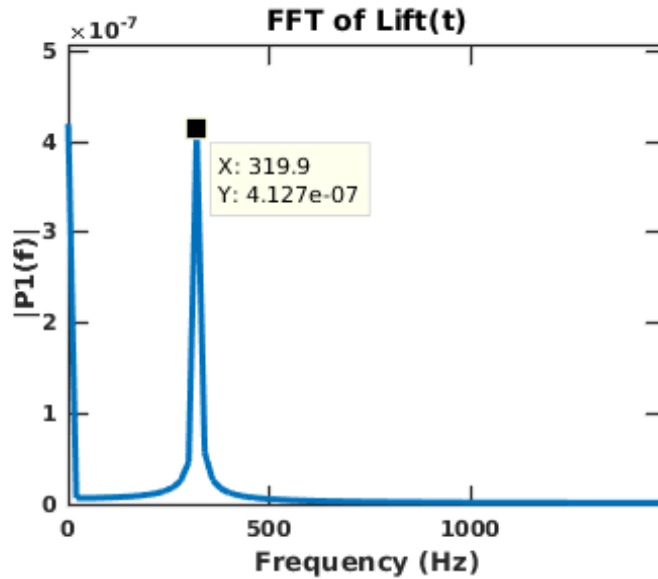


Figure 185. Fast Fourier Transfer Function of oscillation of the displacement in lift direction with $\Theta_0 = 10 \text{ deg}$

If we change the x-axis, using the displacement in scattering direction instead of time, an interesting behavior can be seen. In fact, since the displacement in the scattering direction is of exponential nature, the result is a sort of opposite of the "sweep" function, with the frequency of the displacement in k_i reducing in space. This is because the hemisphere always have a positive acceleration in the scattering direction (being the force in i direction always positive). The scattering vs. lift is shown in Figure 186.

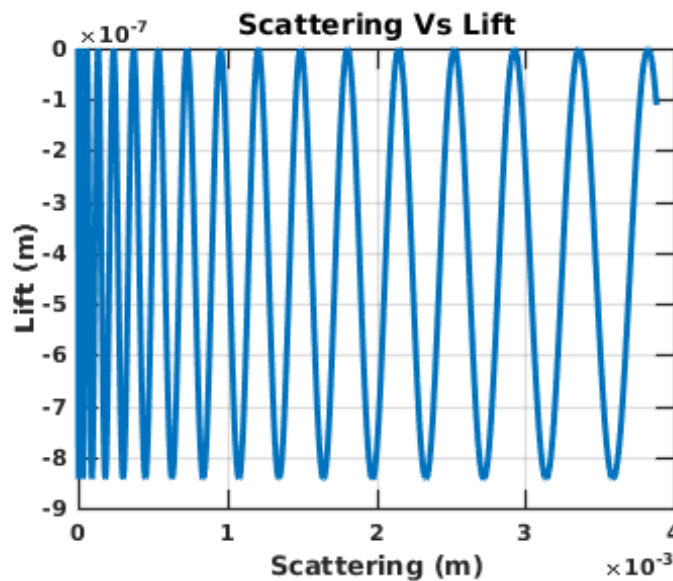


Figure 186. Displacement in scattering Vs lift directions with $\Theta_0 = 10\text{deg}$

The phase diagram (Figure 187 and 188) both for the displacement in lift direction and for the angle of attack confirm the stability of the system given the initial condition on the rotation of $\Theta_0 = 10\text{deg}$.

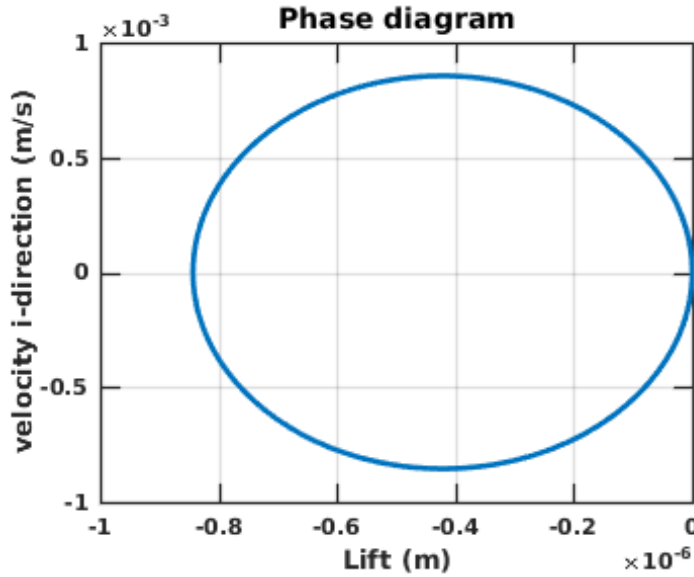


Figure 187. Phase diagram of displacement in lift direction with $\Theta_0 = 10\text{deg}$

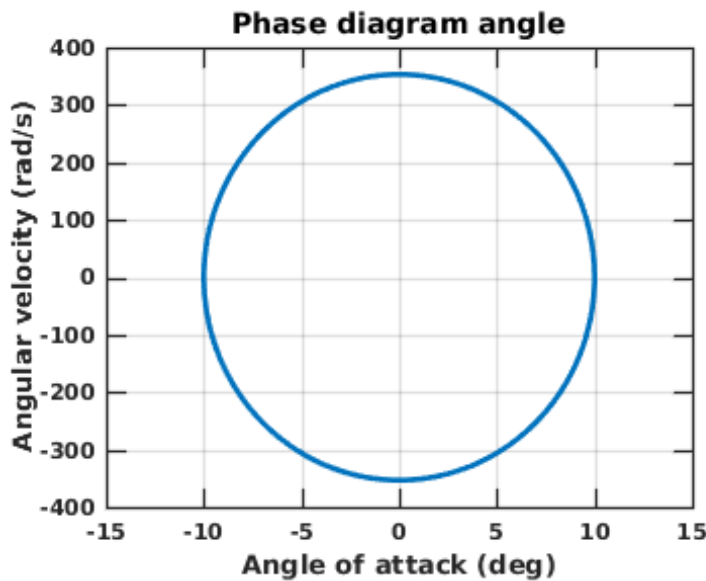


Figure 188. Phase diagram of angle of attack with $\Theta_0 = 10\text{deg}$

This completely symmetric results are expected since both the torque around J_b and the force in k_l direction is odd with respect to $\alpha = 0$. Figures 189 and 190 shows the

angle of attack and Figure 191 shows the Fast Fourier Transfer Function of the simulation with different laser intensity are shown. We can confirm that increasing the intensity of the light, there is an increase of the frequency of oscillation, shown both by a graphical and a numerical (FFT) point of view. This was deduced by ω_0 .

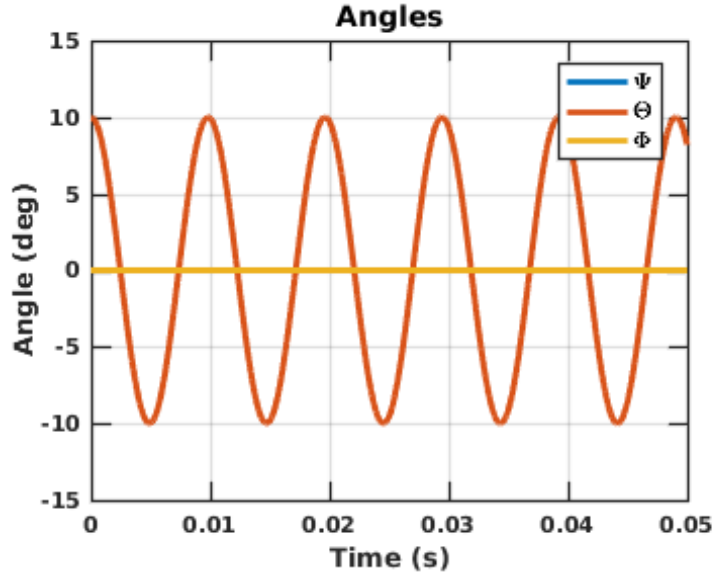


Figure 189. Angle of attack with $\Theta_0 = 10\text{deg}$ and $I = 10^6 \frac{W}{m^2}$

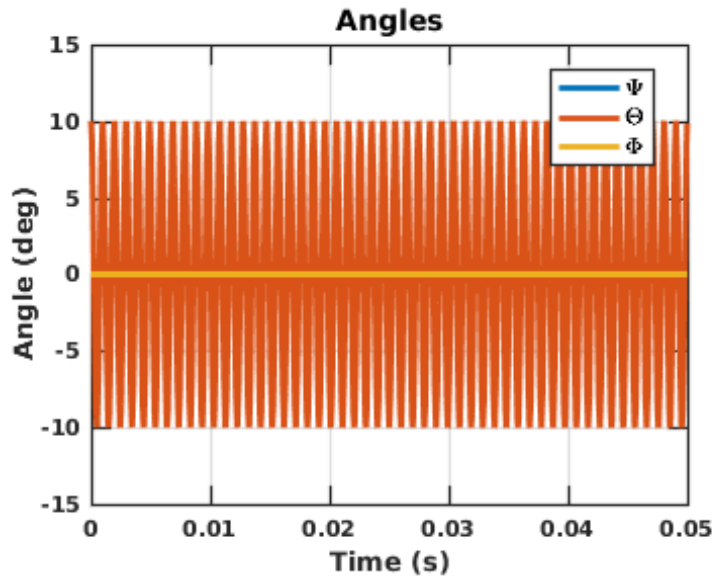


Figure 190. Angle of attack with $\Theta_0 = 10\text{deg}$ and $I = 10^8 \frac{W}{m^2}$

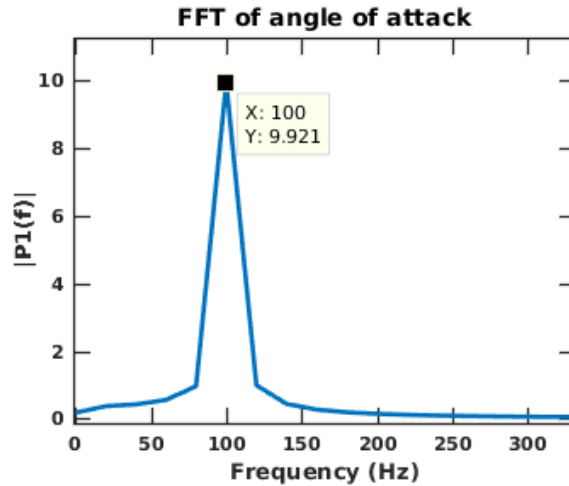


Figure 191. Fast Fourier Transform Function of oscillation of the angle of attack with $\Theta_0 = 10\text{deg}$ and

$$I = 10^6 \frac{W}{m^2}$$

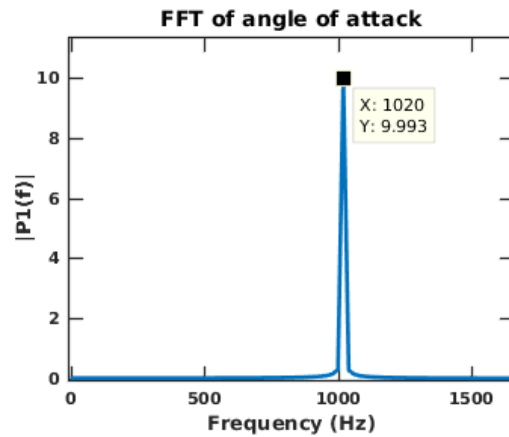


Figure 192. Fast Fourier Transform Function of oscillation of the angle of attack with $\Theta_0 = 10\text{deg}$ and

$$I = 10^8 \frac{W}{m^2}$$

Next, a case around the equilibrium angle $\alpha = 90\text{deg}$ is shown. Therefore, the initial condition for the orientation of the hemisphere is $\mathbf{rot}_{0_{body}} = [0\text{deg}, 110\text{deg}, 0\text{deg}]$. In this case, the pitch angle is limited between $-90\text{deg} < \Theta < 90\text{deg}$. It can be easily seen that if we want to have access to the force and torque coefficients for more than 90deg we have to add 90deg manually to the angle in output from the quaternion equation.

We expected no more a symmetrical response of the system, because even if $\alpha = 90\text{deg}$ is a stable equilibrium point for the angle of attack, the slope of torque coefficients, and so the acceleration, is different for the left and for the right side of $\alpha = 90\text{deg}$. Another difference we expected was an exponential increase of the

displacement in the lift direction, with no more a stable oscillating behavior. This because $\alpha = 90\text{deg}$ is not a stable angle for the displacement states of the system. All the results we obtained confirmed our expectations. Starting with the angle of attack, where the asymmetry is evident with respect to $\Theta = 90\text{deg}$. Higher angles $\Delta\Theta$ can be reached in $\Theta > 90\text{deg}$ with respect to $\Theta < 90\text{deg}$ because in this range the slope of the torque coefficient is much lower (in absolute value), which means lower torque in the opposite direction, and therefore more time to change the direction of the rotation. The opposite happens in the other range, being the slope very high, and therefore feeling the body a higher torque to come back towards $\alpha = 90\text{deg}$. This is shown in Figures 193 to 195.

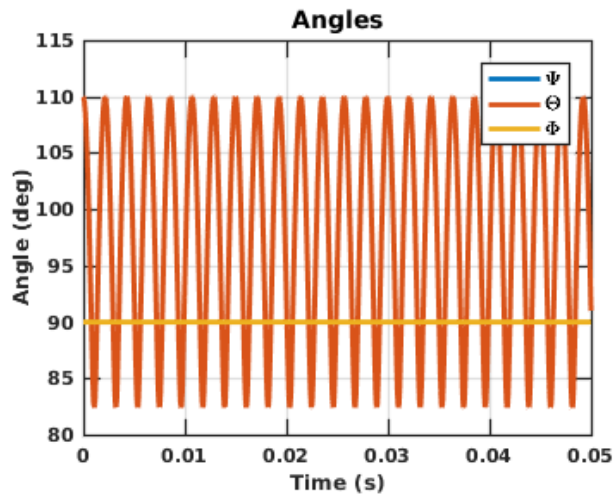


Figure 193. Angles with $\Theta_0 = 110\text{deg}$

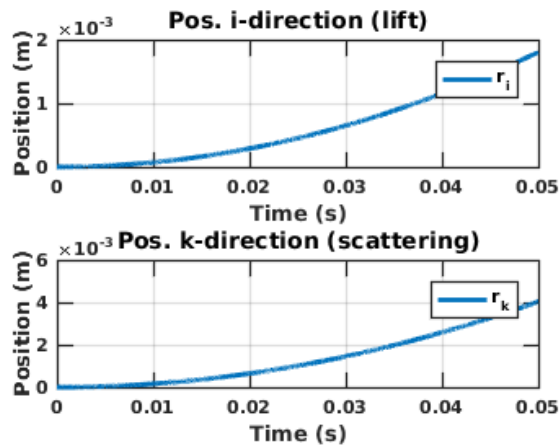


Figure 194. Displacements in scattering and lift directions with $\Theta_0 = 110\text{deg}$

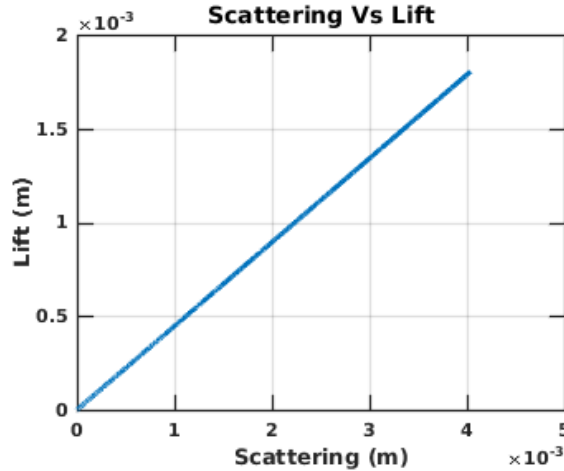


Figure 195 .Displacement in scattering Vs lift directions with $\Theta_0 = 110\text{deg}$

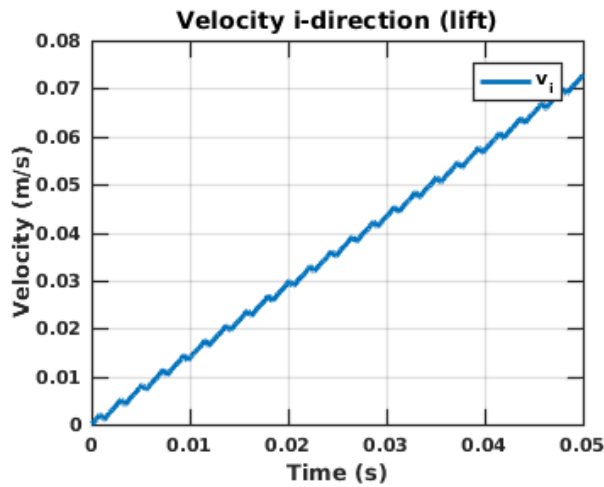


Figure 196. Velocity in lift direction with $\Theta_0 = 110\text{deg}$

It is interesting to show the velocity in lift direction plotted in Figure 196, since it shows small periodic deviation from the straight line. This is due to the fact that the body oscillating in asymmetrical way around $\alpha = 90\text{deg}$, the zero line of the force efficiency coefficient curve is crossed, and therefore there is a short time where the acceleration in the lift direction is negative, before coming back to positive due to the fast opposite torque in the range of $\alpha < 90\text{deg}$. Since it has no more sense to show a phase diagram for the displacement in the lift direction, being it always positive, of exponential behavior and therefore unstable, only the phase diagram for the angle of attack is shown. The phase diagram is shown in Figure 197.

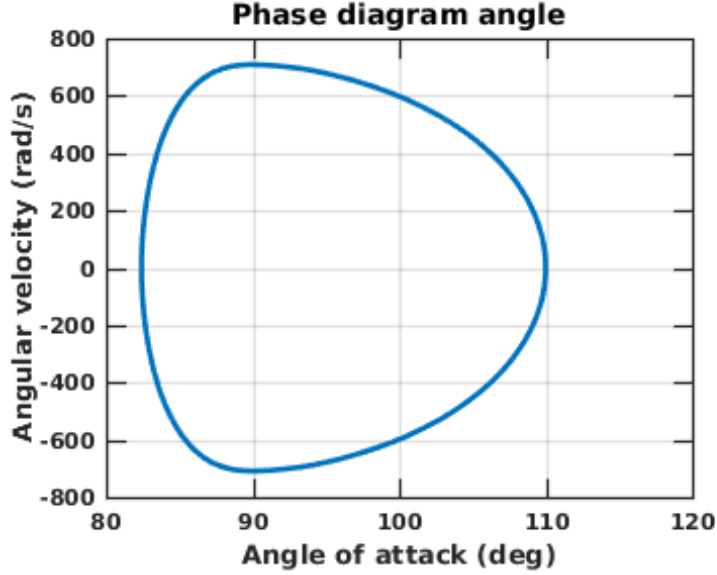


Figure 197. Phase diagram of angle of attack with $\Theta_0 = 110\text{deg}$

The general objective is to control the attitude of the grain. Therefore, the light should be modulated in order to apply the desired torque to the body. We are only looking at the rotational part of the simulation since we already know that it is not possible to control the translational part of the body without being able to control the rotational one. In any case, the displacement in scattering direction could not be controlled. The control we are introducing is directly on the quaternion (orientation) and on the angular velocity. The first step is to define the reference angular velocity and orientation we want to obtain with the control torque. In order to find the quaternion difference \mathbf{q}_{b-ref} between the current state and the desired one, recalling the properties of quaternion, we have to perform multiplications between them. In particular, given the current state \mathbf{q}_i^b and the desired one \mathbf{q}_i^{ref} , we have that $\mathbf{q}_i^{ref} = \mathbf{q}_b^{ref} \mathbf{q}_i^b$, where \mathbf{q}_b^{ref} is the rotation we need in order to switch from the current to the desired orientation. Therefore, we obtain the needed rotation from, $\mathbf{q}_b^{ref} = \mathbf{q}_i^{ref} (\mathbf{q}_i^b)^{-1}$. The control force becomes

$$\mathbf{T}_{control} = -k_q \dot{\mathbf{U}}_q - k_w \dot{\mathbf{U}}_\omega \quad (103)$$

where $\dot{\mathbf{U}}_q$ is the vectorial part of \mathbf{q}_b^{ref} . The control torque $\mathbf{T}_{control}$ is useless as it is defined before: this is due to the fact that the only parameter we can manage is the intensity of the light I , therefore we have to find it in order to have the desired control torque. If we equalize the laser torque \mathbf{T}_{light} with the control torque $\mathbf{T}_{control}$ found performing the simulation, it is possible to manage vectors and matrices in order to have a direct expression of the laser intensity I . Therefore, in a 3D applied force case we would have

$$\mathbf{T}_{control} = \mathbf{T}_{light} = \begin{Bmatrix} C_T \cdot q_{t_y} \\ sign(\alpha) \cdot C_T \cdot q_{t_z} \\ sign(\alpha) \cdot C_T \cdot q_{t_x} \end{Bmatrix} \cdot I \quad (104)$$

which can be expressed as $\mathbf{T}_{control} = \mathbf{Q}_T(\alpha) \cdot I$, being $\mathbf{T}_{control}$ and $\mathbf{Q}_T(\alpha)$ 3x1 vectors and I a scalar 1x1. Pre-multiplying both sides with $(\mathbf{Q}_T(\alpha))^T$ we obtain

$$I = I_{control} = ((\mathbf{Q}_T(\alpha))^T \cdot \mathbf{Q}_T(\alpha))^{-1} \cdot (\mathbf{Q}_T(\alpha))^T \cdot \mathbf{T}_{control} \quad (105)$$

One of the problems of controlling the hemisphere through the intensity of light (and it is the only option we have) is that I can be only greater or equal zero. Therefore, in addition to the last equation we have to impose the following condition $I_{control} \geq 0$. In this first part, actually a 2D force/torque plane simulation is performed. Therefore, considering just the attitude part of the problem, the target is to reach the value of the angle of attack $\alpha = \Theta$ of interest and the same for the angular velocity around the \hat{J}_b direction. Considering just the second row of the system, the previous equation becomes a product of scalars, instead of a composition of products of matrices and vectors

$$I_{control} = sign(\alpha) \cdot \frac{\mathbf{T}_{control}_{j_b}}{C_T \cdot q_{t_z}} \quad (106)$$

Furthermore, in order to simulate a real condition, where the power of a laser is limited, a saturation limit for the intensity of the light; therefore, when the limit is reached, the variable $I_{control}$ is imposed at the limit value I_{limit} . In Figure 198, one can see how the controlled attitude of the particle behaves as predicted. It reaches almost a zero value in angle of attack.

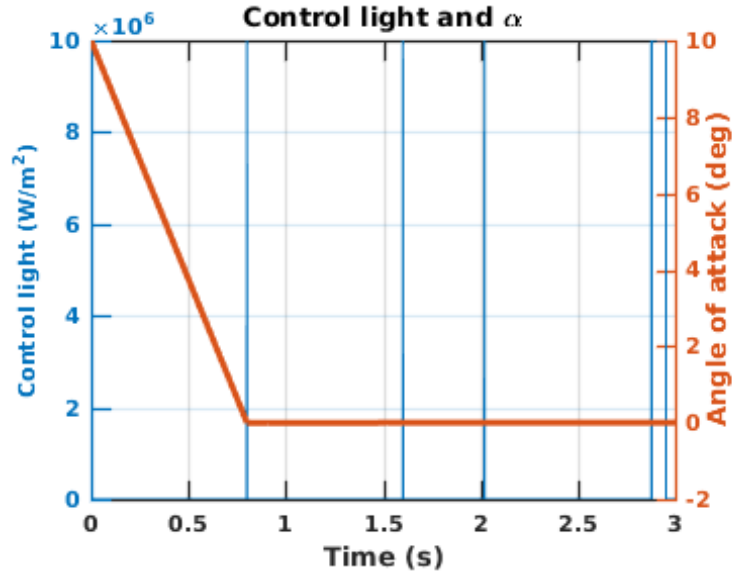


Figure 198. Angle of attack of the hemisphere with the introduction of control with $P_q = 10$, $P_w = 4$ and $\Theta_0 = 10$ deg

Figure 199 zooms in, and shows that the light is activated soon as the angle of attack becomes negative, and it is turned off when the slope of the angle of attack is of the opposite of the angle itself.

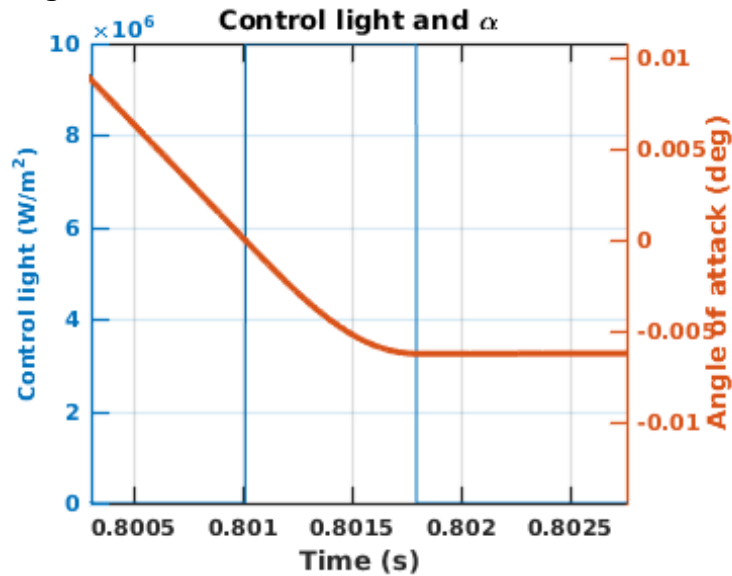


Figure 199. Detailed view of the angle of attack of the hemisphere with the introduction of control with $P_q = 10$, $P_w = 4$ and $\Theta_0 = 10$ deg

In Figure 200, the proportional gain is lower, which leads to a slower dynamics but with lower amplitude of oscillations and frequency of activation of the incident light source. If the proportional gain is higher instead, the dynamics is faster (Figure 201) because we are increasing the stiffness of the system, which results in a more frequent

activation of the laser in order to limit the oscillation within a very small range. The same happens if we change the limit of saturation to the intensity of the light. The higher it is, the faster is the dynamics and the more frequent the activation of the incident light source is.

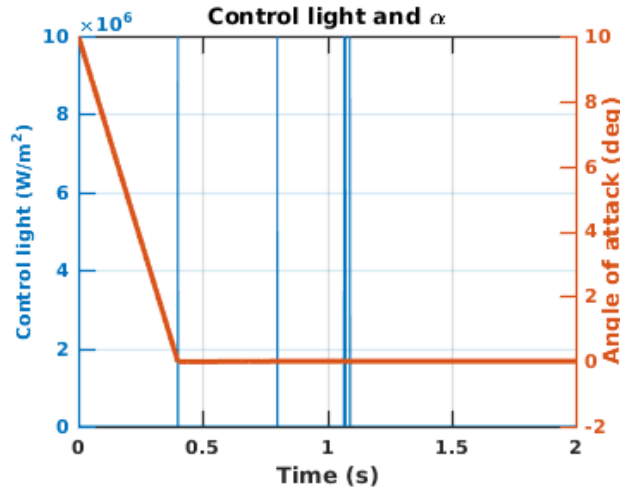


Figure 200. Angle of attack of the hemisphere with the introduction of control with $P_q = 20$, $P_w = 4$ and $\Theta_0 = 10$ deg

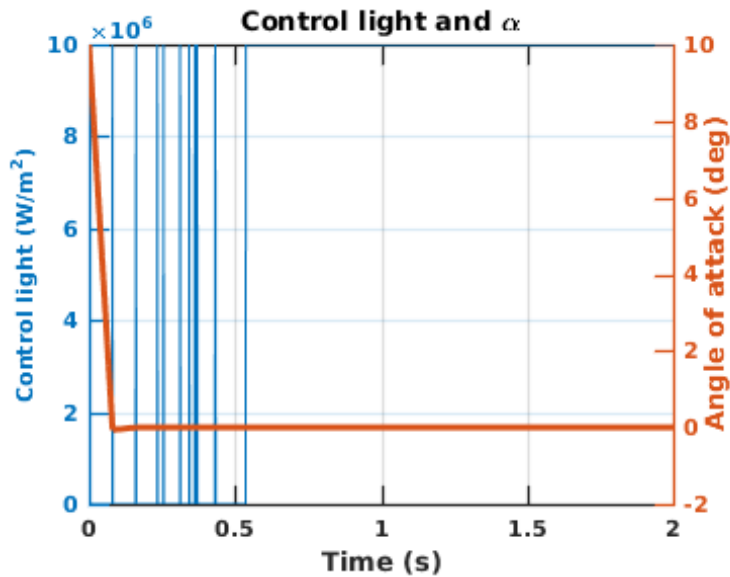


Figure 201. Angle of attack of the hemisphere with the introduction of control with $P_q = 100$, $P_w = 4$ and $\Theta_0 = 10$ deg

10.5.3 Torque due to incident wavefront: aerodynamic analogy

In all the analysis done in the previous subsections, a strong similitude between the hemisphere hit by a set of light rays, and an airfoil immersed in an air stream was considered. Moreover, we discovered that the torque efficiency coefficients are defined in the body-fixed reference frame, as the one for aerodynamic torques. Therefore, we want to force this similitude trying to improve the model introducing the sideslip angle β , and modifying the definition of angle of attack α . This is helpful also because the body is an axis-symmetric one, and therefore we expect a symmetric behavior with respect to the two axes which determine the symmetry. We follow [Zipfel2000]. α is defined as the angle from the projection of the wind x-axis to the body x-axis in the vertical body-symmetry plane and β is defined as the angle between the projection of the body x-axis in the wind plane and the wind x-axis. We can adapt this model to the optomechanics one analyzed in this work. In our model the wind axis is the light one, but it has no sense to talk about relative wind or relative velocity. Therefore, once defined the components of the velocity in body-fixed frame (v, w, u) , we can compute the angles α and β as

$$\begin{aligned}\alpha &= \tan^{-1}\left(\frac{u}{v}\right) \\ \beta &= \sin^{-1}\left(\frac{w}{V}\right)\end{aligned}\tag{107}$$

where $V = \sqrt{v^2 + w^2 + u^2}$. Since the translational part of our system is performed in inertial reference frame, we have to compute v, w and u through a rotation using quaternions. In fact, if we define the quaternion $\mathbf{q}_v^i = [0; \mathbf{v}^i]$, we can rotate it and obtain the components in body-fixed frame \mathbf{v}^b . We can now compute α and β having the velocity components in body-fixed frame. In the hypothesis of small rotations, at least around i_b and k_b , which means $\Theta \gg \Phi, \Psi$, the overall 3D system becomes

$$\mathbf{J}\ddot{\boldsymbol{\theta}} = C_T \cdot I \cdot \mathbf{Q}(\boldsymbol{\gamma})\tag{108}$$

where

$$\begin{aligned}\boldsymbol{\theta} &= \begin{Bmatrix} \Phi \\ \Theta \\ \Psi \end{Bmatrix} \\ \boldsymbol{\gamma} &= \begin{Bmatrix} \alpha \\ \beta \end{Bmatrix} \\ \mathbf{Q} &= \begin{Bmatrix} qt_x \\ qt_z \\ qt_y \end{Bmatrix}\end{aligned}\tag{109}$$

and $\mathbf{J} = \mathbf{I}$ since we are in the fixed-body frame. In matrix form the system is

$$\begin{bmatrix} I_{ii_b} & 0 & 0 \\ 0 & I_{jj_b} & 0 \\ 0 & 0 & I_{kk_b} \end{bmatrix} \begin{Bmatrix} \Phi \\ \Theta \\ \Psi \end{Bmatrix} = C_T \cdot I \cdot \begin{Bmatrix} qt_x(\alpha, \beta) \\ qt_z(\alpha, \beta) \\ qt_y(\alpha, \beta) \end{Bmatrix}\tag{110}$$

There are two issues. First, computing α and β , as defined in the aerodynamic field, gives the problem that if the initial conditions are angles different from zero but velocity components are equal to zero, α and β will be equal to zero; numerical tricks have to be used in order to try to set the correct α and β to compute $\mathbf{Q}(\boldsymbol{\gamma})$. Second, we prefer to have an analytical expression if we want to study the stability of the system and if we want to introduce the control. We want to try to linearize the

non linear term $\mathbf{Q}(\alpha, \beta)$. Therefore, we have $\mathbf{Q}(\boldsymbol{\gamma}) = \mathbf{Q}(\boldsymbol{\gamma}_0) + \left(\frac{\partial \mathbf{Q}}{\partial \boldsymbol{\gamma}}\right)_0 (\boldsymbol{\gamma} - \boldsymbol{\gamma}_0)$, where

$\mathbf{Q}(\boldsymbol{\gamma}_0) = 0$, $\boldsymbol{\gamma}_0 = 0$ and $\left(\frac{\partial \mathbf{Q}}{\partial \boldsymbol{\gamma}}\right)_0$ is the Jacobian of \mathbf{Q} with respect to $\boldsymbol{\gamma}$. Substituting in $\boldsymbol{\gamma}$ the linearization with $\boldsymbol{\theta}$, given $\boldsymbol{\gamma}(\boldsymbol{\theta}_0) = 0$ we obtain

$$\mathbf{J}\ddot{\boldsymbol{\theta}} = C_T \cdot I \cdot \left(\frac{\partial \mathbf{Q}}{\partial \boldsymbol{\gamma}}\right)_0 \left(\frac{\partial \boldsymbol{\gamma}}{\partial \boldsymbol{\theta}}\right)_0 (\boldsymbol{\theta} - \boldsymbol{\theta}_0)\tag{111}$$

where

$$\begin{aligned} \left(\frac{\partial \mathbf{Q}}{\partial \boldsymbol{\gamma}}\right)_0 &= \begin{bmatrix} \frac{\partial q_{t_x}}{\partial \alpha} & \frac{\partial q_{t_x}}{\partial \beta} \\ \frac{\partial q_{t_z}}{\partial \alpha} & \frac{\partial q_{t_z}}{\partial \beta} \\ \frac{\partial q_{t_y}}{\partial \alpha} & \frac{\partial q_{t_y}}{\partial \beta} \end{bmatrix}_0 \\ \left(\frac{\partial \boldsymbol{\gamma}}{\partial \boldsymbol{\theta}}\right)_0 &= \begin{bmatrix} \frac{\partial \alpha}{\partial \Phi} & \frac{\partial \alpha}{\partial \Theta} & \frac{\partial \alpha}{\partial \Psi} \\ \frac{\partial \beta}{\partial \Phi} & \frac{\partial \beta}{\partial \Theta} & \frac{\partial \beta}{\partial \Psi} \end{bmatrix}_0 \end{aligned} \quad (112)$$

are the Jacobian and $\boldsymbol{\theta}_0 = \mathbf{0}$. In regards to the previous equation (top), we hypothesize that the same torque and force efficiency curves can be used both for α and β . Therefore, we can numerically obtain the values for all the components of the jacobian $\left(\frac{\partial \mathbf{Q}}{\partial \boldsymbol{\gamma}}\right)_0$. The problem is instead related to bottom part of the previous equation, where we have to find a relation between the components of $\boldsymbol{\gamma}$ and $\boldsymbol{\theta}$. We don't have a direct relation between $\boldsymbol{\gamma}$ and $\boldsymbol{\theta}$, but we know that

$$\frac{\partial \boldsymbol{\gamma}}{\partial \boldsymbol{\theta}} = \frac{\partial \dot{\boldsymbol{\gamma}}}{\partial \dot{\boldsymbol{\theta}}} \quad (113)$$

and we know [Etkin2006] that we can express α and β function of α , β and the components of the angular velocity in body-fixed frame (p, q, r) :

$$\begin{aligned} \alpha &= q - q_w \sec \beta - p \cos \alpha \tan \beta - r \sin \alpha \tan \beta \\ \beta &= r_w + p \sin \alpha - r \cos \alpha \end{aligned} \quad (114)$$

We can adapt these equations to the light, which has no angular velocity, and is fixed in space and time. In output from the dynamics of our system we have the components of the angular velocity in body-fixed frame (p, q, r) , but we need an expression with α and β function of the angular rates Φ , Θ and Ψ . We got an expression which relates Φ , Θ and Ψ to p, q and r . If we invert this equation we can get to an useful expression:

$$\begin{bmatrix} \Phi \\ \Theta \\ \Psi \end{bmatrix} = \begin{bmatrix} 1 & \sin \Phi \tan \Theta & \cos \Phi \tan \Theta \\ 0 & \cos \Phi & -\sin \Phi \\ 0 & \sin \Phi \sec \Theta & \cos \Phi \sec \Theta \end{bmatrix} \begin{bmatrix} p \\ q \\ r \end{bmatrix} \quad (115)$$

If we calculate p , q and r from the previous equation and we substitute them into α and β we obtain an analytical expression of α and β function of θ that we can differentiate in order to compute $\left(\frac{\partial \gamma}{\partial \theta}\right)_0$. As we said, it is true that for small angles $(p, q, r) = (\Phi, \Theta, \Psi)$, we can (taking care of the hypotheses done) substitute obtaining

$$\begin{aligned} \alpha &= \Theta - \Phi \cos \alpha \tan \beta - \Psi \sin \alpha \tan \beta \\ \beta &= \Phi \sin \alpha - \Psi \cos \alpha \end{aligned} \quad (116)$$

At this point we can compute the Jacobian; considering the last equations, the result is the following

$$\left(\frac{\partial \gamma}{\partial \theta}\right)_0 = \begin{bmatrix} -\cos \alpha \tan \beta & 1 & -\sin \alpha \tan \beta \\ \sin \alpha & 0 & -\cos \alpha \end{bmatrix}_0 \quad (117)$$

If we consider that force(torque) coefficients are really small and therefore negligible in J_i (i_b, k_b) direction, the other Jacobian becomes

$$\left(\frac{\partial \mathbf{Q}}{\partial \gamma}\right)_0 = \begin{bmatrix} 0 & 0 \\ \frac{\partial q_{t_z}}{\partial \alpha} & 0 \\ 0 & \frac{\partial q_{t_y}}{\partial \beta} \end{bmatrix}_0 = \begin{bmatrix} 0 & 0 \\ K_{t_{z\alpha}} & 0 \\ 0 & K_{t_{z\beta}} \end{bmatrix}_0 \quad (118)$$

The product between the two Jacobians results in

$$\left(\frac{\partial \mathbf{Q}}{\partial \gamma}\right)_0 \left(\frac{\partial \gamma}{\partial \theta}\right)_0 = \begin{bmatrix} 0 & 0 & 0 \\ -K_{t_{z\alpha}} \cos \alpha \tan \beta & K_{t_{z\alpha}} & -K_{t_{z\alpha}} \sin \alpha \tan \beta \\ K_{t_{z\beta}} \sin \alpha & 0 & K_{t_{z\beta}} \cos \alpha \end{bmatrix}_0 \quad (119)$$

The overall linearized system becomes

$$\begin{bmatrix} I_{iib} & 0 & 0 \\ 0 & I_{jjb} & 0 \\ 0 & 0 & I_{kkb} \end{bmatrix} \begin{Bmatrix} \Phi \\ \Theta \\ \Psi \end{Bmatrix} = C_T \cdot I \cdot \begin{bmatrix} 0 & 0 & 0 \\ -K_{t_{z\alpha}} \cos \alpha \tan \beta & K_{t_{z\alpha}} & -K_{t_{z\alpha}} \sin \alpha \tan \beta \\ K_{t_{z\beta}} \sin \alpha & 0 & K_{t_{z\beta}} \cos \alpha \end{bmatrix} \begin{Bmatrix} \Phi \\ \Theta \\ \Psi \end{Bmatrix} \quad (120)$$

Since $\theta_0 = \mathbf{0}$, we have that $\delta\theta = \theta - \theta_0 = \theta$. The same happens with $\ddot{\theta} = \delta\ddot{\theta}$, because $\theta_0 = const$ and if we derive, zero is obtained. The introduction of the sideslip angle β changes the overall 3D result. Just using angle of attack α and sideslip angle β , the system is not fully defined: in this way, the "spin" and third angle is not considered. It means that introducing an initial condition for the beta angle different from zero, oscillations both around Φ and Ψ occur. The result is a full rotation of the system. Figure 202 shows an example with initial condition of $\alpha_0 = 10\text{deg}$ and $\beta_0 = 2.25\text{deg}$. The final results confirm the expectations. A stable oscillation of the whole system is obtained.

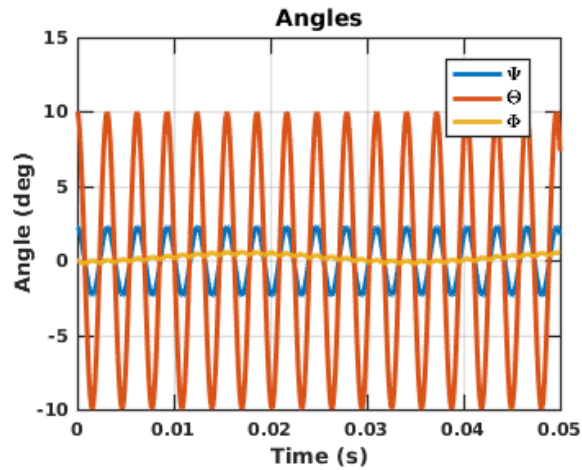


Figure 202. Euler angles with initial conditions equal to $\alpha_0 = 10\text{deg}$ and $\beta_0 = 2.25\text{deg}$. The system is stable

Figure 203 confirms what we expect from the theory, which means that the oscillation of the whole system is still stable for angles in the negative range of $K_{t_{z\alpha}}$ and $K_{t_{z\beta}}$.

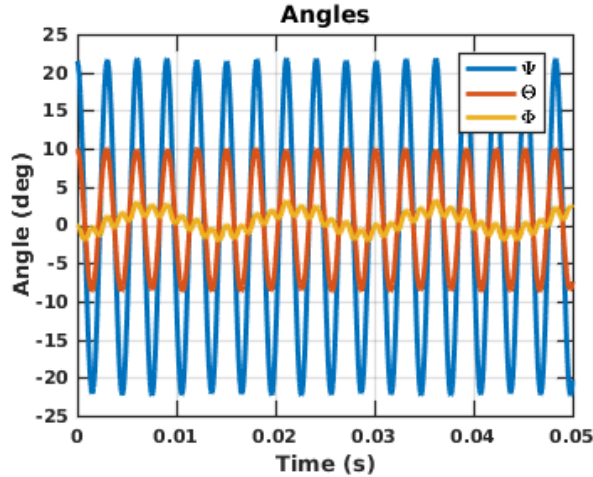


Figure 203. Euler angles with initial conditions equal to $\alpha_0 = 10 \text{ deg}$ and $\beta_0 = 21.5 \text{ deg}$. The system is still stable

When at least one of the coefficients becomes positive, the oscillations diverge and the system becomes unstable (Figure 204), like the one in the next figure, where the initial conditions are $\alpha_0 = 10 \text{ deg}$ and $\beta_0 = 44.5 \text{ deg}$, therefore with $K_{t-\beta} > 0$.

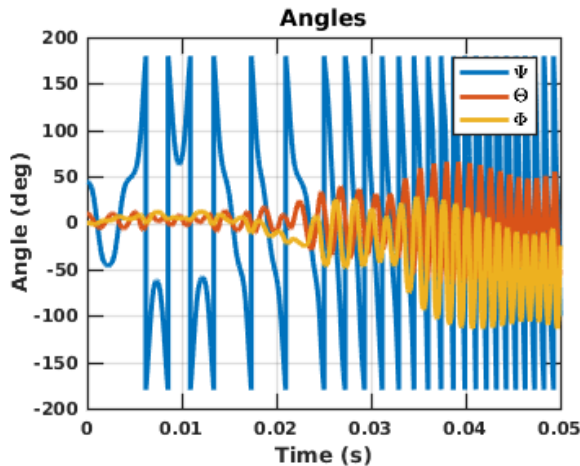


Figure 204. Euler angles with initial conditions equal to $\alpha_0 = 10 \text{ deg}$ and $\beta_0 = 44.5 \text{ deg}$. The system becomes unstable

Using the same equations, we can extend the system to a multi-body one, solving the same differential equations for every hemisphere. For each particle, the system of equations is solved. In Figure 205, we can see different behaviors that occur when the initial orientation (angle of attack α) changes. Wider oscillations components occur for initial angle of attack far from the stable equilibrium angles (-90 deg , 0 deg and 90 deg), but they remain limited.

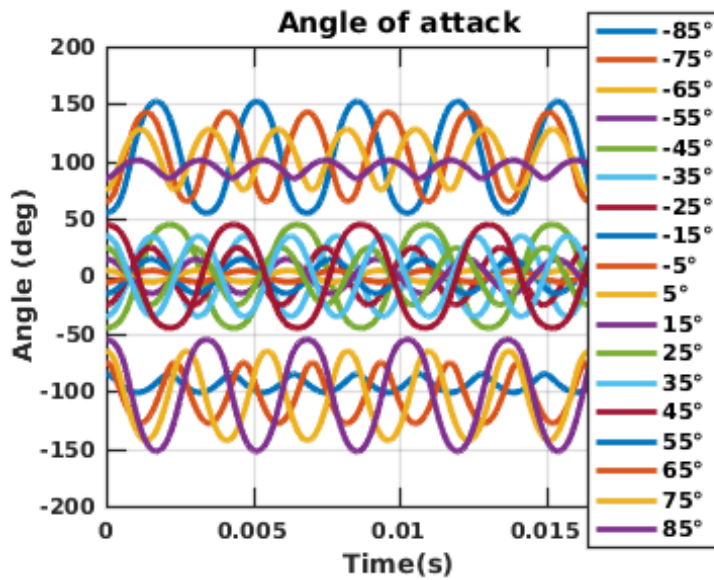


Figure 205. Angle of attack α with initial angular velocity equal to $0 \frac{rad}{sec}$

The phase diagram (Figure 206) for the angle of attack is of greater interest, since it is clearer how the attitude behavior of the particle changes depending on the initial condition. The analysis varying the initial orientation is performed. This familiar representation shows how each particle behaves around the equilibrium angles.

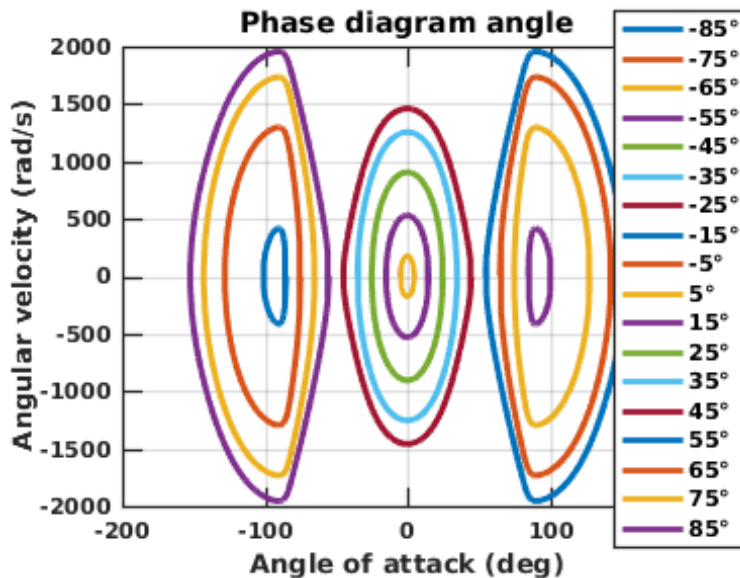


Figure 206. Phase diagram showing periodic motion for a hemisphere at varying of initial angle of attack

α with initial angular velocity equal to $0 \frac{rad}{sec}$

In Figure 207, we can see what changes with the increase the initial angular velocity. As expected (shown in Figure 208), after a certain level of initial angular velocity,

combined with greater initial orientation with respect to $\alpha = 0$, some oscillations are not limited anymore around the closest equilibrium angle. This means that the oscillation is still stable, but with very high amplitude in angle.

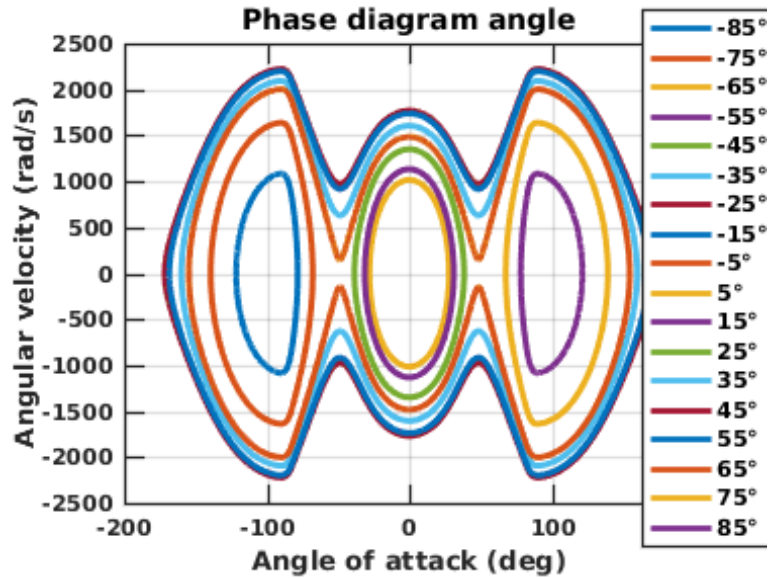


Figure 207. Phase diagram showing periodic motion for a hemisphere at varying of initial angle of attack

α with initial angular velocity equal to $1000 \frac{rad}{sec}$

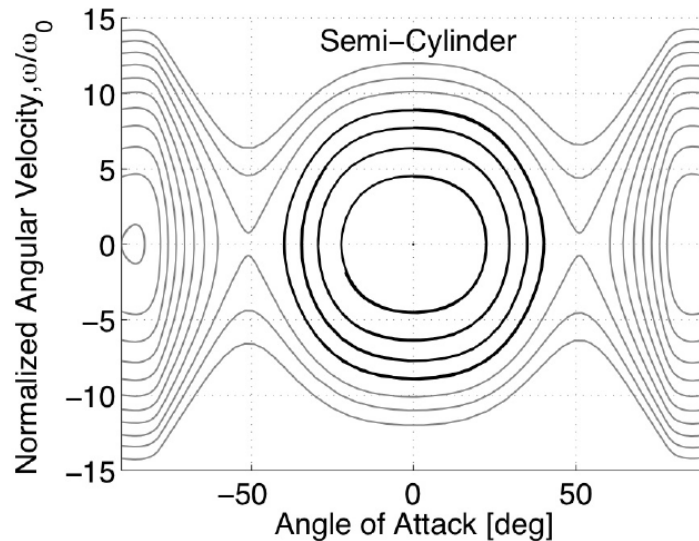


Figure 208. Phase diagram showing periodic rocking motion for a semicircular wing by Swartzlander.

Next, we introduce the idea to control the attitude of a cluster of bodies by considering their rotational average, and so to apply a unique beam of light to control them. The first trial for the control law is to consider the average orientation of the hemispheres and to treat this value as it were the orientation of a bigger rigid body.

The same consideration can be done for the angular velocity. Once decided that the only feasible option is the unique control depending on the states of all the bodies, the immediate thought would be to develop a control law depending on the average orientation. But, how to threat and to evaluate the average orientation? according to the convention used in this thesis, there are two ways: a) create the control law directly through the average quaternion or, b) computing the average orientation using Euler angles. The latter would be easier to implement in the code, the former instead would be more complicated under the theoretical point of view, but more correct and coherent with the development of the code and of the theory used in this chapter. Moreover, also under a real life application point of view it would be correct. Therefore, we decided to proceed with the average considering quaternion. It is not a R^3 algebra, therefore the classical average for each component is not valid. The algorithm suggested by Markley [Markley2007] is implemented. Basically, we want to find the quaternion that should minimize a weighted sum of the squared Frobenius norm of attitude matrix differences, i.e.:

$$\bar{\mathbf{q}} := \arg \min \sum_{i=1}^n w_i \| A(\mathbf{q}) - A(\mathbf{q}_i) \|_F^2 \quad (121)$$

where \mathbf{q}_i are the normalized n attitude estimates and w_i the associated weights. Using the definition of the Frobenius norm, we get to

$$\begin{aligned} \| A(\mathbf{q}) - A(\mathbf{q}_i) \|_F^2 &= \text{Tr}[A(\mathbf{q}) - A(\mathbf{q}_i)]^T [A(\mathbf{q}) - A(\mathbf{q}_i)] \\ &= 6 - 2\text{Tr}[A(\mathbf{q})A^T(\mathbf{q}_i)] \end{aligned} \quad (122)$$

which allows to write the previous equation as $\bar{\mathbf{q}} = \arg \max \text{Tr}[A(\mathbf{q})B^T]$, where $B := \sum_{i=1}^n w_i A(\mathbf{q}_i)$. The matrix B is known as the attitude profile matrix, since it contains all the information related to the attitude. Since we are directly working with quaternions, the form of the last equation can be simplified. In particular, it gets to a form like $\text{Tr}[A(\mathbf{q})B^T] = \mathbf{q}^T K \mathbf{q}$, where K is the symmetric traceless 4×4 matrix

$$K := \begin{bmatrix} B + B^T - \text{Tr}(B)I_{3 \times 3} & \mathbf{z} \\ \mathbf{z}^T & \text{Tr}(B) \end{bmatrix} \quad (123)$$

and \mathbf{z} is defined as $\mathbf{z} := B^T - B$. With few substitution and simplifications, it becomes

$K := 4M - w_{tot} I_{4 \times 4}$, where $w_{tot} := \sum_{i=1}^n w_i$ and $M := \sum_{i=1}^n w_i \mathbf{q}_i \mathbf{q}_i^T$. Finally, the average quaternion can be found by the maximization process $\bar{\mathbf{q}} = \arg \max \mathbf{q}^T M \mathbf{q}$. Therefore,

the average quaternion, which comes from the maximization problem of the last equation is the eigenvector of M corresponding to the maximum eigenvalue. In this way, both the problem of the unit norm of the quaternion and the flaw related to the fact that \mathbf{q} and \mathbf{q}_i represent the same rotation, are avoided, since changing the sign of any \mathbf{q}_i does not change the value of M . If we want to give a physical definition to this maximization problem, it consists in the least square minimization of all the vectorial part of the quaternions. This means that we are looking for the vector (direction) with lower error compared to the whole set of estimates \mathbf{q}_i and to their vectorial part. The final result for a simulation with random initial angle of attack between -2.5deg and 2.5deg is shown in Figure 209. One can see that even if the average angle of attack is kept around 0deg , the angle of attack of every single hemisphere can vary, because of the conservation of momentum.

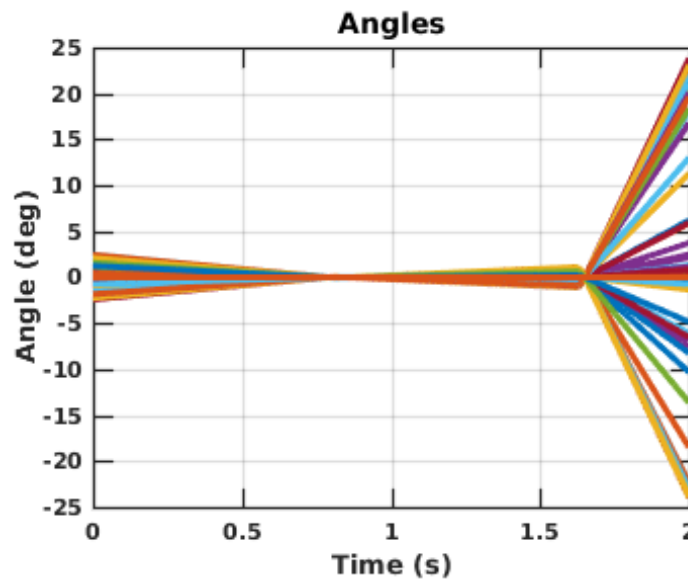


Figure 209. Multi-body system (100 hemispheres) controlled using the average orientation

The promising behavior is the one that in every simulation performed, there is a convergence of all the angles of attack towards 0deg as shown in Figure 210. This means that with proper constraints in the control law, we could keep the variation of α_i close to 0deg and to avoid the subsequent divergence. The simulation was performed in Chrono::Engine, because of the high number of hemispheres simulated (100). The greater the number, the better results we would expect because of a more proper distribution of the initial angles of attack. Future work would involve adding higher order statistical moments (the mean is only the zeroth-moment), to limit the angular instability observed in the previous picture.

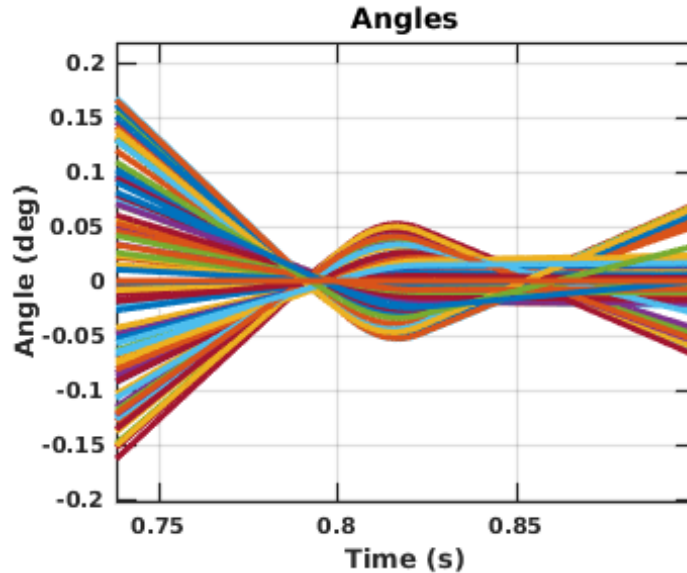


Figure 210. Detailed view of the convergence in the multi-body system (100 hemispheres) controlled using the average orientation

11. Image reconstruction simulation and experiments

Theoretical, numerical, and experimental research was carried out to explore credible limits to the concept of a disconnected “granular imager” controlled by radiation pressure to form an image. This necessitated two separate sub-tasks: radiation pressure demonstrations, and computational imaging studies. According to conventional thinking, freely moving grains in space will not form an acceptable image on a focal plane detector unless the grains can be positioned and maintained to conform to a thin (e.g., less than a fraction of a wavelength) spherical or parabolic surface. Advances in computational imaging provide the potential to relax this requirement. To advance the granular telescope concept, we assumed that the grain orientation could be frozen in space during an image exposure period. We also assumed that the grains, which may number in the hundreds or thousands, could not be fixed in an ideal configuration (e.g., along a parabolic surface). This latter assumption was made after it was determined that an open loop control scheme to fix the orientation of each grain is beyond our reach. Consequently, tip, tilt, and piston deviations from this idea surface results in poor, highly speckled images. However, our experimental measurements, as well as numerically modeled computations, successfully demonstrated that a near diffraction-limited image could be reconstructed from the combined information from twenty or more exposures. By combining lucky imaging, shift-and-add, and multiframe blind deconvolution techniques for 100 speckled frames, we were able to reconstruct an image of a binary light source, even though the system suffered tip/tilt errors as large as 20-40 waves across the baseline of the granular cloud. This fundamental imaging accomplishment provides confidence that more complicated objects can be imaged with this

technique. What is more, this value of ~ 20 waves provides a target for a future system that will control the orientation of the grains. Radiation pressure provides a means controlling grain orientation by means of optical torque. We explored several advanced methods of demonstrating this torque by means of a laser. Earlier work had achieved light-induced torque of optical wings in a liquid. In this study we attempted to eliminate the confounding effects of gravity and heat-induced buoyancy changes. This included experiments using first the heavy liquid sodium polytungstate to achieve neutral buoyance of glass hemispheres, then magnetic levitation of bismuth foil and pyrolytic graphite film, and finally acoustic levitation by means of a standing ultrasonic wave. The later shows the most promise, as we succeeded in levitating optically reflective and refractive objects. We believe a more advanced ultrasound source (we used an audio compression driver) will provide a means to observe radiation pressure and torque on small levitated grains. In summary, a granular imaging space telescope having a poor optical figure was found to be feasible by making use of advanced computational imaging techniques. A control scheme to curtail the wavefront error is a remaining challenge, and the force from radiation pressure may be one of a number of mechanisms that will be needed to stabilize the grains. This study shows, however, that uncharacteristically large values of tip/tilt errors (for a telescope) may be acceptable, thereby lessening the need for sub-wavelength grain control.

11.1 Experimental and Numerical Model in the Far-Field

A set of randomly placed small apertures, each having a random wave front error, was used in place of a continuous error-free aperture in an imaging system. See Figure 211. Using the numerical model, we analyzed the effect of noise, phase aberration, bandwidth, and the effect of element fill factor on the image quality. The speckled intensity profiles of broadband point sources (400-730nm) were restored using multiframe blind deconvolution coupled with lucky imaging. Diffraction limited resolution that is comparable to a continuous aperture of the same baseline was achieved.

Imaging of distant targets typically results in resolution loss due to the diffraction blur, caused by the limited angular extent of the primary aperture. A monolithic aperture with large diameter is desirable. However, the size is limited by the weight, and the cost of construction and maintenance. New computational imaging techniques are being developed to improve the resolution by compensating the hardware limitations with the power of computational post processing. We address the case of an ill-figured multi-aperture system that comprises of an array of very small sized aperture elements, for imaging broadband point sources. An illustration of the randomized aperture scheme, shown in the figure below which depicts a point source (or sources) at an infinite distance from elements that are distributed across a quasi-parabolic surface of baseline D . For a continuous parabolic reflector, a diffraction-limited image would appear on the detector placed at focal distance f . However, tip-tilt and piston errors associated with each aperture element produces speckles, and the image is further degraded as the bandwidth increases.

Furthermore, the distribution may be varying randomly in time, and we therefore assume that little knowledge of the Point Spread Function (PSF) can be obtained. We ask the following the proof of concept question: Is it possible to reconstruct a diffraction-limited image from such a system?

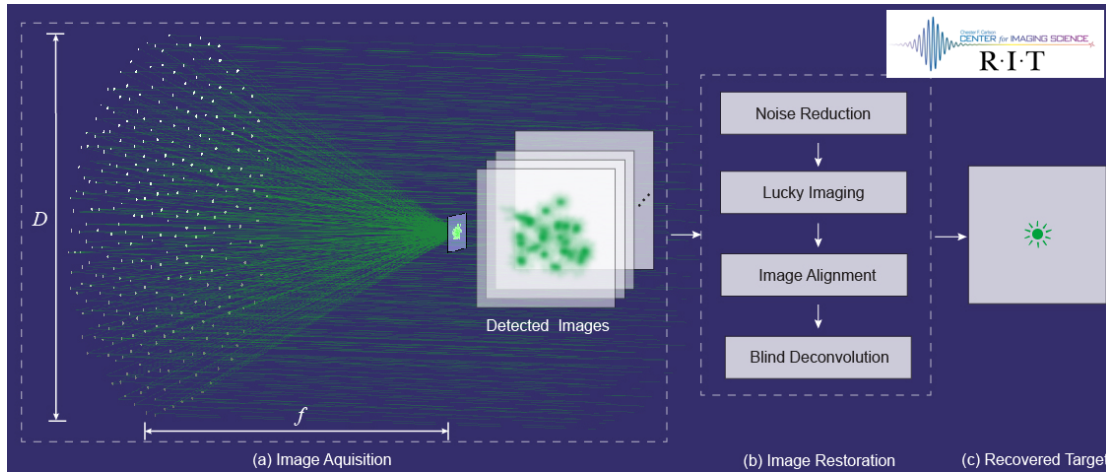


Figure 211. Sketch of granular imager.

Efforts at solving the random distortion problem can be traced back to Wiener. These works rely on the prior knowledge of the PSF or the statistical model of the turbulence. Techniques such as lucky imaging, shift-and-add, cross spectrum analysis, phase retrieval, and phase diversity were also developed for the recovery of images that are affected by the phase aberrations from turbulence. These techniques have proved to produce diffraction limited resolution, but are limited to a relatively narrow bandwidth, or they require reference information. Fergus proposed an unconventional camera lens comprises of an array of randomly placed small mirrors, the system exhibit a static random distortion, which was solved by the used of machine learning method.

We focused on solving a dynamic random distortion problem in a broadband scenario, using the multiframe blind deconvolution techniques. The major advantage of the blind deconvolution compared with other methods is the ability of retrieving a diffraction limited image of an object without reference information and little prior knowledge of the object and PSF. By using multiframe as convergence constraints, the ratio of unknowns (the PSF and the object) to known (recorded image) can be increase from 2:1 in single frame schemes to $N+1:N$ (for $N \gg 1$), which offers great help in restoration of low contrast and high corrupted images. However, most convex optimization based blind deconvolution techniques may stuck at local minima, as the degradation of image quality increases.

To overcome this problem, we propose to couple noise reduction and lucky imaging with a multi-frame blind deconvolution for image restoration.

Experiment: The experimental setup of the random aperture system was shown below (Fig. 212) where a transmissive mask was positioned at the surface of a convex lens of focal length $f=300$ mm. Figure 212 (a) shows the far field experiment with

spatially filtered (SFLT) broadband beam with diameter of D , is diverted by a beam splitter (BS) to produce a binary point light source, and transmitted through a phase mask (PM) and aperture mask (AM) near the front face of a lens L of focal length f . Each aperture element has a diameter d . Using different random masks, multiple images are recorded on the detector array (DA) which is placed in the back focal plane of the lens. Figure 212(b) shows a photo of aperture mask used in far field experiment. A set of 50 thin foil masks was produced, each having $M \sim 130$ randomly placed aperture elements distributed across a $D = 9\text{mm}$ diameter. Each element has a diameter approximately $d = 0.2\text{mm}$. The foil was covered by a layer of wrinkled cellophane to randomize the phase at each pinhole. A laser-driven white light source was spatially and spectrally filtered to produce a collimated polychromatic beam with a wavelength λ ranges from 400 to 730nm. A pinhole with a diameter of $5\ \mu\text{m}$ was used as a spatial filter to produce spatially coherent light. The aperture array is placed within the coherence length of the source, which is about 350 mm. Rays transmitted through the mask was recorded at the back focal plane of the convex lens using a Canon 5D Mark III camera. The pixel pitch of the camera is $6.25\ \mu\text{m}$ and detector size is $24 \times 36\ \text{mm}$. The estimated spectral response of the detector is shown in the figures below. An effective second mutually incoherent light source was also introduced by transmitting the beam through the system at an angle $\theta \sim 1.22\lambda/D$ to form a binary source system.

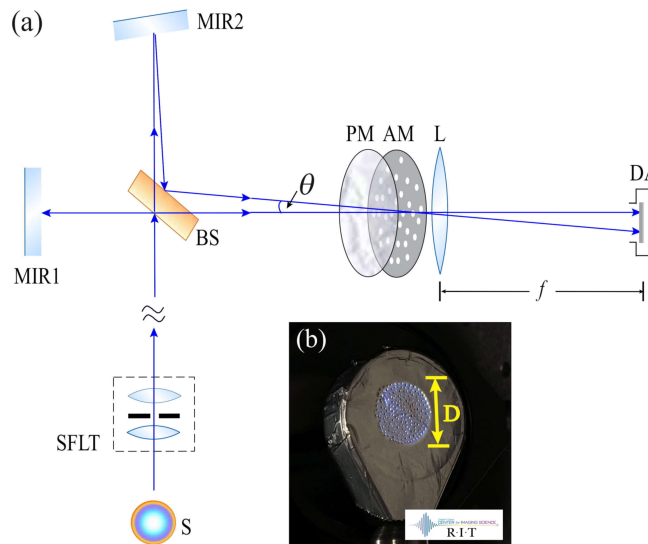


Figure 212. Schematic of randomized aperture imaging system.

Model: An illustration of the numerical model of the randomized aperture system is shown in Figure 213(a). Figure 213 (b) shows an example of pupil plane, which consists of approximately 50 non-overlapping circular aperture elements. Each has a diameter of $d=2r$, and centered randomly at (x_i, y_i) within a baseline of diameter $D=2R$ on an $N \times N$ grid. Figure 213 (c) shows the tip-tilt component of the phase error in pupil plane ($\sigma = 5\lambda/D$). Figure 213 (d) shows the piston component of the phase error in pupil plane (one wave). Mathematically, such an array can be represented by

a sum of a random distribution of complex aperture element functions within a baseline, in pupil plane as

$$U(\hat{\mathbf{x}}) = B(\hat{\mathbf{x}}) \left[\sum_{m=1}^M U_m(\hat{\mathbf{x}}) \right] \quad (124)$$

where B is the amplitude transfer function of the baseline, and M is the number of aperture elements. A circular baseline with radius R (diameter $D = 2R$) may be represented by a super-Gaussian function. The complex pupil function of the m^{th} aperture element may be expressed $U_m = A_m \exp(i \phi_m)$ where A and ϕ are respectively the amplitude and phase functions of the aperture element. We employ a Poisson disk sampling algorithm to generate a non-overlapping circular aperture within the baseline. The amplitude function of each circular aperture with radius r , may also be expressed as a super-Gaussian function. We consider only the lowest order aberrations of piston and tip/tilt phase contributions across each aperture element:

$$\phi = (2\pi/\lambda)(\Delta z_m + x\Delta\alpha_{x,m} + y\Delta\alpha_{y,m}) \quad (125)$$

where λ is the wavelength, Δz is the piston displacement of an aperture element, which has a random uniform pairwise independent distribution with support $[0,\lambda]$, and $\Delta\alpha$ is a random tip/tilt angle, each having a pairwise independent Gaussian random distribution with zero mean and variance of σ^2 .

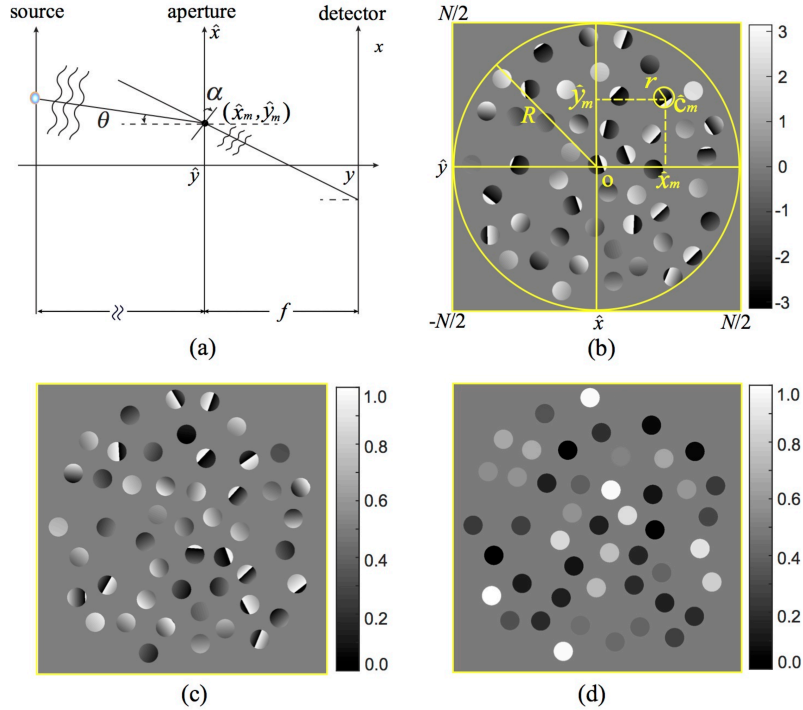


Figure 213. Illustration of numerical model of randomized aperture imaging system in far field scheme.

For a single quasi-monochromatic point source at infinity subtending the optical axis by an angle (θ_x, θ_y) the electric field at a back focal plane of the system may be numerically represented by a Fourier transforms of the field exiting the system aperture

$$E(\mathbf{x}, \lambda) = \iint \exp\left(-i\frac{2\pi}{\lambda f}\hat{\mathbf{x}}\mathbf{x}\right) U(\hat{\mathbf{x}})\psi(\hat{\mathbf{x}})d\hat{\mathbf{x}} \quad (126)$$

where f is the focal length, $\psi = \exp(i(2\pi/\lambda)(x\theta_x + y\theta_y))$ is the phase contribution from the light source. For a polychromatic source the intensity at a focal plane detector may be numerically represented as a incoherent superposition of intensity distributions, each representing a narrow band of wavelengths:

$$g(\mathbf{x}) = \mu_\lambda \sum_\lambda |E(\mathbf{x}, \lambda)|^2 \quad (127)$$

where μ is the spectral distribution of the source and detector. In practice, an object may be decomposed into a distribution of mutually incoherent point sources. In that case the total intensity recorded by the detector may be represented as a linear superposition of the intensity distributions of each source.

For digital detectors, two primary noise sources include photon shot noise and readout noise. Photon noise is caused by the nature of light, and is scene dependent. The photon noise contaminated image is known to have a Poisson distribution. Readout noise associated with voltage fluctuation and amplifier gain, and has a Gaussian distribution with zero mean, and can be modeled as additive noise. An image corrupted by both photon and readout noise can be modeled numerically as

$$g_{\text{noise}} = \frac{1}{c_0} \text{Poisson}(c_0 g) + \text{Gaussian}(0, \sigma_{\text{read}}^2) \quad (128)$$

where g is the ideal noise free image, c_0 is a constant used to adjust the Poisson noise level, and σ_{read}^2 is the variance of Gaussian noise. The signal-to-noise-ratio (SNR) is calculated in unit of decibel (DB) as $\text{SNR} = 10 \log_{10}(\mu/\sigma_n)$ where μ is the mean value of a noise free image, and σ_n is the standard deviation of the noise mixture, i.e., $g_{\text{noise}} - g$. The phase errors, noise, and mirror fill factors are the main factors that affect the quality of the images we obtained from the aperture array system. We show below the system modulation transfer function (MTF) for various amounts of tip-tilt error and piston error in Fig 214 (a) and 214 (b) respectively. As we can see, almost 60% of high frequency information is lost as the tip-tilt error is increased from 0.5 to $700\lambda/D$ and piston error is increased from 0.5 to 1.5 waves. It is also noticed that the loss of frequency details is inverse proportional to the mirror fill factor without phase error, Fig. 214 (c). However, as the phase error increases, the fill-factor no longer serves as a dominant factor to the loss of high frequency details, Fig. 214 (d).

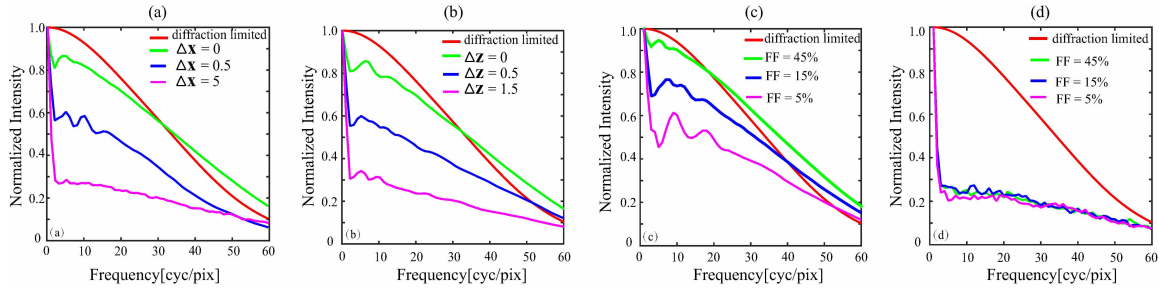


Figure 214. Sensitivity of MTF to (a) tip-tilt error, (b) piston error, (c) fill-factor (FF) without phase error, and (d) fill factor, with phase error (tip-tilt $5\lambda/D$, piston 1 wave).

Image Recovery: Multiframe blind deconvolution algorithms aim to recover the target objects from a set of corrupted observations. Assuming at each time point $n = 1, 2, \dots, N$, the random aperture mirror system produce an image, with a set of image given by $\{g_n\}$. Given a shift-invariant imaging system (or approximately shift-invariant), the image formation process can be modeled as convolution of the object and the system PSF where the recorded n^{th} image g_n may be expressed as a convolution of f with h_n , where f represent the target objects and h_n is the PSF at time point n . Using Borel's convolution theorem, this relationship may be expressed as a

product of the the two Fourier transforms, $F = \text{FT}\{f\}$ and $H_n = \text{FT}(h_n)$, so that $G_n = \text{FT}\{g_n\} = F H_n$. The multiframe blind deconvolution technique is especially suited for cases where PSF is temporally varying and impractical to measure. If prior knowledge of the object is unknown, the multiframe blind deconvolution is usually modeled as a non-negatively constrained minimization problem, which can be solved by either batch or online optimization approaches.

$$\{f, h_n\} = \min_{h_n \geq 0, f \geq 0} \frac{1}{N^2} \sum_{n=0}^N \sum_{\mathbf{u}} |G_n - F H_n|^2(\mathbf{u}) \quad (129)$$

We used an efficient alternating online solution to solve the above equation which gives an iterative update scheme:

$$H_n = H_{n-1} \odot \frac{F_n^T G_n}{F_n^T (F_n H_{n-1})} \quad F_n = F_{n-1} \odot \frac{H_n^T G_n}{H_n^T (H_n F_{n-1})} \quad (130)$$

The iteration stops when all the frames in the sequence are processed, or the accumulative reconstruction error is smaller than some desired value.

Reconstructed Experimental Results: A series of 50 speckled images of a broad band binary light source (400-700nm, continuous), as well as the ground-truth image are obtained using the setup described above. The captured raw image is demosaiced, and multi-frame deconvolution is performed on each channel of the demosaiced color image. As seen in the comparison below (Fig. 215), the line profiles ground-truth image and the reconstructed image are nearly identical. The spatial separation error and peak ratio error of the reconstruction are less than 5% and 25% respectively. Figure 215 shows the peak ratio of the binary source is about 0.9, angular separation is about $1.22\lambda/D$. The data sequence is obtained with 100 different aperture masks, each has $M \sim 90$ non-overlapping aperture elements with a fill-factor of $\sim 15\%$. (a) Examples of most lucky frames. Figure 215 (b) shows examples of least lucky frames; Figure 215 (c) shows the ground truth of the binary source. Figure 215 (d) shows the restoration result of the binary sources. Figure 215 (e) shows a comparison of the line profile ground truth and restoration result showing excellent agreement in relative magnitudes of the two peaks, angular separation, and profiles.

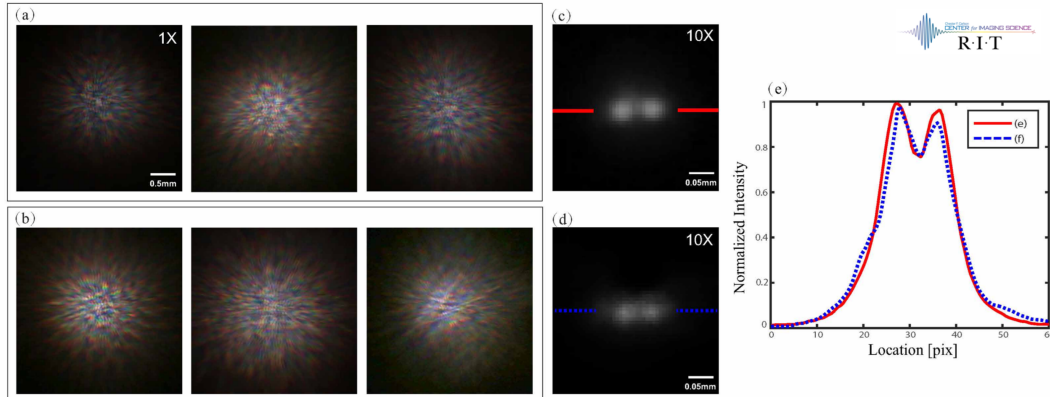


Figure 215. Image reconstruction result from experimental images of a broadband (400-730 nm) binary source.

Reconstructed Numerically Modeled Results: A series of 50 speckled images of a broad band binary light source (400-700nm, 5nm gap) with angular separation of $1.22\lambda/D$ is numerically generated, where λ is the central wavelength. The pupil consists of approximately 150 circular aperture elements of the same sizes. The ratio between the diameter of the aperture element and the baseline of the entire array is 45:1. The wavefront error at each aperture element has a zero mean Gaussian random tip-tilt phase with standard deviation $\sigma = 5\lambda/D$, and a uniformly distributed piston error of one wave. A ground-truth image of the target is also numerically generated using a monolithic pupil with diameter equals to the size of the baseline of the sub-aperture array. The data simulated under this condition exhibit similar features with the data obtained experimentally, therefore an estimation of $5-10 \lambda/D$ tip-tilt error may be made to the experimental data. Poisson noise with scaling factor of $c_0 = 0.5$ is modeled as photon noise. Gaussian noise with zero mean and a variance σ_n equals to 1% of the image intensity is also added as dark noise. The averaged SNR over the entire sequence is about 9.5 decibel. As can be seen the binary sources are successfully reconstructed, as was the case for the experimental data above. The spatial separation error and peak ratio error of the reconstruction are less than 5% and 25% respectively. The agreement between the experimental and numerically modeled results verifies the accuracy of our model (Figure 216). Figure 216 shows the peak ratio of the binary source is 0.9, angular separation is $1.22\lambda/D$. The data sequence is simulated with 100 different aperture masks, each has $M \sim 150$ non-overlapping aperture elements with a fill factor of $\sim 15\%$. The tip-tilt error across each aperture element has a Gaussian distribution with zero mean and $\sigma = 5\lambda/D$, and piston error is one wave. The average SNR of the sequence is about 9.5 decibel. Figure 216 (a) shows examples of most lucky frames. Figure 216 (b) shows examples of least lucky frames; Figure 216 (c) shows ground truth of the binary source. Figure 216 (d) shows the restoration result of the binary sources. Figure 216 (e) shows the comparison of the line profile ground truth and restoration result.

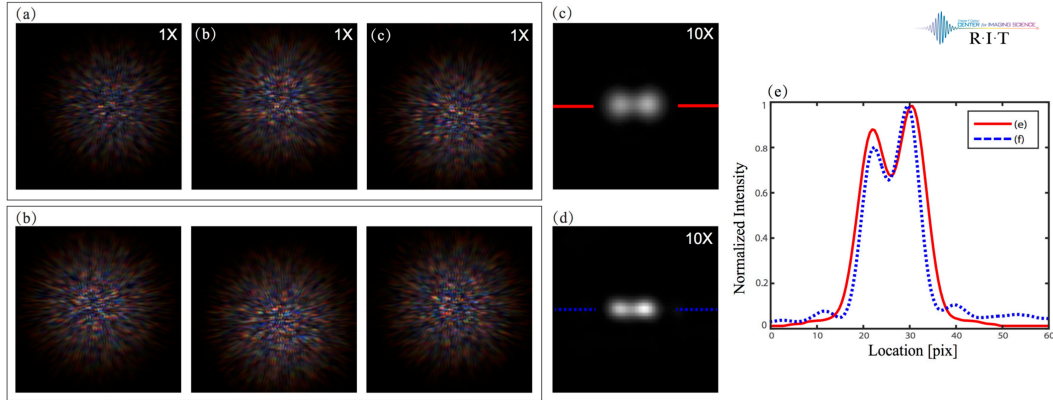


Figure 216. Image reconstruction result from numerical images of a broadband (400-730 nm) binary source in presence of phase aberration and noise.

11.2 Experimental and Numerical Model in the Near-Field

We envisioned two scenarios for a granular imager. The first assumed that light reaching the detector underwent Fraunhofer diffraction owing to the relatively small size of the reflecting elements. Each reflector produced a Fraunhofer wavelet, and the interference of these wavelets in the plane of the detector provided optical information about the light source (e.g., a binary star). In this section we assume light from the reflectors undergoes no diffraction (i.e., negligible Fresnel diffraction). This scenario provides optical information about the source if the un-diffracted beamlets interfere. The illustration below (Figure 217) depicts light from a distant stellar object along the line d_0 , reflecting from a circular reflector, and illuminating a detector array (DA). The bottom row depicts a random circular distribution of reflectors with tip/tilt and piston phase.

In Figure 217, a geometric representation of the near field numerical model of a granular imager is shown. The aperture array consists approximately 50 circular reflecting elements of diameter $d=2r$. The position of each element $c_i = (x_i, y_i, z_i)$ is aligned along a parabolic surface, with its x and y components randomly distributed within a circular baseline of diameter D . Incoming collimated rays directed along the unit vector d_0 are assumed to reflect in the direction $d_{r,i}$ without diffracting as they propagate to the detector array (DA), which is placed at the focal plane of the paraboloid. Respective element and detector surface normals are n_i and n_d .

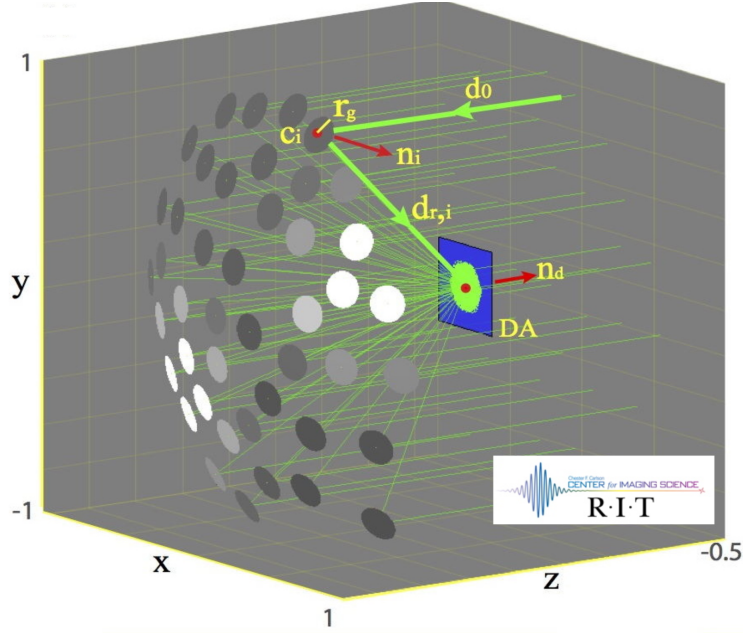


Figure 217. A geometric representation of the near field numerical model of a granular imager.

Near Field Numerical Model: In the near field regime, the numerical model ignores diffraction of the reflected light as it propagates from the aperture to the focal plane detector. That is, we assume the characteristic diffraction distance is much longer than the effective focal length: $\pi r_g^2/\lambda \gg f$. Circular reflective elements with radius r_g are randomly placed within D . Collimated light directed along the direction \mathbf{d}_o are diverted by the i^{th} aperture element along the direction $\mathbf{d}_{r,i}$. If the reflectors conformed to a paraboloid:

$$z = -(x^2+y^2)/4f + f \tag{131}$$

where f is the focal length of the paraboloid, the central reflected rays from each aperture element would coincide at the focal point. In that special case the direction angles of the normal vector of each reflector may be expressed as directional cosine as $\mathbf{n}_{i,0} = \cos^{-1}(\nabla z/|z|)$. In general, the normal vector of each reflector will suffer from random tip-tilt errors and thus the directional angles becomes

$$\mathbf{n}_i = \mathbf{n}_{i,0} + \Delta\theta_i \tag{132}$$

where $\Delta\theta_i = (\Delta\theta_{i,x}, \Delta\theta_{i,y})$ are pairwise independent Gaussian random variables with zero mean and variances σ_0 . The electric field within each reflected beam on the detector plane may be represented as a tilted plane wave scaled by an obliquity factor from both aperture element $\mathbf{d}_o \cdot \mathbf{n}_i$ and the angle upon the detector $\mathbf{d}_r \cdot \mathbf{n}_d$. With two point sources at infinity, the incoming rays are reflected from an element along unit

vectors \mathbf{d}_0^+ and \mathbf{d}_0^- . The two un-diffracted fields in the detection plane may be expressed:

$$E_i^\pm(\mathbf{u}_i, \lambda) = A_i^\pm \exp\left(\frac{ik\mathbf{d}_{r,i}^\pm \cdot \mathbf{u}_i}{\lambda}\right) \exp\left(\frac{ikL_i^\pm}{\lambda}\right) \quad (133)$$

where the amplitudes A_i are zero valued outside the projection area of the i^{th} aperture element, L are full path lengths of rays from the object to the i^{th} mirror and then to the detector, and $k=2\pi/\lambda$. For small angular deviations in the detector plane and for uniform luminous point sources, we make small angle approximations. For two mutually incoherent sources subtending an angle $2\theta_0$, we make use of the relation $\mathbf{d} \cdot \mathbf{d}^+ = \cos(2\theta_0)$. Defining the position vector on detector plane as $\mathbf{x}_d = (x_d, y_d)$, the measured irradiance may be expressed:

$$I(\mathbf{x}_d) = \sum_{\lambda} \left| \sum_{i=1}^M E_i^+(\mathbf{x}_d, \lambda) \right|^2 + \left| \sum_{i=1}^M E_i^-(\mathbf{x}_d, \lambda) \right|^2 \quad (134)$$

Reconstructed Near Field Numerical Images. Figure 218 shows a comparison of both the near field and far field reconstructed images for numerically modeled systems. In both cases a pair of images was reconstructed by use of multiframe blind deconvolution. In Figure 218, both sequences are generated with $M = 50$ non-overlapping sub-apertures (or reflecting elements), and having random tip-tilt error of $\sigma = 10 \lambda/D$ and piston error of $\Delta z = \lambda$. Each sequence consists of $N \sim 60$ images. Figure 218 (a) shows groundtruth image of the binary light sources, and the comparison of the line profile of the ground truth and the recovered results; Figure 218 (b) shows a typical far field image in the sequence, and enlarged part of recover result; Figure 218 (c) shows a typical near field image in the sequence, and enlarged part of recover result. Note that we further adapted the reconstruction algorithm to include lucky imaging and shift-and-add techniques. Although the near-field results appear to reproduce the expected ground truth image, we believe this method requires a deeper examination since there is little evidence of interference in the detector plane.

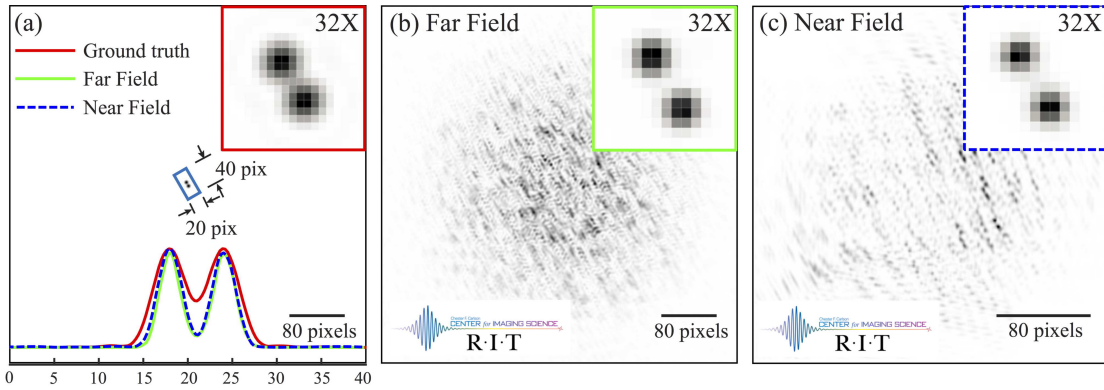


Figure 218. Comparison of image reconstruction results of multiframe blind deconvolution applied to a numerically simulated far field sequence and a near field sequence for monochromatic illumination.

Near Field Experiment: A schematic diagram of near-field experimental setup is shown in Figure 219. In Figure 219, a binary point source is generated by use of beam splitter BS1 and mirrors MIR1 and MIR2. The two beams subtend a non-zero angle and coincide at a glitter-coated black concave surface PS (bottom right). The focal plane ($f = 75$ mm) of the concave surface is reimaged on a detector DA by means of a beam splitter BS2 and relay lens RL. Spectral filter is not shown. Figure 219 (b) shows the glittered surface with each reflected surface having a characteristic size, d , (see magnified image) and illumination area having a diameter D . Spatially and spectrally filtered light was formed into a collimated quasi-monochromatic beam which was divided by a beam splitter (BS) to produce a mutually incoherent binary point source with an angle $\theta_0 \sim 1.5 \lambda/D$. The baseline of the beam has a diameter of $D = 12$ mm. Fine sized craft glitter, each having a diameter $d_g \sim 0.3$ mm, were used as aperture elements. The random aperture condition was achieved by randomly sprinkling glitter across a blackened concave lens (CL), with a focal length of $f_g = 75$ mm. After each image was recorded, the reflecting elements were removed, and a new random surface was prepared. The number of sub-apertures across the full $D = 12$ mm beam diameter ranged from $M = 100$ to 150. The second beam splitter (BS₂) was used to collect the reflected light and direct it toward the detector array of the same camera. Owing to space constraints, the detector could not be placed directly in the focal plane of the concave surface, and thus, a 150 mm relay lens (RL) was used. This configuration is called near field because the beamlets from each reflecting element undergo Fresnel diffraction (rather than Fraunhofer diffraction) upon reaching the detector. The diffraction length of a single reflecting element is l_g ranges from 260 to 450 mm, which is greater than $f_g = 75$ mm. The condition $l_g \gg f_g$ satisfies the near field condition. We assert that the system is nearly shift invariant since the elements roughly conform to a small patch of diameter D on the concave surface. However, as seen in the picture of glitter surface under a 10X microscope (Figure 192), the aperture elements display significant amount of tip-tilt and piston errors. In addition, roughness of the glitter surface is also noticed, which also explains the scattering light

shown in the recorded image. Figure 220 shows a typical near field image from glittered surface using quasi-monochromatic red light.

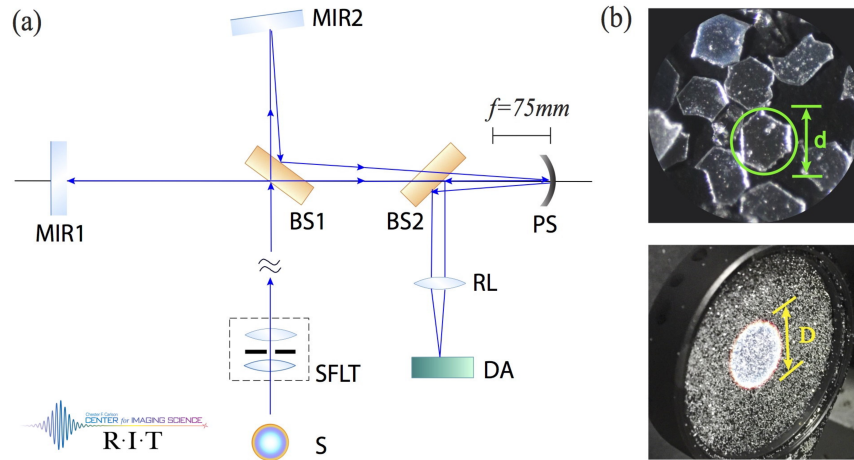


Figure 219. Schematic of randomized aperture imaging system for a near field experiment.

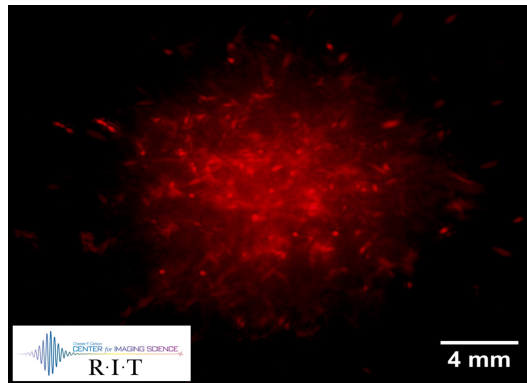


Figure 220. Typical near field image from glittered surface using quasi-monochromatic red light.

Reconstructed Near Field Experimental Images. We recorded $N=50$ glitter images. A typical image is shown above. Ground truth and restored images are shown below, showing good qualitative agreement between the two. Quantitatively, we find the distance between the intensity peaks are in good agreement, with an error of 5%. Furthermore the intensity peaks are equal to within 15%. This is remarkable considering the 10% bandwidth of the quasi-monochromatic light source, and the $\sim 15\lambda/D$ tip-tilt error and a likely piston error of at least several waves. The good agreement between the ground truth and reconstructed images in Figure 221 may be attributed to the high degree of shift invariance of the imaging systems. That is, the speckle data contains multiple overlapping pairs of binary images. The multiframe blind deconvolution scheme is successful at recovering the binary light source. As stated above, however, further study is needed to determine whether sufficient interference is creating the image or whether the numerical processing is simply identifying correlated pairs from independent incoherent glitter elements.

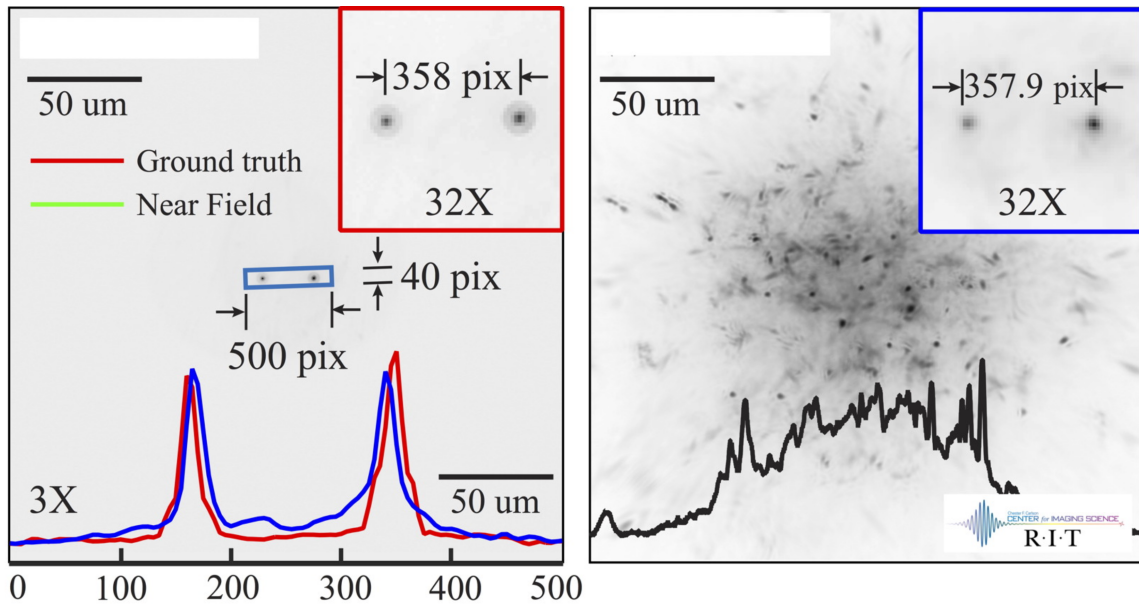


Figure 221. Comparison of ground truth and near field results.

1.2 Pathway for Development of a Technology Roadmap

Technology development for granular imaging systems is needed in several areas. Creating and maintaining a perfectly continuous surface is not likely to be achieved for some time, therefore, sophisticated image processing algorithms will be required to synthesize an astronomical image. For example, taking several short exposures and using speckle imaging techniques would allow for weaker tolerances on the reflective surface. Instead of correcting for atmospheric instabilities, as is typical for speckle imaging, we would correct for the small changes of the mirror surface due to the grains being constantly in motion. Multiframe blind deconvolution is a related technique to process multiple imperfect images to obtain a better estimate of the object. Utilizing multiple clouds, as an imaging array, would be a natural extension that would be applicable to speckle interferometry and increase the effective resolution of the system inversely proportional to the separation of clouds.

Further developments are needed in the area of multistage swarm modeling, simulation, guidance and control, involving both deterministic and probabilistic modeling approaches. The work carried out in Phase II most certainly contributed to these areas. Caltech and JPL are currently collaborating on a CubeSat mission, called the Autonomous Assembly and Reconfiguration Experiment for a Space Telescope (AAReST) and planned for launch in late 2016, that will demonstrate precision flying. Three CubeSat modules will be deployed at low Earth orbit, consisting of a primary module and two outriggers. The outriggers will detach and reattach to the primary module at different attachment points using magnetic latches and

formation/precision flying to change positions. Further testing and theoretical developments are also needed in the area of optical manipulation at large scales, particularly in optimal cloud cooling, trapping, corralling, optical sensing, and guidance via laser beam. Since system-level testing in space would be very costly, system-level and architectural demonstrations involving multiscale modeling and simulation of reflective, refractive, and diffractive architectures in the visible and radar bands will significantly advance the concept.

To enable these advancements, we plan to seek additional funding from other sponsors after Phase II: DARPA and the NASA OCT Game Changing Program, focusing the work on technology demos.

The roadmap for technology maturation, with the key technology milestones/demonstrations that would substantially advance the concept, includes: a) ground tech demos of optical cooling; b) ground tech demos of imaging of trapped cloud in formation with optical bench; c) microgravity demos of optical cooling and system autonomy in KC-135 or ISS; and e) orbital or suborbital low-cost tech demos of integrated optical cooling experiment with Cubesats.

12.1 Expected Technology Developments

Technology Gaps that were identified during Phase II were:

- Need to provide active damping mechanism to keep the particles in the primary mirror together
- Need to evaluate the possibility of obtaining high-res imaging using GI at radar wavelengths
- Need to explore the need for polarization control, and using grains that operate as metamaterials frequency selective surfaces
- Contemplate the GI having a gradient index of refraction, with different grain compositions (Gold reflects IR, Silver reflects visible & UV).

One developing technology we have assumed will continue to improve is fast steering mirrors that are also deformable mirrors. This is used to control both line-of-sight errors in our system and high-spatial frequency errors caused by thermal fluctuations in the cloud of particles. Northrop Grumman's AOA Xinetics is actively developing such mirrors and we can expect they will improve in control authority and number of actuators as our Orbiting Rainbows concept proceeds.

The fields of computational optics, wavefront sensing and control, and computational photography continue to develop at a rapid pace. Although our project has shown initial success with imaging a simulated binary star system through a fully-filled, glitter realization of our Orbiting Rainbows concept, we welcome further advances to reduce the stringent requirements placed on our particle-based mirrors. Since we plan to combine data from multiple images, "Lucky Imaging" is one emerging technology that will help us address image estimation.

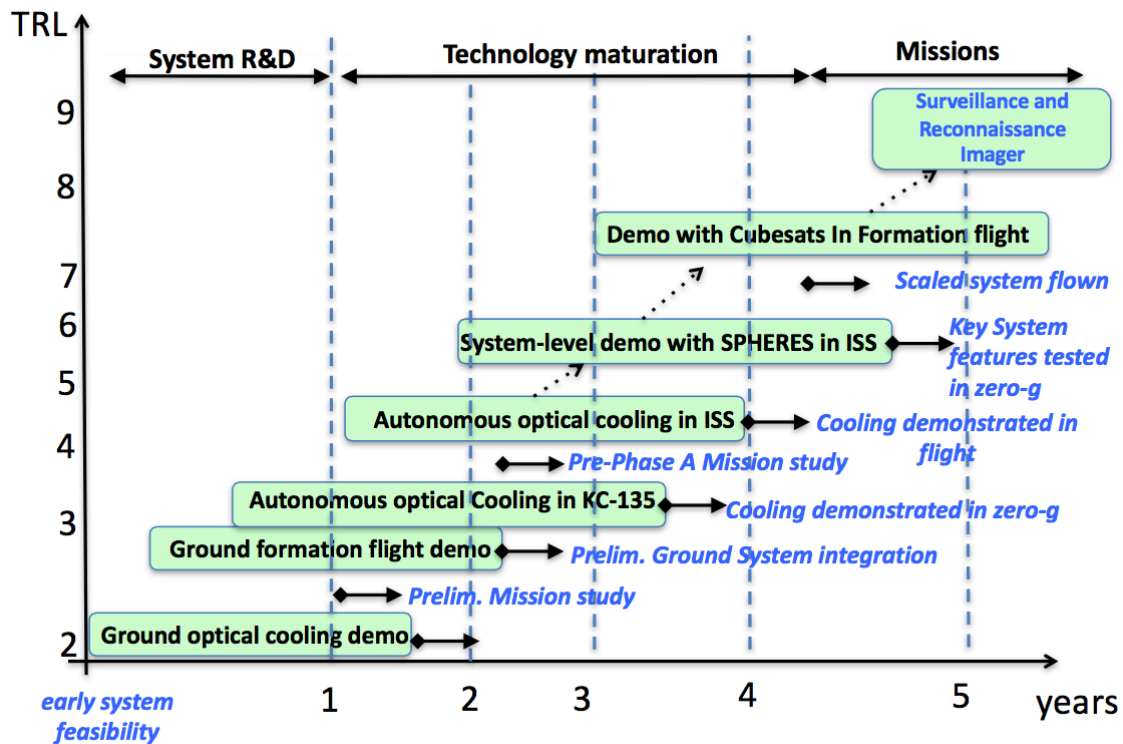


Figure 222. Proposed Roadmap.

12.2 Proposed roadmap

A proposed roadmap for technology maturation of the Orbiting Rainbows Task, with the key technology milestones/demonstrations that would substantially advance the concept, (shown in Figure 222) would include:

1. ground tech demos of imaging of levitated/trapped cloud in optical bench; TRL 3 to 4
 - a. prelim demo: testing of levitation/trapping capability
 - b. interim demo: testing of trapping plus incoherent imaging
 - c. final demo: system level coherent imaging test with minimal trapping capability
2. microgravity demos in KC-135 (only 20 seconds micro-g in parabolic flight) TRL 4 to 5
 - a. flight 1: testing of levitation/trapping capability
 - b. flight 2: testing of trapping plus incoherent imaging
 - c. flight 3: system level coherent imaging test with minimal trapping capability
3. microgravity demos in the ISS - International Space Station (smaller g-level than KC135, longer duration), TRL 5 to 6

- a. ISS rack experiments using reduced optical bench and small vacuum chamber, including: two lasers for cloud containment or electromagnetic trapping, vacuum bottle, grain release mechanism, laser reference source (reference star image), CCD detector (image plane), software processing capability to implement image reconstruction algorithm
4. orbital or suborbital low-cost tech demos of integrated system-level experiment with Cubesats: > TRL 5-6
 - a. flight 1: test of cloud release and containment from one/two Cubesats
 - b. flight 2: test of stabilization of cloud and Cubesats in formation
 - c. flight 3: system-level tests. Three Cubesats, spring ejected, micro thrusters used to maintain a simple equilateral triangle formation for duration of trapping/imaging experiment: two laser sources (one on each Cubesat), one of them releases grains, third Cubesat is optical bench where reference image is formed, and return light is recorded and processed.

13. Papers and reports written as a result of Phase II

Papers:

- Quadrelli, M., Basinger, S., Swartzlander, G.: Dynamics and Control of a Disordered System In Space, AIAA SPACE 2013 Conference, San Diego, Ca, Sept. 2013.
- Quadrelli, M., Basinger, S., Swartzlander, G., Arumugam, D.: Dynamics and Control of Granular Imaging Systems (AIAA 2015-4484), AIAA SPACE 2015 Conference and Exposition, 2015, 10.2514/6.2015-4484.
- Basinger, S., Palacios, D., Quadrelli, M., Swartzlander, G.: Optics of a granular imaging system (i.e. "orbiting rainbows"), Proceedings SPIE paper 9602-13, SPIE Optics/Photonics Conference, UV/Optical/IR Space Telescopes and Instruments: Innovative Technologies and Concepts VII, San Diego, CA, 9-13 August 2015.
- Quadrelli, B.M., Ius, P., Lanzoni, L.: Modeling and Simulation of Trapping Mechanisms of Granular Media In Space, presented at the AIAA SPACE 2016 Conference, Long Beach, CA, Sept. 2016.
- Peng, X., Ruane, G., Swartzlander, G., and Quadrelli, B.M.: Randomized Aperture Imaging, submitted to the Journal of the Optical Society of America – B, 2016.
- Quadrelli, B.M., and Sidick, E.: Unconventional Imaging with Contained Granular Media, to be presented at SPIE Optics and Photonics 2017.
- Quadrelli, B.M., and Bandyopadhyay, S.: Optimal Transport based Control of Granular Imaging Systems in Space, to be presented at 9th International Workshop on Satellite Constellations and Formation Flying, June 19-21, 2017, Univ. of Colorado, Boulder.

Theses:

- Paolo Ius, M.S. Thesis, Polytechnic of Turin (Italy), Physics models and simulation techniques for granular media trapping and control in space environment, February 2016.
- Luca Lanzoni, M.S. Thesis, Polytechnic of Milano (Italy): Physics models and simulation techniques for granular media behavior in space environment, Dec. 2016.

14. Findings and Recommendations

Inspired by the light scattering and focusing properties of distributed optical assemblies in Nature, such as rainbows and aerosols, and by recent laboratory successes in optical trapping and manipulation, we propose a unique combination of space optics and autonomous robotic system technology, to enable a new vision of space system architecture with applications to ultra-lightweight space optics and, ultimately, in-situ space system fabrication. We call this system the Granular Imager (GI).

The paradigm that makes this granular imager possible is based on: a) avoiding any physical structure and sensing/actuation hardware on the primary aperture, thus lowering the system cost (driven by the mass and complexity of the primary); b) using at-a-distance trapping and manipulation to confine and shape the cloud acting as primary aperture; and c) relaxing the optical figure control requirements by doing the best possible job in software with state-of-the-art computational imaging algorithms.

Typically, the cost of a space-borne imaging system is driven by the size and mass of the primary aperture. The solution that we propose uses a method to construct an imaging system in orbit in which the nonlinear optical properties of a cloud of reflective particles, shaped into a stable surface by electromagnetic means, allow one to form a lightweight aperture of an imaging system, hence reducing overall mass and cost. This new concept is based on recent understandings in the physics of optical manipulation of small particles in the laboratory and the engineering of distributed ensembles of spacecraft swarms to shape an orbiting cloud of micron-sized objects. In the same way that optical tweezers have revolutionized micro- and nano- manipulation of objects, our breakthrough concept will enable new large scale NASA mission applications and develop new technology in the areas of Astrophysical Imaging Systems and Remote Sensing because the cloud can operate as an adaptive optical imaging sensor. While achieving the feasibility of constructing one single aperture out of the cloud is the main topic of this work, it is clear that multiple orbiting aerosol lenses could also combine their power to synthesize a much larger aperture in space to enable challenging goals such as exo-planet detection. Furthermore, this effort could establish feasibility of key issues related to material properties, remote manipulation, and autonomy characteristics of cloud in orbit. There are several types of endeavors (science missions) that could be enabled by this type of approach, i.e. it can enable new astrophysical imaging systems, exo-planet search, large apertures allow for unprecedented high resolution to discern continents and important features of other planets, hyperspectral imaging, adaptive systems, spectroscopy imaging

through limb, and stable optical systems from Lagrange-points. Furthermore, future micro-miniaturization might hold promise of a further extension of our dust aperture concept to other more exciting smart dust concepts with other associated capabilities.

14.1 Findings

Our objective in Phase II was to experimentally and numerically investigate how to optically manipulate and maintain the shape of an orbiting cloud of dust-like matter so that it can function as an adaptable ultra-lightweight surface. Our solution is based on the aperture being an engineered granular medium, instead of a conventional monolithic aperture. This allows building of apertures at a reduced cost, enables extremely fault-tolerant apertures that cannot otherwise be made, and directly enables classes of missions for exoplanet detection based on Fourier spectroscopy with tight angular resolution and innovative radar systems for remote sensing. In this task, we have examined the advanced feasibility of a crosscutting concept that contributes new technological approaches for space imaging systems, autonomous systems, and space applications of optical manipulation. The proposed investigation has matured the concept that we started in Phase I to TRL 3, identifying technology gaps and candidate system architectures for the spaceborne cloud as an aperture.

In summary, the findings are the following:

- **Systems Engineering:** the systems engineering part of the study culminated in the determination of a preliminary set of numbers for systems mass, power, and cost for the Granular Imager. Technology readiness levels for the various component technologies were determined. Among these component technologies, in-flight confinement of the cloud is at the lowest TRL (TRL 2), while radar and adaptive optics methodologies are at TRL 9, indicating that priority must be given to the trapping and confinement techniques. Considerations on the effects of the space environment on the charges grains of a Granular Imager cloud, indicate that the Granular Imager cloud should be levitated in a buffer gas (Argon) inside an inflatable envelope, to eliminate the risk of orbital debris generation.
- **Multistage wavefront sensing and control:** The challenge of a wavefront control system for a granular imager is to correct for the scattered speckle field. It is unlikely that a single deformable optic will have both the range and control accuracy to correct for such roughness. Therefore, we opted for a staged control architecture. The wavefront control process follows the following steps: a) Granular Cloud Shaping – Grains are trapped in an optical trap, where they are shaped into a parabola; b) Sub Aperture Coarse Alignment – The trapped grains may be broken into regions or sub-apertures. Correcting for coarse misalignments between sub-apertures, corrects the low spatial frequency surface roughness of our granular imager, thereby making the PSF of the granular imager more compact; c) *Figure Control* – Now that each sub-aperture is controlled globally with respect to each other, we can control the figure of each

sub-aperture; d) *Computational Imaging* - A combination of PSF deconvolution techniques and computational imaging will be used to compensate for less-than-ideal imaging as a result of the granular nature of the primary mirror.

- **Application of Granular Imager to Exoplanet Search:** We presented some ideas regarding the optics and imaging aspects of a *granular spacecraft*. Granular spacecraft are complex systems composed of a spatially disordered distribution of a large number of elements, for instance a cloud of grains in orbit. An example of application is a spaceborne observatory for exoplanet imaging, where the primary aperture is a cloud instead of a monolithic aperture. The application considered so far was a reflective imaging system for astrophysics, but many unexplored applications of granular spacecraft are yet to be discovered.
- **Application of Granular Imager in Radar and Microwave bands:** Granular media in space can be used in the radar and microwave bands to enable imaging of previously inaccessible regions of targets with high geophysical variations with time, such as comets. The means of imaging, which includes a re-direction of energy, can permit higher resolution imaging as well. Applications include both tomographic and topographic radar imaging. The effect of the granular media cloud geometry plays a significant role in the scattering process. In addition, the spatial randomness effects the beam collimation and can have an effect on the imaging qualities as it effects effective aperture, coverage, and resolution of the radar techniques. These must be studied to inform about the control of the granular media clouds in space for future re-directed imaging applications. The techniques need to be studied for a specific set of tomographic and topographic applications. The tools and models will need to be advanced to permit application in three-dimensions, which will be required for the application studies. A system engineering study is also needed to study the applicability and feasibility of the technique, as well as an estimate of cost for typical space radar applications where a granular cloud media is to be used. A study is also advised to study the benefits of active vs. passive clouds, which includes imaging, cost, and applications.
- **Optical response:** we conducted experiments and simulation of the optical response of a granular lens. In all cases, the optical response, measured by the Modulation Transfer Function (MTF), of the hexagonal reflectors was closely comparable to that of the spherical mirror. We conducted the analyses further by evaluating the sensitivity to fill factor and grain shape, and we found a marked sensitivity to fill factor and no sensitivity to grain shape. However, we found that at fill factors as low as 30%, the reflection from a granular lens is still excellent. In fact, we replaced the monolithic primary of an existing integrated model of an optical system (W-First Coronagraph) with a granular lens, and we found that excellent contrast levels are provided by the granular lens that can be useful for exoplanet detection.
- **Image reconstruction techniques:** We numerically and experimentally

explored the concept of random aperture imaging system using random masks and phase masks for polychromatic light sources (400-730 nm). The diffraction limited resolution was achieved for a polychromatic binary light source using Multi-frame blind deconvolution techniques from both experimental (tip-tilt aberration about $5-10 \lambda/D$), and numerical data in presence of phase aberration up to $20\lambda/D$, and piston phase up to 1.5λ , and noise (SNR about 1.9 decibel). The agreement between the experimental and numerically models results verifies the accuracy of our model, allowing the model to be used as a tool to characterize the system performance when variable such as grain size, wavelength band, noise, or aberration is changed. We applied multiframe blind deconvolution to experimental and numerical data and found the expected image of a binary light source. Further study is suggested because significant interference is not evident. Without interference, the images of each member of the binary object would correspond to the size of an individual glitter. In contrast, interference would provide a size approaching the diffraction limit of the baseline.

- **Ion trapping experiments and simulations:** We developed techniques for the modeling and simulation of trapped granular media, within the context of the Granular Imager project. After describing the physics of trapped granular media in space, we discussed the methodologies used to stably confine and shape such a medium using electromagnetic fields. The numerical models have also been validated with results in the literature, obtaining excellent agreement. The results of the numerical tests indicate that it is possible, with structural arrangements of rings and plates at different levels of electrostatic potential, to stably confine one or more charged particles, when driven by voltages that can be modulated in time and space. On the experimental side, we have successfully stably levitated single particles and aggregates of multiple particles inside an ion trap. While the ion trap technique is very promising for the Granular Imager, we were able to levitate grains with a q/m ration comparable to that of 10-100 micron grains (mass of the order of the nanogram, and charges of the order of 10^5 electron charges). We were successful in stably trapping and levitating single particles and aggregates of particles in air. Once levitated, these clouds of grains displayed a remarkable regularity and stability over time, typical of Coulomb crystal behavior. This was expected. The particles used were in the 30-100 micron diameter range. The charge to mass ratio of the ion trap was tailored for optimal levitation of nanogram particles, so larger size grains could not be contained due to their excessive mass. Consequently, further work will require ion traps with larger electrostatic potentials, or particles with larger electron charge to compensate for the larger mass.
- **Buoyant liquid experiments:** The dynamics of a hemisphere in a near-neutral buoyant liquid was found to exhibit the characteristics predicted in our numerical model. The hemisphere exhibited light induced translation and rotation. Further modeling is required to explore whether a similar orientation would occur if laser heating of the liquid produced a flow that torques the

particle. Overall, the buoyant liquid experiments were not conclusive due to spurious induced thermal disturbances, and prompted the need to consider alternative levitation techniques such as electrostatic, magnetic, or acoustic.

- **Magnetic and acoustic levitation:** The intrinsic transverse stiffness of magnetic traps make them ill-suited for demonstrations of radiation pressure unless the trapped particles are very small. There are confounding effects that also make magnetic traps non-ideal for this work. For example, the magnetic susceptibility is temperature dependent, and thus laser heating may form hot-spots in the diamagnetic materials that will cause light-induced motion from temperature induced magnetic inhomogeneity. This will mask the effect of radiation pressure. The observation of radiation pressure dynamics will be difficult owing to eddy current damping. An acoustic levitation apparatus appears to be a promising method of providing two degrees of freedom to an optical element without the negative consequences of surface contact forces or heating of a buoyancy-reducing liquid. Unlike optics with benefits from coherent lasers with planar wave fronts, the waves emitted from acoustic sources are seldom characterized. There are many components and parameters which affect the acoustic wave front, including complicated compression driver designs, the frequency and output power, horn impedance, diaphragm distortion from the reflected wave, and heating of the voice coil. Although the speaker was driven in the ultrasonic frequency range, we could hear distinct hissing from the speaker, owing to the fact that we were driving them very hard. While we were successful at levitating optical elements, continued work is needed to achieve a larger trapping area and a more robust acoustic emission source.

14.2 Recommendations

To make the Granular Imager a reality, we recommend the following:

- An extensive ground testing program to further experiment with levitation techniques of confined granular media, and with guiding techniques enabling precision positioning and pointing of cluster of reflective grains
- Need to evaluate the idea of changing the primary mirror particle density for different types of telescope (Closer particle density --> UV telescope, Less dense particles --> IR telescope)
- Determine if the system requires a Sun-shade for thermal stabilization
- Determine how the GI parameters (e.g., fill factor, area, density, etc.) should be changed to allow the GI telescope to allow follow-up observations within a larger timeline
- Determine the cross-over point in terms of the number of photons between a glass mirror and a GI primary mirror
- Determine if the GI can make polarization measurements
- Conduct a specific trade study between a continuous membrane vs. a GI aperture for different sizes
- Strive to infuse the GI technology development in the next NASA decadal survey.

Our concept is to ultimately enable the large-scale electromagnetic utilization of an active cloud of incoherent matter. Near-term proof-of-concept space demonstrations might be possible within a decade, but laboratory-scale tests on Earth are possible much sooner. This concept is technically feasible given that it is drawn from real-world examples of dust/droplet systems like rainbows. Our solution would completely rewrite our approach to ultra-large space-based telescopes for potential NASA applications. All the foundations of the concept are solidly based on established physical laws. The challenge is extending what has been proven in small lenses in an Earth environment to a space environment under various forces and the means to predict and control those forces for a long time to get the full benefit of the concept. There is no guarantee that this breakthrough innovative system will meet the configuration or design of a large aperture system at various parts of the electromagnetic spectrum, but even if a few of those areas are or can be identified, the benefit to NASA will be immense.

15. Bibliography

- [Andersen2011] Andersen, T., and Enmark, A.: Integrated Modeling of Telescopes, Springer Astrophysics and Space Science Library, vol. 377, 2011.
- [Ashkin1970] Ashkin, A.: Acceleration and trapping of particles by radiation pressure, Phys. Rev. Lett. 24. 156-159, 1970.
- [Ashkin1978] Ashkin, A.: Trapping of atoms by resonance radiation pressure, Phys. Rev. Lett. 40. 729-732, 1978
- [Ashkin1986] Ashkin, A., Dziedzic, J.M., Bjorkholm, J.E., and Chu, S., Observation of a single-beam gradient force optical trap for dielectric particles, Optics Letters 11(5), pp. 288–290, 1986.
- [Ashkin1997] Ashkin, A., Optical trapping and manipulation of neutral particles using lasers, Proc. Natl. Acad. Sci. 94, 4853-4860 (1997)].
- [Ayers1988] Ayers, G.R., Dainty, J.C., “Iterative blind deconvolution method and its applications,” Optics Letters Vol. 13 No. 7 (1988)
- [Ball] <http://www.ballaerospace.com/page.jsp?page=259>
- [Bandyopadhyay2014] Bandyopadhyay, S., Chung, S.-J., and Hadaegh, F. Y., “Probabilistic Swarm Guidance using Optimal Transport,” Proc. IEEE Conf. Control Applicat., Antibes, France, Oct. 2014, pp. 498–505.
- [Barton2001] Barton, I.M., Britten, J.A., Dixit, S.N., Summers, L.J., Thomas, I.M., Rushford, M.C., Lu, K., Hyde, R.A. and Perry, M.D., “Fabrication of large-aperture lightweight diffractive lenses for use in space,” Applied Optics, 40(4) 447-451 (2001).
- [Beavers1989] Beavers, W.I., Dudgeon, D.E., Beletic, J.W., and Lane, M.T., “Speckle Imaging through the Atmosphere,” The Lincoln Laboratory Journal, Vol. 2, Number 2 (1989).
- [Bekey1999] Bekey, I.: An extremely large, yet ultra-lightweight space telescope and array, NIAC Phase I report, 1999.
- [Bekey2005] Bekey, I.: Extremely Large Swarm Array of Picosats from Microwave/RF Earth Sensing, Radiometry and Mapping, NIAC Phase I report, 2005.

- [Bohren1998] Bohren CF, Huffman DR. Absorption and scattering of light by small particles. New York: Wiley-Interscience; 1998.
- [BornWolf1964] Born, M., and Wolf, E.: Principles of Optics, 2nd edition, Pergamon Press, 1964, pp. 400
- [Brady2009] Brady, D.J., Hagen, N.: Multiscale lens design, *Opt. Express* 17, 10659-10674, 2009
- [Chrichton2000] Philip L. Marston and James H. Crichton: Radiation torque on a sphere caused by a circularly-polarized electromagnetic wave, *Phys. Rev. A* **30**, 2508, 1984.
- [Cubesat2016] Cubesat NRC report, <http://www.nap.edu/catalog/23503/achieving-science-with-cubesats-thinking-inside-the-box> [NASA2007] Science Plan for NASA's Science Mission Directorate, 2007-2016.
- [Davis2012] Davis, E.J., and Schweiger, G.: *The Airborne Microparticle*, Springer, 2012.
- [Dienerowitz2010] Dienerowitz, M.: Plasmonic Effects upon Optical Trapping of Metal Nanoparticles, PhD Thesis University of St. Andrews, U.K., 2010.
- [Etkin2000] Etkin, B.: *Dynamics of Atmospheric Flight*. Dover Publications, 2000.
- [Fienup1980] Fienup, J.R. and Feldkamp, G.B., "Astronomical Imaging By Processing Stellar Speckle Interferometry Data," *SPIE Proc.* 243-16 (1980).
- [Friedlander1977] Friedlander, S. K.: *Smoke, Dust, and Haze*, John Wiley & Sons, 1977.
- [Fuchs1989] Fuchs, N.A.: *The Mechanics of Aerosols*, Dover Publications, 1989.
- [Giveon2007] Give'on A. et al., "Broadband wavefront correction algorithm for high-contrast imaging systems," *Astronomical Adaptive Optics Systems and Applications III*, edited by Robert K. Tyson, Michael Lloyd-Hart, *Proc. Of SPIE Vol. 6691*, 66910A, (2007).
- [Giveon2006] Give'on A., Kasdin N.J., Vanderbei R.J., and Avitzour Y., "On representing and correcting wavefront errors in high-contrast imaging systems." *JOSA A*, 23, May (2006).
- [Gonsalves1982] Gonsalves, R.A., "Phase retrieval and diversity in adaptive optics," *Opt. Eng.* 21, 829-832 (1982).
- [Gosh1995] Gosh, P.K.: *Ion Traps*, Clarendon Press, Oxford 1995.
- [Grzegorzcyk2006a] Grzegorzcyk, T., Kemp, B. A., Kong, J.A.: Trapping and binding of an arbitrary number of cylindrical particles in an in-plane electromagnetic field, *J. Opt. Soc. Am. A*, 23(9) Sept. 2006.
- [Grzegorzcyk2006b] Grzegorzcyk, T., Kemp, B. A., Kong, J.A.: Passive guiding and sorting of small particles with optical binding forces, *Opt. Lett.*, 31(22), Nov. 2006.
- [Grzegorzcyk2014] Tomasz M. Grzegorzcyk et al.: Optical Mirror from Laser-Trapped Mesoscopic Particles, *Physical Review Letters*, 112, 023902 (2014).
- [Gu2006] Xiang Gu; Yunhua Zhang; Xiangkun Zhang, "Near-Field Radar Imaging Simulation using FDTD Method," *Antennas, Propagation & EM Theory*, 2006. ISAPE '06, 26-29 Oct. 2006. doi: 10.1109/ISAPE.2006.3532
- [Hyde2003] Hyde, R.A., "Eyeglass: Large Aperture, Lightweight Space Optics", LLNL Report UCRL-ID-151390 (2003).
- [Ingleby2005] Ingleby, H.R. and McGaughey, D.R., "Real data results with wavelength-diverse blind deconvolution," *Opt. Lett.* 30 No. 5, 489-491 (2005).
- [Irvine1965] Irvine, W. M., Light scattering by spherical particles: Radiation pressure, asymmetry factor, and extinction cross section, *J. Opt. Soc. Am.* 55, 16-21 (1965)

- [Jee1988] Jee, Y., Becker, M. R., and Walser, R. M., Laser-induced damage on single-crystal metal surfaces, *J. Opt. Soc. Am. B* 5, 648-659 (1988)
- [Kokhanovsky2006] Kokhanovsky, A. A.: *Cloud Optics*, Springer, 2006.
- [Kundur1996] Kundur, D. and Hatzinakos, D., "Blind Image Deconvolution," *IEEE Signal Process. Mag.* 13, 43-64 (1996).
- [Labeyrie1979] Labeyrie, A.: *Standing Wave and Pellicle: A Possible Approach to Very Large Space Telescopes*, *Astronomy and Astrophysics*, 77, L1-L2, 1979.
- [Labeyrie2005] Labeyrie, A., M. Guillon and J.-M. Fournier: *Optics of "Laser Trapped Mirrors" for large telescopes and hypertelescopes in space*, *SPIE Proc.* 5899, 2005.
- [Labeyrie1970] Labeyrie, A.: *Attainment of diffraction limited resolution in large telescopes by Fourier analysing speckle patterns in star images*. *Astron. Astrophys.* 6(1):85–87, 1970.
- [Lee1990] Lee SC. *Dependent scattering of an obliquely incident plane wave by a collection of parallel cylinders*. *J Appl Phys* 1990;68(10):4952–7.
- [Lewis2011] Lewis, W. E., et al: *Geostationary Doppler Radar and tropical cyclone surveillance*, *J. Atmos. Ocean. Tech.*, 2011, DOI: 10.1175/JTECH-D-11-00060.1.
- [Li2005] Li, Xu; Taflove, Allen; Backman, Vadim, "Modified FDTD near-to-far-field transformation for improved backscattering calculation of strongly forward-scattering objects," *Antennas and Wireless Propagation Letters, IEEE*, vol.4, no., pp.35,38, 2005. doi:10.1109/LAWP.2005.845038
- [Lo2006] Lo, A.S. and Arenberg, J., "Architectures for space astronomical telescopes using Fresnel optics", *Proc. SPIE 6265, Space Telescopes and Instrumentation I*, (June 2006).
- [Major2005] Major, F.G., V.N. Gheorghe, and G. Werth: *Charged Particle Traps. Physics and Techniques of Charged Particle Field Confinement*, Springer, 2005.
- [Markley2007] Markley, L., et al. "Averaging Quaternions", *Journal of Guidance, Control, and Dynamics*, Vol. 30, No. 4 (2007), pp. 1193-1197.
- [McCormack2006] McCormack, et al., *Laser Trapping of Mirrors in Space*, NIAC Phase I report, 2006.
- [Meinel2002a] A.B. Meinel, A.B. and Meinel, M.P., "Large membrane space optics: Imagery and aberrations of diffractive and holographic achromatized elements of high diffraction order," *Opt Eng* 41(8), pp 1995-2007 (2002).
- [Meinel2002b] Meinel, A.B. and Meinel, M.P., "Parametric dependencies of high-diffraction-order achromatized aplanatic configuration that employ circular or cross-linear diffractive optical elements," *AO* 41(34), pp 7155-7166 (2002).
- [Mettler2005] Mettler E., Breckenridge W.G., and Quadrelli M.B.: *Large Aperture Telescopes in Formation: Modeling, Metrology, and Control*, *The Journal of the Astronautical Sciences*, vol. 53, no.5 October-December 2005, pp.391-412.
- [Mettler2004] Mettler, E., et al: *Earth atmosphere observatory formation at L2*, *AIAA Space 2004 Conference and Exposition*.
- [Michel2012] Michel, R., et al: *A Geostationary Optical Seismometer, Proof of Concept*, *IEEE Transactions on Geoscience and Remote Sensing*, vol. 51, no. 1, Jan. 2012, 695.
- [Mosier1998] Mosier, G., M., Fermiano, K. Ha, P. Bely, R. Burg, D. Redding, A. Kissil, J. Rackozy, L. Craig: "Fine Pointing and Control for a Next generation Space Telescope, Part of the SPIE Conference on Space Telescopes and Instruments, V, Kona, Hawaii. March 1998.

- [Mosier2000] Mosier, G., Parrish, K., Fermiano, M., Redding, D., Kissil, A., Papalexandris, M., Craig, L., Page, T., and Shunk, R.: NGST Performance Analysis using Integrated Modeling, NGST Monograph, no. 6, August 2000, Publication of the Next Generation Space Telescope Project Office, <http://www.jwst.nasa.gov/doclist/bytitle.html>.
- [MOIRE] [http://www.darpa.mil/Our_Work/TTO/Programs/Membrane_Optic_Imager_Real-Time_Exploitation_\(MOIRE\).aspx](http://www.darpa.mil/Our_Work/TTO/Programs/Membrane_Optic_Imager_Real-Time_Exploitation_(MOIRE).aspx)
- [Molmud1960] Molmud, P., "Expansion of a Rarefield Gas Cloud into a Vacuum," *The Physics of Fluids* 3, 362-366 (1960).
- [Mulser1985] Mulser, P. Radiation pressure on macroscopic bodies, *J. Opt. Soc. Am. B* 2, 1814-1829 (1985)
- [NASA2004] NASA Earth Science Technology Office, "Active and Passive Microwave Technologies Working Group Report", 2004
- [NASAESTO2016a] NASA ESTO Lidar Investment Strategy Update Community Forum - February 24, 2016
- [NASAESTO2016b] NASA ESTO Microwave Remote Sensing Investment Strategy Update Community Forum - March 17, 2016
- [NRC2007] NRC-DS, 2007: Earth Science and Applications from Space: National Imperatives for the Next Decade and Beyond. National Research Council, The National Academies, Committee on Earth Science and Applications from Space: Community Assessment and Strategy for Future, The National Academies Press, Washington, D.C., ISBN: 978-0-309-10387-9, 476 pp.
- [Palmer1980] Palmer, A.J.: Nonlinear Optics in Aerosols, *Optics Letters*, vol. 5, no. 2, February 1980
- [Palmer1983] Palmer, A.J.: Plasmon-Resonant Aerosols for Space Optics, *J. OP. Soc. America*, vol. 73, no. 11, November 1983.
- [Palmer1991] Palmer, A.J.: Radiation-induced Orientation of Atmospheric Aerosols, *J. OP. Soc. America A*, vol. 8, no. 2, February 1991.
- [Paxman1992] Paxman, R.G., Schulz, T.J. and Fienup, J.R., "Joint estimation of object and aberrations by using phase diversity," *J. Opt. Soc. Am. A*, Vol. 9, No. 7 (1992).
- [Peng2016] Peng, X., Ruane, G., Swartzlander, G., and Quadrelli, B.M.: Randomized Aperture Imaging, submitted to the *Journal of the Optical Society of America – B*, 2016.
- [Peral2015] Peral E., S. Tanelli, Z. Haddad, O. Sy, G. Stephens and E. Im, "Raincube: A proposed constellation of precipitation profiling radars in CubeSat," 2015 IEEE IGARSS, Milan, 2015, pp. 1261-1264. doi: 10.1109/IGARSS.2015.7326003
- [Pratt1972] Pratt, W.K., "Generalized Wiener Filtering Computation Techniques", *IEEE Transactions on computers*, c-21 (7), (July 1972).
- [Quadrelli2003] Quadrelli, M.B: Dynamics and Control of Novel Orbiting Formations with Internal Dynamics, in *The Journal of the Astronautical Sciences*, vol.51, no. 3, July-September 2003, pp. 319-337.
- [Quadrelli2012] NIAC Phase 1 Final Report on Orbiting Rainbows, http://www.nasa.gov/directorates/spacetech/niac/2012_phase_I_fellows_quadrelli.html#U4KL68bxVEI
- [Quadrelli2013] Quadrelli, M., Basinger, S., Swartzlander, G.: Dynamics and Control of a Disordered System In Space, AIAA SPACE 2013 Conference, San Diego, Ca, Sept. 2013.

- [Quadrelli2015a] Marco B. Quadrelli, Scott Basinger, Grover Swartzlander, Darmin Arumugam: Dynamics and Control of Granular Imaging Systems (AIAA 2015-4484), AIAA SPACE 2015 Conference and Exposition, 2015, 10.2514/6.2015-4484.
- [Quadrelli2015b] Scott A. Basinger, David M. Palacios, Marco B. Quadrelli, Grover A. Swartzlander: Optics of a granular imaging system (i.e. “orbiting rainbows”), Proceedings SPIE paper 9602-13, SPIE Optics/Photonics Conference, UV/Optical/IR Space Telescopes and Instruments: Innovative Technologies and Concepts VII, San Diego, CA, 9-13 August 2015.
- [Quadrelli2016] Quadrelli, B.M., Ius, P., Lanzoni, L.: Modeling and Simulation of Trapping Mechanisms of Granular Media In Space, presented at the AIAA SPACE 2016 Conference, Long Beach, CA, Sept. 2016.
- [Shapiro1964] Shapiro, I.I., Jones, H.M., Perkins, C. W.: Orbital Properties of the West Ford Dipole Belt, Proceedings of the IEEE, May 1964.
- [Shvedov2010] Vladlen G. Shvedov, Andrei V. Rode, Yana V. Izdebskaya, Anton S. Desyatnikov, Wieslaw Krolikowski, and Yuri S. Kivshar: Giant Optical Manipulation, Phys. Rev. Lett. 105, 118103 (2010).
- [Schafer2008] Schafer J, Kienle A. Scattering of light by multiple dielectric cylinders: comparison of radiative transfer and Maxwell theory. Opt Lett 2008;33(20):2413–5.
- [Scharmer2010] Scharmer, G.B., Lofdahl, M.G., van Werkhoven, T.I.M. de la Cruz Rodriguex, J., “High-order aberration compensation with multi-frame blind deconvolution and phase diversity image restoration techniques”, A&A Vol. 521, A68 (2010).
- [Scheider2010] Understanding the Finite-Difference Time-Domain Method, John B. Schneider, www.eecs.wsu.edu/~schneidj/ufdtd, 2010.
- [Schroeder2000] Schroeder, D.: Astronomical Optics, Academic Press, 2000.
- [Schulz1993] Schulz, T.J., “Multiframe blind deconvolution of astronomical images”, J. Opt. Soc. Am A, 10:1064-1073, 1993.
- [Shuster2014] Shuster, D.G.: “Dynamic Response of Dielectric Lenses Influenced by Radiation Pressure”. Master's thesis. Rochester Institute of Technology, 2014.
- [Simpson2012] Simpson, S. H., Hanna, S., Peterson, T. J., and Swartzlander, G. A. Jr. Optical lift from dielectric semicylinders, Optics Letters 37, 4038-4040 (2012).
- [Smith2007] Smith, E.A., et al: 2007b: NIS White Paper. [Available at <http://nis.ssec.wisc.edu/>]
- [Stahl2010] Stahl, H. P., Survey of Cost Models for Space Telescopes, Optical Engineering, Vol. 49, No. 5, May 2010.
- [Stevens2016] Stevens, B.L., Lewis, F.L., Johnson, E.N.: Aircraft Control and Simulation, Wiley, 2016.
- [Summers2009] Summers, M. D.: Optical Micromanipulation of Aerosols, PhD Thesis University of St. Andrews, U.K., 2009.
- [Swartzlander2011] Swartzlander G. A., Peterson, T. J., Artusio-Glimpse A. B., Raisanen A. D.: Stable optical lift. Nature Photonics, Nature Photonics 5, pp.48–51, 2011.
- [Taflove2000] A. Taflove and S. Hagness, Computational Electrodynamics - the finite difference time-domain method, 2nd ed. Norwood, MA: Artech House, 2000, pp. 197–201.
- [Tan2010] Tan, T.; Potter, M., "Optimized Analytic Field Propagator (O-AFP) for Plane Wave Injection in FDTD Simulations," Antennas and Propagation, IEEE

- Transactions on, vol.58, no.3, pp.824,831, March 2010. doi: 10.1109/TAP.2009.2039310.
- [Thurman2010] S.T. Thurman and J.R. Fienup, "Application of the General Image Quality Equation to Aberrated Imagery," *Appl. Opt.* 49, 2132-2142 (2010).
- [Trauger2014] Trauger, J., Moody, D. and Gordon, B., "Complex apodized Lyot coronagraph for exoplanet imaging with partially obscured telescope apertures", *Techniques and Instrumentation for Detection of Exoplanets VI*, edited by Stuart Shaklan, *Proc. of SPIE 2014*, Vol. 8864, 886412.
- [Tsiotras1996] Tsiotras, P., Longuski, J.M.: Analytic Solution of Euler's Equations of Motion for an Asymmetric Rigid Body". In: *ASME Journal of Applied Mechanics*, Vol 63, No. 1, pp.149-155, 1996.
- [Tyson1997] Tyson, R., *Principles of Adaptive Optics*, Academic Press, 1997.
- [vanKampen1998] van Kampen, W. and Paxman, R.G., "Multi-Frame Blind Deconvolution of Infinite-Extent Objects", *Proc. SPIE Vol. 3433*, Propagation and imaging through the Atmosphere II (July 1998).
- [Verma2008] Verma, N.K.: Multiparticle Trajectory Simulation for Ion Trap Mass Spectrometers, M.A. Thesis, Indian Institute of Technology, July 2008.
- [Villani2008] Villani, C., *Optimal transport: Old and New*, Springer Verlag, 2008.
- [Weigelt1977] Weigelt, Gerd, "Modified astronomical speckle interferometry 'speckle masking'," *Optical Communications* 21 (1) 55 (1977).
- [Yavuz1964] Yavuz, D.: Frequency and Focal Region Properties of Random Sparse Arrays, *IEEE Transactions on Antennas and Propagation*, vol. AP-32, no. 5, May 1964.
- [Zhao2005] Zhao, F.: Development of high-precision laser heterodyne metrology gauges, *SPIE Proc. Vol. 5634*, 14 Feb. 2005, *Advanced Sensor Systems and Applications II*, Yun-Jiang Rao; Osuk Y. Kwon; Gang-Ding Peng, Editors, pp.247-259.
- [Zaroodny1955] S. J. Zaroodny, An Elementary Review Of The Mathieu-Hill Equation Of Real Variable Based On Numerical Solutions, Memorandum Report No. 878, APRIL 1955, pp.6-7.
- [Zipfel2000] Zipfel, P.: *Modeling and Simulation of Aerospace Vehicle Dynamics*, AIAA Education Series, 2000.